

AD-A083 703

COLLEGE OF AERONAUTICS CRANFIELD (ENGLAND)

F/G 20/4

INVESTIGATION OF THREE-DIMENSIONAL SHOCK WAVE BOUNDARY LAYER IN--ETC(U)

JAN 80 H KUBOTA

AFOSR-76-3006

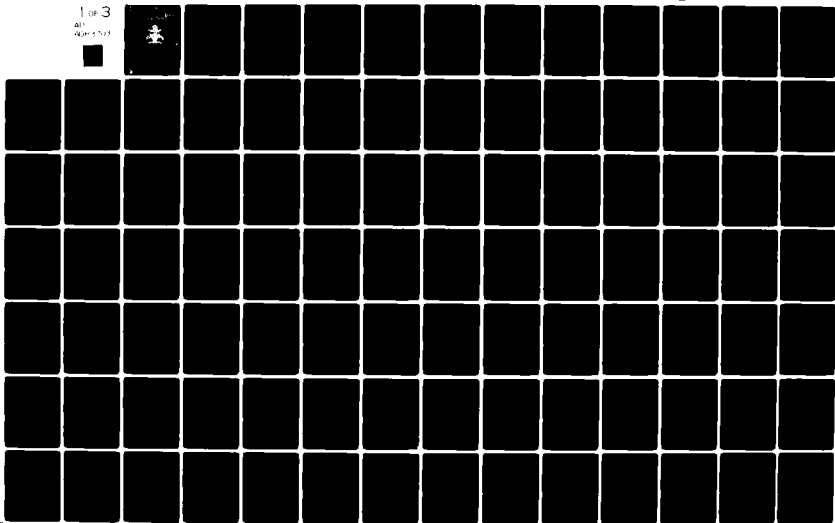
COA-8001

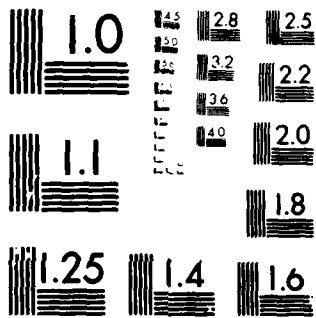
NL

UNCLASSIFIED

1 of 3

AD-A083 703





MICROCOPY RESOLUTION TEST CHART  
NATIONAL BUREAU OF STANDARDS-1963-A

②

LEVEL

# Cranfield

College of Aeronautics

ADA083703



DTIC  
ELECTE  
S APR 29 1980 D  
A

## INVESTIGATIONS OF THREE-DIMENSIONAL SHOCK WAVE BOUNDARY LAYER INTERACTIONS.

H. Kubota

January 1980

FINAL SCIENTIFIC REPORT for the period : JUNE 1976 - OCTOBER 1979.

Approved for public release ; distribution unlimited

PREPARED FOR AIR FORCE WRIGHT AERONAUTICAL LABORATORIES , UNITED STATES AIR FORCE  
AND  
EUROPEAN OFFICE OF AEROSPACE RESEARCH AND DEVELOPMENT , LONDON , ENGLAND.

FINAL FILE COPY

80 4 28 114

UNCLASSIFIED

SECURITY CLASSIFICATION OF THIS PAGE (When Data Entered)

REPORT DOCUMENTATION PAGE		14 READ INSTRUCTIONS BEFORE COMPLETING FORM
1. REPORT NUMBER	2. GOVT ACCESSION NO.	3. RECIPIENT'S CATALOG NUMBER
	AD-A083 703	COA-8001
4. TITLE (and Subtitle) INVESTIGATION OF THREE-DIMENSIONAL SHOCK WAVE BOUNDARY LAYER INTERACTIONS. (A Flow-Field Model of the Glancing Shock/Turbulent Boundary Layer Interaction).		5. TYPE OF REPORT & PERIOD COVERED Final Scientific Report June 1976 - October 1979
7. AUTHOR(s) 10 H. KUBOTA		6. PERFORMING ORG. REPORT NUMBER C o A Report 8001
9. PERFORMING ORGANIZATION NAME AND ADDRESS College of Aeronautics, <del>Cranfield Institute of Technology,</del> Cranfield, Bedford MK43 0AL, (England.)		8. CONTRACT OR GRANT NUMBER(s) 15 AFOSR-76-3006 New
11. CONTROLLING OFFICE NAME AND ADDRESS AFFDL/FXG Wright Patterson AFB, Ohio 45433		10. PROGRAM ELEMENT, PROJECT, TASK AREA & WORK UNIT NUMBERS
14. MONITORING AGENCY NAME & ADDRESS (if different from Controlling Office) EOARD/LNV Box 14 FPO N.Y. 09510		12. REPORT DATE 11 January 1980
		13. NUMBER OF PAGES 242 12 243
		15. SECURITY CLASS. (of this report) Unclassified
		15a. DECLASSIFICATION/DOWNGRADING SCHEDULE
16. DISTRIBUTION STATEMENT (of this Report) Approved for Public Release, Distribution Unlimited.		
17. DISTRIBUTION STATEMENT (of the abstract entered in Block 20, if different from Report)		
18. SUPPLEMENTARY NOTES		
19. KEY WORDS (Continue on reverse side if necessary and identify by block number) Three-Dimensional Separation      Shock Wave/Boundary Layer Interaction Turbulent Boundary Layer Flow Field Description Surface Measurement		
20. ABSTRACT (Continue on reverse side if necessary and identify by block number) Three-dimensional glancing-shock/turbulent boundary-layer interaction has been investigated at the Cranfield Institute of Technology in two separate test programmes using a 2.5 x 2.5 inch intermittent tunnel and a 9 x 9 inch continuous tunnel, at a Mach number of approximately 2.5. The experimental results include oil-flow pictures, vapour-screen photographs, surface static pressure distributions, local heat transfers, liquid crystal pictures of surface temperature, and viscous layer surveys. Contd...		

087350

The test data indicate that the interaction region consists of two different viscous flows, (1) the side-wall boundary layer and (2) an induced layer originating near the shock generator root and crossing the path of the side-wall boundary layer. In this flow field model, no flow separation appears as long as the surface stream lines of the side-wall boundary layer can be pliable enough to be bent along the edge of the induced layer, even when the surface-flow deflection exceeds the shock angle. However, an ordinary separation does take place when the induced layer forces the surface stream lines to deflect beyond a maximum permissible angle.

Approved For	<input checked="" type="checkbox"/>
WHIS Class	<input type="checkbox"/>
DDC TAB	<input type="checkbox"/>
Unannounced	<input type="checkbox"/>
Justification	<input type="checkbox"/>
By	
Dist	
Availability	
Dist	special

## C O N T E N T S

1. INTRODUCTION
  - 1.1. Shock Boundary-Layer Interaction
  - 1.2. The Present Experimental Study
  
2. EXPERIMENTAL PROGRAMMES
  - 2.1. 2.5 x 2.5 Inch Wind Tunnel Test Programme
    - 2.1.1. Wind Tunnel Facility and the Test Conditions
    - 2.1.2. Test Configuration
    - 2.1.3. Test Techniques
  - 2.2. 9 x 9 Inch Wind Tunnel Test Programme
    - 2.2.1. Wind Tunnel Facility and the Test Conditions
    - 2.2.2. Test Configuration
    - 2.2.3. Test Techniques
  
3. EXPERIMENTAL TECHNIQUES AND THE ARRANGEMENTS
  - 3.1. Schlieren Techniques
  - 3.2. Oil-Flow Pictures
  - 3.3. Vapour-Screen Pictures
  - 3.4. Static Pressure Distribution Measurements
  - 3.5. Heat Transfer Measurements
    - 3.5.1. A Modified Princeton University Slug Calorimeter Technique
    - 3.5.2. Thin-Film-Gauge Calorimeter Technique
  - 3.6. Encapsulated Liquid Crystal Technique
  - 3.7. Viscous Layer Surveys
  
4. EXPERIMENTAL RESULTS
  - 4.1. Presentations of Experimental Results
  - 4.2. The Stability and Repeatability of the Flow Fields
  - 4.3. Flow Field Studies Made Using the Oil-Flow and Vapour-Screen Techniques
    - 4.3.1. Oil-Flow Patterns on the Tunnel Side Wall
    - 4.3.2. Oil-Flow Patterns on the Shock Generator Surface
    - 4.3.3. Vapour-Screen Pictures
  - 4.4. Wall Surface Flow Features Indicated by the Static-Pressure and Heat-Transfer Distributions
    - 4.4.1. Static Pressure Fields
    - 4.4.2. Heat Transfer Distributions
    - 4.4.3. Surface Temperatures
    - 4.4.4. Static-Pressure and Heat-Transfer Distributions
  - 4.5. Viscous Layer Surveys

Approved For

DTIC Class

DDC TAB

Unannounced

Justification

By

Date

Approved

Signature

Position

Organization

Address

City

State

Country

Telephone

Facsimile

Telex

Radio

Other

Remarks

Comments

Notes

References

Attachments

Enclosures

Signatures

Initials

Stamps

Seals

Labels

Markers

Indicators

Alarms

Warnings

Errors

Messages

Notifications

Alerts

Announcements

Reports

Documents

Records

Files

Directories

Indexes

Searches

CONTENTS (Contd.)

5. HEAT TRANSFER IN THE INTERACTION REGION
    - 5.1. Heat Transfer Measurement in the Shock Region
    - 5.2. Typical Heat Transfer Distributions
  
  6. THREE-DIMENSIONAL FLOW SEPARATION IN THE INTERACTION REGION
    - 6.1. Definition of Three-Dimensional Separation
    - 6.2. Angular Momentum Conservation Concept of the Surface Flow Convergence
      - 6.2.1. Consideration of the Oil-Flow Convergence
      - 6.2.2. Review of McCabe's Theory
      - 6.2.3. Angular-Momentum Conservation Concept
      - 6.2.4. Analysis of the Angular-Momentum Conservation Concept
  
  7. FLOW FIELD STRUCTURE IN THE INTERACTION REGION
    - 7.1. Flow Structure near the Shock Generator
    - 7.2. 'Double Viscous-Layer Model'
    - 7.3. An Hypothesis for the Appearance of Flow Separation
  
  8. CONCLUSIONS AND REMARKS
  
  9. ACKNOWLEDGEMENTS
  
  10. REFERENCES
    - 10.1. References
    - 10.2. Bibliography
  
  11. APPENDICES
-

## FIGURES

### FIGURE NO.

### TITLE

- |    |   |
|----|---|
| 1  | An Example of High Local Heating  |
| 2  | An Example of Shock-Induced Boundary-Layer Separation   |
| 3  | Typical Two-Dimensional Shock Boundary-Layer Interactions   |
| 4  | Some Experimental and Theoretical Results of Two-Dimensional Shock Boundary-Layer Interaction           |
| 5  | Glancing Shock Boundary-Layer Interaction   |
| 6  | Maskell's Separation Models   |
| 7  | Quasi-Two-Dimensional Flow Field  |
| 8  | Surface-Flow Patterns in the Corner Flow  |
| 9  | Shock Generator Angle to Induce Incipient Flow Separation as Calculated According to McCabe's Criterion |
| 10 | Separated Flow-Field Models of Glancing Interaction Region  |
| 11 | A Numerical Solution of Glancing Interaction  |
| 12 | 2.5 x 2.5 Inch Intermittent Wind Tunnel   |
| 13 | 9 x 9 Inch Continuous-Running Wind Tunnel   |
| 14 | Working Section of the 2.5 x 2.5 Inch Tunnel  |
| 15 | Model Geometry in the 2.5 x 2.5 Inch Tunnel   |
| 16 | Boundary-Layer Properties in the 2.5 x 2.5 Inch Tunnel  |
| 17 | Roughness Elements to Modify the Test Boundary Layer  |
| 18 | Working Section of the 9 x 9 Tunnel   |
| 19 | Model Geometry in the 9 x 9 Tunnel  |
| 20 | Boundary-Layer Properties in the 9 x 9 Inch Tunnel  |
| 21 | Oil-Flow Visualization  |
| 22 | Vapour-Screen Method  |
| 23 | Arrangement of Surface Static Pressure Holes and Data Logging System                                    |
| 24 | Temperature-Time Histories for the Slug-Calorimeter Technique   |
| 25 | Slug Calorimeter Installation   |
| 26 | The Stagnation Temperature Correction   |
| 27 | Results of Bare-Plate Heat Transfer Measured by the Slug Calorimeter (2.5 x 2.5 Inch Tunnel)            |
| 28 | Temperature Variations in the 9 x 9 Inch Tunnel during the Running Time of Typically 90 Minutes         |
| 29 | Temperature-Time History of a Thin-Film-Gauge in the Continuous-Running Tunnel                          |

FIGURES (CONTD.)

<u>FIGURE NO.</u>	<u>TITLE</u>
30	Thin-Film-Gauge Calorimeter Installation
31	The Measured Temperature Behaviour
32	Results of Bare Plate Heat Transfer Measured by the Thin-Film-Gauge Calorimeter (9 x 9 Inch Tunnel)
33	Encapsulated Liquid Crystal Technique
34	Boundary-Layer Survey Stations and Probes
35	Co-ordinate Systems for Experimental-Data Presentation
36	Measured and Calculated Shock Angles
37	Typical Oil-Flow Patterns
38	Convergence Lines of Side-Wall Surface Flow
39	Deflection Angles of Side-Wall Surface Flow
40	Detailed Oil-Flow Patterns on the Shock Generator Surface
41	Typical Vapour-Screen Pictures
42	Shock Locations as Measured from the Schlieren and Vapour-Screen Pictures
43	Isobars on the Side-Wall Surface
44	Heat Transfer on the Side-Wall Surface
45	Typical Encapsulated Liquid Crystal Pictures (2.5 x 2.5 Inch Tunnel)
46	Isothermals on the Side-Wall Surface (9 x 9 Inch Tunnel)
47	Typical Streamwise Static Pressure Distributions
48	Static-Pressure and Heat-Transfer Distributions
49	Correlation between Static Pressure and Heat-Transfer
50	Viscous-Layer Survey Results
51	Adiabatic Wall Temperature Distributions
52	Recovery Factor Patterns
53	Typical Heat Transfer Distributions
54	Surface-Flow Convergence Patterns
55	Boundary-Layer Stream Tube Near the Surface-Flow Convergence Line
56	Co-ordinate Systems for Surface-Flow Deflection Analyses
57	Surface-Flow Convergence-Line Angle vs. Shock Generator Angle
58	Flow Structure Near the Shock Generator Root
59	'Double Viscous-Layer' Model
60	Attached and Separated Flow Models
61	Correlation of Convergence Line Angle with the Appearance of Flow Separation

## A P P E N D I C E S

- A. The Derivation of the Boundary Layer Profiles
  - B. Heat Transfer Measurements
    - B1. Quasi-Transient Calorimeter Techniques
    - B2. Slug Calorimeter Technique
    - B3. Thin-Film-Gauge Calorimeter Technique
    - B4. Equivalent Thermal Capacity of the Thin-Film-Gauge Calorimeter
    - B5. Electronic Circuits for the Thin-Film-Gauge Calorimeter Technique
  - C. Schlieren Pictures
  - D. Oil-Flow Patterns
  - E. Vapour-Screen Pictures
  - F. Static Pressure Distributions
  - G. Heat Transfer Distributions
  - H. Encapsulated Liquid Crystal Pictures (2.5 x 2.5 Inch Tunnel)
  - I. Surface Temperature Distributions (9 x 9 Inch Tunnel)
-

## 1. INTRODUCTION

### 1.1 Shock Boundary-Layer Interaction

On the surface of high speed vehicles in transonic, supersonic and hypersonic flow, shocks generated by the vehicle geometry can interact with the surface boundary layers. The interaction can cause a number of problems when designing the vehicles, such as local heating (Fig.1a) and boundary-layer separation. The local heating problem sometimes requires the vehicle to employ heat-resisting materials over a large area of the surface.

These problems arise because high flight speeds generate high temperatures in the boundary layer and high pressures on the vehicle surface. Shock wave boundary layer interaction will usually increase the local pressure still further and this often implies a corresponding increase in local heat transfer as shown in Fig.1b, taken from Neumann (Ref.19). If the interaction is strong enough to cause separation then the whole aerodynamic performance may be affected with phenomena such as buffet, wing-rock and wing-drop limiting manoeuvrability. These limitations are often most severe at transonic speeds and an example of shock-induced separation is shown in Fig.2 taken from Kubota et al.(Ref.2).

In the case of two-dimensional shock boundary-layer interaction (Fig.3, from Kuchemann et al., Ref.3), theoretical and experimental investigations have had some success in confirming the general flow features of the interaction. Fig.4 (from Horstman et al., Refs. 4 and 5) shows some examples in which there is good agreement between the experimental results and theoretical predictions. However, for three-dimensional interaction which is the more practical case, there are still a number of unresolved problems because

of the complicated flow structure and the experimental difficulties involved in the full resolution of the physical phenomena.

Glancing interaction is one of the most typical three-dimensional shock boundary-layer interactions. This consists of an oblique shock glancing across a boundary layer growing along a wall placed at right angles to the shock-wave surface. In most of the experimental investigations, a turbulent boundary layer growing along a flat plate (called the side wall in this paper) is employed as the test boundary layer, and the oblique shock is generated by a wedge mounted normally on the plate. The test arrangement is shown in Fig.5 together with typical patterns of flow properties over the interaction region.

In the interaction region the static pressure and heat transfer distributions on the side wall are very similar (Fig.5). For a weak shock, the pressure and heat transfer are gradually decreasing with increasing distance from the shock generator. As the shock strength (pressure ratio across the shock) is increased, the distributions show two peaks, one near the shock and the other near the shock generator. The side-wall boundary layer is heavily skewed near the shock, because the surface streamlines are deflected much more than the streamlines at the edge of the boundary layer which only turn to lie parallel to the shock generator surface. With increasing shock strength, the surface flow deflection angle increases and eventually exceeds the shock angle. As a result, the highly deflected surface-flow forms a particular line on the side wall upstream of the shock at about the shock-wave angle. In front of this particular line, the surface streamlines tend to coalesce with it. However, behind the line, the surface streamlines run nearly parallel to it or they approach it at a

small angle. This coalescence of the upstream surface-stream lines suggests a three-dimensional flow separation, similar to Maskell's 'ordinary separation' (Ref.6). As shown in Fig.6, in Maskell's definition of the ordinary separation, the separation line is an envelope of surface stream lines (or surface friction lines) converging asymptotically from each side. However, the surface flow found in this interaction is typical of what most investigators regard as ordinary separation (refer to the oil-flow picture in Fig.5).

One of the earliest experimental studies was performed by Stanbrook (Ref.7). He proposed that a pressure ratio across the shock of 1.5 was sufficient to induce 'separation' at Mach numbers from 1.6 to 2.0. McCabe (Ref.8) developed an approximate theory for the surface-flow deflection in a quasi-two-dimensional flow field. This quasi-two-dimensional flow field model is an idea based on a two-dimensional interaction caused by a normal shock (Fig.7a). It is reasonable to imagine that a sectional view of the glancing interaction region normal to the shock is similar to this two-dimensional interaction. It may also be proper to assume that all flow characteristics are locally regarded as constant along lines parallel to the shock (Fig.7b). Thus, the quasi-two-dimensional flow field model is introduced to give the idealized surface-flow patterns illustrated in Fig.7c. McCabe used this flow field for his theory and further assumed that all vorticity in the side-wall boundary layer is convected with the free stream velocity. McCabe's theoretical surface-flow deflection angle generally agrees well with the experimental maximum surface-flow angle, when the shock is not too strong. As an extension of this theory, he also tried to predict the shock generator angle to induce 'separation', by introducing a criterion derived

from the geometrical considerations of the quasi-two-dimensional flow field. He predicted that the 'separation' is incipient when the deflected surface-flow becomes aligned with the shock (Fig.7c-2). This prediction gives slightly higher shock generator angles than his experimental results at Mach numbers of 2 and 3. Korkegi (Ref.9) generalized McCabe's theoretical prediction by using a first order approximation to give a term being roughly proportional to the shock strength. He proposed that 'incipient separation' takes place when the product of the free stream Mach number and the shock generator angle reaches 0.364 radians (this corresponds to a pressure ratio across the shock of 1.63). He also suggested that, to obtain better agreement with experimental results, the product of the Mach number and the shock generator angle should be approximately 0.3 (which corresponds to a pressure ratio of 1.5). These mathematical and empirical criteria are shown in Fig.9, compared with some experimental incipient separation data defined according to McCabe's criterion. As shown in the figure, these criteria roughly coincide with the experimental results. In other words, these criteria provide a good prediction of the shock generator angle at which the surface-flow deflection becomes equal to the shock angle. However, they do not provide any clarification of 'incipient separation' itself.

Recent experimental investigations have supplied a great deal of flow field data for the interaction region. Many interpretations of the flow field data have brought diverse explanations of the interaction phenomena. For instance, the 'corner'flow in the interaction region is not quasi-two dimensional but 'conical' as shown in Fig.8, so McCabe's criterion may not be applied to define 'incipient separation'. This is because the 'conical'

flow field allows an attached convergent surface-flow even when the surface flow deflection exceeds the shock angle (Fig.9c). The occurrence of 'separation' is just one of the points of controversy.

Oskam et al. (Refs. 10-12) discussed in some detail the uncertainty in McCabe's criterion, mostly on the interpretation of their own oil-flow pictures accompanied by viscous layer surveys. They concluded that, even when the surface-flow deflection exceeded the shock angle, the interaction region still kept an attached flow pattern. Although the oil streak lines were converging and tended to coalesce upstream of the shock, the lines did not converge into a single line and the region in which the oil coalescence occurred was growing in size in a direction along the shock. This was consistent with the idea of an interaction region increasing its size with distance along the shock.

Peake (Refs.13 and 14) presented a different view based on his detailed measurements of wall surface flow patterns, surface static pressures and viscous layer properties. In particular he noticed the coalescence of oil-flow in a region where the surface static pressure peaked. He therefore suggested that the 'three-dimensional separation line' produced a free shear layer which rolled up into a flattened vortex within the depth of the side-wall boundary layer and that there appeared to be no sudden eruption of vortical fluid from the surface. He also remarked that the development of the viscous layers with increasing shock generator angle was so gradual that it was difficult to pin down the exact shock generator angle needed to induce 'incipient separation' without adopting McCabe's criterion.

Neumann, Hayes and Token (Refs.15-20) mainly concentrated on investigations of the heat transfer, which is very important for direct practical applications. According to their studies, the heat transfer distributions in a direction normal to the free stream show a good correlation with the surface static pressure distributions, as shown in Fig.5b. These distributions also have a very high 'peak' near the shock generator root, and sometimes show a small 'peak' close to the surface-flow coalescence in the corresponding oil-flow picture. The presence of two 'peaks' may correspond to the reattachment and separation lines caused by a 'separation vortex' which was suggested by Token with his 'vortex dominated flow field model' as illustrated in Fig.10a.

Very recently, Hung et al. (Refs.21 - 22) reported a 'numerical solution of three-dimensional shock wave and turbulent boundary-layer interaction'. This solution showed good agreement with some experimental data at the Mach number of 6, as shown in Fig.11, except for the static pressure distribution near the shock generator when the shock was very strong. They remarked that further study is needed to understand the details of viscous interaction, the problem of three-dimensional separation being quite different from the two-dimensional phenomenon. They also pointed out that three-dimensional turbulence modelling is a key issue for further numerical simulation.

### 1.2. The Present Experimental Study

The present paper attempts to build a flow field model of the three-dimensional glancing shock/turbulent boundary-layer interaction region, on the strength of (i) oil-flow patterns (on both the side wall and the shock generator surface); (ii) vapour-screen pictures; (iii) surface static

pressure distributions and (iv) heat transfer distributions. The experimental results were obtained at the Cranfield Institute of Technology with two separate test programmes conducted in the 2.5 x 2.5 inch intermittent tunnel and the 9 x 9 inch continuous-running tunnel, at a Mach number of approximately 2.5. Some of the experimental data from the intermittent tunnel has already been reported by Dickman (Ref.23), Davenport (Ref.24) and Kubota (Ref.25).

The new flow field model of the interaction region consists of two different viscous layers, (1) the side-wall boundary layer and (2) the 'induced layer' originating near the shock generator root and crossing the path of the side-wall boundary layer. The flow field model leads to the following hypothesis. As long as surface stream lines of the side-wall boundary layer are pliable enough to be 'bent' along the edge of the induced layer, no separation appears there even if the surface-flow deflection exceeds the shock angle. An 'ordinary separation' takes place when the induced layer forces the surface stream lines to deflect beyond a maximum permissible angle depending on the side-wall boundary-layer properties. The surface stream lines then lift off from the wall surface, sliding over the induced layer and become involved in a vortical free layer, as shown in Fig.10b. The maximum permissible angle may be determined by a simple angular momentum relation.

The 'ordinary separation' in the present paper is defined by limiting stream lines leaving the surface at a particular line (separation line) lying on the side wall. This separation will be marked by surface stream lines converging and coalescing into a single line, which can be experimentally detected using surface-flow visualisation, (oil-flow pictures).

## 2. EXPERIMENTAL PROGRAMMES

Experimental data presented in this paper were taken in two separate wind tunnel test programmes, at almost the same Mach number of approximately 2.5. The main difference between these two test programmes was in the scale of the shock boundary-layer interaction region to be investigated.

A small-scale test programme was conducted in the 2.5 x 2.5 inch intermittent supersonic wind tunnel (Fig.12). The results of this programme have been partially reported by Dickman (Ref.23), Davenport (Ref.24) and Kubota (Ref.25). The large-scale test programme was undertaken in the 9 x 9 inch continuous-running supersonic wind tunnel (Fig.13) and some data obtained in it have been presented by Kubota (Ref.25).

In both the test programmes, the interaction region was provided by locating a wedge in the tunnel working section so that an oblique shock generated by it could glance across the turbulent boundary layer growing on the tunnel side wall.

### 2.1 2.5 x 2.5 inch Wind Tunnel Test Programme

#### 2.1.1. Wind Tunnel Facility and the Test Conditions

The intermittent wind tunnel has a cross section of 2.5 inches by 2.5 inches at its working section, and a two-dimensional unsymmetrical supersonic nozzle (Fig.14). By interchanging supersonic nozzles a range of the test Mach number from 1.6 to 4.3 is available.

The wind tunnel is 'driven' by air at atmospheric pressure sucked down into an evacuated tank. The low pressure tank has a volume of approximately 1600 cubic feet and can be evacuated by a 25 kilowatt electrically driven pump.

Stagnation conditions for this tunnel are, therefore, nearly atmospheric and tend to fluctuate from day to day with changing weather.

#### Stagnation Pressure and Test Mach Number

The stagnation pressure was measured using a Pitot probe set up in the tunnel settling chamber and connected to a mercury manometer. This pressure was approximately 50 mmHg lower than atmospheric due to the pressure drop across the silica-gel drying system. Throughout this test programme, the stagnation pressure was  $710 \pm 10$  mmHg.

The static pressure was measured via a tapping suitably placed in the top liner of the tunnel.

These measured stagnation and free-stream static pressures determined the free-stream Mach number, through the isentropic flow relations. In this test programme which used a 'Mach 2.5' nozzle section, the test Mach number was calculated to be  $2.41 \pm 0.03$ . The Schlieren system showed that the flow was steady during the 30 seconds of useful running time.

#### Stagnation Temperature

The stagnation temperature was measured by means of a Chromel-Almel thermocouple located in the tunnel settling chamber. This thermocouple was connected with a thermocouple multimeter. The stagnation temperature for this test programme was in a range of  $290 \pm 10$  degrees Kelvin.

It was also found that the stagnation temperature tended to decrease by 3 to  $4^{\circ}\text{K}$  during the tunnel run. This temperature behaviour is thought to be due to the admittance of air from the atmosphere, through a large volume of inlet piping and the silica-gel drying system.

### Reynolds Number

Isentropic flow relations determined the free-stream temperature for the measured stagnation temperature. Southerland's law was then used to calculate the free-stream viscosity, while the equation of state provided the air density. Thus, after measuring the free-stream Mach number, the unit free-stream Reynolds number was estimated to be approximately  $2.5 \times 10^5$  per inch.

#### 2.1.2 Test Configuration (See Fig.15)

### Shock Generator

To generate the shock to interact with the test boundary layer, a variable-angle wedge was mounted on a quadrant suspended from the tunnel top liner. The pivot point of the wedge was designed to coincide exactly with its leading edge resting on the top liner surface. This configuration made it possible to increase the wedge angle up to approximately 10 degrees without the wind tunnel choking.

The wedge had a chord of 3.5 inches and spanned the tunnel test section. Sealing grooves were cut on both sides of the wedge, in order to prevent pressure leakage between the wedge and the side walls.

The trailing edge of the wedge generated an expansion fan, and the oblique shock from the wedge leading edge reflected from the tunnel bottom liner and interacted with the boundary layer there. These phenomena limited the effective test area. The flow field was therefore restricted to the region upstream of the wedge trailing edge and some distance away from the tunnel

bottom liner; i.e. a zone approximately 4 inches in length and 2 inches in width.

On the top surface the oblique shock did not occur exactly at the wedge leading edge, but approximately 0.15 inches upstream of it, (according to Schlieren photographs) presumably due to an influence of the top-liner boundary layer. It must be stressed that no two-dimensional flow separation was observed at the wedge-top liner 'corner' with the angles used in this experiment.

#### Test Boundary Layer

The test boundary layer was a fully turbulent boundary layer growing along the tunnel side wall. The boundary layer was surveyed by using Pitot and static-pressure probes (described in the next chapter) connected to a multi-tube mercury manometer. These surveys were made at five stations along a swept line lying 2 inches upstream of the oblique shock at the shock generator angle of 5 degrees (Fig.16a). The survey stations were selected so as to give the undisturbed boundary-layer properties in almost the same distance from the shock.

The Pitot-probe surveys showed that static pressures in the side-wall boundary layer were almost constant (within  $\pm 3\%$ ) and equal to the external-flow static pressure and the free-stream static pressure measured on the tunnel top liner.

The measured static and total pressure distributions in the boundary layer enabled the density and velocity profiles to be calculated by the method described in Appendix A. The boundary-layer properties and the velocity

profiles are shown in Figs.16b and 16c. The boundary layer thickness (defined by the point where 0.995 of the external-flow velocity is reached) was typically 0.2 inches. The corresponding displacement and momentum thicknesses were estimated to be approximately 0.07 inches and 0.015 inches respectively.

#### Modification of the Test Boundary Layer

For some of the tests an attempt was made to increase the side-wall boundary-layer thickness by using vortex generators, roughness elements and air injection. Many configurations were tried at various locations in the tunnel. The most effective type of disturbance was a group of small poles (0.5 inches in height, 0.5 inches in length and 0.1 inches in width) stuck on the tunnel side wall a little upstream of the supersonic nozzle throat (Fig.17). This type of roughness increased the boundary layer thickness to approximately 0.3 inches. Meanwhile, the corresponding displacement and momentum thicknesses were increased to 0.085 and 0.018 inches respectively. These modified boundary-layer properties are plotted in Fig.16b together with the original properties.

This device also 'flattened' the boundary-layer thickness distribution over the flow field, as shown in Fig.16b. It seems that this device invigorated the side wall boundary layer and made it more resistant to change.

### 2.1.3 Test Techniques

With the test configuration using the original side-wall boundary layer (without the roughness elements) the following test techniques were applied:

- (1) Schlieren, normal to the tunnel side wall
- (2) Oil-flow on the side wall and on the shock generator surface.
- (3) Vapour-screen in cross sections normal to the free stream.
- (4) Static pressure distribution measurements on the side wall.
- (5) Heat transfer measurements on the side wall, by using a quasi-transient 'slug calorimeter' technique.
- (6) Encapsulated liquid crystal coatings to give surface temperature patterns on the side wall.
- (7) Viscous layer surveys using Pitot probes and a yaw meter.

The results obtained with these techniques in this test configuration will be specified as pertaining to Model A.

In the modified test boundary layer, the following techniques were applied:

- (1) Schlieren
- (2) Oil-flow
- (3) Vapour-screen

The results will be specified as referring to Model AM.

## 2.2 9 x 9 inch. Wind Tunnel Test Programme

### 2.2.1 Wind Tunnel Facility and the Test Conditions

The continuous-running tunnel has a cross section of 9 inches by 9 inches at the working section, and a two-dimensional supersonic nozzle (Fig.18). The supersonic nozzle is also interchangeable to cover a range of Mach number from 1.7 to 2.5. This tunnel is driven by a centrifugal compressor with two 373 kilowatt electric motors.

The stagnation pressure is automatically maintained at a pre-set value in the range from 0.7 to 14.7 p.s.i.a. The stagnation temperature could be controlled in the range approximately from 5°K lower to 10°K higher than the ambient temperature, by regulating the amount of water in the tunnel cooling system. However, it is difficult to control the temperature accurately because the adjustment involves a long time constant (approximately from 1.5 to 2.5°K/Min.).

### Stagnation Pressure and Test Mach Number

For this test programme, the stagnation pressure was preset to be approximately 4 p.s.i.a. The stagnation pressure was monitored from the pressure gauge mounted in the tunnel control panel. When higher accuracy of the measured stagnation pressure was required, such as in the boundary layer surveys, a Pitot probe set up in the tunnel settling chamber was used to provide it through the diaphragm-type pressure transducer of a scanning valve system (described in the next chapter). The stagnation pressure was estimated to be  $4.0 \pm 0.2$  p.s.i.a.

The free-stream static pressure was obtained on the tunnel top-liner surface at two stations located between the supersonic nozzle throat and the test region (Fig.18). The pressures measured on the top liner were confirmed to be almost equal to the real free-stream static pressure during the survey through the boundary layer.

These measured stagnation and free-stream static pressures gave the test Mach number, in the same way as in the 2.5 x 2.5 inch wind tunnel test programme. The test Mach number was calculated to be  $2.30 \pm 0.05$ .

#### Stagnation Temperature

To measure the stagnation temperature, a Chromel-Almel thermocouple probe was mounted in the tunnel settling chamber and continuously indicated the stagnation temperature during the tunnel running time.

For the heat transfer measurements, it was required to maintain a low stagnation temperature to provide a large difference between the wall temperature and the air recovery temperature. In this case, the stagnation temperature was kept between 282 and 285 degrees Kelvin, by fully operating the tunnel cooling system. For other measurements, the temperature lay in the range from 283 to 293 degrees Kelvin.

#### Reynolds Number

In the same way as in the 2.5 x 2.5 inch wind tunnel test programme, the unit free-stream Reynolds number was estimated to be approximately  $0.8 \times 10^5$  per inch, for the stagnation pressure of 4 p.s.i.a.

### 2.1.2. Test Configuration (See Fig.19)

#### Shock Generator

A thin wedge was mounted on a rotating disk (9 inches in diameter) mounted in the tunnel side wall. This wedge was made from a  $\frac{1}{8}$ " flat plate with the leading edge chamfered to an angle of  $15^{\circ}$ . The chord was 6" and the span 7" so that the model occupied about 80% of the working section width.

The shock generator angle was pre-set by turning the disk. The pivot point did not coincide with the wedge leading edge hence the wedge leading edge moved with changing shock generator angle. The movement was approximately 0.8 inches in both the directions parallel and normal to the tunnel liner, for an angle change of 0 to 15 degrees. It was checked that the space between the wedge leading edge and the tunnel bottom liner was always larger than 1 inch in order to avoid interference from the boundary layer growing along the tunnel bottom liner.

This experimental configuration provided a test flow area of approximately 6 inches by 6 inches, without any interference from shock reflections, trailing edge and the tunnel-liner boundary layers.

#### Test Boundary Layer

The test boundary layer was the fully developed turbulent boundary layer growing along the tunnel side wall. This boundary layer was surveyed using pitot and static-pressure tubes (with the same dimensions as in the previous test programme) connected to the pressure transducer of the scanning valve

system. Boundary layer surveys were made without the wedge at three stations. These stations were located along a line normal to the free stream, 4.1 inches upstream of the rotatory-disk centre (Fig.20a).

The survey showed that the static pressure in the side-wall boundary layer was constant and equal to the external-flow static pressure and the free-stream static pressure measured on the tunnel top liner, (to within  $\pm 5\%$ ).

The boundary-layer properties and the velocity profiles are presented in Figs.20b and 20c. The boundary layer thickness (defined by a point where 0.995 of the external-flow velocity is reached) was approximately 0.62 inches, and the corresponding displacement and momentum thicknesses were estimated to be 0.15 and 0.040 inches respectively. These results confirm that the side-wall boundary layer was almost uniform over the test area.

### 2.2.3. Test Techniques

In this test programme, the following test techniques were applied:

- (1) Schlieren, normal to the tunnel side wall.
- (2) Oil-flow visualization on the side wall and on the shock generator surface.
- (3) Vapour-screen pictures of cross sections normal to the free stream.
- (4) Static pressure distribution measurements on the side wall.
- (5) Heat transfer measurements on the side wall, using a quasi-transient 'thin-film-gauge calorimeter' technique.

The results obtained with these techniques in this test programme will be specified as referring to Model B.

### 3. EXPERIMENTAL TECHNIQUES AND THE ARRANGEMENTS

#### 3.1. Schlieren Techniques

Schlieren pictures were taken for all model configurations to check that the test flow pattern was as required. The pictures were taken normal to the tunnel side walls and the knife-edge was adjusted so as to give good contrast.

For Models A and AM, the configuration of the shock generator (suspended from the tunnel top liner) allowed glass windows to be fitted on both sides of the tunnel test section. Hence a conventional single pass Schlieren system was used and this gave good quality pictures.

In the case of Model B the wedge was mounted on an aluminium disk, free to rotate within the tunnel side wall, made from steel. Hence a glass window could be fitted on one side only. Therefore the disk surface was mechanically polished to be as smooth as possible and a double-pass Schlieren system was used. Although this optical system could not escape some interference due to the roughness of the disk surface, the Schlieren pictures were adequate.

#### 3.2. Oil-Flow Pictures

To visualize the surface flow on the tunnel side wall and on the shock generator surface (Fig.21), a mixture of titanium dioxide suspended in motor oil was used. A drop of oleic acid was added to the mixture to prevent coagulation of the titanium dioxide.

The surfaces to be painted with the white oil mixture were prepared with a matt-black finish to provide the greatest photographic contrast.

To avoid smeared oil traces of the surface flow patterns (caused by stopping the tunnel) the pictures were taken through the glass windows while the tunnel was running, except for some pictures of the shock-generator surface flow patterns.

### 3.3 Vapour-Screen Pictures

To visualize the flow features in cross sections of the test flow field normal to the free stream (Fig.22), the vapour-screen technique was applied. The principle of this technique is as follows.

As the air expands through the supersonic nozzle into the tunnel working section and cools, the moisture in the air tends to condense out forming a fog. The fog particles can scatter light in proportion to the number of particles per unit volume. Therefore, when illuminated by a narrow 'sheet' of light they build up a 'vapour-screen' which indicates disturbed fog caused from disturbances in the flow field. (Details are given in the paper by McGregor, Ref.26).

In the application of this technique to the present experiments, two important questions arose. They were how to control the fog density and how to increase the contrast of the vapour-screen pictures.

For Models A and AM tested in the intermittent tunnel, a small steam-boiler with an electric heater was used to supply enough fog in the working section. The steam was injected into the tunnel settling chamber. After filling the settling chamber with the steam, the tunnel was started. This procedure

provided enough time in which to take the pictures (approximately 5 seconds). However, condensation of the steam also formed water droplets on the cooled window glass and tended to spoil the pictures taken. The glass window had to be cleaned after every run.

In the case of Model B, the continuous-running tunnel made it easy to control the density of the fog. By injecting a given amount of water into the tunnel settling chamber, a sufficient density of the fog was obtained for long enough to take a picture.

In practice it was difficult to determine quantitatively the amount of injected steam or water to give the best vapour-screen pictures. The fog density depended critically on the ambient conditions. By eye it was hard to distinguish the blurred vapour-screen images. Therefore, in most cases contrast of the photographs taken needed to be improved. This improvement was done photographically by recopying or reprinting the pictures. However, this photographic process tended to emphasize any marks or scratches on the pictures.

In the present programmes, the illumination used was a 250 W slide-projector. A loaded slide with a small slit produced a sheet of light which was further narrowed using a convex lens. The sheet was approximately 0.2 inches thick across the test section. The pictures were taken on Kodak Trix-pan film (ASA 400) with an exposure time of 1 to 4 seconds for an aperture of  $f/4$ . The film developer was Paterson ACUSPEED FX-20 which can increase the effective film speed by up to three times. The recopy and reprint of the pictures employed ILFORD PANF film (ASA 50) and ILFOSPEED 4.1 M printing paper respectively.

#### 3.4. Static Pressure Distribution Measurements

The static pressure distributions were measured by means of holes (0.02 inches in diameter) arranged over the side wall of the 2.5 x 2.5 inch tunnel and on the metal disk of the 9 x 9 inch-tunnel side wall. The distributions of these holes in the two tunnels are shown in Fig.23a and Fig.23b.

On the side-wall of the 2.5 x 2.5 inch tunnel, two hundred and ten pressure tappings were arranged in seven rows of 30 tappings. On the metal disk of the 9 x 9 inch tunnel wall one hundred and fifty-six orifices were arranged in 6 rows.

The measured pressures were indicated by a digital voltmeter on the control panel of the scanning valve system feeding a diaphragm-type pressure transducer (Fig.23c). The system was calibrated with the known ambient pressure and a low pressure (approximately 0.05 mmHg) provided by a vacuum pump, for each individual scanning port (30 stations for Model A and 93 stations for Model B).

Particularly for Model A, tested in the intermittent tunnel, the tunnel running time of less than 30 seconds was too short to measure the correct pressures. This was because the lines connecting the tappings to the scanning valve system had a large volume which filled too slowly to allow the measured pressures from reaching their final values. This pressure delay was improved by using a guillotine clamp to enable accumulation of the pressures through repeated tunnel-running. The clamp allowed the pressure to build up in the lines when the tunnel was running and trap them when the tunnel stopped. This procedure was repeated several times until the measured pressures reached their equilibrium state.

### 3.5. Heat Transfer Measurements

To measure the heat transfer distributions a quasi-transient calorimeter technique was applied. Both the experimental procedure and the type of calorimeter employed, were different between the two tunnel test programmes. This was because of a basic difference between the two sets of test conditions, i.e. intermittent and continuous.

In the 2.5 x 2.5 inch tunnel test programme, a modified Princeton University slug-calorimeter technique was used. Meanwhile, for the 9 x 9 inch tunnel test programme, a thin-film-gauge calorimeter technique was devised and developed.

The principles of these two techniques are discussed in Appendix B.

#### 3.5.1. A Modified Princeton University Slug Calorimeter Technique

The original technique using the Princeton University type of slug calorimeter is fully described by Oskam et al. in Ref.27. The modified technique is detailed by Davenport in Ref.24. Some discussion of these techniques is given in Appendix B2.

#### The Original Technique

When a piece of metal (slug) of known characteristics is exposed to a thermal medium, the temperature variation of the slug with time can give the heat transfer rate between the slug surface and the medium directly.

The Princeton University type of calorimeter employs a copper slug which can be heated by a tiny jet of hot air and insulated from the metal container

by a nylon phenolic material. When the tunnel is started the tiny jet of hot air is supplied to maintain the slug at the temperature of the wall surrounding it, which is higher than the adiabatic wall temperature (or recovery temperature) of the test flow. When the data acquisition system is ready, extra heat is added to the slugs to raise their temperature, typically by  $20^{\circ}\text{K}$  (see Ref.27). When the heating jet is stopped, the data acquisition system is started and the slugs are allowed to cool naturally, down through the wall temperature to eventually reach the adiabatic wall temperature, (Fig.24a). By evaluating the gradient of the slug-temperature time history at the point where the slug temperature crosses the wall temperature, the heat transfer rate from the wall to the air can be determined (see Appendix B2).

#### The Modified Technique

In the modified technique, the "tiny jet of hot air" was not used. Instead the temperature difference to drive the slug calorimeter was provided by the difference between the wall temperature and the adiabatic wall temperature. This was done because it was found that heat convection during the heating process disturbed the test wall surface and hence affected neighbouring gauges.

The experimental procedure was as follows. The slug calorimeters, as well as the tunnel side wall, were left to reach room temperature. When the intermittent tunnel was started, the slugs were cooled by the air flow down to the adiabatic wall temperature. The temperature-time history is shown in Fig.24b. The slugs have much smaller thermal capacities than the tunnel

wall and hence they cooled more quickly. Therefore, the only time that the slug temperatures coincided with the wall temperature was at  $t = 0$ ; i.e. at the moment that the tunnel was started. Hence the heat transfer rates were derived from the temperature-time plots by measuring the slope at  $t = 0$ .

#### Test Surface Installation

To accommodate the slug calorimeters in the tunnel side wall, an aluminium plug of 2 inches diameter was used, having three insulated slugs on its flat surface (Fig.25a). Two wall temperature sensors (Chromel-Alumel thermocouples embedded in copper) were also flush with the surface. The plug was kindly loaned by Princeton University and had been used in an earlier study by Oskam et al. (Ref.27).

To mount the plug in the test section, an eccentric rotatable system was fabricated. A 4 inch diameter plug was fitted into a hole of equal diameter in the tunnel side wall. In the 4 inch diameter plug, a 2 inch diameter hole was drilled 0.75 inches off centre. The 2 inch diameter plug holding the slug calorimeters was fitted in this hole. The whole system is illustrated in Fig.25b. Rotation enabled a wide range of measuring stations to be covered.

#### Data Acquisition System and Data Reduction

Chromel-Alumel thermocouples embedded in the slugs and the plug container gave the temperature data to be used in calculating the heat transfer rates. The thermocouple leads were joined to a series of linear amplifiers and the

amplified signals were recorded by an ultra-violet recorder. This measurement system was calibrated using the water-bath method, in advance of the tunnel test.

When the tunnel was running, the slug temperatures dropped, approaching the adiabatic wall temperature exponentially. In contrast the tunnel wall temperature changed very little because of its large thermal capacity. However, it was also observed that the freestream stagnation temperature decreased by approximately 3 to 4°K, in the first 12 seconds of the running time. This temperature behaviour was because initially the tunnel sucks through the air that has been filling the intake duct and settling chamber. Subsequently the tunnel draws in the colder fresh air from outside the laboratory. Because of this temperature variation the measured slug temperatures had to be corrected, as shown in Fig.26.

From the corrected temperature time-history, the temperature gradient at  $t = 0$  was evaluated. This gradient gave the heat transfer rate,  $q$ , from the relation:

$$q = - \frac{C_s}{A_s} \frac{dT_s}{dt} \quad (3 - 1)$$

where  $T_s$  is the slug temperature while  $C_s$  and  $A_s$  are respectively thermal capacity and surface area of the slug calorimeter.

The adiabatic wall temperature,  $T_{aw}$ , is calculated from the measured stagnation temperature,  $T_o$ , and the measured free stream Mach number,  $M_1$  by

$$T_{aw}/T_o = (1 + r \frac{\gamma-1}{2} M_1^2) / (1 + \frac{\gamma-1}{2} M_1^2) \quad , \quad (3 - 2)$$

where  $r$  and  $\gamma$  are respectively the recovery factor and the ratio of specific heats, which may be taken as 0.89 (for a turbulent boundary layer) and 1.4. In the present test conditions, the ratio of the wall temperature,  $T_w$ , to the adiabatic wall temperature can be written as

$$T_w/T_{aw} = 1.06 T_w/T_o \quad (3 - 3)$$

and the temperature difference to drive the slug calorimeter is approximately

$$T_w - T_{aw} = 18^\circ K . \quad (3 - 4)$$

Using the slug calorimeter technique, the heat transfer to the side-wall with no shock generator (bare plate heat transfer) was measured as shown in Fig.27. In the figure, the local Stanton number  $C_h$  is defined by

$$C_h = q/\rho_1 u_1 C_p (T_w - T_{aw}) \quad (3 - 5)$$

where  $C_p$  is specific heat of the air while  $\rho_1$  and  $u_1$  are respectively the density and the velocity of the free stream. The results show values approximately 10% higher than a prediction based on Van Driest II theory (Ref.31).

### 3.5.2 Thin-Film-Gauge Calorimeter Technique

Details of the thin-film-gauge calorimeter technique are described in Appendix B3, relating to the quasi-transient method used in the continuous-running tunnel.

### Outline of the Technique

The thin film gauge is usually employed as a thermometer, especially in short duration tunnels with a high ratio of stagnation temperature to wall temperature ( $T_o/T_w$ ). The resistance of the gauge changes almost in proportion to its temperature. This resistance variation is calculated by operating the gauges at a constant current and measuring the changing voltage drop across the film.

If the intensity of the input electric current is increased then the gauge can become a heater and locally raise the temperature of the substratum. Therefore if the thermal characteristics of the gauge and its substratum are known, the gauge-substratum combination is usable as a calorimeter with a 'built-in-heater and thermometer'.

The advantages and disadvantages of this technique as compared with the previous slug-calorimeter technique are as follows:

(1) Since the gauge film thickness is of the order of  $0.1\mu\text{m}$ , the thermal resistance between the 'thermometer' and the 'surface' is extremely small. This makes it easy to obtain a very high sensitivity calorimeter which can respond to small changes in heat transfer and which has a quick response time.

(2) The thermal capacity of the gauge is much smaller than that of the substratum. If the substratum is used as the test surface, the temperature of the calorimeter will be virtually identical to that of the test surface. As a result, the measured heat transfer is expected to be very close to the real heat transfer from the test surface.

(3) To read the temperature some electric current must pass through the 'thermometer'. This electric current could cause some heating which disturbs the surface temperature to be measured. To reduce this disturbance to a negligible level, the intensity of the input electric current must be carefully chosen, especially for tunnels with a low temperature difference ( $T_o - T_w$ ).

#### Quasi-Transient Technique in the Continuous-Running Tunnel

The quasi-transient technique was used for the measurements made in the continuous wind-tunnel. The tunnel is in the laboratory and the walls are normally at room temperature. The tunnel is equipped with a heat exchanger (water cooler) to keep the air stagnation temperature constant during the run. By operating the cooler at maximum conditions it is possible to hold  $T_o$  below  $T_w$  for a considerable time because of the large thermal capacity of the tunnel test section walls. The tunnel conditions were monitored by the stagnation temperature,  $T_o$ , and the reference wall temperature measured on the metal disk surface,  $T_{wr}$ . Strictly speaking the stagnation and wall temperatures were changing slightly with time, throughout the tunnel run, as shown in Fig.28. In the figure, the temperatures are plotted against the gauge station numbers measured in turn, with the interval time of approximately 2 minutes between readings. However, as indicated in the same figure, the difference between the reference wall temperature and the adiabatic wall temperature (calculated in the same manner as in 3.5.1.) could be maintained at almost a constant value in the range from 16 to 18°K.

The procedure to obtain the temperature time history (Fig.29) is as follows. The gauge to be operated was heated to a temperature from 3 to 5<sup>o</sup>K higher than the reference wall temperature. This was done by passing a steady current of around 30mA through the gauge. When the gauge temperature had nearly reached its new temperature, the gauge was switched over to a much smaller electric current of 3mA to measure the gauge temperature. As the gauge-substratum combination (calorimeter) was cooled by the air-stream, the indicated gauge temperature exponentially approached the local wall temperature. This process provided the temperature-time history which when compared with the corresponding history for wind-off conditions can be reduced to a heat transfer coefficient by the method described in Appendix B3.

#### Thin-Film-Gauge Calorimeter Installation

The calorimeter itself is no different from the standard thin film gauge. The arrangement of the 63 gauges used is shown in Fig.30a.

The gauges were platinum films sintered on a Pyrex glass plate at its surface. (The sintering process is described in Refs. 28-30). The size of these gauges was approximately 0.2 inches long and 0.04 inches wide. The Pyrex glass plate was 6 inches long and 5 inches wide, while its thickness was  $0.058 \pm 0.001$  inches. Through this glass plate, 0.04 inch diameter holes were drilled at each end of all the gauges. A silver paint was used to draw lead lines through the holes, from the gauge ends to the back surface of the glass plate. On the silver-paint lines of the back surface, copper leads were soldered. The Pyrex plate was flush mounted in the rotatable metal disk of the tunnel side wall, by using peisin wax.

The copper leads were drawn out of the tunnel side wall through a small hole on the disk.

The gauges were calibrated with a silicon-oil bath method, in advance of installing in the metal disk. Although the resistance of the 63 gauges ranged from 16 to 71 ohms, the temperature coefficient of resistance was measured as always lying in the range  $2.13 \pm 0.07/^{\circ}\text{K}$  for a 1.00mA input electric current.

To measure the reference wall temperature, a Copper-Constantan thermocouple was flush mounted on the metal disk surface, upstream of the gauge plate.

#### Installation of the Electronics

For the quasi-transient calorimeter technique, an electronic system was prepared. The block diagram is shown in Fig.30b, together with data acquisition system, and the detailed circuits are presented in Appendix B5.

The electronic system consisted of three principal units, the Wheatstone-bridge balance circuit, the current regulator and the amplifier. The Wheatstone bridge network incorporated the usual balancing arms so that steady signals were 'removed'. Hence the amplifier only receives the voltage differences emanating from variations in gauge resistance. The Wheatstone bridge circuit used 'thick film' resistors to obtain high temperature stability and a low level of noise. The current regulator was designed to supply 5 different intensities of electric current in the range from 0.3 to 50.0mA, by handling toggle switches on the control panel of the system.

This was necessary because the gauges manufactured had widely differing resistances which therefore required different electric currents for heating the calorimeters and measuring the local surface temperatures. The regulated current varied less than 0.1% for resistances ranging from 10 to 150 ohms. The amplifier was built up from two operational-amplifier integrated circuits. The minimum gain margin per amplifier was designed to be more than 60 db, to provide high stability. The complete amplifier circuit gave more than 50 db maximum amplification with high stability.

In all of this electronic system, the noise level converted to input signal was less than 0.05 $\mu$ V, and the zero-point drift converted was from 10 to 20 $\mu$ V/hour for normal operation after 30 minutes warming up.

#### Data Acquisition System and Data Reduction

The thin film gauges gave the variation of local wall-surface temperatures with time. The thermocouple embedded in the tunnel side-wall surface indicated the reference wall temperature. The tunnel thermometer system with thermocouple transducer provided the stagnation temperature. The signals of these temperatures were properly amplified with linear amplifiers, and filtered through a C-R filter with a time constant of 60 milliseconds. They were recorded by an ultra-violet recorder, whilst being continually monitored (by means of a digital voltmeter for the local wall-surface temperatures, a thermocouple multimeter for the reference wall temperature and the tunnel thermometer system for the stagnation temperature).

When the calorimeter of the gauge-substrate combination was operated through the heating process, the gauge temperature approaches the local wall

surface temperature exponentially. Some typical time histories of the recorded gauge-temperatures are shown in Fig.29b. As discussed in Appendix B3, this gauge-temperature,  $T_g$ , ought to behave in the form given by

$$T_g = T_{wl} + (T_{gi} - T_{wl}) \exp \left[ - \frac{A_s}{C_s} (h_a + h_w) t \right] \quad (3 - 6)$$

or

$$\ln \left( \frac{T_g - T_{wl}}{T_{gi} - T_{wl}} \right) = - \frac{A_s}{C_s} (h_a + h_w) t, \quad (3 - 6)'$$

where  $T_{wl}$  and  $T_{gi}$  are the local wall-surface temperature and initial gauge temperature, and  $h_a$  and  $h_w$  are the heat transfer coefficients to the air and to the wall (heat loss). Typical measured gauge-temperature data treated by using equation (3 - 6)' are plotted in Fig.31, where  $T_{gi}^* = A T_{gi}$ ,  $A$  being an arbitrary constant.

According to (3 - 6)', the temperature data ought to lie on a straight line (Fig.31). However, the measured temperature data actually deviate from the expectation, in the first 2 - 5 seconds after switching the calorimeter system from heating to cooling. This temperature behaviour is considered to be due to a transitional temperature re-distribution in the calorimeter (Appendix B4). After this short transition period, the temperature data followed the line predicted by (3 - 6)'.

In the present data reduction, the following formula derived from (3 - 6)' was employed:

$$h_a + h_w = - \frac{C_s}{A_s} \frac{1}{\Delta t} \frac{\sum_n \left( [T_g(t_n) - T_{wl}] \ln \left[ \frac{T_g(t_n + \Delta t) - T_{wl}}{T_g(t_n - \Delta t) - T_{wl}} \right] \right)}{\sum_n [T_g(t_n) - T_{wl}]} \quad (3 - 7)$$

The sampling interval time,  $\Delta t$ , was chosen to be one second.

The heat loss ( $h_w$ ) was measured when the tunnel was not running (wind-off). It was assumed that this  $h_w$  was not changed by running the tunnel (wind-on).

To examine the influence of the heating process on the temperature data obtained, some measurements in the wind-off condition were conducted while changing the intensity of the heating current and the heating time (which changes the gauge temperatures). Typical data from these tests are also plotted in Fig.31 (labelled as wind-off cases).

It was found that the heating process had little influence on the temperature data in the range to be used for the data reduction of (3 - 7). This view was further strengthened by measurements of the heat loss ( $h_w$ ). For all gauges (whose individual resistances, surface areas and hence heating conditions, differed widely) it was found that

$$\frac{A_s}{C_s} h_w = 0.1042 \pm 0.0068 \quad (3 - 8)$$

This result for the heat loss also showed that the thermal capacity of the calorimeters was almost in proportion to the gauge surface area, since the Pyrex glass plate with a uniform thickness ( $0.058 \pm 0.001$  inches) was expected to give a constant heat loss over the test surface. This result is consistent with the effective thermal capacity discussed in

Appendix B4. The equivalent thermal capacity per unit area,  $C_g/A_g$ , was calculated to be 0.0414 Btu/ft<sup>2</sup>F for the parabolic thermal model. Using this model the measured heat transfer on the side-wall without the shock (bare plate heat transfer) is as shown in Fig.32. In the figure the local Stanton number is defined as

$$C_h = h_a / \rho_1 u_1 C_p \quad (3 - 9)$$

The average local Stanton number over the test surface is

$$(C_{h_o})_{\text{avg.}} = 0.00188 \pm 0.00027 \quad (3 - 10)$$

Although the measurements show a 15% scatter the average value of  $1.88 \times 10^{-3}$  agrees well with the prediction from the Van Driest II theory (Ref.31) of

$$(C_{h_{VD}}) = 0.00181 \quad (3 - 11)$$

using test conditions of

Mach number = 2.3 ,

stagnation temperature = wall temperature = 285°K ,

Reynolds number =  $0.8 \times 10^5$  and

momentum thickness = 0.040 inches.

Using this flat-plate boundary layer, the influence of the input electric current to the gauge when being used as a surface thermometer was examined. These data are also shown in Fig.31, for current intensities of 3 and 6mA. It is obvious that this level of current intensity had little influence on the measured data.

The measurement error is estimated to be within  $\pm 15\%$ . This figure is a little worse than that of the previous slug-calorimeter technique. However it must be remembered that the present stagnation pressure is only about  $\frac{1}{4}$  of that used in the intermittent tunnel.

### 3.6 Encapsulated Liquid Crystal Technique

To visualize the global temperature distributions on the side wall surface, encapsulated liquid crystals were used in the manner illustrated in Fig.33. These liquid crystals respond to small differences in temperature by showing bright colours. When illuminated with white light and cooled through their sensitive temperature span, they show a continually varying colour spectrum from colourless to violet, successively through blue, green, yellow, red and again colourless. This colour change is fully reversible. The model painted with them can stand repeated use without cleaning and recoating, which is not the case for phase-change paints. The encapsulated liquid crystals are soluble in water so that they can be sprayed on the model surface to form a layer of uniform thickness. Further information can be found in Refs.32 and 33.

In the tests conducted in the intermittent tunnel, the experimental procedure was very simple. Finished matt-black board was prepared for the side wall. The encapsulated liquid crystals, diluted with the same amount of hot water (approximately  $50^{\circ}\text{C}$ ), were sprayed on the board and left to dry. Before the tunnel run the board was always allowed to reach its equilibrium temperature (room temperature). When the tunnel was started and the air began to cool the board surface, the encapsulated liquid crystal

layer showed the surface temperature patterns changing with time. The varying coloured pictures of the surface temperature pattern were taken by a motor-driven camera.

The sensitive temperature range of the liquid crystals greatly affected the quality of the pictures obtained. As described previously, this tunnel provided approximately  $18^{\circ}\text{K}$  difference between the wall temperature and the adiabatic wall temperature. The sensitive temperature range of the liquid crystals used was chosen so as to have a  $5^{\circ}\text{K}$  span at approximately  $5^{\circ}\text{K}$  below room temperature; i.e.  $5\text{-}10^{\circ}\text{C}$  sensitive liquid crystals for the winter season and  $18\text{-}23^{\circ}\text{C}$  sensitive ones for the summer season. The duration of the test was from 10 to 15 seconds (for the hard-board surface used above).

The materials of the side wall had a great influence on the quality of the pictures. An epoxy-resin board covered with copper film gave uniform thermal properties over the test surface. However, the pictures obtained on this board tended to be 'smeared' by thermal conduction through the copper film. Although a wooden board (birch) gave good coloured pictures, fibres of the wood surface spoiled the surface temperature distributions. Of all the surfaces tested it was found that the smooth face of standard hard-board gave the best results. The reference surface temperature was measured with a single thin film gauge.

The liquid crystal layer was illuminated at approximately 45 degrees to avoid white-light reflections from the wall surface caused by the small grains of the encapsulated liquid crystals. The light source was a 250 W slide-projector. The camera to record the coloured temperature pattern was located so as to take pictures nearly normal to the light direction, for the same

reason as above. Kodak Ektachrome ASA 400 films were used with an exposure time of 1/60 seconds at an aperture of f/5.6. To strengthen the colour contrast of the pictures, a special development process was used which increased the effective film speed by a factor of 4.

### 3.7 Viscous Layer Surveys

To survey the boundary layer growing along the tunnel side wall and the viscous layers in the interaction region, some small probes and a probe drive system were employed.

The probes were individually designed to measure the total pressure (Pitot pressure), the static pressure and the flow yaw-angle. The shapes and dimensions of these probes are shown in Fig.34. These were made from hypodermic tubing.

The probe drive system was designed to move the Pitot probes normal to the tunnel side wall and also to pitch them so that the probes could be aligned with the local direction of the flow. Determination of the distance of the probes from the wall surface was made by a micrometer built into the drive system. The yaw angle of the probes was measured directly by a pointer moving over a calibrated scale.

The measured total and static pressures were used to obtain other properties in the viscous layer. The method of analysis is described in Appendix A.

#### 4. EXPERIMENTAL RESULTS

##### 4.1 Presentation of Experimental Results

Some typical experimental results are introduced in this chapter, together with some discussion and interpretation. All the experimental results (for both the tunnel test programmes) are given in the Appendices as listed below.

- (1) Schlieren photographs in Appendix C.
- (2) Oil-flow patterns in Appendix D.
- (3) Vapour-screen pictures in Appendix E.
- (4) Wall-surface static pressure distributions in Appendix F.
- (5) Wall-surface heat transfer distributions in Appendix G.
- (6) Encapsulated Liquid Crystal Pictures in Appendix H.
- (7) Wall-surface temperature distributions in Appendix I.

In the figures two different types of Cartesian co-ordinate systems are used, of which the origins coincide with the shock generator leading edge on the tunnel side wall. For one of the co-ordinate systems, the X, Y and Z axes are defined in directions parallel and normal to the free stream. The other consists of the  $X_g$  and  $Y_g$  axes which are respectively defined in directions along and normal to the shock generator surface. A length  $X_g$  is also employed to specify a distance in the free stream direction measured from the location of the shock wave. The details are shown in Fig.35.

##### 4.2 The Stability and Repeatability of the Flow Fields

The schlieren system was continually used to monitor the flow. At the beginning of each test programme the shock generator was taken through the full range of operating angles. Notes were made of any unsteadiness resulting from either shock induced separation or choking of the flow.

For shock generator angles ( $\delta_s$ ) up to  $9^\circ$  with models A and AM, and up to  $15^\circ$  using model B the flow was both stable and repeatable. A comparison between the measured shock-wave angles and those predicted by the inviscid, oblique-shock theory is shown in Fig.36. The agreement in the ranges of  $\delta_s$  given above is good.

With model A the flow chokes intermittently at  $\delta_s = 10^\circ$  and chokes completely when  $\delta_s = 11^\circ$ . For model AM these values of  $\delta_s$  are lowered about half a degree.

For model B inviscid flow theory predicts a Mach reflection at  $\delta_s = 16^\circ$  but this was not observed from the schlieren picture. However the oil-flow picture at  $\delta_s = 15^\circ$  did show a surface-flow pattern bending round to form a rather unsteady dead-flow region in the vicinity of the bottom wall. This seemed to be due to the fully-deflected side-wall boundary layer interacting with the bottom liner (Appendix D4-f).

All models behaved as expected in the useful operating range of  $\delta_s$ . There were no spurious compression or expansion waves to upset the required flow field.

#### 4.3. Flow Field Studies Made Using the Oil-flow and Vapour Screen Techniques

##### 4.3.1. Oil-Flow Patterns on the Tunnel Side Wall

As the shock generator angle increased, the oil-flow pictures on the tunnel side wall showed a surface flow pattern converging toward and into a line near the shock. Meanwhile a divergent surface-flow pattern was observed near the shock generator root, for all shock generator angles. For these general flow features, there was no difference between Models A, AM and B.

Typical oil-flow pictures are presented in Fig.37, together with sketches of the most prominent features.

(1) Surface-Flow Convergence

In the oil flow pictures, two types of surface-flow convergence are observed. They are shown in Fig.37, by using solid and broken lines which are respectively named *complete* and *incomplete* convergence. The convergence line on the side wall (whether complete or incomplete) is labelled (A) in the sketches e.g. Fig.37.

Complete Surface-Flow Convergence

A strong surface-flow convergence into a single line appears extensively at  $\delta_s = 9^\circ$  for Models A and AM (e.g. Figs.37b - 37c), at  $\delta_s \geq 11^\circ$  for Model B (e.g. Fig.37f), and locally near the shock generator at  $\delta_s < 9^\circ$  for Models A and AM (e.g. Fig.37a). The convergence line (indicated by a solid line) originates in the vicinity of the shock generator leading edge and runs a little upstream of the shock. Ahead of this convergence line the oil streak lines completely converge into it. Downstream of the line, the oil coalescence is not clear and the streak lines look as if they are parallel to the line. However, in this region, careful observation confirms that some streak lines do in fact emerge *from* the line while a low speed surface-flow area is formed between the convergence line and the shock location behind it.

Incomplete Surface-Flow Convergence

In the picture of Model B at  $\delta_s = 11^\circ$  (Fig.37e), it can be seen that the above complete surface-flow convergence disappears at a certain distance from the shock generator, and the oil streak lines near the convergence line tend to swing downstream from the 'disappearance point'. This alteration

of surface flow behaviour along the convergence line can be found in most pictures showing some complete convergence, (e.g. Figs.37b - 37c and 37e - 37f). In an incomplete convergence region the oil streak lines never converge into a single line, but they still tend to coalesce near the shock over a 'convergence zone' which grows in size along the shock. The centre of these streak lines converging into a zone is indicated by a broken line in Fig.37.

The surface-flow pattern forming the incomplete convergence zone can be seen particularly well at  $\delta_s = 10^\circ$  for Model B (Fig.37d). In this case, the incomplete convergence line originates near the shock generator leading edge.

Thus, there is a limit to the existence of complete surface-flow convergence in terms of distance from the shock generator leading edge and this distance depends strongly on the shock generator angle. The relation between this distance and the shock generator angle is shown in Fig.38.

#### Boundary Line between the Inner and Outer Surface Flows

The convergence line described above (whether complete or incomplete) can be used as a boundary line to divide the interaction region into an inner and an outer surface-flow region. The outer surface flow is upstream of the convergence line and comes from the upstream undisturbed surface flow of the side-wall boundary layer.

The inner surface flow originates in a divergent surface-flow region (mentioned below) near the shock generator root and runs downstream of the convergence line. It is clear that the boundary line develops from the incomplete convergence line to the complete convergence line, as the shock generator angle is increased.

(2) Surface-Flow Divergence

In the oil-flow pictures on the side-wall, a surface-flow divergence is also found (at any shock generator angle) along the shock generator root. The divergent surface-flow pattern is typical of that produced by 'ordinary flow-reattachment'. In the centre of the divergent surface-flow region, it is possible to draw an 'envelope' of the oilstreak lines. In Fig.37 the line is marked as divergence line. The divergence line starts in the vicinity of the shock generator leading edge and runs downstream whilst moving away slightly from the shock generator root.

(3) Surface-Flow Deflection Angle

As the shock generator angle increases, the side-wall surface-flow deflection angle grows rapidly and eventually exceeds the shock angle, as observed in the oil-flow pictures already discussed. In the early stage of the growth ( $\delta_s > 9^\circ$  in Fig.37), the maximum surface deflection is close to that of the convergence line. As the surface-flow convergence line strengthens to form a complete convergence (e.g.  $\delta_s > 9^\circ$  in Fig.37), the maximum deflection angle becomes larger than the convergence line angle. In this case, the maximum flow deflection appears near the shock generator root, where the above surface-flow divergence is observed. The maximum surface-flow deflection angle is plotted in Fig.39, with respect to the shock generator angle, together with the surface-flow angle of the convergence line. In this figure, the flow angles are defined relative to the shock generator surface. The figure shows that the maximum surface-flow deflection angle can be much

higher than McCabe's prediction, (see Fig.39). It must also be stressed that, even when the surface-flow deflection exceeds the shock angle the surface-flow pattern does not always show the complete convergence which is one of the features needed to confirm flow separation. In other words, the condition of separation or even 'incipient separation' is not defined by the surface-flow deflection angle exceeding the shock angle.

#### 4.3.2. Oil-Flow Patterns on the Shock Generator Surface

In Fig.37, the oil-flow pictures on the shock generator surface show some interesting features. The detailed shock-generator flow patterns for Model B are presented in Fig.40. Two shock generator angles ( $\delta_s = 10^\circ$  and  $13^\circ$ ) are shown because they produce the incomplete and complete types of convergence on the side-wall surface as previously described. The oil-flow pictures (Figs. 37 and 40) show that the shock generator surface flow is divided, by two narrow compression zones, into three regions of convergent, accelerated and undisturbed flow.

The oil-flow pictures (e.g. Fig. 40a) shows that a narrow compression zone originates from the shock generator leading edge, at a point inside the side-wall boundary-layer edge, and spreads downstream. This compression zone divides a slender flow-region near the shock generator root. In this region, a convergent surface-flow is observed, and is labelled *convergence B* in the sketches. This convergence region grows in size with increasing shock generator angle. When the side-wall surface flow indicates complete convergence (convergence A), the convergence B produces a narrow foamy zone

developing downstream. This convergence B is caused by two different surface flows. One of them, which is inboard of the convergence line B, is connected with the side-wall surface flow, by way of the shock generator root. The other is supplied from outboard of the compression zone. Outside the compression zone, an accelerated region is observed. This region lies inboard of another compression zone which starts from the leading edge at a point located roughly two side-wall boundary-layer thicknesses away from the shock generator root. In the accelerated region, the surface flow is accelerated toward the shock generator root. (The outer compression zone is not clear at  $\delta_g = 13^\circ$  in Fig.40, since the picture was taken after the tunnel stop. The compressions for Models A and AM were weak, due to the existence of the tunnel liner boundary layer.)

#### 4.3.3. Vapour-Screen Pictures

Typical vapour-screen pictures are presented in Fig.41, together with sketches showing the most important features. In the figure, the approximate locations of the shock and the surface-flow convergence and divergence regions (as found from the corresponding schlieren and oil-flow pictures described above) are all marked.

#### Shock Waves

In the vapour-screen technique, the shock is rendered visible by a sudden change of the fog density per unit volume across it, the number of fog particles being almost proportional to the air density. In the vapour-screen pictures, the shock is detected as a boundary line between lighter and darker regions, as shown in the sketches. The shock position is close to

that measured from the corresponding schlieren picture, in the inviscid external-flow region. The shock wave approaches the side-wall in the form of a lambda shock over a distance from two to four side-wall boundary-layer thicknesses.

The approximate locations of the shocks as measured by the schlieren and vapour-screen techniques are compared with each other, in Fig.42. The 'vapour-screen shock' tends to appear a little upstream of the 'optical shock'; i.e. the vapour-screen shock angle is from one to two degrees larger than the optical one. This difference corresponds to a change of free-stream Mach number of less than 0.1 (for ideal air). Although the reason for this difference is not certain, it is likely that the moisture added to the tunnel air for the vapour-screen tests changed the physical properties of the test flow.

#### Small Vortex Swirling near the Shock Generator Root

The vapour-screen pictures of Model B (Figs.41c - 41e) show some interesting features near the shock generator root. In this region the pictures contain a small light, circular area. Particularly in Fig.41c, the light circular area can be seen to contain a darker core. (Although the other pictures also show a similar region, the evidence is not so clear.) The light circular area looks similar to those produced by vortices in general vapour-screen pictures, (the radial acceleration of the circular flow sweeps away the heavy fog particles from the centre of the flow to the outer region). On the side-wall surface 'beneath' the small light circular area, there is a thin dark layer spreading across the wall. This shadowy zone is similar to regions of boundary layer flow in general vapour-screen pictures. It must be emphasised that these flow features are observed for all the wedge generator angles tested.

With the help of the corresponding oil-flow pictures, the following interpretation of the flow field is made. The oil-flow divergence line is located near the junction of the small light circular area with the thin dark zone (as marked in the vapour-screen pictures). The convergence line B is near the other side of the light circular area, on the shock generator surface. In the flow region near the shock generator root, the surface-flow on the shock generator surface (which is accelerated toward the shock generator root and converges into the convergence line B) lifts up from the shock generator surface at the convergence line B, and re-attaches to the side-wall surface at the divergence line, by way of a small vortex swirling near the shock generator root. This interpretation also explains the appearance of divergent flow on the side-wall, (which exists at any shock generator angle, even when no surface-flow convergence is observed on the side-wall). The existence of a small vortex near the shock generator root would mean that the divergence line is the re-attachment line 'behind' the vortex.

In the case of Model AM (Figs.41a-41b), the 'thick dark zone' comes up onto the shock generator surface, as if a thick 'vortical' flow exists at the corner.

#### Viscous Layer

As noted, the viscous layer shows as a thin dark zone on the side-wall surface. It is further observed that this dark zone has its minimum thickness near the location of the convergence line A.

#### 4.4. Wall Surface Flow Features Indicated by the Static Pressure and Heat-Transfer Distributions

##### 4.4.1. Static Pressure Fields

The isobar patterns on the side-wall surface are presented in Fig.43, for Model A at  $\delta_s = 5, 7$  and  $9$  degrees and for Model B at  $\delta_s = 7, 10$  and  $13$  degrees. These isobars were obtained by interpolating the measured static pressure distributions to be discussed in section 4.4.4.

The isobar patterns indicate that the static pressures on the side-wall surface gradually increase across the shock, regardless of the steep change of the external-flow pressure expected from inviscid theory.

This slow growth of the wall-surface static pressures is caused by the viscous interaction between the shock and the boundary layer on the side-wall surface.

The 2.5 x 2.5 inch wind tunnel test programme was conducted using a relatively small test flow area. From the results a suggestion was made in Ref.23 as follows.

The static pressure on the side wall requires approximately ten side-wall boundary-layer thicknesses to reach its maximum value, and the upstream influence due to pressure propagation through the subsonic region of the viscous layer can appear up to approximately six side-wall boundary-layer thicknesses ahead of the shock. These conclusions were made on the basis of the quasi-two-dimensional isobar patterns shown for example in Figs. 43a - 43c. In the figures, the isobars run nearly parallel to the shock, except in a region near the tunnel bottom liner where the shock reflection disturbs the flow field.

The next test programme used the larger test flow field of the 9 x 9 inch tunnel. As shown in Figs. 43d - 43f, the isobars in the larger flow field show that the pressure distribution is not quasi-two-dimensional but more 'conical' in nature. In a small limited region just ahead of the shock, the isobars run roughly parallel as in a quasi-two-dimensional flow but overall it can clearly be seen that the isobars spread over the side wall in a roughly conical fashion from an origin near the shock generator leading edge. Hence it is not particularly useful to measure the pressure propagation distance in terms of the undisturbed side-wall boundary-layer thickness, since this is constant whereas the pressure field is growing radially outwards in a roughly conical fashion. The earlier comments concerning the quasi-two-dimensional nature of the pressure field are probably conditioned to the small test flow field in which the measurements were taken.

(Similar comments can be made for the oil-flow patterns in Fig.37.

Although the complete surface-flow convergence line in the Model A configuration seems to run parallel to the shock, it behaves in a more 'conical' fashion for Model B in the larger test flow field.)

It must be stressed that the basic pattern of the isobars does not vary noticeably with increasing shock generator angle. For both Models A and B, the pattern remains the same but the pressure gradient across the shock is steepened.

#### 4.4.2 Heat Transfer Distributions

The heat transfer patterns over the test surface are shown in Fig.44, where the local Stanton number is presented for the same experimental conditions as for the pressure fields described above. These patterns were again

obtained by interpolating the measured heat transfer distributions to be discussed in Section 4.4.4.

Fig.44 gives a basic pattern of the heat transfer field as described in detail later. The basic pattern is illustrated in Fig.44a on which the most significant surface-flow features from the oil-flow pictures are superimposed. This pattern consists of three individual heat-transfer peaks which can be distinguished from each other as follows.

- (i) The high heat-transfer 'peak' (A) appears near or a little upstream of the surface-flow convergence line.
- (ii) Another high 'peak' (B) takes place closely to the shock generator root, namely, where the surface-flow divergence is observed.
- (iii) The weak 'peak' (C) is found clearly in the case of Model A, upstream of the peak (A). The location of this peak is a little upstream of a surface-flow zone where the oil streak lines start to bend to form the surface-flow convergence.

#### Model A

The original interpretation (Ref.24) of the heat transfer data from Model A was made under the assumption that the temperature difference ( $T_w - T_{aw}$ ) was constant over the interaction region. However, more recent measurements for Model B have shown that it is necessary to take account of the local variation of ( $T_w - T_{aw}$ ), particularly downstream of the shock, as discussed in Section 5.1. This is because the temperature difference was small for both Models A and B, so that the local variation of  $T_{aw}$  (and to a less extent the variation in  $T_w$ ) cannot be ignored in analyzing the local Stanton number

from measured heat-transfer-rate data. It is now believed that Figs.44b - 44d for Model A underestimate the real value of the Stanton number, particularly downstream of the shock.

In Figs. 44b and 44c, at  $\delta_s = 5$  and 7 degrees respectively, the heat transfer 'peak' (A) appears near the calculated shock location near where the surface-flow convergence line lies. This peak is represented by the contour of  $C_h/C_{ho} =$  from 1.2 to 1.4 in the figures. The 'peak' (C) is found upstream of the 'peak' (A) as separately indicated by  $C_h/C_{ho} > 1.2$ . Downstream of the shock, the local variation of  $(T_w - T_{aw})$  gives the misleading result of the local Stanton number reducing with distances from the shock. This erroneous behaviour will be clarified in Section 5.1. In Fig. 44d for  $\delta_s = 9^\circ$ , the local variation of  $(T_w - T_{aw})$  suggests an illusory deep valley between the shock and the shock generator root. However, the 'peak' (B) is still clearly observed close to the shock generator root, as indicated by  $C_h/C_{ho} > 1.4$ .

#### Model B

The local Stanton numbers for Model B were analyzed from measured heat-transfer coefficient data. (Refer to Appendix B). In this method of analysis, the local variation of  $(T_w - T_{aw})$  is much less important. Through all of the shock generator angles used, ranging from  $\delta_s = 7$  to 13 degrees (Figs.44e - 44g), the basic pattern of the heat transfer does not vary noticeably but the heat transfer 'peaks' become more prominent with increasing shock generator angle.

The heat transfer 'peak' (A) appears just ahead of the surface-flow convergence line, as represented by  $C_h/C_{ho} > 1.0$  in Fig.44e and  $C_h/C_{ho} > 1.5$

in Figs. 44f - 44g. This 'peak' (A) is located more upstream of the shock and covers a much wider area, than that found for Model A. The difference in appearance of the 'peak' (A) between Models A and B is quite consistent with the corresponding oil-flow patterns (Fig.37). The oil-flow pictures show that the surface-flow convergence in the test conditions of Model B takes place further upstream of the shock and is less concentrated than for Model A. It is concluded that the appearance of 'peak' (A) is closely connected with the surface-flow convergence.

The heat-transfer 'peak' (C) cannot be observed in Figs.44f - 44g, owing to the coarseness of the 'isotherms' used. However, the 'peak' (C) can be seen from the heat transfer distributions shown in Appendix G, Fig.G2. A shallow 'trough' appears in the 'peak region' (A) as if it separates the 'peak' (C) from the main 'peak' (A). The location of this shallow 'trough' approximately coincides with the surface stream lines beginning to bend towards the plane of the shock. This heat transfer behaviour is almost the same as in Model A showing clear distinguishment between the 'peaks' (A) and (C).

The high heat transfer 'peak' (B) is very evident in Figs.44f - 44g with  $C_h/C_{ho}$  reaching values as high as 3. The heat transfer in this region close to the shock generator root will be discussed in detail in Section 4.4.4.

#### 4.4.3. Surface Temperatures

The surface temperature patterns are presented in two ways; i.e. by using the encapsulated liquid crystal pictures for Model A, and surface temperatures measured with the thin-film gauges for Model B.

Typical encapsulated liquid crystal pictures are shown in Fig.45, for  $\delta_s = 7$  and 9 degrees. In the figure, the 'blue-tone' and 'yellow-tone' zones shows higher and lower temperature regions respectively. (In Fig.45, the 'blue-tone' and 'yellow-tone' zones are respectively shown as 'dark' and 'light' greys. Since the colour photographs show only two main colours they have been printed in black and white for convenience.) The colour patterns change with time after the tunnel starts. The time indicated in the figure is within the period when the colour pictures give the most information about the general surface-temperature patterns. The detailed temperature-time histories are presented in Appendix H.

It is suggested that the higher and lower temperature zones correspond to the lower and higher heat-transfer-rate regions respectively. This is because the temperature patterns were obtained under a 'hot wall' condition at the moment that the intermittent tunnel started, and the thermal capacity of the wall-surface material is regarded as constant over the test surface. Then, if the thermal conduction on the wall surface can be ignored, the wall surface is cooled in proportion to the product of heat transfer coefficient ( $h$ ) and temperature difference ( $T_w - T_{aw}$ ). This idea makes it possible to compare these surface temperature patterns with the heat transfer patterns based on heat-transfer-rate data (Figs.44b - 44d).

One can clearly find some correspondence between the colour and heat transfer patterns. The colour patterns show lower temperature regions at two locations for all the shock generator angles tested; i.e. near the shock and near the shock generator root, (Fig.45). One of the lower temperature regions indicates that a high heat transfer zone exists near the shock. This high

heat-transfer zone corresponds to the heat transfer 'peak' (A) (Fig.44a). The encapsulated liquid crystal pictures also suggest that the 'peak' (A) could be spreading more extensively along the shock than in Figs.44b - 44d. The second lower temperature zone corresponds to the high heat-transfer 'peak' (B) lying close to the shock generator root. However, it must be stressed that these coloured surface-temperature patterns cannot directly give absolute quantity of the local Stanton number since they are also influenced by the local variations of the temperature difference ( $T_w - T_{aw}$ ).

The measured surface-temperature patterns for Model B are presented in Fig.46. These patterns indicate a low temperature zone between the shock and the surface-flow convergence line, for all shock generator angles, as indicated by  $T_{wl} - T_{wr} < - 2^\circ\text{K}$ . A high temperature region is observed downstream of the shock, as represented by  $T_{wl} - T_{wr} > + 2^\circ\text{K}$ . These temperature data will be used in Section 5.1. to discuss the heat transfer data measured across the shock.

#### 4.4.4. Static-Pressure and Heat-Transfer Distributions

Typical wall-surface static pressure distributions in the free-stream or external-flow directions are presented in Fig.47.

The pressure distributions plotted in Fig.47a for Model A, were measured in the free stream direction on the tunnel centre line ( $Y = 1.25$  inches). These distributions show that the wall-surface static pressure gradually increases across the shock. No noticeable alteration of the basic distribution pattern is observed for shock generator angles ranging from

5 to 9 degrees, though the corresponding oil-flow pictures indicate considerable change of the surface-flow pattern from the incomplete convergence to the complete convergence (Figs.37a - 37b).

The pressure distributions in Fig.47b for Model B were measured along lines parallel to the shock generator surface. In this figure, a slight alteration of the distribution pattern is observed as the shock generator angle is changed from 10 to 13 degrees. The region near the shock position tends to be 'flattened' with increasing shock generator angle. This tendency appears more strongly at  $Y_g = 2.04$  than  $Y_g = 1.04$  inches. The alteration of the pressure distribution pattern is consistent with the change of oil-flow pattern (Figs.37d - 37f). As the shock generator angle increases from 10 to 13 degrees, the incomplete convergence of the surface-flow changes to a complete convergence, and, with increasing distance from the shock generator, the complete convergence line is followed by an extensive low-speed zone between itself and the shock located downstream of it. Fig.47b shows that this is precisely the region in which the pressure is 'flattened' (rising slowly). The positions of the complete convergence line and the shock are marked on the figures. The surface pressure only begins to rise rapidly again once it has passed the shock location.\*

In Fig.48, typical heat-transfer and static-pressure distributions in the direction *normal* to the free-stream or the external-flow are presented. Locations of the shock and the surface-flow convergence line are indicated on the figure. As described previously, the static pressures gradually increase across the shock. However, the heat transfer distributions have very complicated patterns. (In Figs.48a - 48b for Model A, a high heat transfer region is

\* This flattening of the pressure distribution is thought to be an indication of sudden viscous layer thickening.

observed near the tunnel bottom liner at  $Y = 2.5$  inches. Since this is caused by interference from the tunnel liner, the present discussion omits this region.)

#### Surface-Flow Convergence Region

The surface-flow convergence brings about the high heat transfer 'peak' (A) near itself or, in most of cases, outside it. However, no noticeable peak of the static pressures is detected in this region. Although Scuderi (Ref.34) proposed a power law correlation between the heat transfer and the static pressure in this region, the present experimental data do not show any correlation between them at all. As noted in Section 4.4.2., the heat-transfer 'peak' (A) is connected only with the surface-flow patterns.

#### Interaction Region downstream of the Shock

Downstream of the shock, both the static pressure and the heat transfer tend to increase as the shock generator surface is approached, (except in Fig.48b where the heat transfer is considered to be under-estimated because of the local variation of  $(T_w - T_{aw})$ , as noted earlier). Neumann et al. (e.g. Ref.17) proposed a correlation between the static pressure and the heat transfer in this region. This correlation is tried in Fig.49. In Fig.49a, the local Stanton numbers are plotted with respect to the static pressure and compared with the well-known power law correlation for two-dimensional aerodynamic peak heating:

$$\frac{C_{h \max}}{C_{h \text{ ref}}} = \left( \frac{P_{\max}}{P_{\text{ref}}} \right)^n \quad (4 - 1)$$

where  $n = 0.8$  for a turbulent boundary layer. (Refer to Back et al., Ref.35 or Neumann, Ref.1) . However, the present experimental results show little correlation between pressure and heat transfer in this region. In Fig.49b, the maximum heat transfer of the 'peak' (B) is considered in streamwise direction, while correlated with the corresponding static pressure.

Both  $\{(C_h/C_{ho})_{\max}/(P/P_1)_{\max}^{0.8}\}$  and  $n$  are plotted versus non-dimensional streamwise distance using the undisturbed side-wall-boundary-layer thickness. The figure shows that the three-dimensional interaction can give rise to higher heat transfer than the two-dimensional case, particularly near the shock generator leading edge region.

The heat transfer in the three-dimensional interaction region will be further discussed in Section 5.

#### 4.5 Viscous Layer Surveys

Typical viscous-layer properties measured using static and pitot pressure probes, and a yaw meter, are presented in Fig.50 for Model A with  $\delta_g = 5, 7$  and  $9$  degrees. The experimental results are presented using the  $(X_g, Y_g, Z)$  co-ordinate system. Thus the streamwise and cross-flow velocity components,  $u$  and  $v$  respectively, are defined in directions parallel and normal to the external flow downstream of the shock. The survey results show that the side-wall boundary layer is skewed a great deal and warped near the shock. The salient features of the flow are as follows.

- (1) The undisturbed side-wall boundary layer upstream of the shock, has no detectable flow-deflection and shows a velocity profile typical of a fully turbulent boundary layer. Thus, as expected, the flow is quasi-two-dimensional. (Refer to Fig.16). In the interaction region downstream of the shock, this boundary layer has been changed dramatically into a complex three-dimensional zone of highly skewed flow. The flow deflection angle is zero in the inviscid external region, because the external flow is parallel to the shock generator direction ( $X_g$  axis). As the side wall is approached so the flow direction yaws or skews.
- (2) At  $\delta_s = 5$  and 7 degrees, the local flow deflection in the outer part of the boundary layer inclines lightly towards the shock generator, as the distance from the wall is decreased. (See 0.2 inches  $< Z < 0.4$  inches in Fig.50a). In this flow region, the local static pressure changes down rapidly from the external-flow pressure to the wall-surface pressure (Fig.50b) and the local Mach number exceeds the external-flow Mach number (Fig.50c). This flow behaviour suggests that the three-dimensional glancing shock interaction provides a flow region similar to the 'supersonic tongue' of two-dimensional normal shock interaction. (Refer to Fig.7). In the case  $\delta_s = 9^\circ$  a similar flow behaviour can be detected (weakly) in the region of 0.3 inches  $< Z < 0.6$  inches.
- (3) In the inner region,  $Z < 0.2$  inches for  $\delta_s = 5$  and 7 degrees, the local flow deflection angle increases steadily as the wall is approached and reaches the surface-flow deflection angle (obtained from the oil-flow picture) at  $Z = 0$ , (Fig.50a). In this flow region, the local static pressure is almost constant (Fig.50b) while the local Mach number simply

decreases to zero at the wall (Fig.50c). The corresponding velocity profiles show the typical patterns of a highly skewed 'boundary layer' (Figs.50d - 50e). The cross-flow velocity component is considerable near the wall.

- (4) The distribution of the local flow deflection angle for  $\delta_s = 9^\circ$  is in striking contrast to those at  $\delta_s = 5$  or 7 degrees (Fig.50a). Below  $Z = 0.1$  inches, the local deflection angle increases rapidly, overshoots the oil flow angle at the surface, then swings back to match it at  $Z = 0$ . The corresponding streamwise velocity profile has a point of inflection and a lower region of reduced velocity (Fig.50d).

5. HEAT TRANSFER IN THE INTERACTION REGION

5.1. Heat Transfer Measurement in the Shock Region

In the previous section, it was mentioned that local variations of the temperature differences ( $T_w - T_{aw}$ ), i.e. between the wall and adiabatic wall temperatures, greatly affected the interpretation of measured heat-transfer-rate data, particularly when the absolute value of ( $T_w - T_{aw}$ ) is small. This is because the local Stanton number,  $C_h$ , is defined by

$$C_h = q / \rho_1 u_1 C_p (T_w - T_{aw}) \quad (3 - 5)$$

where  $q$  is the measured heat transfer rate while  $\rho_1$ ,  $u_1$  and  $C_p$  are the free stream density, the free stream velocity and the specific heat respectively. However, the local variation of ( $T_w - T_{aw}$ ) is much less important if the local Stanton number is obtained from measured heat-transfer-coefficient data,  $h_a$ , as given by

$$C_h = h_a / \rho_1 u_1 C_p \quad (3 - 9)$$

which does not involve the term ( $T_w - T_{aw}$ ).  $C_h$  was derived from (3 - 5) in the Model A tests but from (3 - 9) in the Model B tests.

During the heat transfer measurements on Model B, the local wall-surface temperature,  $T_{wl}$ , was also measured (Fig.46). This temperature data gave the local variation of ( $T_w - T_{aw}$ ), i.e. ( $T_{wl} - T_{awl}$ ), through a thermal balance on the wall surface (Appendix B4); i.e.

$$h_a (T_{wl} - T_{awl}) = h_w (T_{wr} - T_{wl}) \quad (5 - 1)$$

(the heat transfer from the calorimeter to the air)

(The heat transfer from the inner wall to the calorimeter)

where  $T_{wr}$  is the reference wall temperature and  $h_w$  is a heat-loss coefficient. The results of  $(T_{wl} - T_{awl})$  are presented in Fig.51, for the bare-plate case and the interaction cases at  $\delta_s = 7, 10$  and  $13$  degrees. (In the present results, the measured wall reference temperature is adjusted by using the 'undisturbed' free-stream adiabatic-wall temperature assuming a recovery factor of  $r = 0.89$ ). In the figure  $(T_{wl} - T_{awl})$  for the bare-plate case is given by the solid-round symbols and shows an almost flat distribution over the test surface. However, for the interaction cases,  $(T_{wl} - T_{awl})$  has a significant local variation downstream of the shock; i.e. more than  $10^\circ\text{K}$ . This local variation is much larger than the expected change of local adiabatic-wall temperature across the shock, which is estimated to be  $2 - 4^\circ\text{K}$  for  $\delta_s = 7^\circ - 13^\circ$  assuming a constant recovery factor of  $r = 0.89$ . The actual recovery factor has been calculated from the measured temperature data by

$$r = \frac{T_{awl} - T_\infty}{T_o - T_\infty}, \quad (5 - 2a)$$

$$T_\infty = T_o / (1 + \frac{\gamma-1}{2} M^2) \quad (5 - 2b)$$

where  $T_o$  is the stagnation temperature and  $\gamma$  the ratio of specific heats, while  $M$  is taken to be local external-flow Mach number; i.e.  $M_1$  and  $M_2$  upstream and downstream of the shock respectively. The recovery factor distributions are presented in Fig.52a, and the patterns over the test surface are shown in Figs.52b - 52d. Although the accumulated calculation errors reduce the accuracy of the results, the recovery-factor behaviour is fairly clear. As the flow goes downstream the recovery factor decreases

in the region between the surface-flow convergence line and the shock, but, downstream of the shock, it quickly increases almost in proportion to the distance from the shock and approaches unity.

It can now be estimated how much the local variation of  $(T_w - T_{aw})$  affects the local Stanton number previously obtained from the heat-transfer-rate data of Model A by assuming that  $(T_w - T_{aw})$  is equal to constant. From (3 - 5) and (3 - 9) it can be shown that

$$C_h^* = C_h \frac{T_{wl} - T_{awl}}{T_w - T_{aw}} \quad (5 - 3)$$

where  $C_h^*$  is the corrected local Stanton number and  $C_h$  is the value computed assuming  $(T_w - T_{aw})$  to be constant. When the local value of the recovery factor is known, the variation of  $(T_w - T_{aw})$  can be calculated from

$$(T_{wl} - T_{awl})_{cal.} = (T_w - T_o) + (1 - r)(T_o - T_\infty) \quad (5 - 4)$$

If the absolute value of  $(T_w - T_o)$  is large enough to neglect the second term in (5 - 4), then it is clear from (5 - 3) that  $C_h^*$  can be regarded as equal to  $C_h$ . However, in the present test conditions for Model A,  $(T_w - T_o) = 5^\circ\text{K}$  at the maximum, so the second term cannot be ignored. This second term can be estimated to vary locally from  $7.5^\circ\text{K}$  to  $22.5^\circ\text{K}$  for the recovery factor ranging from 0.85 to 0.95 (as expected from Fig.52 for Model B), and give approximately  $\pm 40\%$  ill-interpretation of the local Stanton number under the assumption of constant  $(T_w - T_{aw})$ .

## 5.2. Typical Heat Transfer Distributions

Some typical heat transfer results for Model B are plotted in Fig.53 and compared with Neumann's results (Ref.17), which were measured at almost the same shock pressure ratio.

In the interaction region between the shock and the shock generator root, there is good agreement between the three sets of data. In all of the cases, the heat transfer rises to 'peak' (B) near the shock generator root. However, in the region ahead of the shock ( $Y/Y_s > 1$  in Fig.53), the agreement is confused by various patterns of the 'peak' (A). The heat-transfer results in this region probably indicates how important the individual test conditions are and perhaps how only the grossest flow characteristics are likely to be common when comparing different test data in different wind tunnels.

## 6. THREE-DIMENSIONAL FLOW SEPARATION IN THE INTERACTION REGION

### 6.1. Definition of Three-Dimensional Separation

As noted previously, the oil-flow pictures on the side wall show that the surface flow in the interaction region is highly deflected with increasing shock generator angle and forms a convergence zone near the shock (convergence A in Fig.37). When the shock generator angle exceeds a certain value, this surface-flow convergence zone produces a 'complete convergence line' a little upstream of the shock. See Fig.54. In front of this line, the oil-streak lines coalesce with it. However, behind the line, the oil-streak lines run nearly parallel to it. This oil-flow behaviour is as shown by 'convergence pattern I' in the figure. This is not like 'convergence pattern II' indicating the surface-flow coalescence into a single line on both sides of it, which is typical of Maskell's ordinary flow separation (Fig.6b, taken from Ref.6) and commonly accepted to be a type of three-dimensional separation. However, the present paper shows that the surface-flow convergence pattern I also belongs to the same category of ordinary flow separations as Maskell's. This assertion is based on Lighthill's 'skin-friction-line topology' (see Ref.37 or the excellent review of Tobak et al., Ref.38), as follows.

The flow separation is easily and clearly defined by using the 'limiting-stream-line concept'. The limiting stream line is the closest stream line to the wall surface in the attached flow field. Thus for attached flow this stream line coincides with the 'surface stream line' (which is employed in other parts of this paper) and is in contact with the 'skin-friction line' (surface shear-stress trajectory). Three dimensional separation can be

defined as follows. When the limiting stream line leaves the wall surface, the main flow separates from the wall at the separation point of the limiting stream line. Now having given a clear definition, what is required is proof.

The limiting-stream-line concept is not sufficient to give conclusive *evidence* of three-dimensional flow separation in the oil-flow pictures, for the following reasons.

After the limiting stream line rises up from the wall surface, no trace of its behaviour can be obtained on the wall surface. The separation line lies exactly on a line at which the limiting stream line disappears from the wall surface. Even after the disappearance of the limiting stream line from the wall surface, the oil-streak line is left on the surface and moves with the skin friction. Thus, the oil-streak lines cannot directly indicate behaviour of the limiting stream line in the vicinity of the separation line.

Introduction of the 'skin-friction-line' concept makes it possible to clarify the flow behaviour in the vicinity of the separation line. The skin-friction line is defined everywhere on the wall surface and the separation line coincides with a skin-friction line (showing an envelope of an infinite number of skin-friction lines). Using Lighthill's simple argument it is possible to discuss how the limiting stream line leaves the wall surface in the vicinity of the separation line. A stream tube is supposed to be on the wall surface near the separation line as shown in Fig.55a. The width and height of the rectangular stream tube are  $n$  and  $h$  respectively (which are assumed to be finite but nearly 'infinitesimal' so that the local resultant velocity vectors are coplanar and form a linear profile). Then the mass flux through the stream tube is given by

$$\dot{m} = \rho h n U^* \quad (6 - 1)$$

where  $\rho$  is the density and  $U^*$  the mean resultant velocity in the cross section of the stream tube. The skin-friction may be written as

$$\tau = \mu \left( \frac{U^*}{h/2} \right) \quad (6 - 2)$$

where  $\mu$  is the coefficient of viscosity so that

$$U^* = \tau h / 2\mu \quad (6 - 3)$$

Hence,

$$\dot{m} = \rho h^2 n \tau / 2\mu = \text{constant} \quad (6 - 4)$$

yielding

$$h = \left( \frac{2\mu\dot{m}}{\rho n \tau} \right)^{\frac{1}{2}} \quad (6 - 5)$$

Equation (6 - 5) shows that the height of the limiting stream tube on the wall increases rapidly towards infinity, when either the width ( $n$ ) or the skin-friction ( $\tau$ ) approaches zero. Therefore, if any limiting stream line is situated in the stream tube, the limiting stream line must leave the wall surface (and the flow is separated) in either of the following cases:

- (i) The skin-friction vanishes on the wall, as in Maskell's singular separation at a singular point, (Fig.6a).
- (ii) The width of the stream tube, namely the distance between the adjacent friction lines becomes zero, as in Maskell's ordinary separation along the separation line (Fig.6b).

The latter case clearly occurs in the surface-flow convergence pattern I in Fig.54, upstream of the complete convergence line. The distance between adjacent oil-streak lines indicating the skin-friction lines reaches zero.

The side-wall boundary layer upstream of the complete convergence line must be separated at the line, without the need to refer to the downstream surface-flow pattern.

## 6.2. Angular Momentum Conservation Concept of the Surface Flow Convergence

### 6.2.1. Consideration of the Oil-Flow Convergence

The oil-flow pictures on the side wall show the following behaviour of the surface-flow convergence near the shock (convergence A), as described in Section 4.3.1.

- (i) The surface flow can preserve an incomplete convergence pattern (showing attached flow), even if the surface-flow deflection exceeds the shock angle (Fig.37d).
- (ii) Even when the shock generator angle is large enough to produce surface-flow convergence (showing separated flow), the complete convergence line can change at a certain distance from the shock generator into an incomplete convergence zone which bends round in the downstream direction. (Figs.37b - 37c and 37e - 37f).

These experimental facts suggest that the appearance of flow separation in the interaction region does not depend on the surface-flow deflection angle exceeding the shock angle (as proposed by McCabe, Ref.8), but on other flow conditions. The suggestion made here is that there is a limit to the angle through which the lower part of the boundary layer can be deflected or skewed. The maximum permissible angle of the surface-flow deflection is being discussed in the following Sections.

### 6.2.2. Review of McCabe's Theory

McCabe (Ref.8) developed a simple approximate theory which related the surface-flow deflection to the external flow conditions. In this theory, circulation around a rectangular vortex tube is considered in a quasi-two-dimensional flow field assuming that the boundary layer thickness is infinitesimal so that the flow can slip at the wall surface (Fig.56a). The vortex tube has a height equal to the boundary-layer thickness and is initially situated upstream of the shock so as to be normal to the free stream in a spanwise sense. Then, the circulation around this vortex tube is given by

$$\sum_{\substack{\text{boundary} \\ \text{layer}}} \delta\omega_1 \delta x_1 \delta z_1 = \left( \frac{\partial u}{\partial z} \delta x_1 \right)_{\substack{\text{boundary} \\ \text{layer}}} dz = u_1 \delta x_1 \quad (6 - 6)$$

where  $\delta\omega_1$  is local vorticity for a vortex-tube element with height  $\delta z_1$  (normal to the wall) and width  $\delta x_1$  (parallel to the free stream), while  $z$  is the displacement from the wall,  $u$  the streamwise velocity and  $u_1$  the free-stream velocity. This vortex tube travels downstream at the external flow velocity and passes through the shock into the interaction region. In this process, the vortex tube is assumed to retain a rectangular cross section with its height constant but its width changing to maintain continuity of the flow. Downstream of the shock, the vortex tube axis has been swept relative to the external flow direction, owing to the existence of oblique shock, so unit spanwise-length of the vortex tube has been also changed, (Fig.56a). In this flow region, the circulation around the vortex tube is given in the external flow direction, as

$$\int_{\text{boundary layer}} \delta\omega_2 \cos\zeta \delta x_2 \tan\zeta \delta z = \int_{\text{boundary layer}} -\frac{\partial v}{\partial z} \delta x_2 \tan\zeta dz = v_w \delta x_2 \tan\zeta \quad (6-7)$$

where  $\delta\omega_2$ ,  $\delta x_2$  and  $\delta z_2$  are downstream value corresponding to  $\delta\omega_1$ ,  $\delta x_1$  and  $\delta z_1$  mentioned above,  $\zeta$  is the sweep angle of the vortex tube relative to the external flow and  $v_w$  is the cross-flow velocity at the wall.

Conservation of the circulation needs (6-7) to be equal to (6-6), then

$$\int_{\text{boundary layer}} \delta\omega_1 \delta x_1 \delta z_1 = \int_{\text{boundary layer}} \delta\omega_2 \delta x_2 \sin\zeta \delta z_2 \quad (6-8)$$

so that

$$u_1 \delta x_1 = v_w \delta x_2 \tan\zeta \quad (6-9)$$

The surface-flow deflection angle relative to the external flow,  $\epsilon$ , is defined by

$$\tan\epsilon = v_w / u_2 \quad (6-10)$$

where  $u_2$  is the downstream external-flow velocity.

Substituting (6-9) into (6-10) and calculating the changes of flow properties across the shock, gives

$$\tan\epsilon = \frac{\cos^2(\beta - \delta_g) - \cos^2\beta}{\cos^2\beta \tan(\beta - \delta_g)} \quad (6-11)$$

where  $\beta$  is the shock angle and  $\delta_g$  the shock generator angle.

For a given upstream Mach number, this equation enables the variation of  $\epsilon$  with  $\delta_g$  to be calculated.

McCabe also predicted the shock generator angle to induce incipient flow separation for given upstream Mach number, by introducing a geometrical criterion that the separation appears when the surface-flow becomes aligned with the shock, i.e.  $\epsilon = \beta - \delta_g$ . Using (6 -11), the shock generator angle for the incipient separation is calculated by

$$\cos^2(\beta - \delta_g) = \cos\beta \quad (6 -12)$$

which is the form given by Korkegi (Ref.9).

McCabe's theory shows fairly good agreement with the experimental maximum surface-flow deflection angles, when the shock is not very strong, (Fig.39 and Fig.57 mentioned later). However, the primary assumption of infinitesimal boundary-layer thickness makes it impossible to include any details of the skewed boundary layer, e.g. the velocity profile. Moreover, his criterion for the incipient separation cannot always agree with experimental results, as noted.

For the skewed boundary layer, a more realistic (and more complicated) treatment was given by Lowrie (Ref.39 or the Review by Green, Ref.3). Lowrie's analysis of the cross flow in the boundary layer is an extension to compressible flows of the suggestion made by Johnston (Ref.40) that the cross-flow velocity is proportional to the streamwise velocity defect in low-speed boundary layer. Lowrie employed the momentum and energy equation in his analysis, while assuming isentropic flow in the interaction region, and obtained the streamwise and cross-flow velocities in an outer part of the boundary layer as functions of the pressure rise and isobar direction. Green further developed this theory for the cross-flow in the inner part of the boundary layer, through Lowrie's 'junction point criterion' for the

junction between the outer and inner layers. Although this analysis gives a useful theoretical basis for the cross flow behaviour, it includes a number of physical factors which are very difficult to either estimate or measure. This makes comparison with experimental data very dubious.

### 6.2.3. Angular-Momentum Conservation Concept

The analyses of McCabe and Lowrie suggest a simple approach to the determination of the maximum permissible surface-flow deflection angle. This approach is to assume that angular momentum is conserved along each stream tube in the side-wall boundary layer. The angular-momentum conservation concept is an extension of McCabe's theory, i.e. replacement of the total-circulation in the boundary layer by the angular momentum along a stream tube. This change means that the boundary layer condition of no-slip at the wall can be satisfied. The viscous flow can now satisfy Johnston's cross-flow model near the wall.

Fig.55a shows a rectangular stream tube altering its cross section and resultant velocity vector whilst approaching a surface-flow convergence line. (Although the stream tube is drawn to run along the wall for convenience, similar stream tubes are obtained everywhere through the skewed boundary layer.) The stream tube is defined by constant mass-flux,  $\dot{m}$ , through it, i.e.

$$\dot{m} = \rho U^* hn = \text{constant} \quad (6-13)$$

where  $\rho$  is density and  $U^*$  the resultant velocity, while  $h$  and  $n$  are height and width of the stream tube respectively. The alteration of the resultant velocity vector brings about a change of the velocity components parallel and normal to the free stream,  $U$ ,  $V$  and  $W$  respectively

corresponding to co-ordinate axes X, Y and Z (Fig.55b). If it is assumed that the principal angular-momentum ( $H^*$ ) related to the resultant velocity vector ( $U^*$ ) is conserved along the stream tube and  $W$  is small enough to be neglected in comparison with  $U$  and  $V$ , then  $U$  and  $V$  are uniquely related, see later (equation 6 -15a). The principal angular-momentum flux is defined using the mass flux and the vorticity,  $\Omega$ , as

$$H^* = k^2 \dot{m} \Omega = \text{constant} , \quad (6 -14)$$

where  $k$  is the radius of gyration, assumed constant.

Hence

$$H^* = k^2 \dot{m} \frac{\partial U^*}{\partial Z} = k^2 \dot{m} \left( \frac{\partial U}{\partial Z} \sin \zeta - \frac{\partial V}{\partial Z} \cos \zeta \right) = \text{constant}, \quad (6 -15a)$$

$$\tan \zeta = - \frac{\partial U}{\partial Z} / \frac{\partial V}{\partial Z} \quad (6 -15b)$$

where  $Z$  is the displacement from the wall and  $\zeta$  is the angle of the principal angular momentum axis to the free stream. Since the change of the streamwise velocity ( $U$ ) must have a limit depending on the flow field conditions (such as pressure rise), so the cross-flow velocity ( $V$ ) also has a maximum. From these limits the maximum permissible surface-flow deflection can be determined.

For the analysis presented here, it is more convenient to use a co-ordinate system which is valid through the skewed boundary layer over the whole interaction region and which needs no transformation of  $X$  and  $Y$  co-ordinates. A unit flow segment of the stream tube is defined by satisfying the condition that its area projected onto the wall is constant through the boundary layer. Equating the projected area to that at the external flow, means that

$$nU^* \Delta t = n_e U_e \Delta t \quad (6 -16)$$

where  $n$  is the width of the streamtube,  $\Delta t$  is unit time and suffix  $e$  denotes the value at the external flow. Substituting (6 -16) into (6 -13), gives

$$\frac{\rho}{\rho_e} \cdot \frac{h}{h_e} = \text{constant} \quad (6 -17)$$

along the stream tube. The inviscid external flow is regarded as parallel to the wall, so that an inviscid stream tube is constant in thickness over the interaction region. Taking  $h_e$  to be constant in this region a transformation of  $Z$  is introduced from (6 -17) as follows,

$$z = \int_0^Z (\rho/\rho_e) dZ \quad (6 -18)$$

#### 6.2.4. Analysis of the Angular-Momentum Conservation Concept

The following assumptions are made in this analysis.

- (1) The boundary layer is thin and the flow deflection is small, so that the velocity and angular-momentum components normal to the wall may be neglected in comparison with the components parallel to the wall.
- (2) The maximum permissible surface-flow deflection angle is determined by the greatest change of flow conditions along the stress tube, which occurs at or near the shock location. Therefore, a stream tube crossing the shock is employed in the analysis.  
(The discussion ought strictly to be made upstream of the surface-flow convergence line, Fig.55b).

The co-ordinate axes for this analysis,  $x$ ,  $y$  and  $z$ , together with the corresponding velocity components,  $u$ ,  $v$  and  $w$ , are defined in directions

parallel and normal to the external flow (Fig.56b). The angular momentum divided by  $mk^2$ , (H) is given by (6 -15), as

$$H_1 = \frac{\rho_1}{\rho_{1e}} \frac{\partial u_1}{\partial z} \quad , \quad (6 -19a)$$

$$H_2 = \frac{\rho_2}{\rho_{2e}} \left( \frac{\partial u_2}{\partial z} \sin\zeta - \frac{\partial v_2}{\partial z} \cos\zeta \right) \quad , \quad (6 -19b)$$

$$\tan\zeta = - \frac{\partial u_2 / \partial z}{\partial v_2 / \partial z} \quad (6 -19c)$$

where suffices 1, 2 and e denote conditions upstream and downstream of the shock and at the external flow respectively, and  $\zeta$  is an angle of principal angular-momentum relative to the external flow, while  $z$  is the transformed displacement given by (6 -18), as

$$z = \int_0^{z_1} (\rho_1 / \rho_{1e}) dz_1 = \int_0^{z_2} (\rho_2 / \rho_{2e}) dz_2 \quad . \quad (6 -20)$$

Consider an idealized boundary layer in which the streamwise velocity and density profiles at the two stations are similar to each other,

i.e. 
$$u_2 = C_u u_1 \quad , \quad (6 -21a)$$

$$\rho_2 = C_\rho \rho_1 \quad (6 -21b)$$

where  $C_u$  and  $C_\rho$  are constants determined by the flow field conditions.

To give the greatest change of the streamwise velocity profile (see assumption 2), these constants are evaluated from the oblique shock relations

$$C_u = \cos\beta / \cos(\beta - \delta_s) \quad , \quad (6 -22a)$$

$$C_\rho = \tan\beta / \tan(\beta - \delta_s) \quad (6 -22b)$$

where  $\delta_s$  and  $\beta$  are the shock generator angle and shock wave angles respectively. For the conservation of angular momentum  $H_1 = H_2$ .

The cross-flow velocity profile is obtained in the following manner.

Substituting (6 -21) into (6 -19) gives

$$\sin\zeta = C_u , \quad (6 -23a)$$

$$\frac{\partial v_2}{\partial z} = -\sqrt{1 - C_u^2} \frac{\partial u_1}{\partial z} \quad (6 -23b)$$

where  $\zeta$  is independent of  $z$  through the boundary layer.

Since  $v = 0$  in the external flow, the integration of equation (6 -23b) can be written as

$$v_2 = \sqrt{1 - C_u^2} (u_{1e} - u_1) \quad (6 -24)$$

which is the cross-flow velocity profile. However, it does not give zero velocity at the wall. So, it is a solution in an 'outer layer' only.

According to Johnston's cross-flow model in the 'inner layer' near the wall, the streamwise and cross-flow velocity profiles may be related to each other by

$$v_2 = Au_2 \quad (6 -25)$$

where  $A$  is independent of  $z$ . Substituting (6 -25) and (6 -21) into (6 -19) gives

$$\tan\zeta = -1/A , \quad (6 -26a)$$

and hence

$$\frac{\partial u_2}{\partial z} = \frac{1}{\sqrt{1 + A^2}} \frac{\partial u_1}{\partial z} \quad (6 -26b)$$

where  $\zeta$  must be chosen between  $\pi/2$  and  $\pi$  to satisfy equation (6 -26).

The integration of equation (6 -26) gives

$$u_2 = u_1 / \sqrt{1 + A^2} . \quad (6 -27)$$

To satisfy equations (6 -27) and (6 -21a),  $C_u$  and  $A$  must be related by

$$A = \sqrt{1 - C_u^2} / C_u . \quad (6 -28)$$

Hence, the inner cross-flow velocity profile is given by

$$v_2 = \sqrt{1 - C_u^2} u_1 . \quad (6 -29)$$

The equations for the inner and outer profiles, (6 -29) and (6 -24), can be matched at the point where

$$u_1 = u_{1e}/2 \quad (6 -30)$$

or, using (6 -21a)

$$u_2 = u_{2e}/2 . \quad (6 -31)$$

The direction of surface-flow must coincide with that of the corresponding skin-friction, so that

$$\tan \epsilon = \lim_{z \rightarrow 0} \left( \frac{\partial v_2}{\partial z} / \frac{\partial u_2}{\partial z} \right) \quad (6 -32)$$

where the surface-flow angle,  $\epsilon$ , is defined relative to the external flow. Substituting the inn-layer velocity profiles (6 -27) and (6 -29) into (6 -32), the surface-flow deflection angle is given by

$$\tan \epsilon = \frac{\sqrt{1 - C_u^2}}{C_u} = \sqrt{\frac{\cos^2(\beta - \delta_s)}{\cos^2 \beta} - 1} . \quad (6 -33)$$

For a given upstream Mach number (6 -33) enables the variation of  $\epsilon$  with  $\delta_s$  to be calculated. The calculated results of (6 -33) for various Mach numbers and shock generator angles are presented in Fig.57. They

are compared with experimental surface-flow convergence-line angles obtained from both the present measurements and some earlier work. The experimental angles for both complete and incomplete convergences are indicated using solid and open symbols respectively. The figure shows that the angle predicted by (6 -33) agrees reasonably well with the condition for appearance of the complete surface-flow convergence. In the figure, the complete convergence line angle does not coincide with the shock wave angle.

This analysis of the angular momentum conservation concept brings out some other interesting points. Firstly, the location of the junction between the inner and outer parts of the boundary layer occurs at a point where the streamwise velocity ( $u_2$ ) is half the external-flow velocity ( $u_{2e}$ ), as given by (6 -31). Provided that the streamwise velocity profile is conventional and decreases monotonically towards the wall surface then (6 -24) and (6 -29) give the maximum cross-flow velocity at the junction point as

$$(v_2/u_{2e})_{\max} = \sqrt{1-C_u^2} / 2C_u = \frac{1}{2} \sqrt{\frac{\cos^2(\beta-\delta_2)}{\cos^2\beta} - 1} . \quad (6 -34)$$

Experimental data taken from the boundary-layer surveys of Lowrie (Ref.39) and Peake (Ref.13) suggest that this analytical result is physically reasonable as shown in the following table:

<u>REFERENCE</u>	<u>TEST CONDITIONS</u>	<u>EXPERIMENTAL MAXIMUM CROSS-FLOW VELOCITY RATIO</u>	<u>CORRESPONDING STREAMWISE VELOCITY RATIO</u>	<u>MAXIMUM CROSS-FLOW VELOCITY RATIO FROM EQUATION (6 -34)</u>
Lowrie (Ref.39)	M = 2.5, $\delta_s = 6^\circ$	0.15 - 0.18	0.55 - 0.62	0.16
Peake (Ref.14)	M = 2, $\delta_s = 8^\circ$	0.14 - 0.20	0.45 - 0.52	0.22
	M = 4, $\delta_s = 8^\circ$	0.15 - 0.17	0.45 - 0.50	0.15

When the surface-flow becomes aligned with the shock,  $\epsilon = \beta - \delta_s$ , so that from equation (6 -33)

$$\cos^2 \epsilon = \cos \beta$$

which is the same result as obtained by McCabe.

This means that if McCabe's criterion for separation is accepted then both theories predict the same wedge angle to cause separation. However, as pointed out above, McCabe's criterion is not accepted here and a better alternative based on the conservation of  $H^*$  is shown in Fig.57.

## 7. FLOW FIELD STRUCTURE IN THE INTERACTION REGION

### 7.1 Flow Structure near the Shock Generator

The oil-flow pictures taken on the shock generator surface show that two groups of compression waves affect that surface and expansion waves between them accelerate the surface flow toward the shock generator root (Figs.37 and 40). A flow mechanism which could generate these compression and expansion waves is illustrated in Fig.58a which shows a shock envelope around the shock generator, together with a typical vapour-screen picture indicating the sectional view of the flow field normal to the free stream. The side-wall boundary layer forces the oblique shock to become detached near the shock-generator leading-edge root. The vapour-screen picture suggests that the shock envelope approaches the side wall in the form of a lambda shock.

A sectional view of this shock envelope in the  $x - z$  plane is imagined to be as drawn in Fig.58b, where a typical oil-flow picture on the shock generator surface is also presented. In the figure, the front shock originates from a group of compression waves springing from the growth of the displacement thickness of the side-wall boundary layer. This front shock results from adverse pressure propagation through the subsonic portion of the boundary layer. It is well known in two-dimensional flow that a similar process to this induces a very thick subsonic layer on the wall surface. Although the present flow is three-dimensional, the flow in the  $x - z$  plane which cuts the shock envelope roughly at right angles seems to behave in a similar way. It follows that a recovery in thickness of the side-wall boundary layer thins the thickened subsonic layer while shedding expansion waves. This recovering side-wall boundary layer thins locally near the shock-

generator leading edge root (Fig.58b). The second group of compression waves are produced by the corner boundary layer growing along the shock generator root.

As indicated in the oil-flow picture of Fig.58b, the first and second groups of compression waves form the outer and inner compression zones on the shock generator surface, while the expansion waves give rise to the accelerated region in between.

The accelerated region drives the shock generator surface flow to deflect toward the shock generator root. Meanwhile, the growth of the corner boundary layer with a thick subsonic region pushes some shock-generator surface flow away from the corner. As a result of these actions, a surface-flow convergence (convergence B, Fig.37) is formed on the shock generator surface near the root.

## 7.2. 'Double Viscous-Layer Model'

Many flow field models of the glancing shock boundary-layer interaction region have been proposed and discussed over the past fifteen years. The most popular is the 'vortex dominated model' which may be developed from an idea based on a conical flow field model, (see Fig.10). This model consists of a 'separation vortex (or bubble)' situated between a 'separation line' running a little upstream of the shock and a 'reattachment line' lying near the shock generator root. When the shock generator angle is fairly large, this model could be suitable for interpreting some well-known experimental results, especially the surface flow patterns which were most often available. The

typical interpretation may be summarised as follows.

- (i) A side-wall surface-flow convergence (convergence A) observed in the oil-flow pattern a little upstream of the shock indicates a three-dimensional separation line. In the vicinity of this flow convergence, the corresponding surface pressure distribution tends to have a small peak or flattened part which suggests a rapidly thickened separated layer being unable to withstand a strong adverse pressure gradient.
- (ii) Oil streak lines diverging near the shock generator root are caused by a reattachment line just behind the 'separation vortex'. Near the reattachment line, the impingement of air entrained by the vortex yields a peak in the heat transfer distribution and a crest in the surface static pressure plateau.

However, this flow field model does not explain all the present experimental results obtained in the two separate test programmes, as mentioned below.

#### Oil-Flow Pictures

The 'complete surface-flow convergence (convergence A)' on the side wall may be taken as evidence of 'separation' appearing in this region. However, before the appearance of the separation line on the side wall, there is already evidence of a small separation vortex near the shock generator root, as indicated by the typical oil-flow pattern of flow reattachment, (Fig.37 and Section 4.3.1.).

#### Vapour-Screen Photographs

The vapour-screen photographs show that a small vortex is swirling near the shock generator root and a thick shadowy zone is located between the shock

generator root and the side-wall surface-flow convergence line (convergence A). However, these features are observed at all shock generator angles so that no particular change of pattern suggesting the appearance of a 'separation vortex' can be detected. (Figs.41e - 41e and Section 4.3.3.).

### Heat Transfer

Even before the 'complete surface-flow convergence' (convergence A) takes place on the side wall, the heat transfer distribution has two 'peaks' (at least), ahead of the shock and near the shock generator root. (Figs. 44e - 44g and Section 4.4.2.).

A flow field model which is consistent with these flow features is the 'double viscous-layer model' illustrated in Fig.59 and discussed below.

#### (1) The Viscous Flow Separating from the Shock Generator Surface and Reattaching to the Side Wall Surface

The oil-flow pictures and the vapour-screen photographs for the shock generator surface at any angle to the free stream, show that a spanwise surface flow on the shock generator is accelerated toward the side wall through the 'accelerated region' (Fig.37 or 40) and a small vortex is swirling near the shock generator root (Fig.41). It is considered that the small vortex is caused from the spanwise surface flow separating at its convergence line (convergence line B) from the shock generator surface and reattaching to the side wall at the divergence line near the shock generator root (Fig.59). This flow structure indicates that some viscous flow growing on the shock generator surface comes into the side wall surface, by way of the edge of the small 'roller vortex' in the corner. This impingement of the viscous flow produces a 'close packed' surface-flow on the side wall

near reattachment, as suggested by the oil streak lines with fine intervals in this region. The impingement gives rise to the heat transfer peak (peak **ⓑ**) near the shock generator root (Figs.44e - 44g). This peak is therefore not connected with the main separation (at the convergence line A), namely the side-wall boundary-layer separation.

(2) The Viscous Layer Induced on the Side Wall Surface

On the side-wall surface, the impingement of the viscous flow from the shock generator surface produces a viscous layer in the vicinity of the reattachment. This 'induced layer' is accelerated toward the shock by the surface static pressure gradient (Fig.43) and crosses the path of the side-wall boundary layer coming into the region, so drawing a boundary line on the side wall surface between itself and the side-wall boundary layer as illustrated in Fig.59. This process causes the surface-flow convergence (convergence A) near the shock location (Fig.37).

(3) The Side-Wall Boundary Layer upstream of the Inviscid Shock

Upstream of the calculated shock, the surface static pressure distribution shows an extensive region of adverse pressure gradient propagated through the subsonic region of the side wall boundary layer (Fig.43). This pressure propagation causes the shock to take a lambda configuration near the side wall surface, as shown in the vapour-screen pictures (Fig.41). As a result the gradual compression of the side-wall boundary-layer flow tends to increase the heat transfer. As the convergence line A is approached so the surface streamlines swing round and pack closer together which gives rise to the heat transfer peak **Ⓐ** .

(4) Boundary Region between the Side-Wall Boundary Layer and the Induced Layer

When the shock generator angle is not large, the surface static pressure gradient on the side wall is not very steep (Figs.43a - 43b and 43d - 43e). The induced layer cannot develop fully over the interaction region. The side-wall boundary layer may turn around the edge of the induced layer while keeping its surface stream lines in contact with the side wall surface (Figs.59 and 60a). This process yields an attached flow field showing the incomplete oil-flow convergence (convergence A) on the side wall surface near the shock location (Figs.37a and 37d).

With increasing shock generator angle, the steepened surface static pressure gradient (Figs.43c and 43f) accelerates the induced layer further upstream so that the front edge of the induced layer presents a large angle to the free stream. In this case, the side wall boundary layer can ride over the induced layer and its surface stream lines separate from the side wall surface

(Figs.59 and 60b). (Refer to Section 6.1). This situation represents a flow separation similar to Maskell's 'ordinary separation', and the corresponding oil-flow pictures show the complete surface-flow convergence (convergence A) on the side wall upstream of the shock (Figs.37b - 37c and 37e - 37f).

When this ordinary separation takes place, the side-wall boundary layer and some viscous flow of the induced layer are transformed into a separated free layer (Fig.60b). This process looks similar to 'separation in the vortex dominated model'. However, the present experimental results show a different separation pattern from that of the vortex dominated model in two ways.

First, the appearance of the surface-flow divergence pattern (showing a flow-reattachment) near the shock generator root, as well as the heat transfer peak **(B)** near it, has no connection with occurrence of the main separation

(the complete convergence A) on the side wall, as noted in Figs.37 and 44. Secondly, the present vapour-screen pictures do not show any particular flow features to give evidence of the separation vortex originating from the main separation on the side wall, Fig.41. Thus, it is considered that the side-wall boundary layer separation does not produce a strong vortex but a vortical free layer, and the free layer near the shock generator can become involved with the small vortex swirling at the shock generator root (Fig. 60b).

### 7.3. An Hypothesis for the Appearance of Flow Separation

In the 'double viscous-layer flow field model' proposed in the last Section, the occurrence of side-wall boundary-layer separation is not directly connected with the surface-flow angle on the side wall exceeding the shock angle. The discussion here has been based on experimental results showing 'conical' flow features; e.g. the interaction region grows in a radial direction. The fact that the present interaction region is 'conical' in nature casts doubt on McCabe's criterion for incipient separation which was based on a quasi-two-dimensional view of the flow.

This point may be confirmed by Fig.61 in which a correlation of the surface convergence-line angle with the appearance of side-wall boundary-layer separation is presented, for both the experimental data of the present study and a number of other references. In the figure, the ratio of experimental convergence-line angle to the theoretical prediction (the angular momentum conservation concept proposed here and McCabe's theory) is plotted versus the shock strength represented by static pressure ratio across the shock.

Following McCabe's criterion, Korkegi proposed a pressure ratio of 1.5 to induce incipient separation. However, in the current work the incomplete type of surface-flow convergence can appear even when the pressure ratio is far beyond 1.5. The condition for the appearance of separation, defined by complete surface-flow convergence on the side wall, occurs when the surface-flow angle on the convergence line exceeds a maximum permissible angle. This angle is better predicted by the angular momentum conservation concept, than by McCabe's theory, though neither theory gives particularly good agreement with the experimental data, see Fig.61.

The following hypothesis is proposed. An ordinary separation occurs on the side wall in the interaction region, when the induced layer forces the surface stream lines of the side-wall boundary layer to deflect beyond a maximum permissible angle. This angle is not the shock angle.

---

## 8. CONCLUSIONS AND REMARKS

(1) The three dimensional glancing shock turbulent boundary-layer interaction region consists of two different viscous layers; i.e. (i) the side-wall boundary layer growing along the flat wall and (ii) the induced layer originating on the shock generator surface near the root and crossing the path of the side-wall boundary layer.

(2) As long as the surface stream lines of the side-wall boundary layer are pliable enough to be bent along the edge of the induced layer, no flow separation appears on the side wall even if the surface-flow deflection exceeds the shock angle. An ordinary separation takes place when the induced layer forces the side-wall surface stream lines to deflect beyond a maximum permissible angle.

(3) McCabe's criterion is not suitable for deciding the incipient flow separation on the side wall, since the interaction is not quasi-two-dimensional. As defined here separation occurs when the surface-flow deflection exceeds the maximum permissible angle. This angle may be determined by an angular momentum relation for the side-wall boundary layer.

(4) If the heat transfer distribution in the interaction region is to be measured under conditions when the temperature difference ( $T_w - T_{aw}$ ) is small, it is essential to take into account the local variations in both  $T_w$  and  $T_{aw}$ , particularly in the neighbourhood of the shock.

## 9. ACKNOWLEDGEMENTS

The author wishes to thank Professor J.L. Stollery and Dr. D.I.A. Poll for many helpful discussions and valuable comments on the subject of this paper. He is also indebted to Mr. S.W. Clark and his staff of the Aerodynamics workshop in helping with the experimental study.

10. REFERENCES

10.1. References

1. Neumann, R.D. Special Topics in Hypersonic Flow. AGARD Lecture Series No.42, July 1972.
2. Kubota, H. High-Speed Wind Tunnel Testing with Models for Aerodynamic Configuration Study, Part 1. Niwa, Y. TR-A-643, The Technical Research & Development Yamamoto, K. Institute, Japan Defence Agency, July 1975. Baba, H.
3. Green, J.E. Interaction between Shock Waves and Turbulent Boundary Layers. 'Prog. in Aerospace Sci.', Vol.11, pp 235. (Pergamon Press, 1970).
4. Horstman, C.C. Shock-Wave-Induced Turbulent Boundary-Layer Separation at Hypersonic Speeds. Kussoy, M.I. AIAA Paper No. 75-4, January 1975. Coakley, T.J. Rubesin, M.W. Marvin, J.G.
5. Horstman, C.C. Reynolds Number Effects on Shock Wave-Turbulent Boundary-Layer Interactions. Settles, G.S. AIAA J. Vol.15, No.8, August 1977. Vas, I.E. Bogdonoff, S.M. Hung, C.M.
6. Maskell, E.C. Flow Separation in Three Dimensions. RAE Report, Aero.2565, November 1955.
7. Stanbrook, A. An Experimental Study of the Glancing Interaction between a Shock Wave and a Turbulent Boundary Layer. ARC C.P. No.555, July 1960.
8. McCabe, A. The Three-Dimensional Interaction of a Shock Wave with a Turbulent Boundary Layer. Aero. Quart. August 1966.
9. Korkegi, R.H. A Simple Correlation for Incipient Separation of a Turbulent Boundary Layer Due to a Skewed Shock Wave. AIAA J. Vol.11, No.11, November 1973.
10. Oskam, B. Study of Three-Dimensional Flow Fields Generated by the Interaction of a Skewed Shock Wave with a Turbulent Boundary Layer. Bogdonoff, S.M. AFFDL TR-75-21, February 1975 or Vas, I.E. An Exploratory Study of a Three-Dimensional Shock Wave Boundary Layer Interaction at Mach 3. AGARD C.P. 168, May 1975.

11. Oskam, B.  
Vas, I.E.  
Bogdonoff, S.M. Mach 3 Oblique Shock Wave/Turbulent Boundary Layer Interactions in Three Dimensions. AIAA Paper No.76-336, July 1976.
12. Oskam, B.  
Vas, I.E.  
Bogdonoff, S.M. Oblique Shock Wave/Boundary Layer Interactions in Three Dimensions at Mach 3. AFFDL TR-76-48, Part I, January 1976. AFFDL TR-76-48, Part II, March 1978.
13. Peake, D.J.  
Rainbird, W.J. The Three-Dimensional Separation of a Turbulent Boundary Layer by a Skewed Shock Wave and its Control by the Use of Tangential Air Injection. AGARD CP 168, May 1975.
14. Peake, D.J. Three-Dimensional Swept Shock/Turbulent Boundary Layer Separations with Control by Air Injection. N.R.C. Aero. Report LR-592, July 1976.
15. Neumann, R.D.  
Burke, G.L. The Influence of Shock-Wave Boundary-Layer Effects on the Design of Hypersonic Aircraft. AFFDL TR-68-152, March 1969.
16. Token, K.H. Heat Transfer due to Shock Wave/Turbulent Boundary Layer Interactions on High Speed Weapon Systems. AFFDL TR-74-77, April 1974.
17. Neumann, R.D.  
Token, K.H. Prediction of Surface Phenomena Induced by Three-Dimensional Interactions on Planer Turbulent Boundary Layers. Paper No. 74-058, Int. Astronautical Fed., 25th Congress, September 1974.
18. Hayes, J.R. Prediction Techniques for the Characteristics of Fin Generated Three Dimensional Shock Wave/Turbulent Boundary Layer Interactions. AFFDL TR-77-10, May 1977.
19. Neumann, R.D. Prediction Techniques for the Characteristics of the 3-D Shock Wave Turbulent Boundary-Layer Interactions. AIAA Paper No. 77-46, January 1977 or AIAA J. Vol.15, No.10, October 1977.
20. Hayes, J.R. Optical Flow Field Data on Fin Interaction at Mach 3 AFFDL TM-78-42-FXG, March 1978.
21. Hung, C.M.  
MacCormack. R.W. Numerical Solution of Three-Dimensional Shock Wave and Turbulent Boundary-Layer Interaction. AIAA J. Vol.16, No.10, October 1978.
22. Hung, C.M.  
Horstman, C.C. Computation of Three-Dimensional Turbulent Separated Flows of Supersonic Speeds. AIAA J. Vol.17, No.11, November 1979.

AD-A083 703

COLLEGE OF AERONAUTICS CRANFIELD (ENGLAND)

F/6 20/4

INVESTIGATION OF THREE-DIMENSIONAL SHOCK WAVE BOUNDARY LAYER IN--ETC(U)

JAN 80 H KUBOTA

AFOSR-76-3006

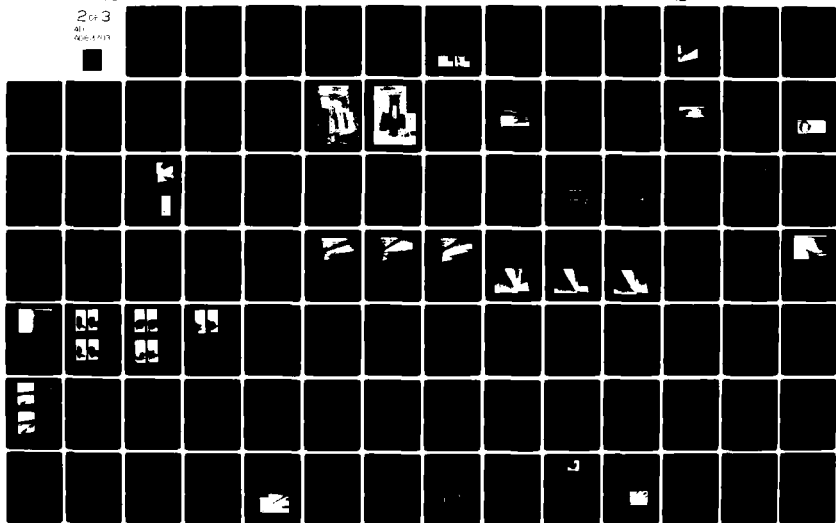
UNCLASSIFIED

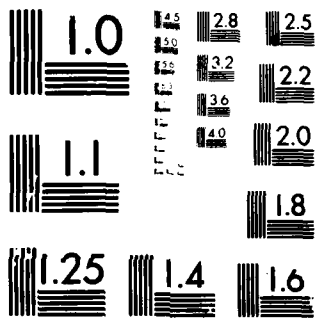
COA-8001

NL

2 of 3

41  
906-1113





MICROCOPY RESOLUTION TEST CHART  
NATIONAL BUREAU OF STANDARDS-1963-A

23. Dickman, C.A. Glancing Interaction with a Turbulent Boundary Layer.  
CoA Memo 7706, Cranfield Institute of Technology, August 1977.
24. Davenport, N.C. Heat Transfer in a Region of Glancing Shock Wave Boundary Layer Interaction.  
CoA Memo 7806, Cranfield Institute of Technology, July 1978.
25. Kubota, H. A Flow Field Model of the Glancing Shock and Turbulent Boundary-Layer Interaction Region.  
CoA Memo 7901, Cranfield Institute of Technology, May 1979.
26. McGregor, I. Flow Visualization in Wind Tunnels using Indicators.  
AGARD Ograph 70, April 1962.
27. Oskam, B.  
Vas, I.E. Heat Transfer Measurements using the 'Quasi-Transient' Technique, presented to the 45th Meeting of the Supersonic Tunnel Association, Sandia Corp. Labs. April 1976.
28. Busing, J.R. On the Joule Heating Method of Calibrating Thin Film Resistance Thermometers.  
CoA Report Aero. 183, Cranfield Institute of Technology, May 1965.
29. Murthy, A.V. Studies in Hypersonic Viscous Interactions.  
Ph.D. Thesis, Cranfield Institute of Technology, December 1972.
30. Holden, M.S. Heat Transfer in Separated Flow.  
Ph.D. Thesis, Faculty of Engineering, University of London, November 1963.
31. Van Driest, E.R. The Problem of Aerodynamic Heating.  
Aero. Eng. Rev. Vol.15, No.10, October 1956.
32. Scholer, H. Application of Encapsulated Liquid Crystals on Heat Transfer Measurements in the Fin-Body Interaction Region at Hypersonic Speed.  
AIAA Paper 78-777, 1978.
33. Klein, E.J. Liquid Crystals in Aerodynamic Testing.  
Aeronautics & Astronautics, July 1968.
34. Scuderi, L.F. Expressions for Predicting 3-D Shock Wave-Turbulent Boundary Layer Interaction Pressures and Heating Rates.  
AIAA Paper 78-162, January 1978.
35. Back, L.H.  
Cuffel, R.F. Changes in Heat Transfer from Turbulent Boundary Layers Interacting with Shock Waves and Expansion Waves.

36. Goldberg, T.J. Three-Dimensional Separation for Interaction of Shock Waves with Turbulent Boundary Layers. AIAA J. Vol.11, No.11, November 1973.
37. Lighthill, M.J. Attachment and Separation in Three-Dimensional Flow. 'Laminar Boundary Layers', pp 72-82. (Oxford University Press, 1963).
38. Tobak, M. Topology of Two-Dimensional and Three-Dimensional Separated Flows. AIAA Paper No. 79-1480, July 1979.
39. Lowrie, B.W. Cross-Flows Produced by the Interaction of a Swept Shockwave with a Turbulent Boundary Layer Ph.D. Thesis, Cambridge University, 1965.
40. Johnston, J.P. On the Three-Dimensional Turbulent Boundary Layer Generated by Secondary Flow. J. Basic Eng. Series D, Trans. ASME 82.

10.2. Bibliography

(Viscous Interaction)

41. Schlichting, H. Boundary Layer Theory (McGraw-Hill Book Company, 1960)
42. Liepmann, H.W. Roshko, A. Elements of Gasdynamics. (John Wiley & Sons, 1960).
43. Stollery, J.L. Viscous Interaction Effect on Re-entry Aerothermodynamics; Theory & Experimental Results. AGARD Lecture Series No.42, July 1972.
44. Henderson, L.F. The Reflection of a Shock Wave at a Rigid Wall in the Presence of a Boundary Layer. J. Fluid Mech. Vol.30, Part 4, 1967.

(Two-Dimensional Shock Boundary-Layer Interaction - Theory)

45. Stewartson, K. Williams, P.G. Self-Induced Separation. Proc. Roy. Soc. A 312, 1969.
46. Stewartson, K. On Laminar Boundary Layers near Corners. Quart. J. Mech. & Applied Math. Vol.XXIII, Part 2, 1970 or On Supersonic Laminar Boundary Layers near Convex Corners. Proc. Roy. Soc. A 319, 1970.
47. Rizzetta, D.P. Asymptotic Solutions of the Energy Equation for Viscous Supersonic Flow past Corners. Phys. Fluids, Vol.22, No.2, February 1979.

48. Gautier, B.G.  
Ginoux, B.G. A Theoretical Study of Wall Cooling Effects upon Shock Wave-Laminar Boundary Layer Interaction by the Method of Lees-Reeves-Klineberg.  
Tech. Note 71, Von Karman Institute, May 1971.
49. Wilcox, D.C. Calculation of Turbulent Boundary-Layer Shock-Wave Interaction.  
AIAA J. Vol.11, No.11, November 1973.
50. Shang, J.S.  
Hankey, W.L. Numerical Solution for Supersonic Turbulent Flow over a Compression Ramp.  
AIAA J. Vol.13, No.10, October 1975.
51. Viegas, J.R. Numerical Investigation of Turbulence Models for Shock-Separated Boundary-Layer Flows.  
AIAA J. Vol.16, No.4, April 1978.
52. Inger, G. Theoretical Study of Reynolds Number and Mass Transfer Effects on Normal Shock-Turbulent Boundary Layer Interaction.  
Z. Flugwiss. Weltraumforsch. 2, Heft 5, 1978.
53. Dolling, D.S.  
Ginoux, J.J. Effect of Shock Impingement on Heat Transfer.  
Tech. Note 115, Von Karman Institute, January 1976.

(Two-Dimensional Shock Boundary-Layer Interaction - Experiment)

54. Bogdonoff, S.M.  
Kepler, C.E. Separation of a Supersonic Turbulent Boundary Layer.  
J. Aero. Sci., June 1955.
55. Green, J.E. Reflexion of an Oblique Shock Wave by a Turbulent Boundary Layer.  
J. Fluid Mech. Vol.40, Part 1, 1970.
56. Reda, D.C.  
Murphy, J.D. Shock Wave/Turbulent Boundary-Layer Interactions in Rectangular Channels.  
AIAA J. Vol.11, No.2, February 1973 and Side-Wall Boundary-Layer Influence on Shock Wave/Turbulent Boundary-Layer Interactions.  
AIAA J. Vol.11, No.10, October 1973.
57. Law, C.H. Supersonic Shock Wave-Turbulent Boundary Layer Interactions.  
AIAA Paper No. 75-832, 1975.
58. Settles, G.S.  
Vas, I.E.  
Bogdonoff, S.M. Details of a Shock-Separated Turbulent Boundary Layer at a Compression Corner.  
AIAA J. Vol.14, No.12, December 1976.
59. Chew, Y.T. The Boundary Layer Development Downstream of a Shock Interaction at an Expansion Corner.  
A.R.C. 37, 863, August 1978.

(Three-Dimensional Shock Boundary Layer Interaction - Theory)

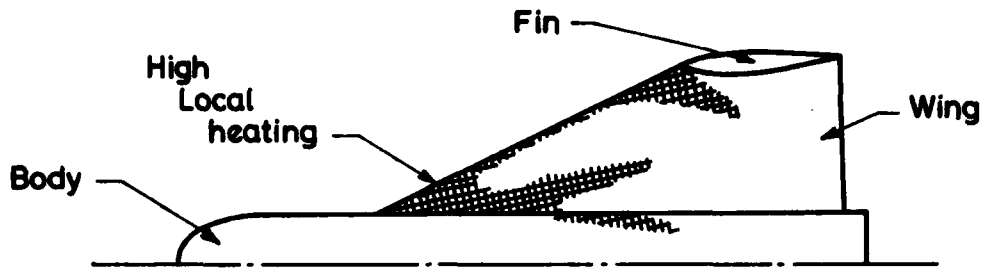
60. Myring, D.F. The Effect of Sweep on Conditions at Separation in Turbulent Boundary-Layer/Shock-Wave Interaction Aero. Quart. May 1977.
61. Shang, J.S.  
Hankey, W.L. Numerical Solution of the Navier-Stokes Equations for a Three-Dimensional Corner. AIAA J. Vol.15, No.11, November 1977.
62. Vatsa, V.N.  
Werle, M.J. Quasi-Three-Dimensional Laminar Boundary-Layer Separations in Supersonic Flow. J. Fluids Eng., Trans. ASME 634, December 1977.

(Three-Dimensional Shock Boundary-Layer Interaction - Experiment)

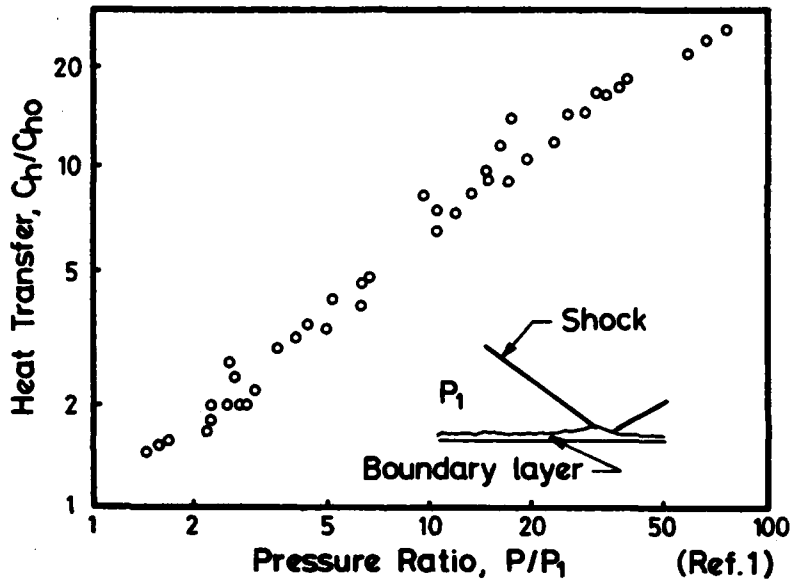
63. Stalker, R.J. Sweepback Effects in Turbulent Boundary-Layer Shock-Wave Interaction. J. Aero/Space Sci., May 1960.
64. Watson, R.D. A Study of Hypersonic Corner Flow Interactions. AIAA J. Vol.9, No.7, July 1971.
65. Coleman, G.T.  
Stollery, J.L. Incipient Separation of Axially Symmetric Hypersonic Turbulent Boundary Layers. AIAA J. Vol.12, No.1, January 1974.
66. Cooper, J.R.  
Hankey, W.L. Flowfield Measurements in an Asymmetric Axial Corner at  $M = 12.5$ . AIAA J. Vol.12, No.10, October 1974.
67. Kipke, K.  
Hummel, D. Untersuchungen an langsangestromten Eckenkonfigurationen im Hyperschallbereich. Z. Flugwiss. 23, Heft 12, 1975.
68. Freeman, L.M.  
Korkegi, R.H. Experiments on the Interaction with a Turbulent Boundary Layer of a Skewed Shock Wave of Variable Strength at Mach 2.5. ARL 75-9182, May 1975.
69. Schepers, H.J. Untersuchgen der wandnahen Stromung und des Wärmeübergangs im Bereich langsangestromter Ecken bei Hyperschallanstromung. DLR-FB 76-02, August 1975
70. Korkegi, R.H. On the Structure of Three-Dimensional Shock-Induced Separated Flow Regions. AIAA J. Vol.14, No.5, May 1976.
71. Settles, G.S.  
Perkins, J.J. Investigation of Three-Dimensional Shock/Boundary Layer Interactions at Swept Compression Corners. AIAA Paper 79-1498, July 1979.

(Heat-Transfer or Skin-Friction in Supersonic and Hypersonic Flow)

72. Burbank, P.B. Distribution of Heat Transfer on a 10 Cone at Angles of Attack from 0 to 15 for Mach Numbers of 2.49 to 4.65 and a Solution to the Heat-Transfer Equation that Permits Complete Machine Calculation.  
NASA MEMO 6-4-59L, June 1959.
73. Seban, R.A. Heat Transfer to Separated and Reattached  
Emery, A. Subsonic Turbulent Flows Obtained Downstream of  
Levy, A. a Surface Step.  
J. Aero/space Sci., December 1959.
74. Cheng, H.K. Boundary-Layer Displacement and Leading-Edge  
Hall, J.G. Bluntness Effects in High-Temperature Hypersonic  
Golian, T.C. Flow.  
Hertzberg, A. J. Aero/Space Sci., May 1961.
75. Ginoux, J.J. A Steady-State Technique for Local Heat-Transfer  
Measurement and its Application to the Flat Plate.  
J. Fluid. Mech. 1964.
76. Hopkins, E.J. An Evaluation of Theories for Predicting Turbulent  
Inoue, M. Skin Friction and Heat Transfer on Flat Plates  
at Supersonic and Hypersonic Mach Numbers.  
AIAA J. Vol.9, No.6, June 1971.
77. Hopkins, E.J. Hypersonic Turbulent Skin-Friction and Boundary-  
Keener, E.R. Layer Profiles on Nonadiabatic Flat Plates.  
Polek, T.E. AIAA J. Vol.10, No.1, January 1972.
78. Schultz, D.L. Heat-Transfer Measurements in Short-Duration  
Jones, T.V. Hypersonic Facilities.  
AGARD Ograph No. 165, February 1973.
79. Edwards, A.J. Heat-Transfer Distributions on a 70 Delta Wing  
with Flap-Induced Separation.  
I.C. Aero Report 75-01, Imperial College of  
Science and Technology, March 1975.
80. Richards, B.E. Laminar Film Cooling Experiments in Hypersonic Flow.  
Stollery, J.L. J. Aircraft, Vol.16, No.3, March 1979 or  
Film Cooling in Hypersonic Flow (Richards, B.E.)  
Ph.D. Thesis, Faculty of Engineering,  
University of London, January 1967.
81. Murthy, V.S. Wall Shear Stress Measurements in a Shock-Wave  
Boundary-Layer Interaction.  
AIAA J. Vol.16, No.7, July 1978.

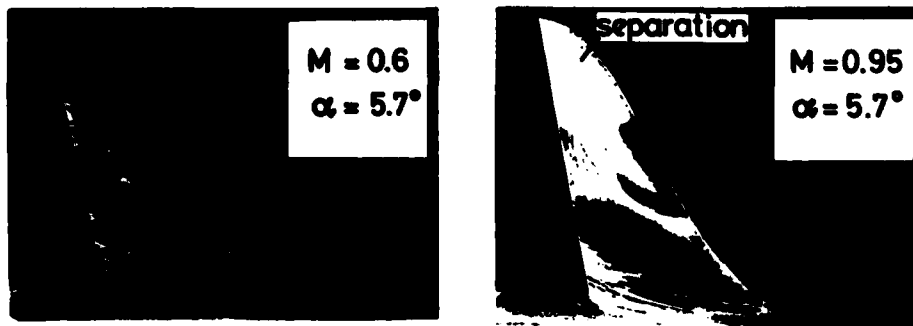


(a) Local heating



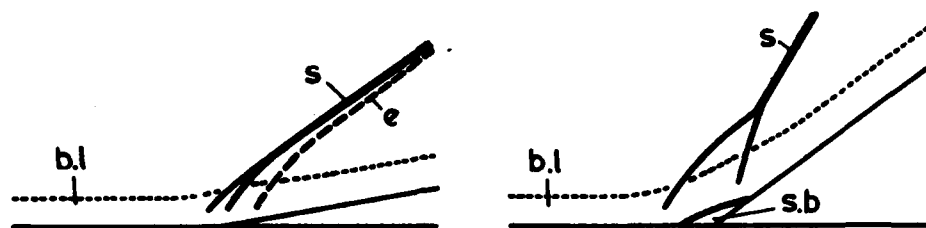
(b) Heat transfer v's pressure ratio

Figure 1. An example of high local heating.

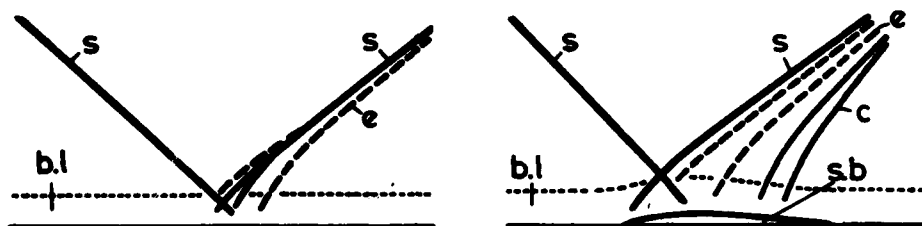


(Ref. 2)

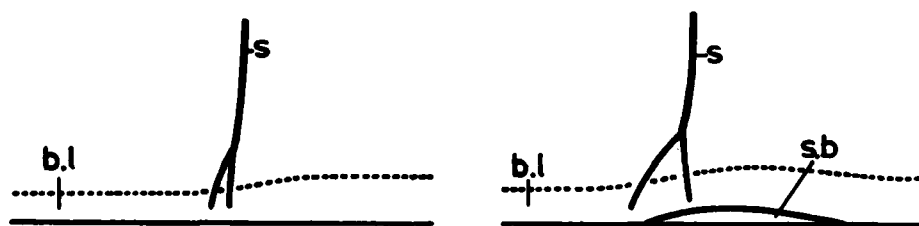
Figure 2. An example of shock-induced boundary-layer interactions.



(a) Compression Corner



(b) Incident Shock



(c) Normal Shock

b.l boundary layer  
 c compressions  
 e expansions  
 s shock  
 s.b separation bubble

Figure 3. Typical two dimensional shock boundary-layer interactions.

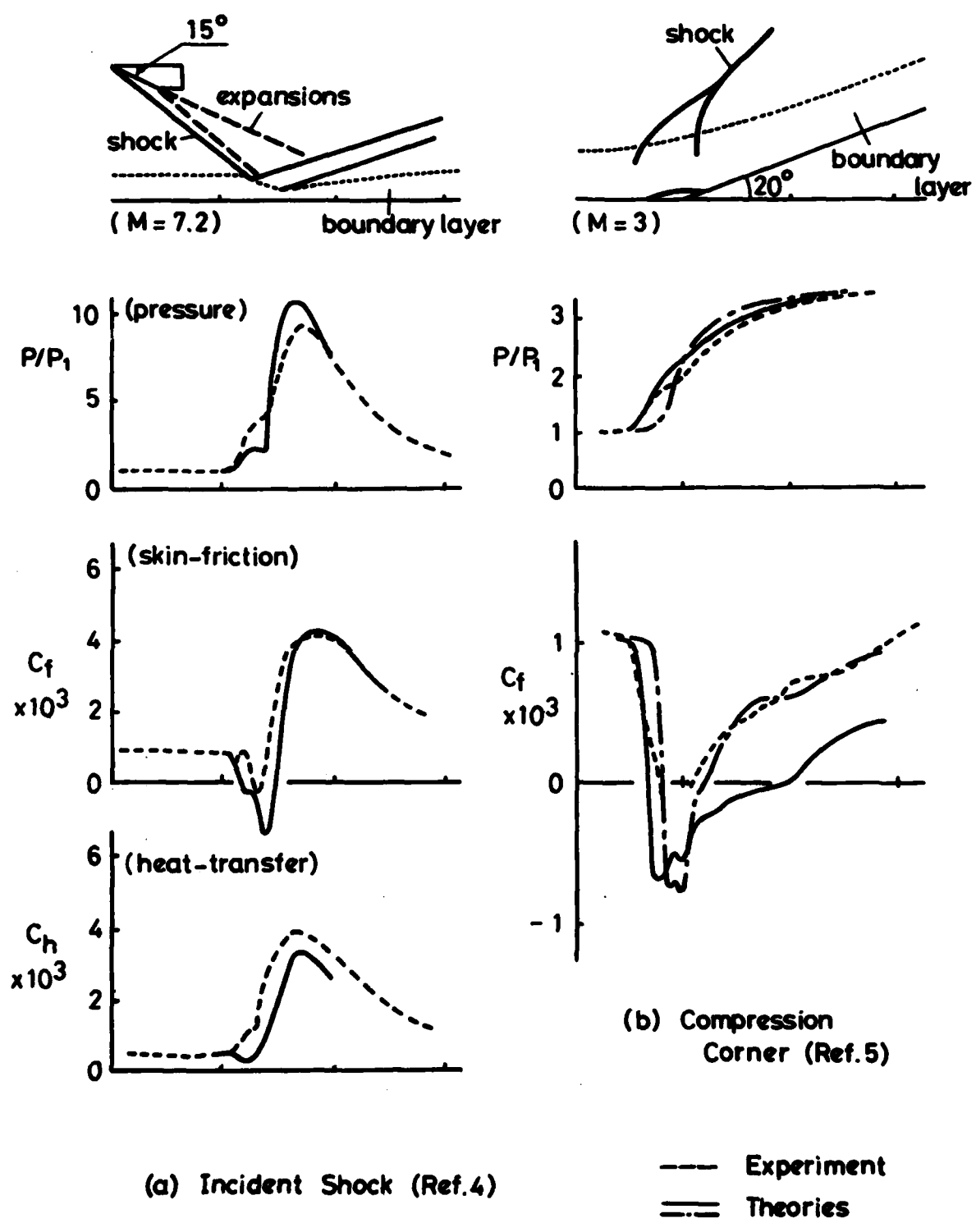
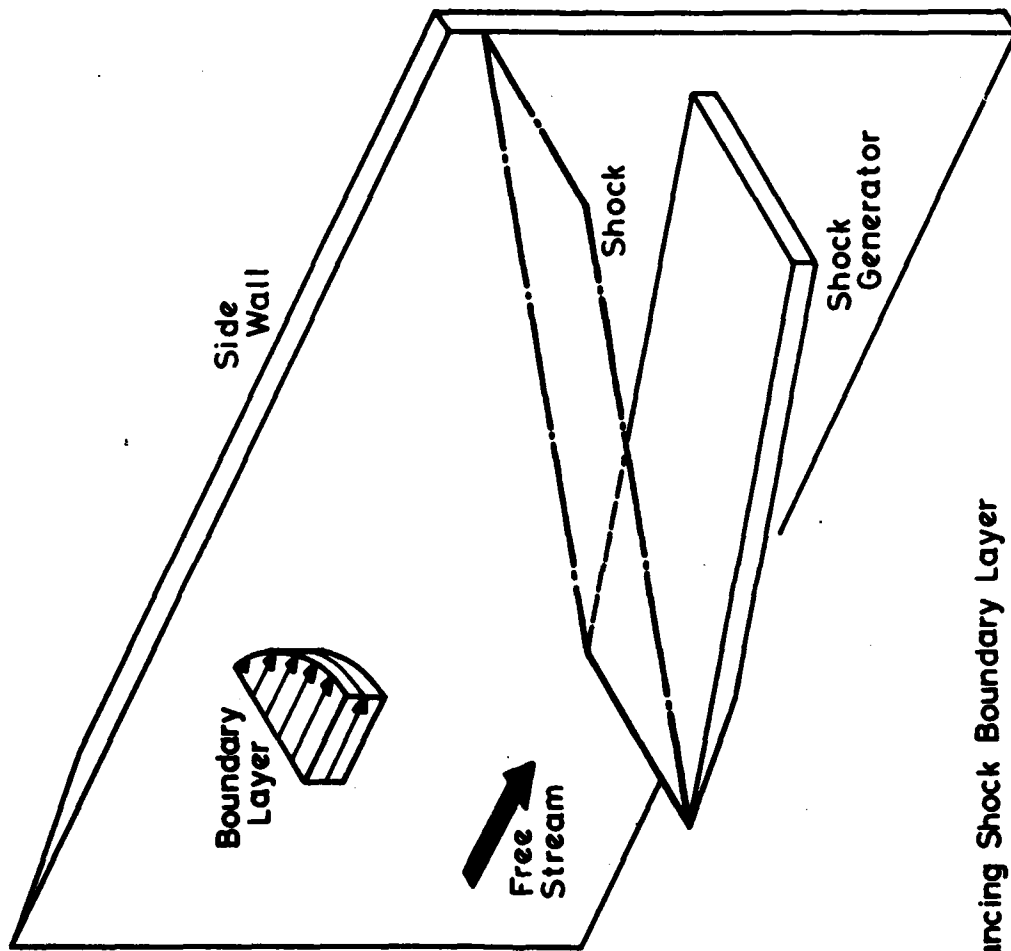
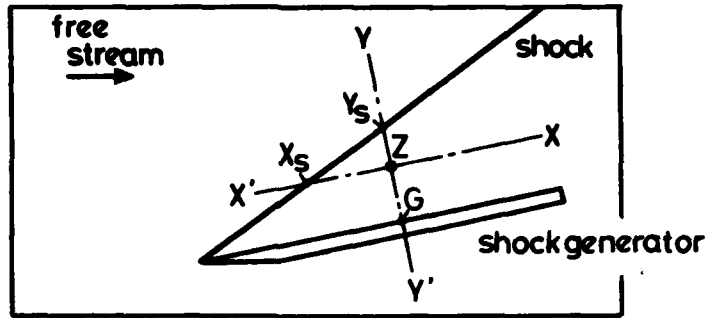


Figure 4. Some experimental and theoretical results of two dimensional shock boundary-layer interaction.

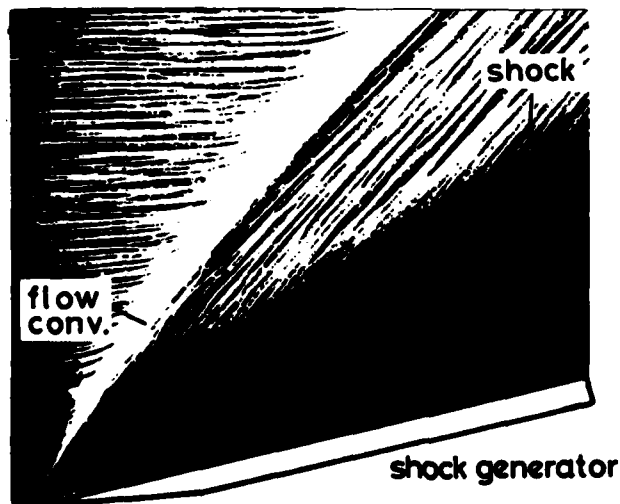
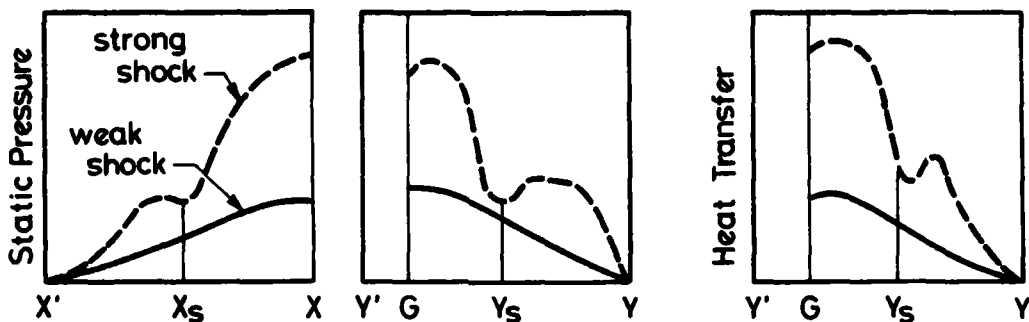


(a) A Glancing Shock Boundary Layer Interaction Model

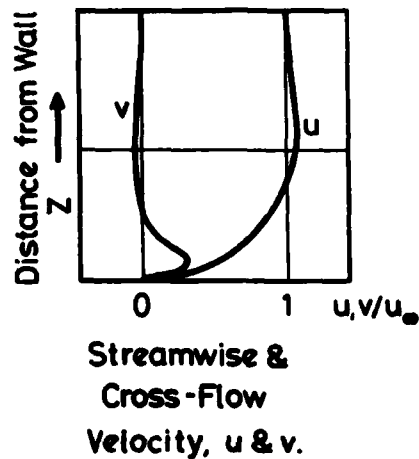
Figure 5. Glancing shock boundary-layer interaction



(Plane View of the Interaction Region)

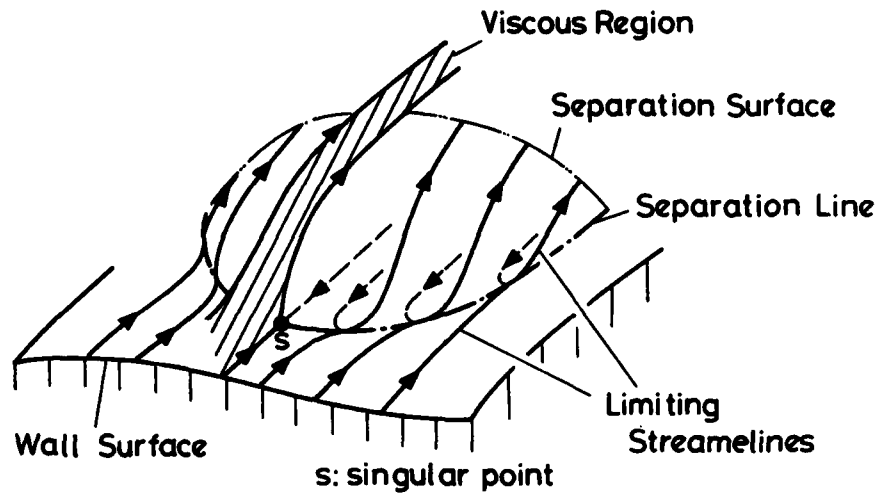


Oil-Flow Picture

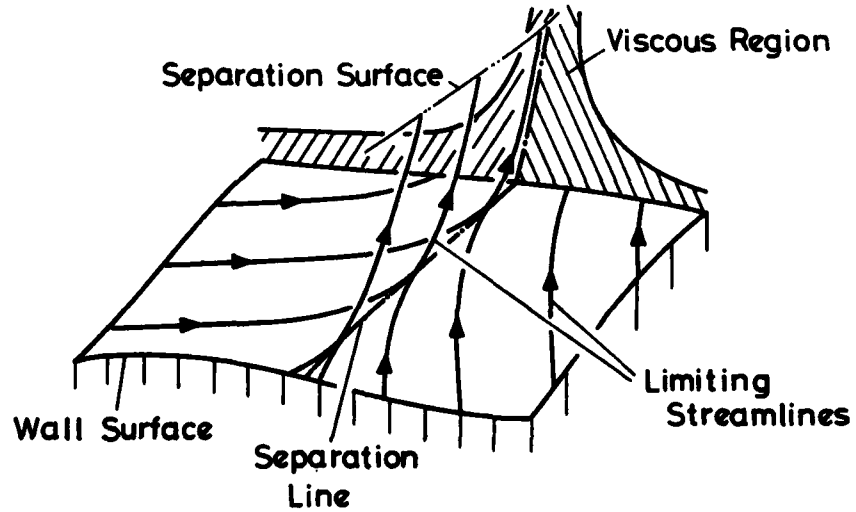


(b) Flow Features in the Interaction Region

Figure 5. Glancing shock boundary-layer interaction.

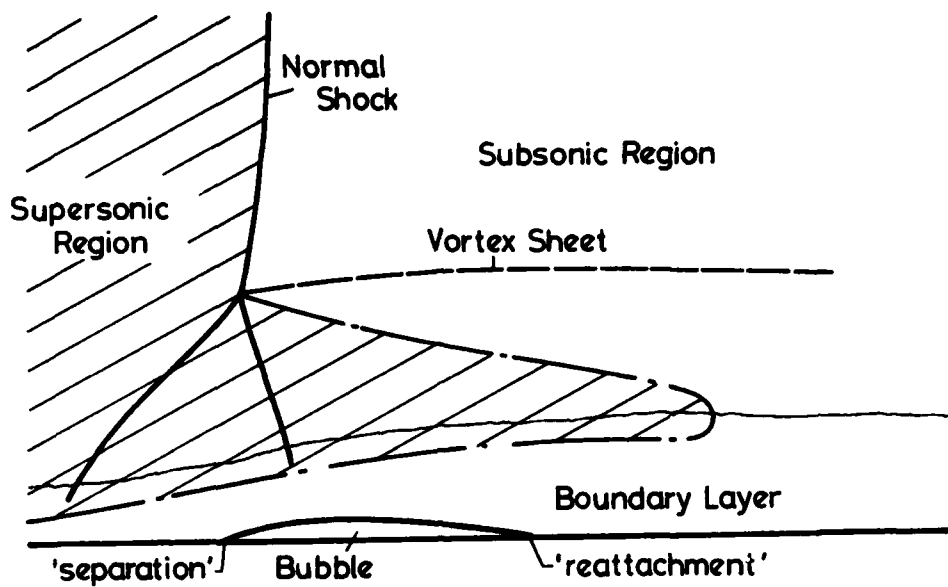


(a) Singular Separation

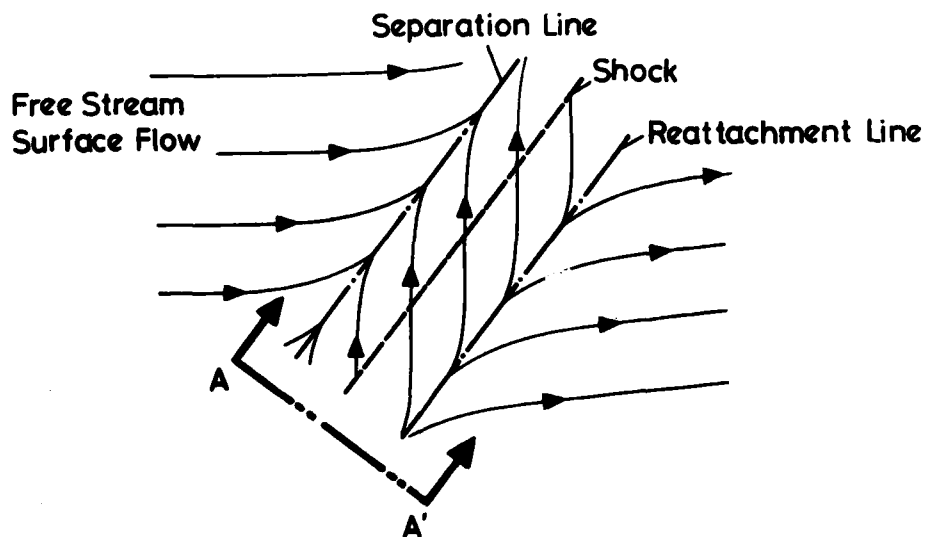


(b) Ordinary Separation

Figure 6. Maskell's separation models.



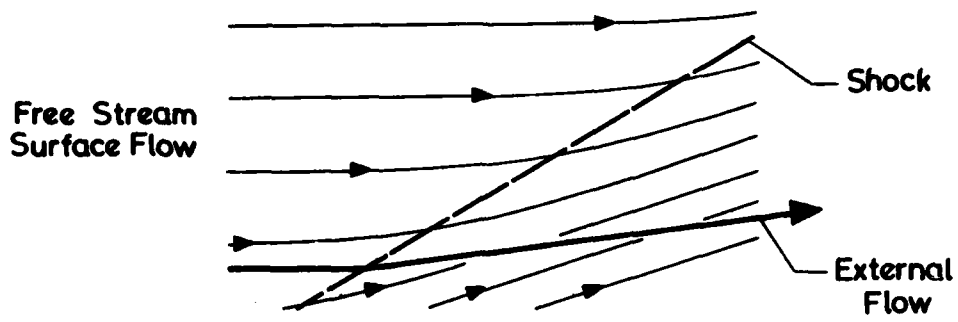
(a) Normal Shock Boundary Layer Interaction



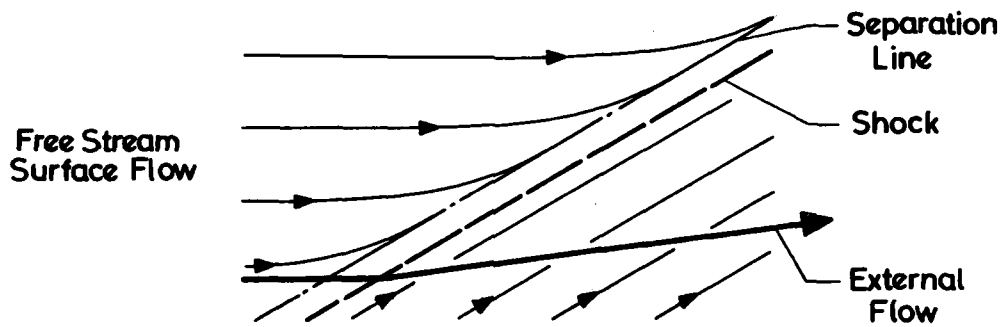
(b) Quasi-Two-Dimensional Glancing Interaction Region with a Similar Sectional View A-A' to the Above Normal Shock Interaction

Figure 7. Quasi-two-dimensional flow field.

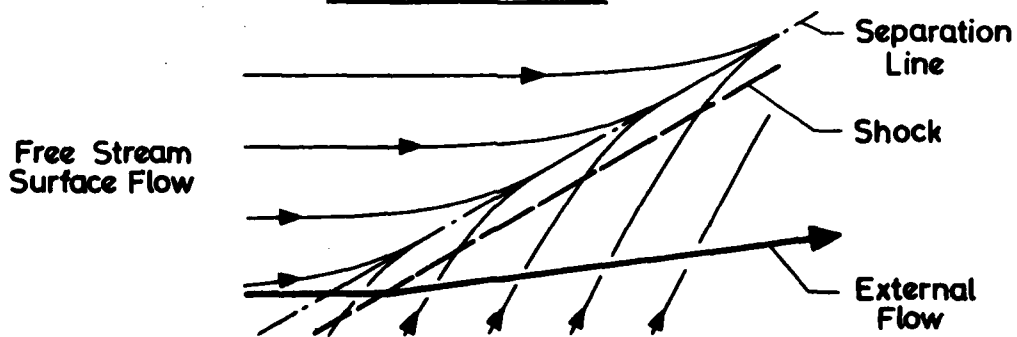
ATTACHED FLOW



INCIPIENT SEPARATION



SEPARATED FLOW



(c) Quasi-2-D surface flow.

Figure 7. Quasi-two-dimensional flow field.

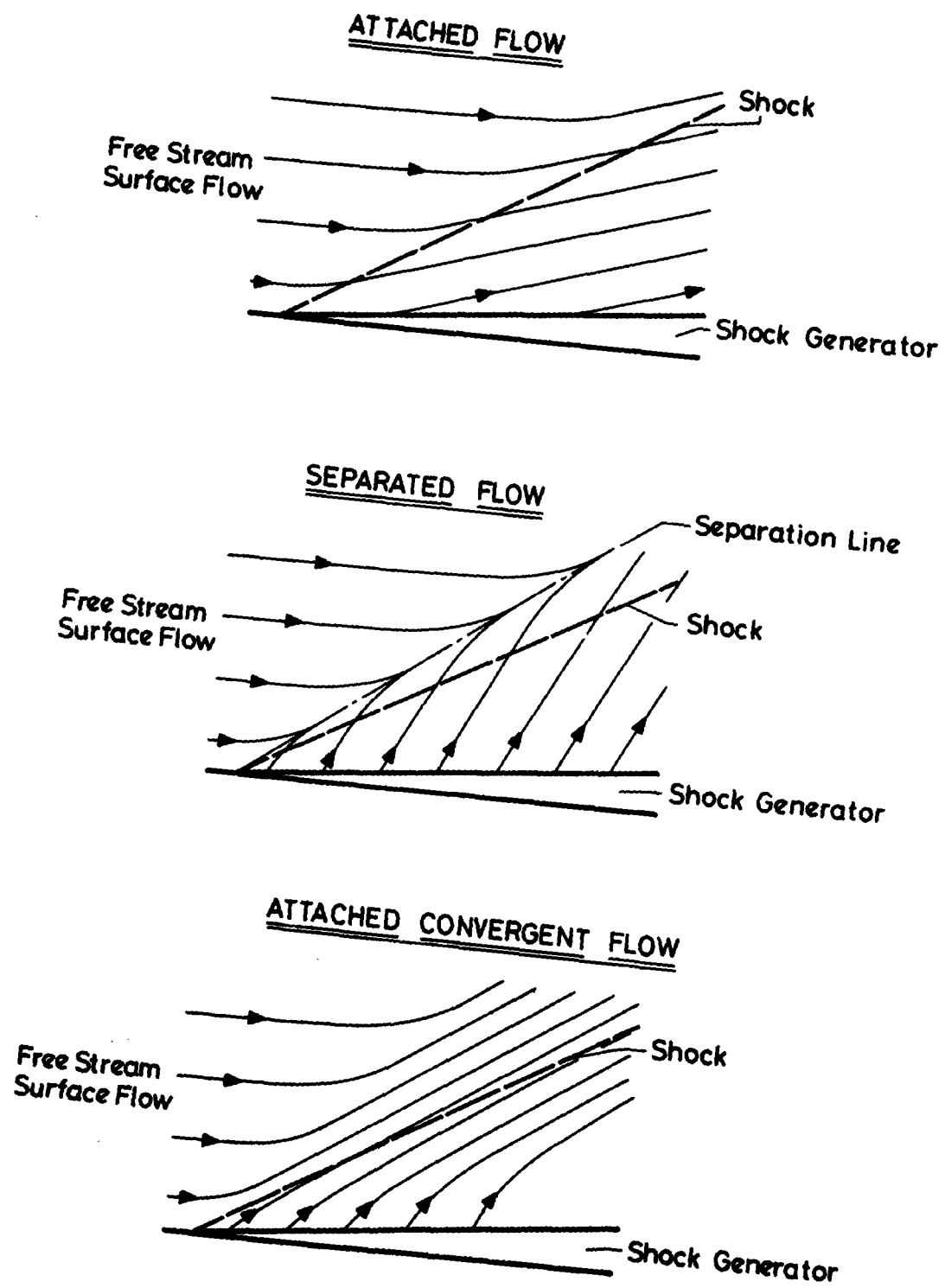
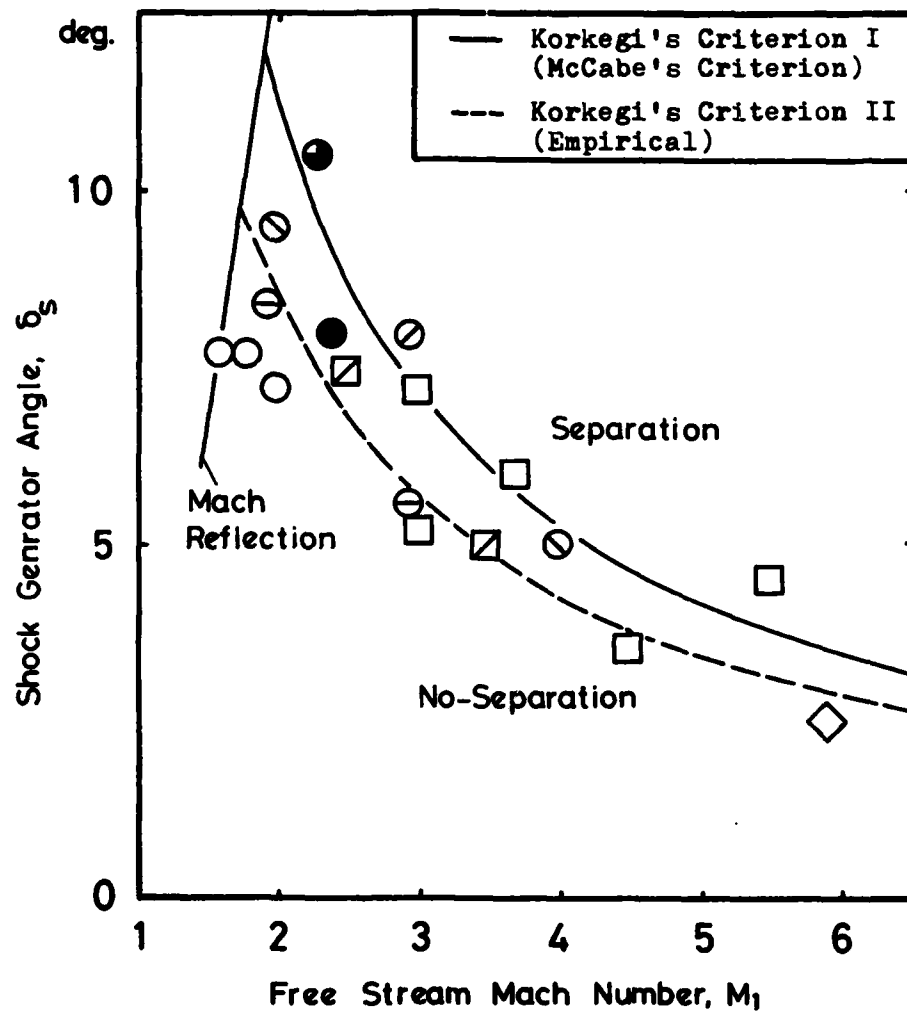


Figure 8. Surface flow pattern in the corner flow.



Experiments	
○ Stanbrook (Ref. 7)	◻ Lowrie (Ref. 39)
⊙ McCabe (Ref. 8)	◇ Goldberg (Ref. 36)
⊙ Oskam (Ref. 10)	● The Present (2.5 x 2.5 Tunnel)
⊙ Peake (Ref. 13)	● (9 x 9 Tunnel)
□ Neumann (Ref. 17)	

Figure 9. Shock generator angle to induce incipient flow separation as calculated according to McCabe's criterion.

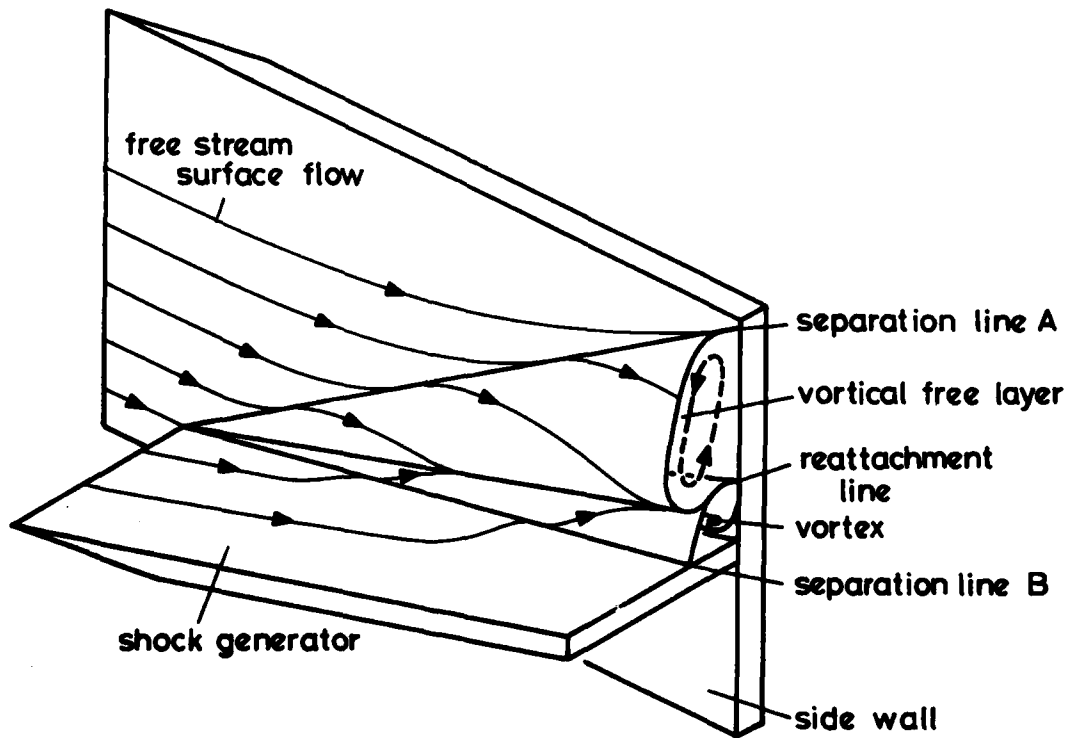
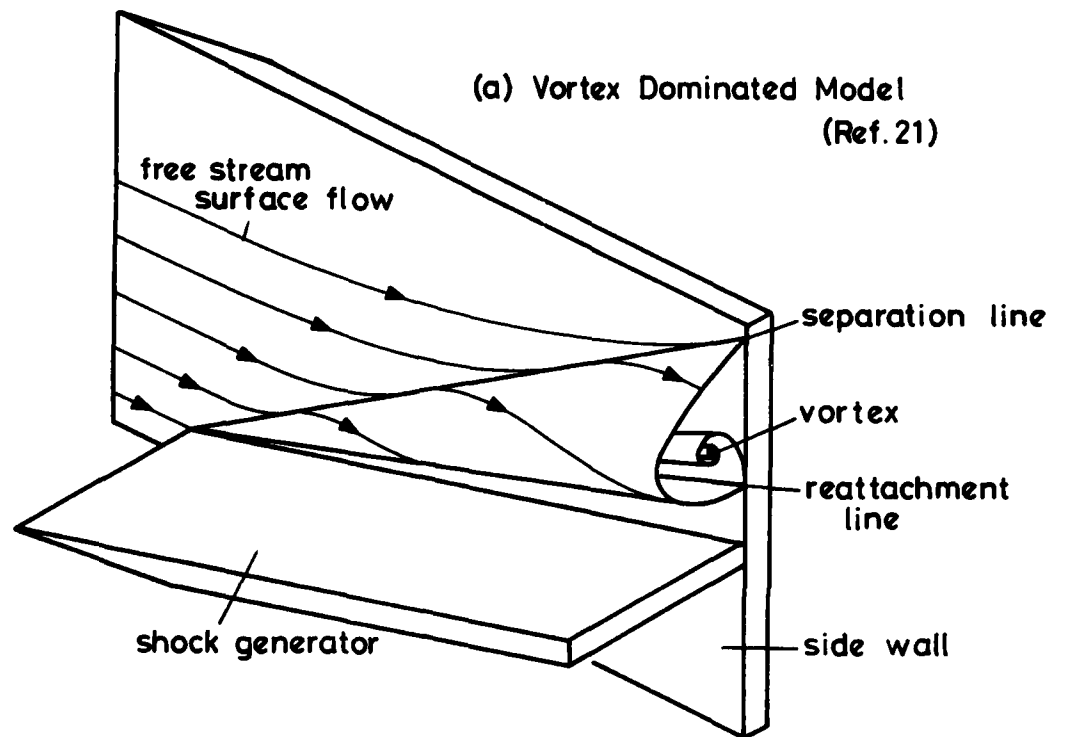
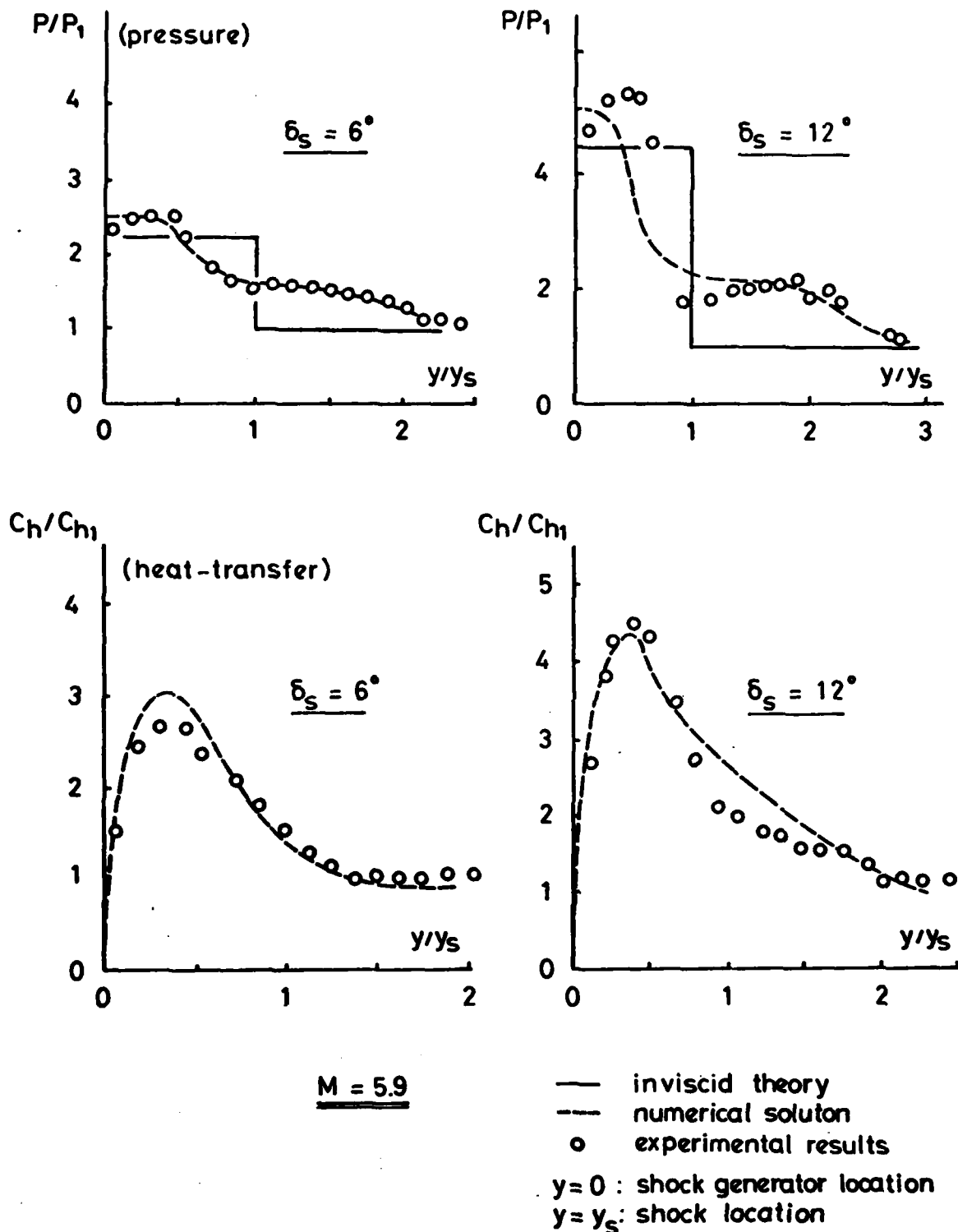


Figure 10. Separated flow-field models of glancing interaction region.



(From Ref. 22)

Figure 11. A numerical solution of glancing interaction.

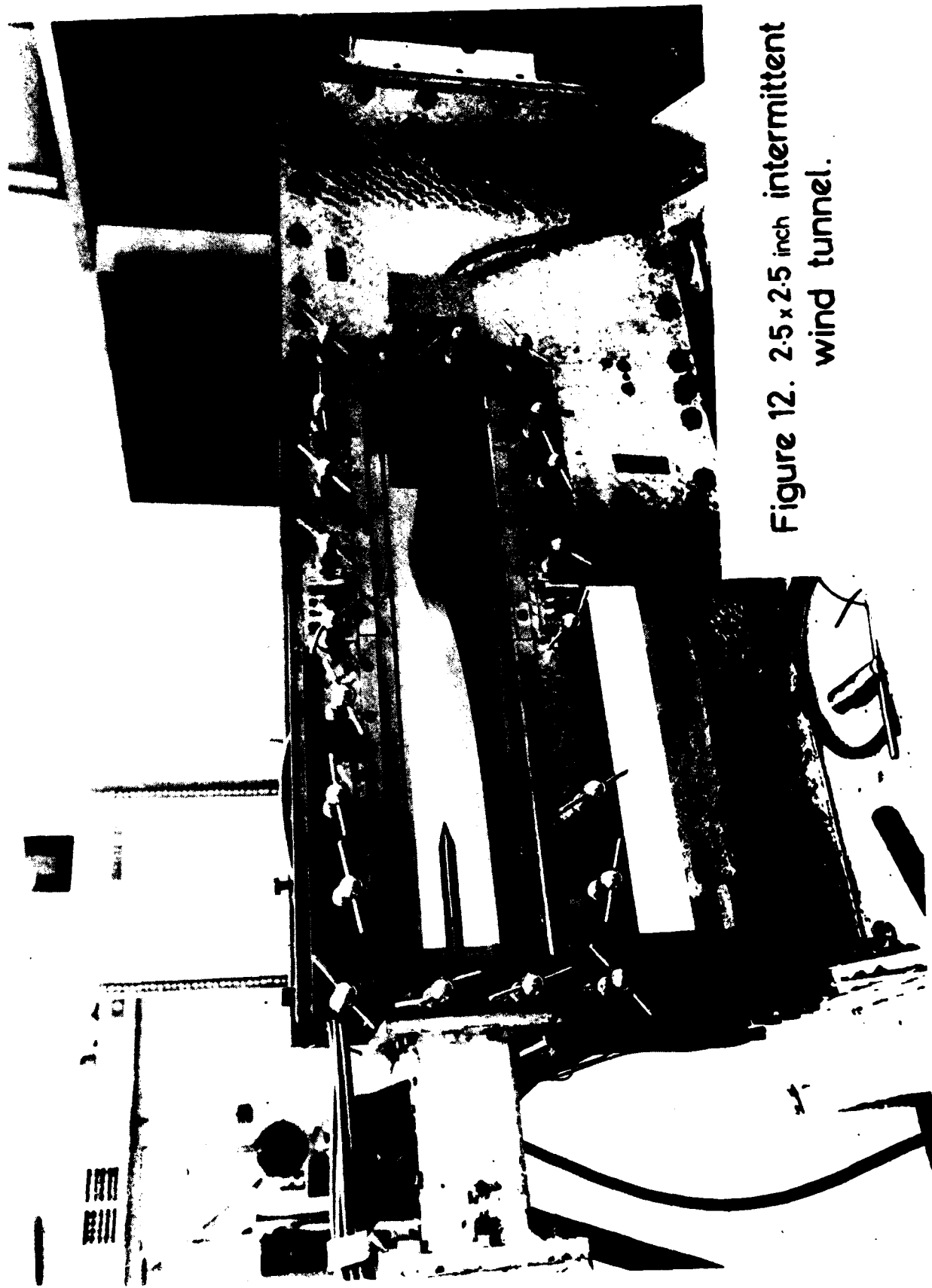


Figure 12. 2.5 x 2.5 inch intermittent  
wind tunnel.

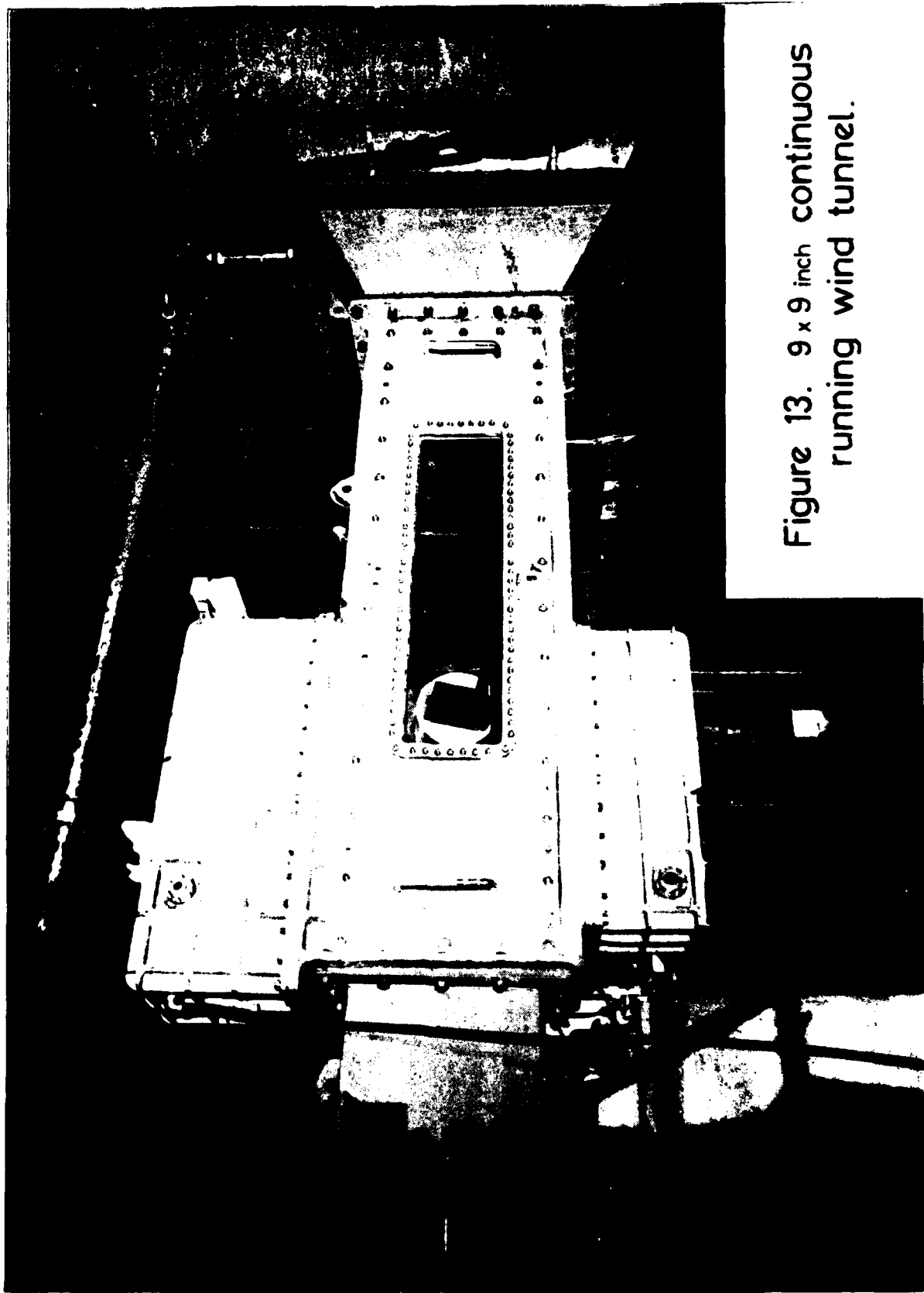


Figure 13. 9 x 9 inch continuous running wind tunnel.

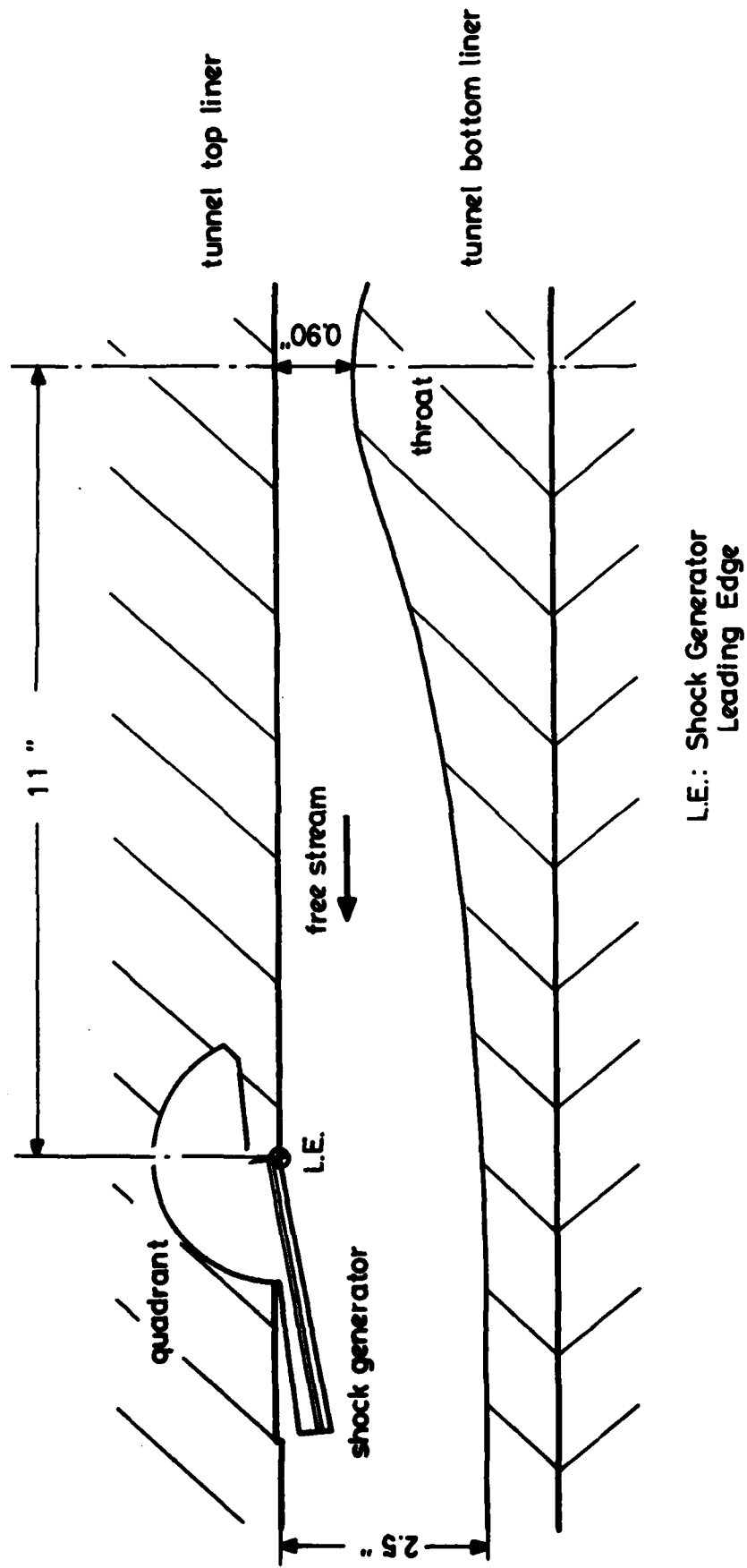
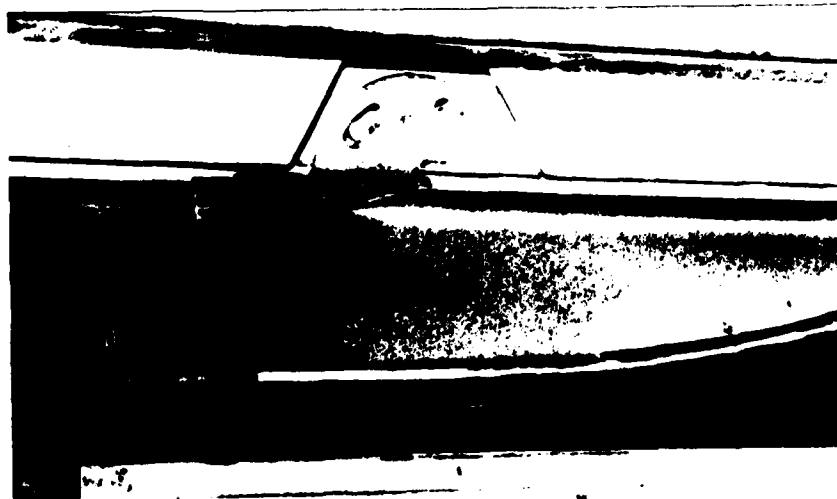
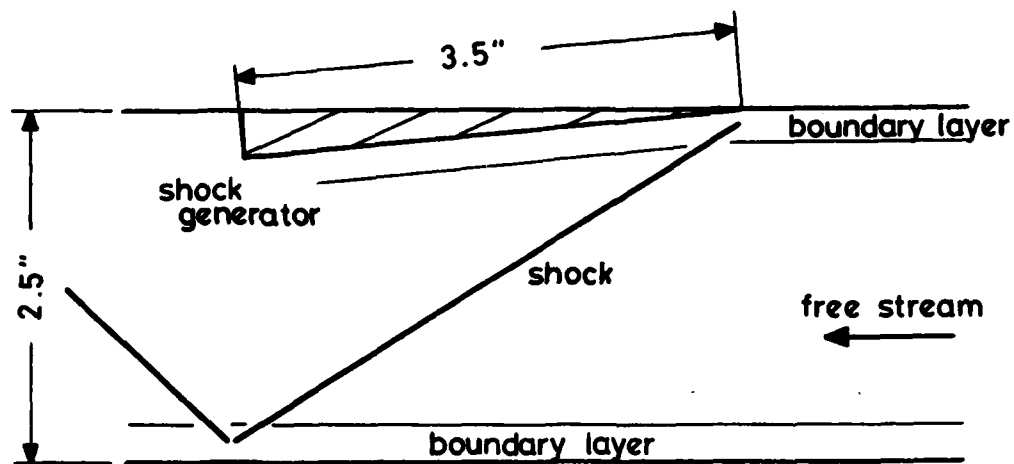


Figure 14. Working section of the 2.5 x 2.5 inch tunnel.



(Model A Arrangement)

Figure 15. Model geometry in the 2.5 x 2.5 inch tunnel.

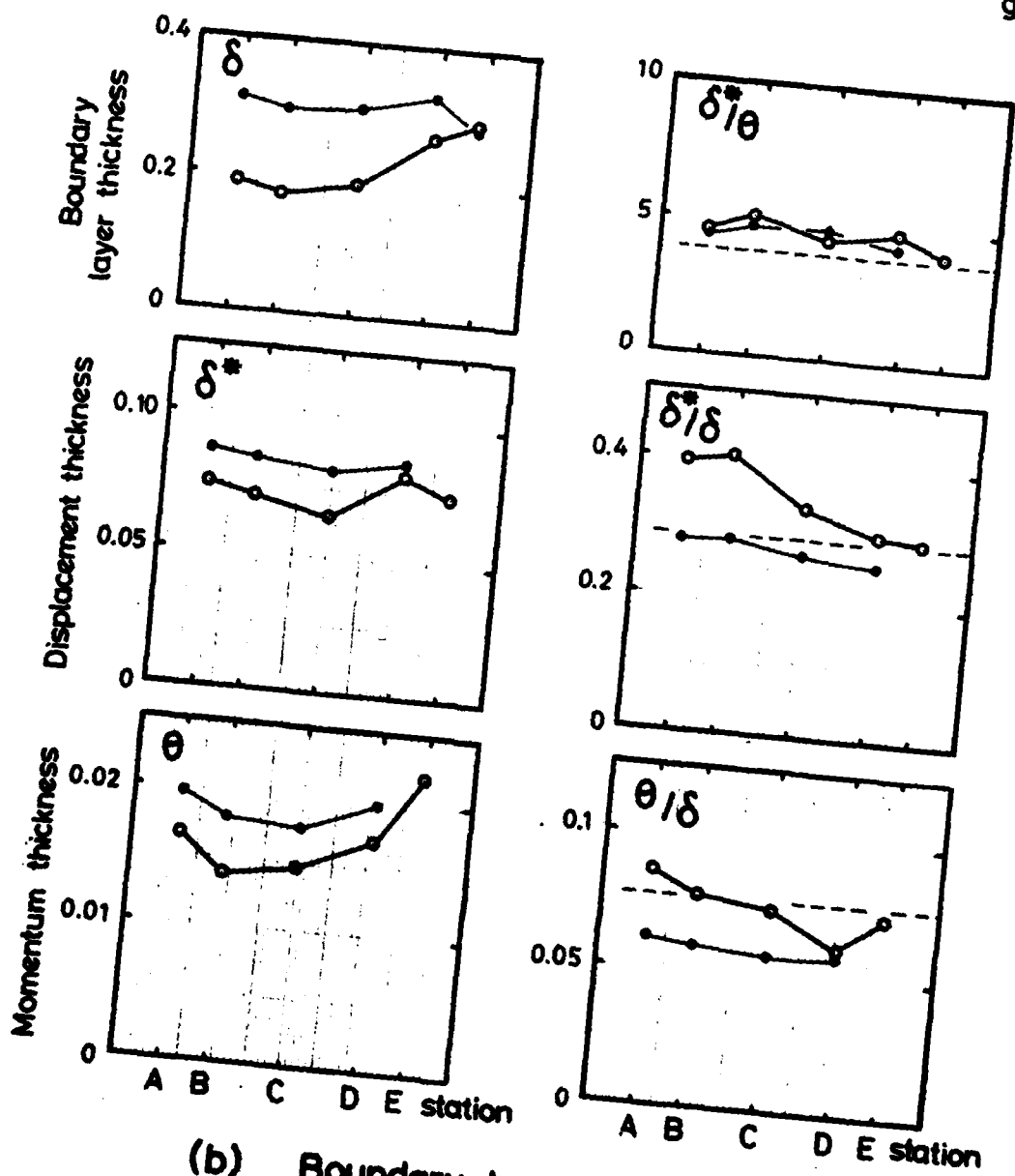
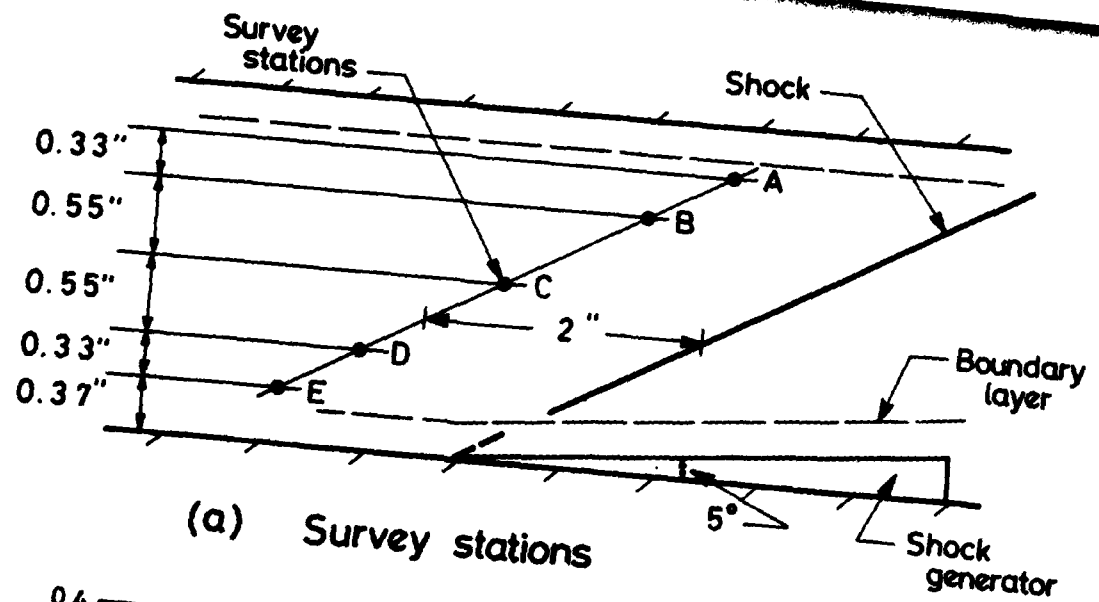
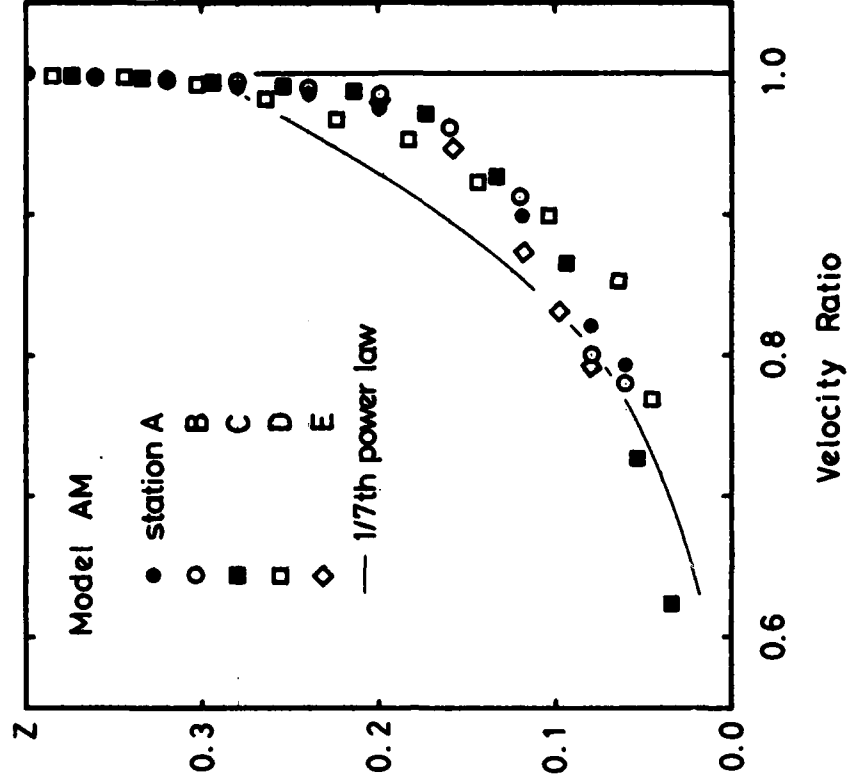
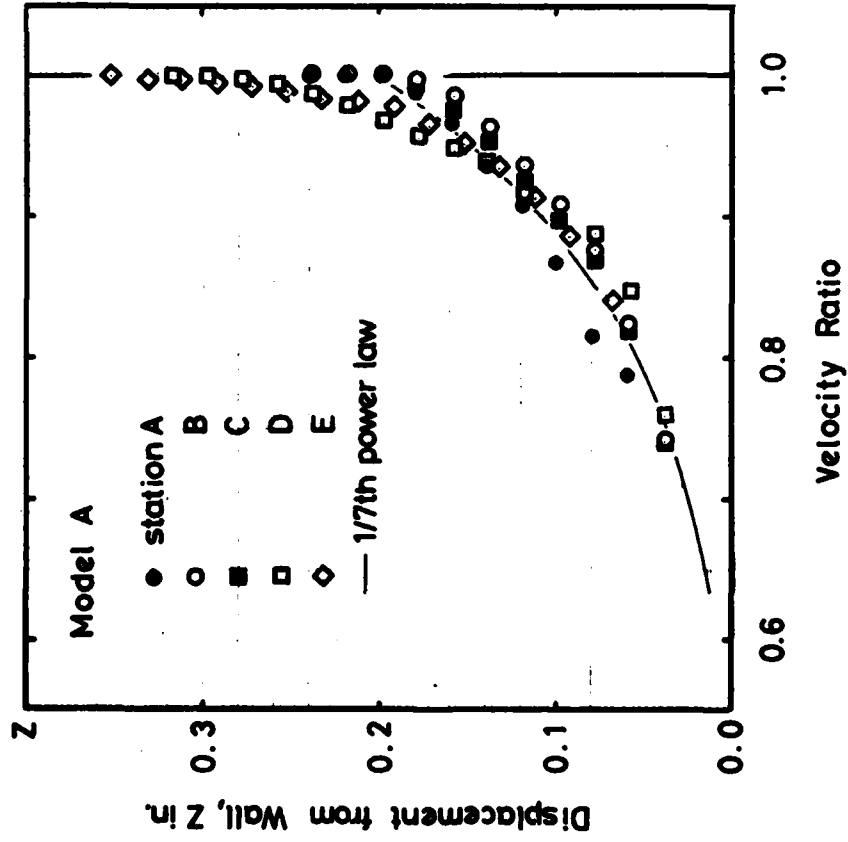
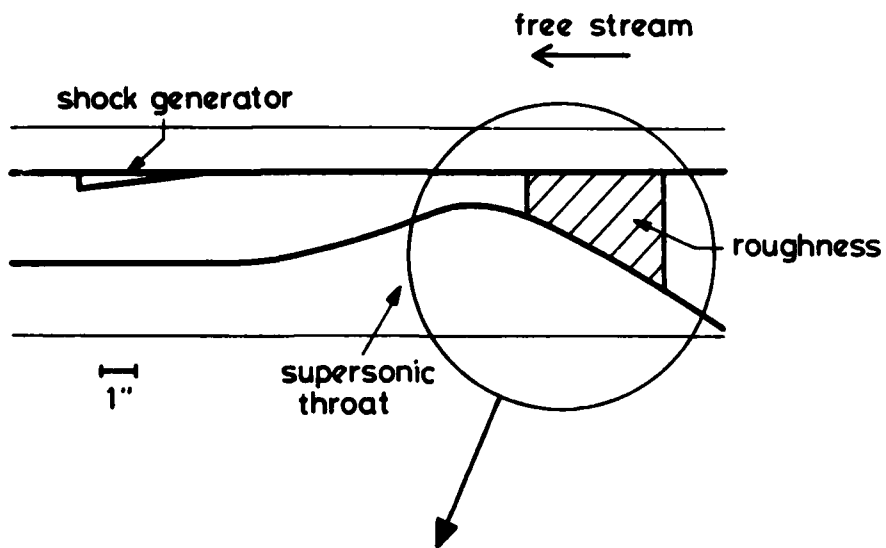


Figure 16. Boundary-layer properties in the 2.5x2.5 inch tunnel.



(c) Velocity Profiles

Figure 16. Boundary-layer properties in the 2.5 x 2.5 inch tunnel.



(Roughness Arrangement)

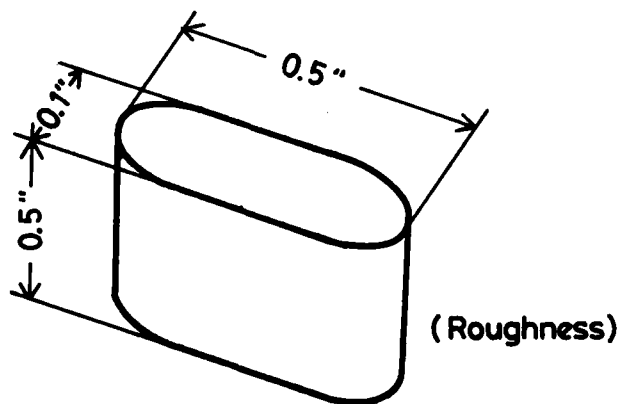
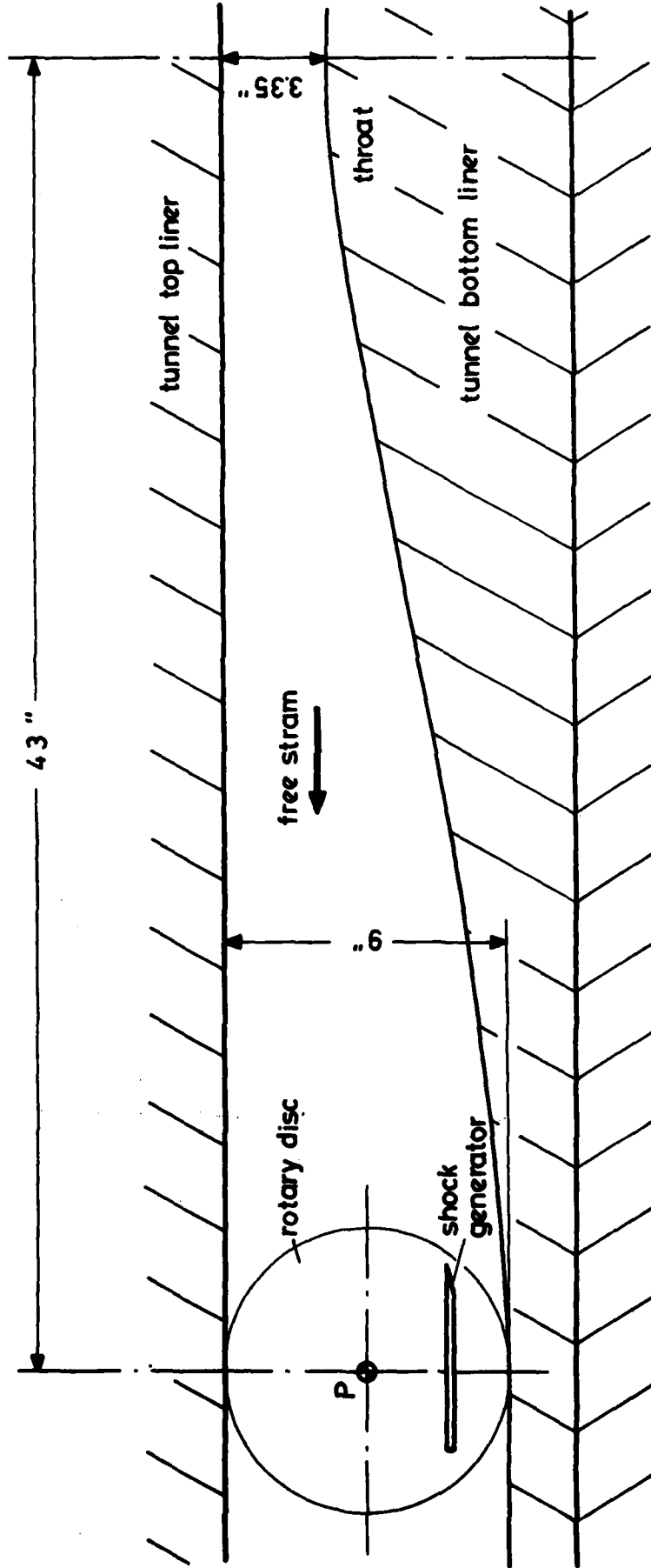
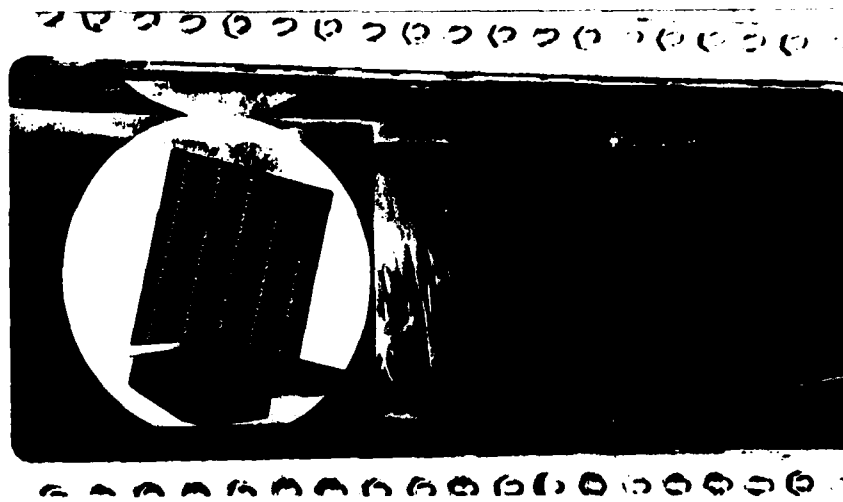
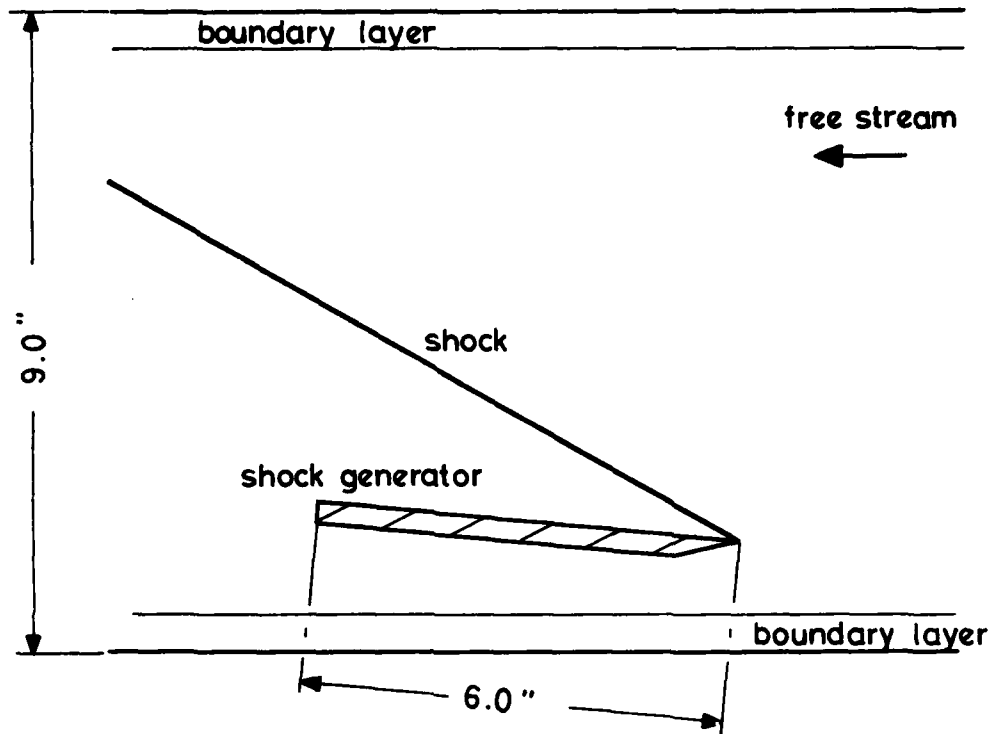


Figure 17. Roughness elements to modify the test boundary layer.



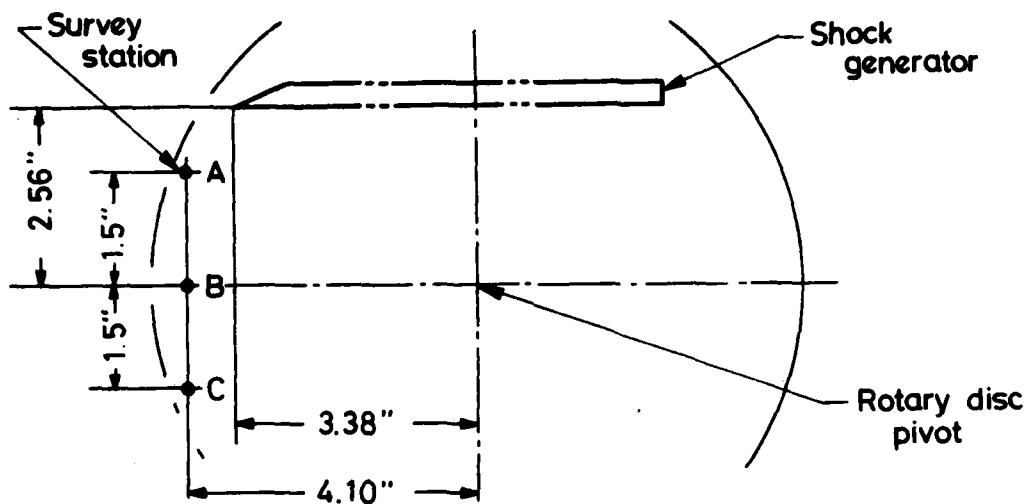
P: Rotary Disc Pivot

Figure 18. Working section of the 9 x 9 inch tunnel.

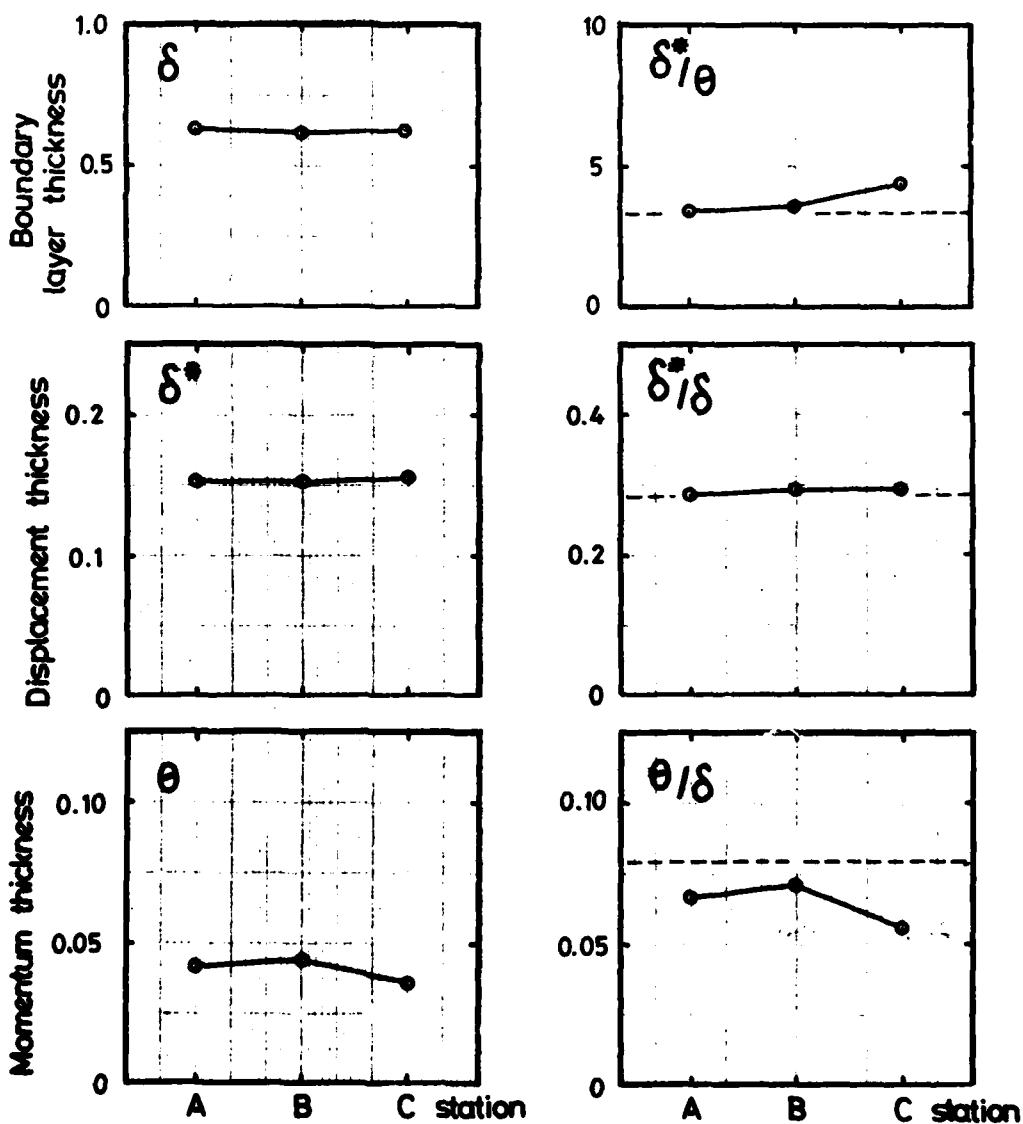


(Model B Arrangement)

Figure 19. Model geometry in the 9 x 9 inch tunnel.

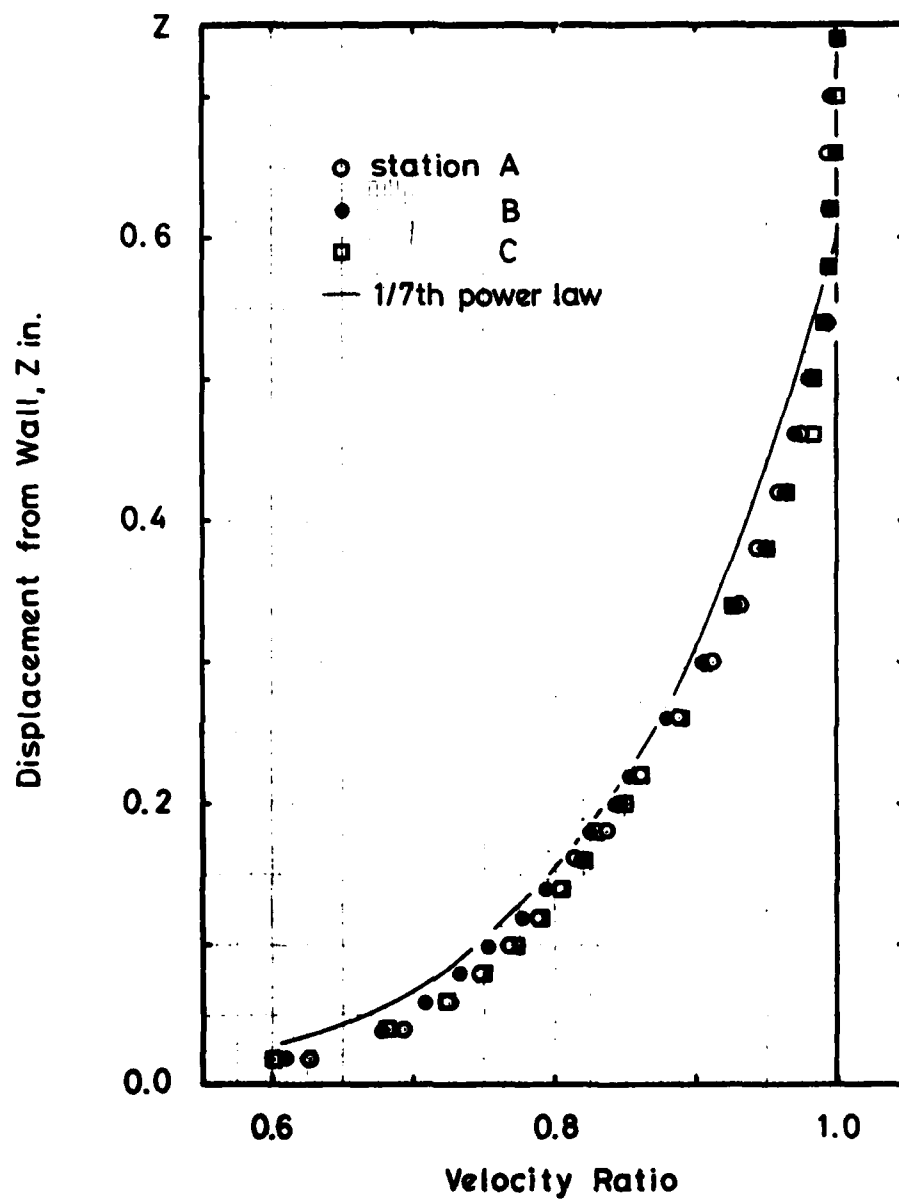


(a) Survey stations



(b) Boundary layer properties

Figure 20. Boundary-layer properties in the 9 x 9 inch tunnel



(c) Velocity Profiles

Figure 20. Boundary-layer properties in the 9x9 inch tunnel.

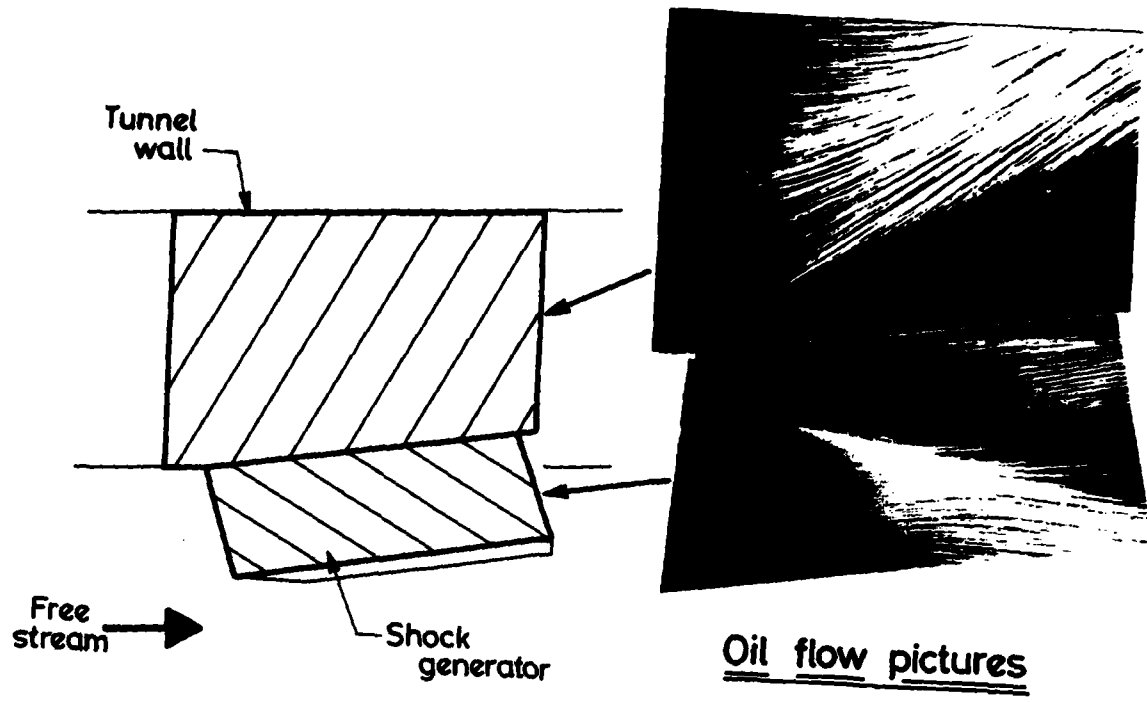


Figure 21. Oil flow visualization

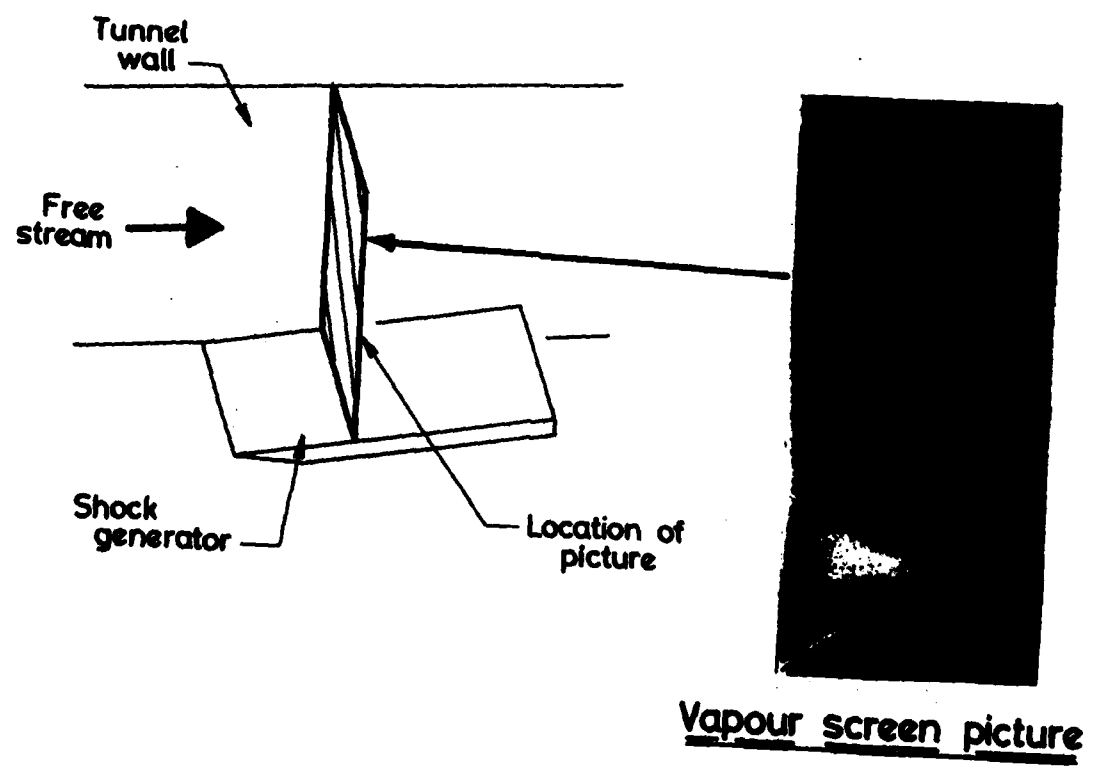
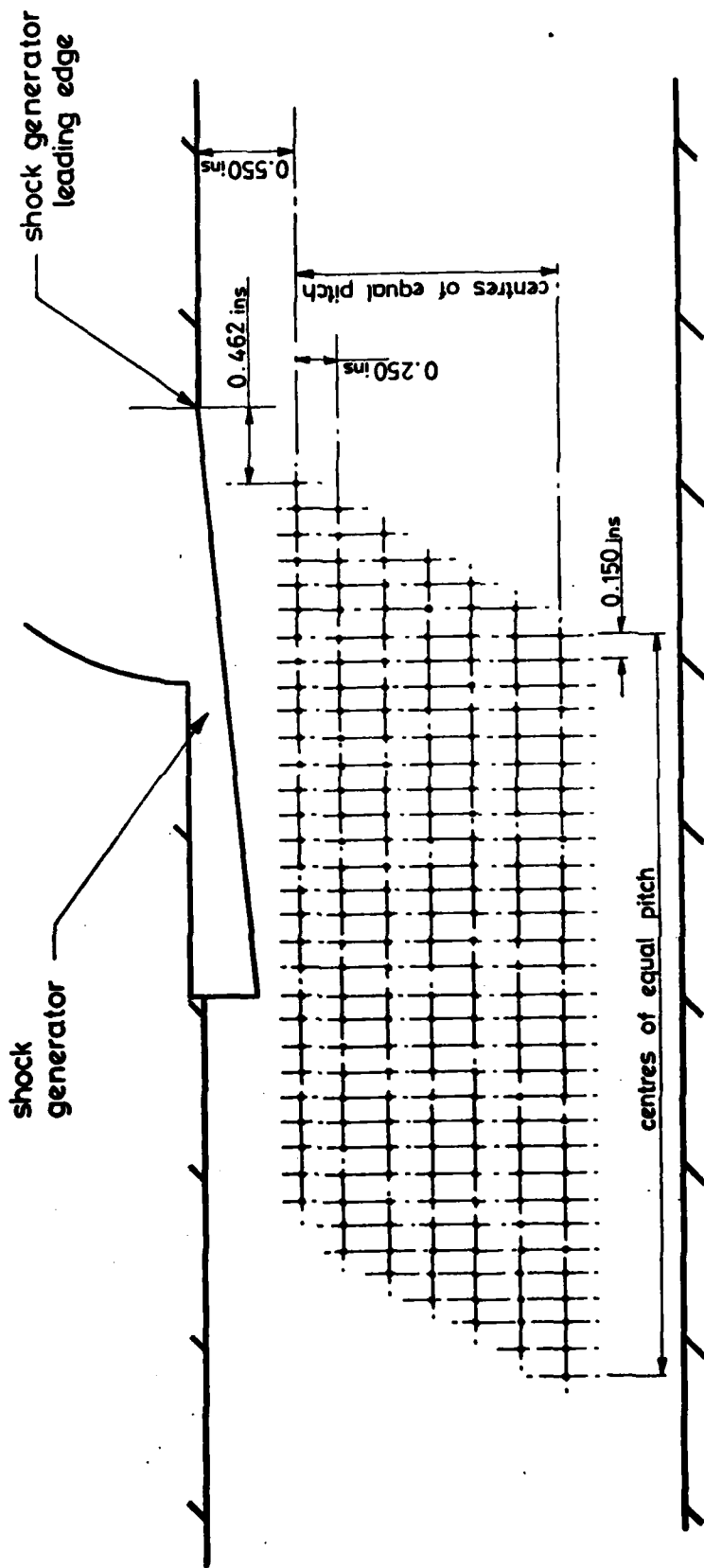
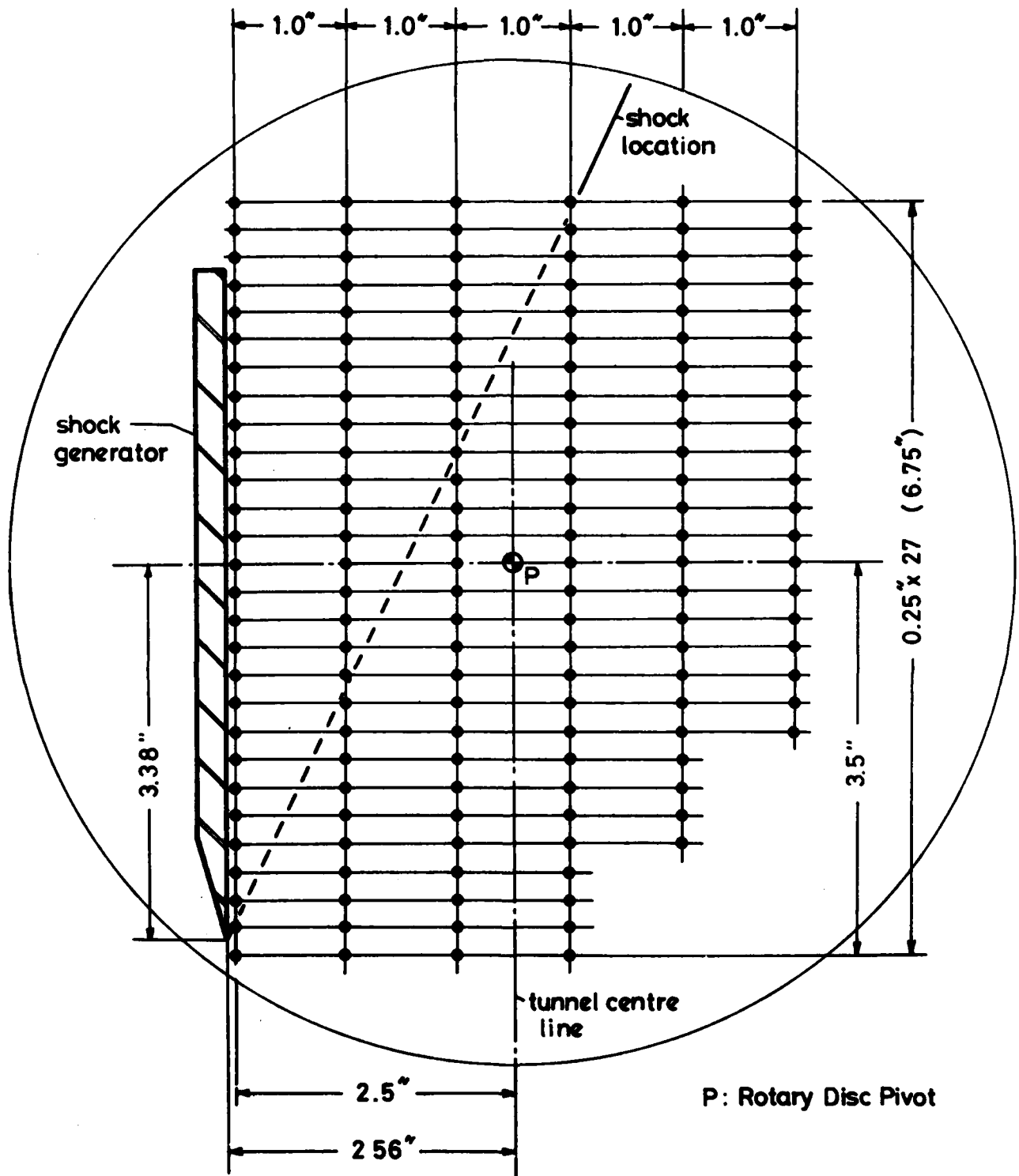


Figure 22. Vapour-screen method.



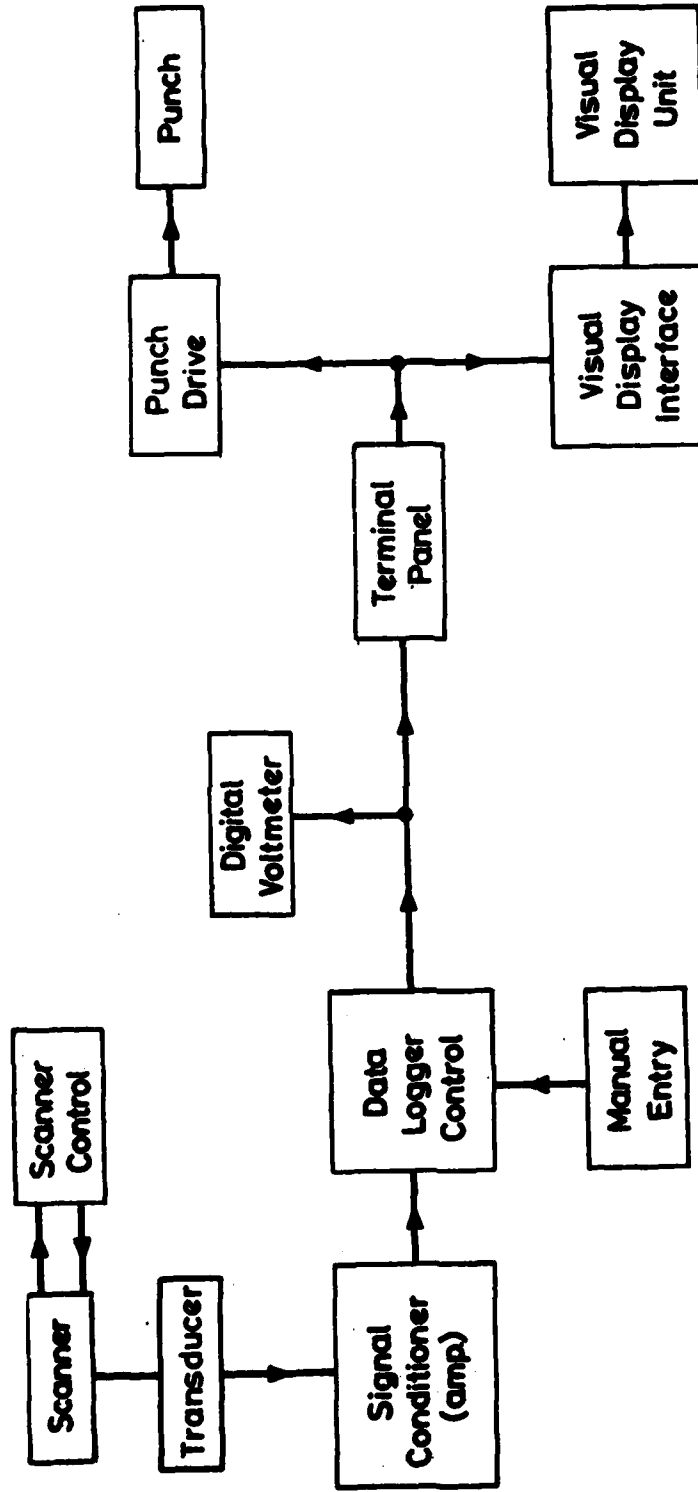
(a) Pressure stations in the 2.5 x 2.5 ins tunnel

Figure 23. Arrangement of surface static holes.



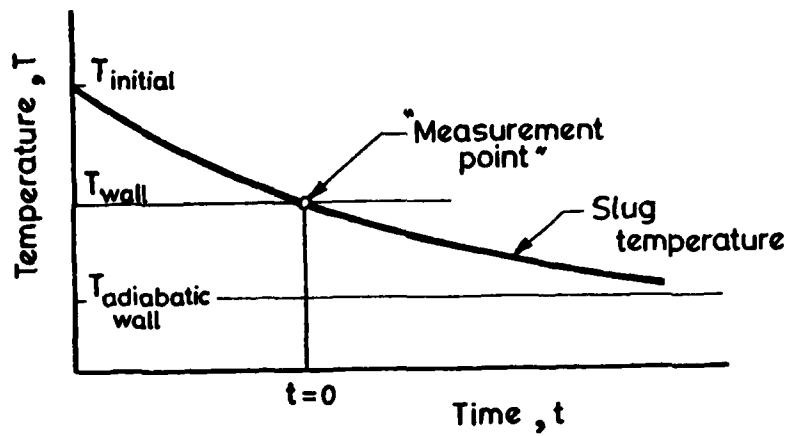
(b) Pressure stations in the 9x9 ins tunnel

Figure 23. Arrangement of surface static pressure holes.

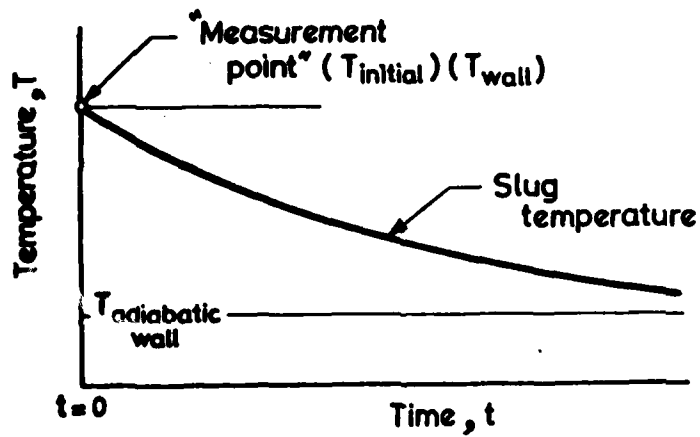


(c) Pressure Data Logger

Figure 23. Arrangement of data logging system.

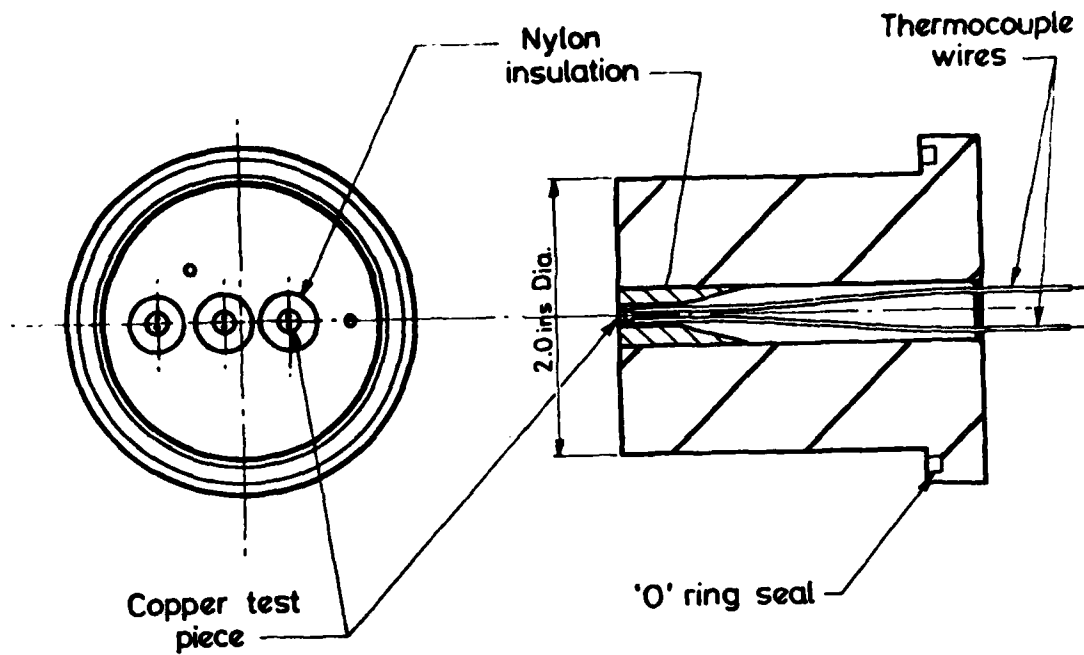


(a) Original technique

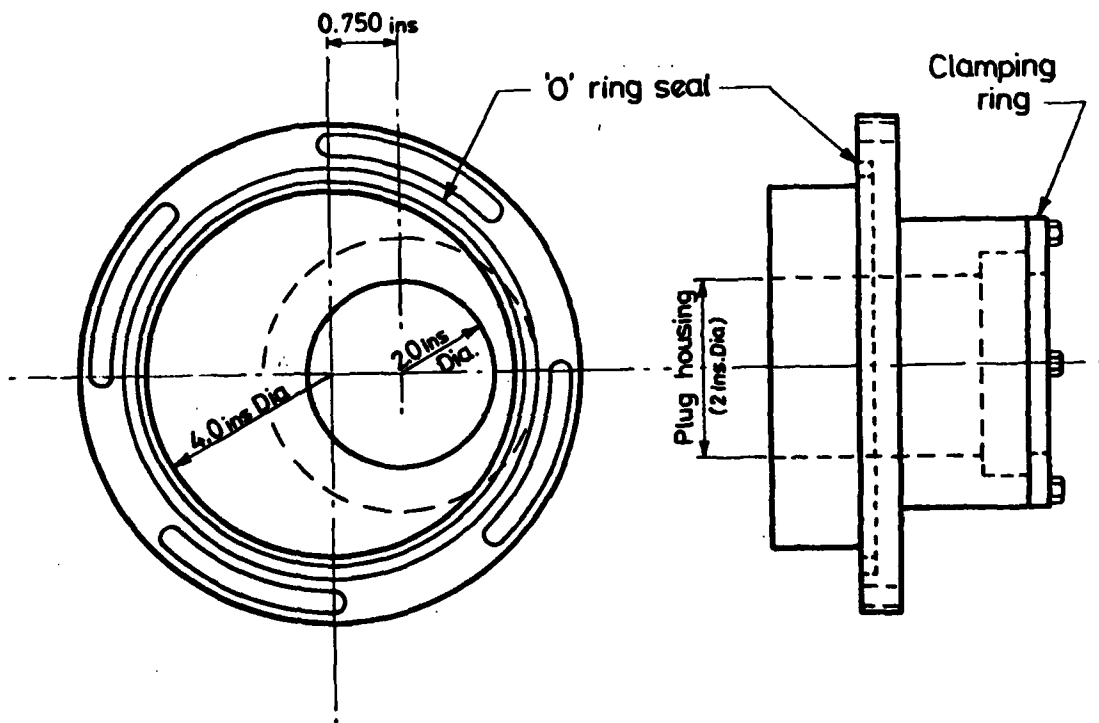


(b) Modified technique

Figure 24. Temperature-time histories for the slug calorimeter technique.



(a) Thermocouple Plug



(b) Eccentric Rotable

Figure 25. Slug calorimeter installation.

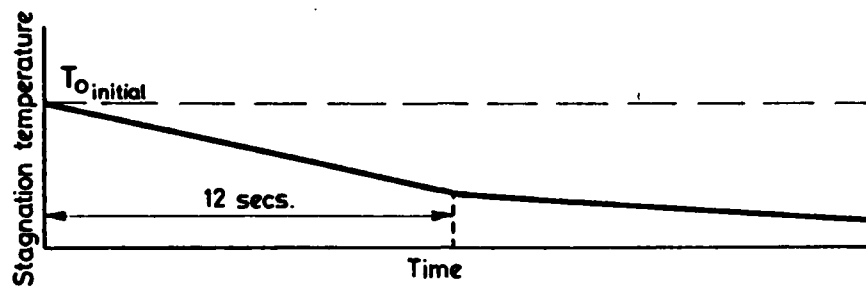
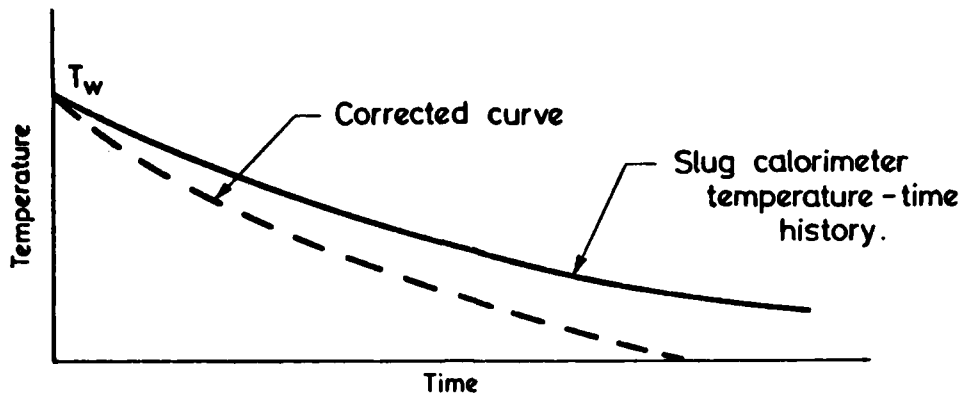


Figure 26. The stagnation temperature correction.

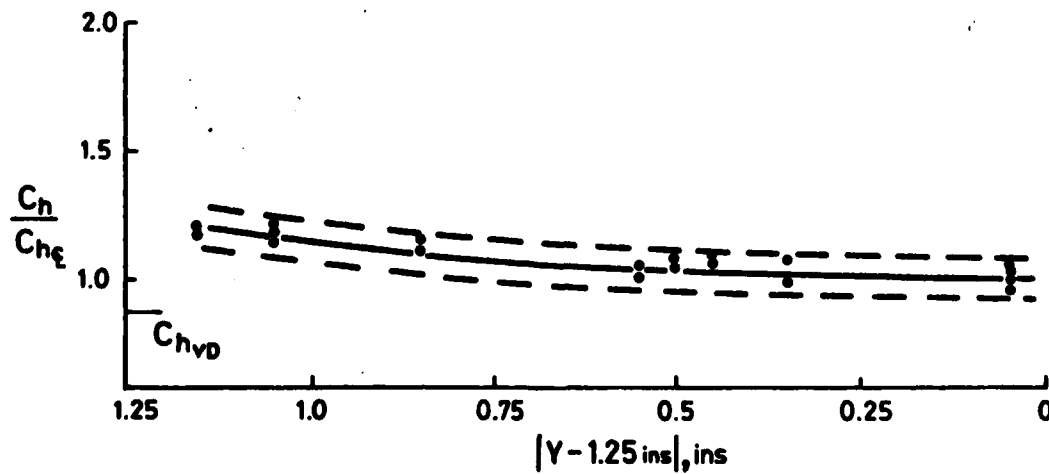


Figure 27. Results of bare plate heat transfer measured by the slug calorimeter (2.5 x 2.5 inch tunnel).

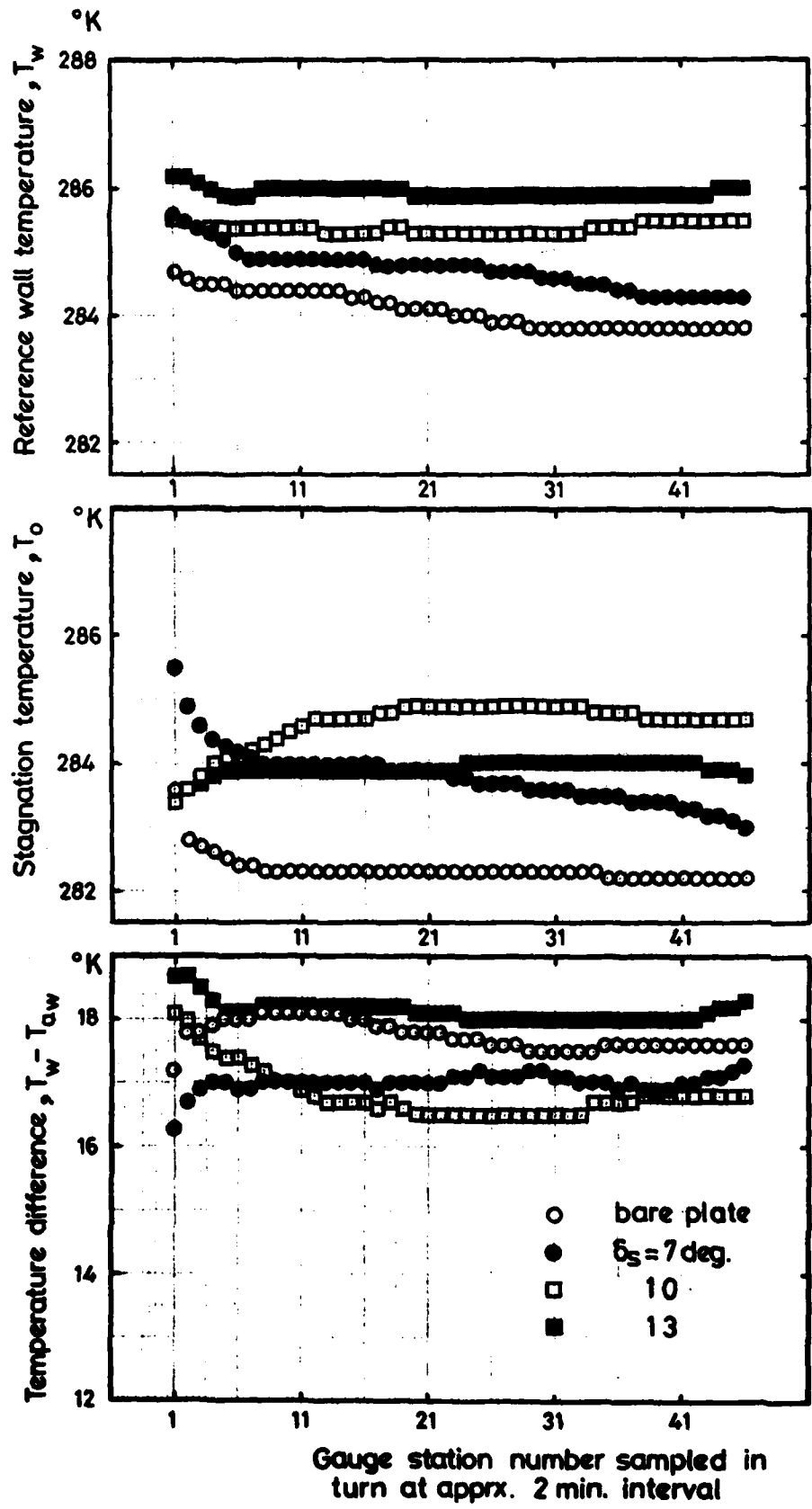
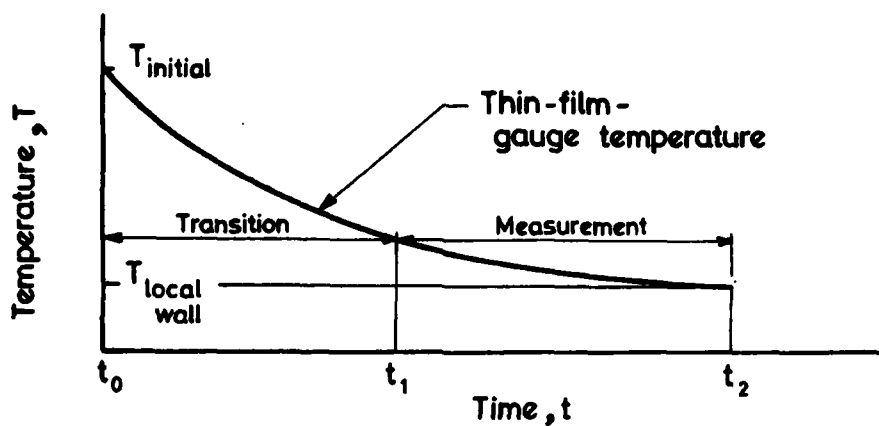
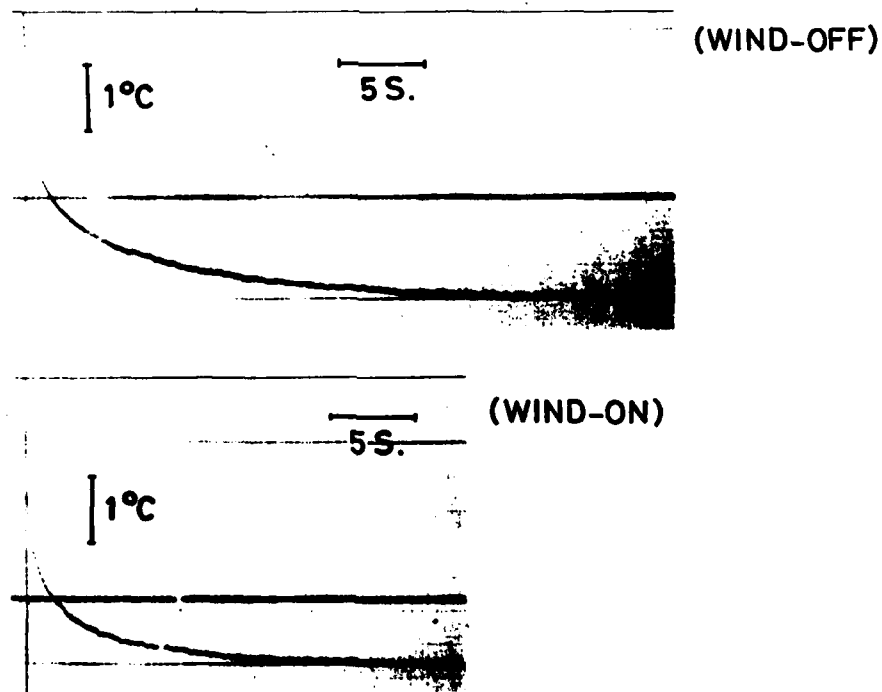


Figure 28. Temperature variations in the 9 x 9 inch tunnel during the running time of typically 90 mins.

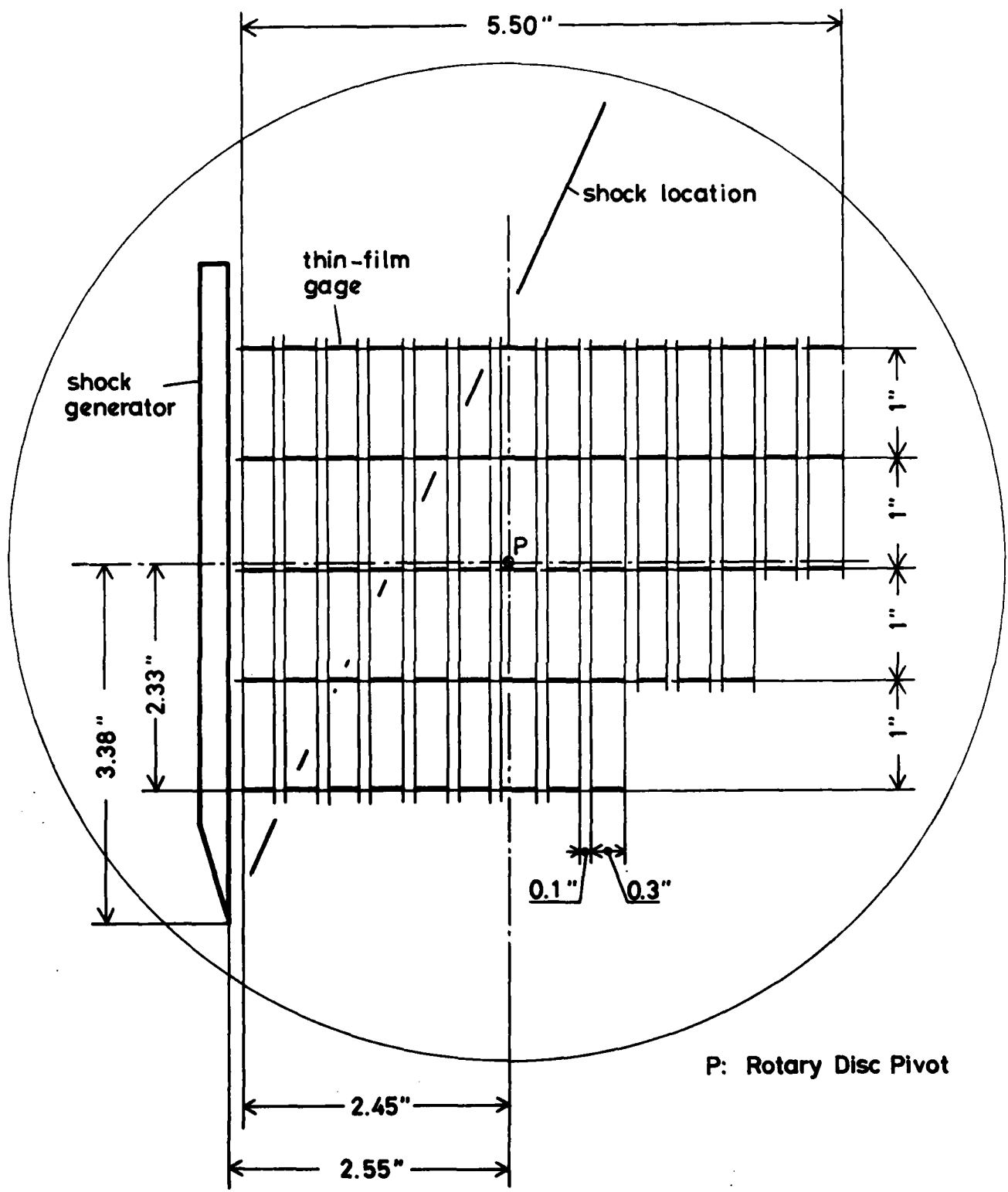


(a) Gauge temperature time history.



(b) Actual temperature time history.

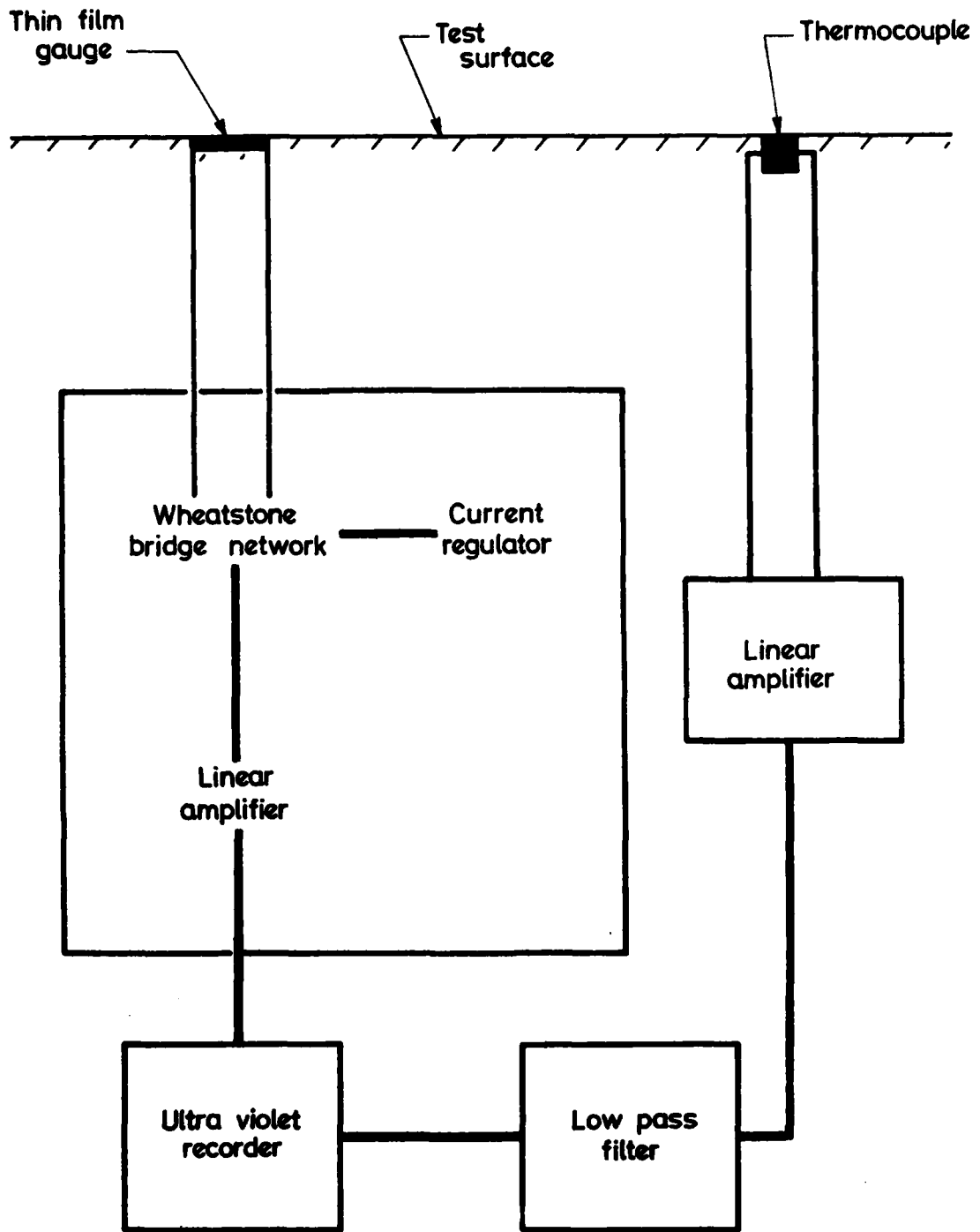
Figure 29. Temperature-time history of a thin-film-gauge in the continuous running tunnel.



P: Rotary Disc Pivot

(a) Gage Installation

Figure 30. Thin-film-gauge calorimeter installation.



(b) Electronics installation.

Figure 30. Thin-film-gauge electronics installation.

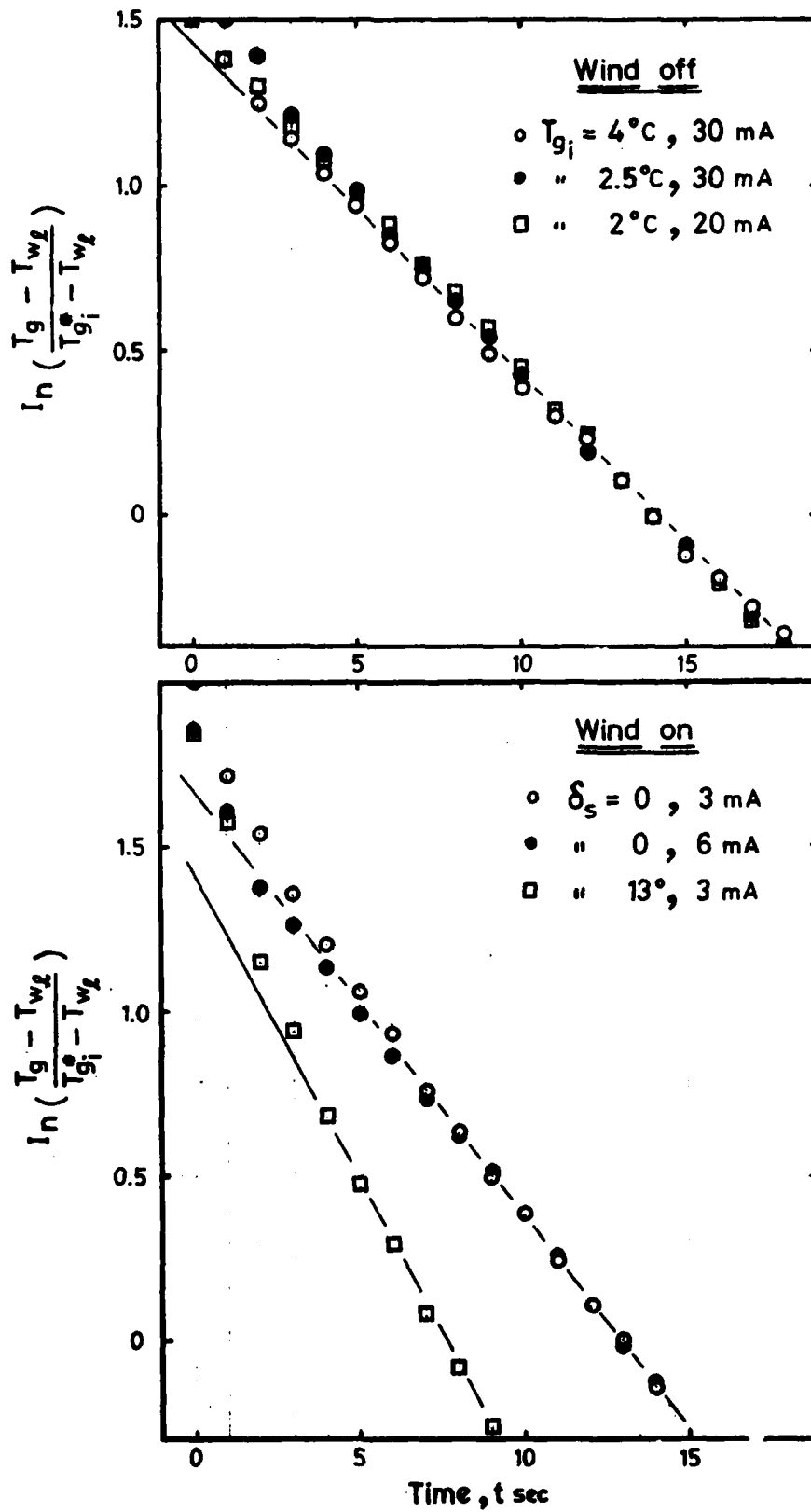


Figure 31. The measured temperature behaviour.

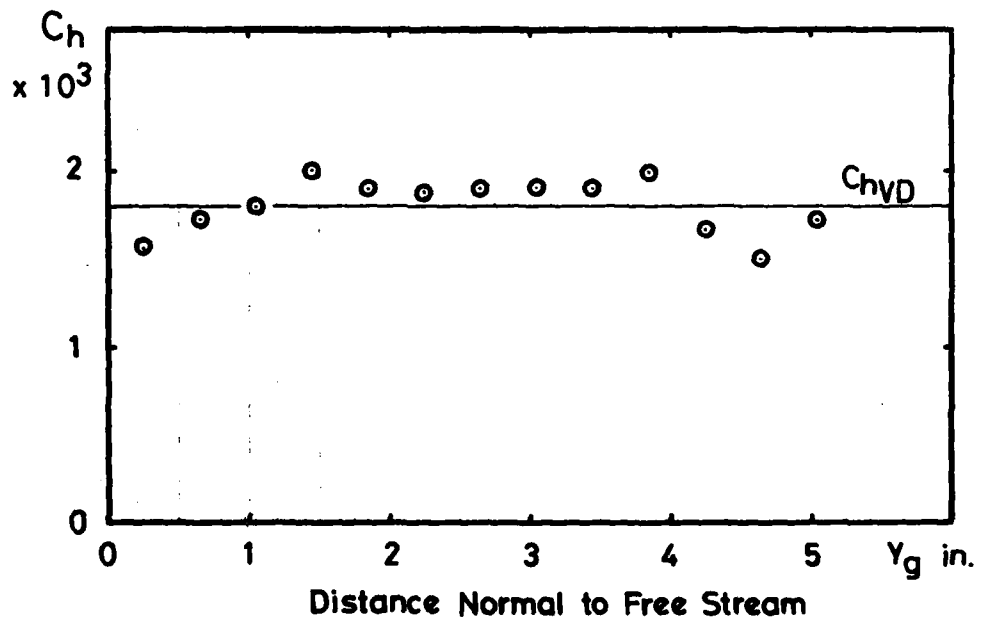
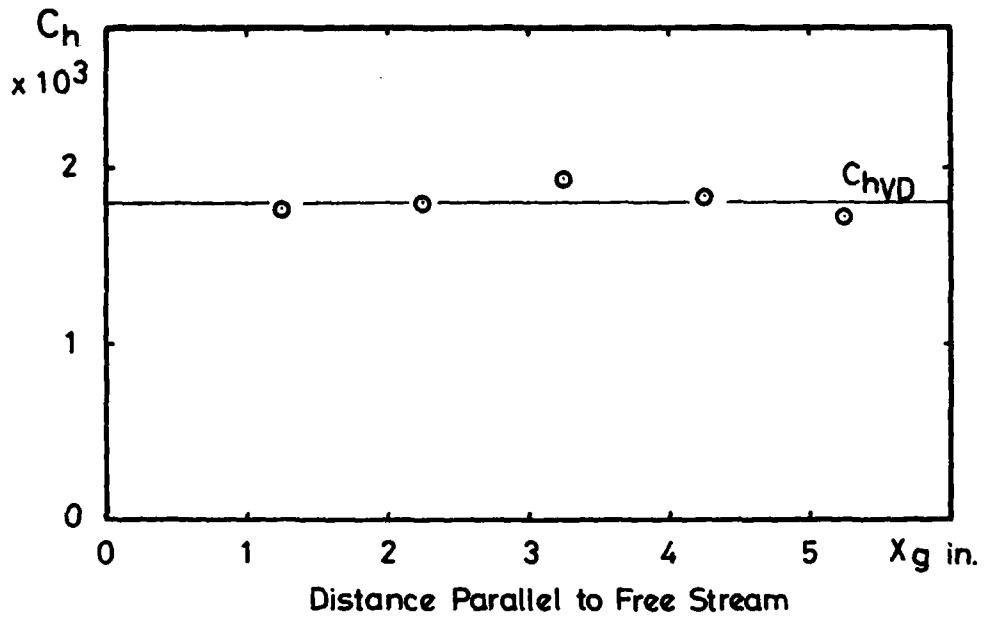
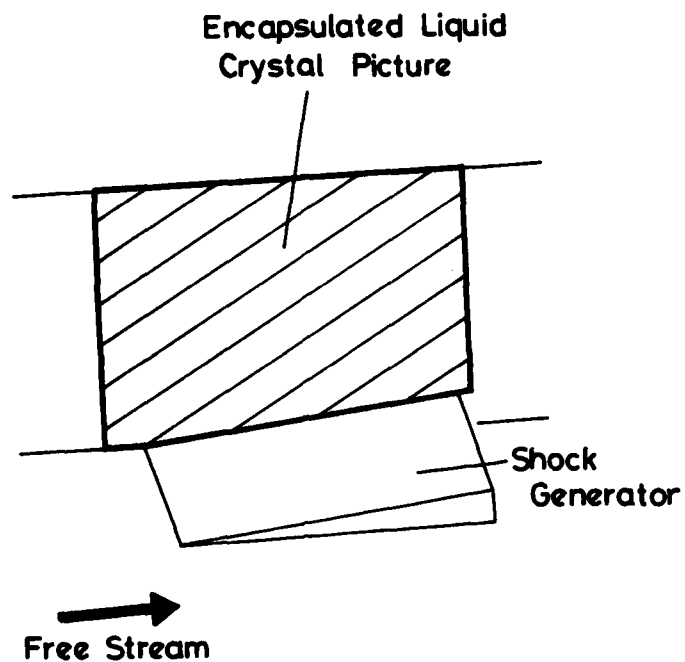
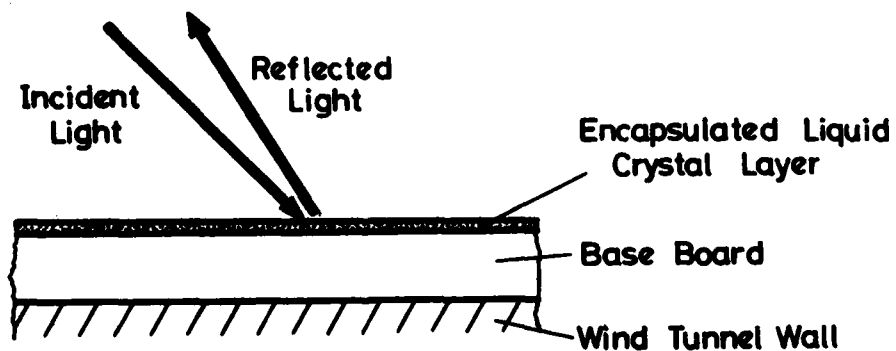


Figure 32. Results of bare plate heat transfer measured by the thin-film-gauge calorimeter (9x9 inch tunnel).

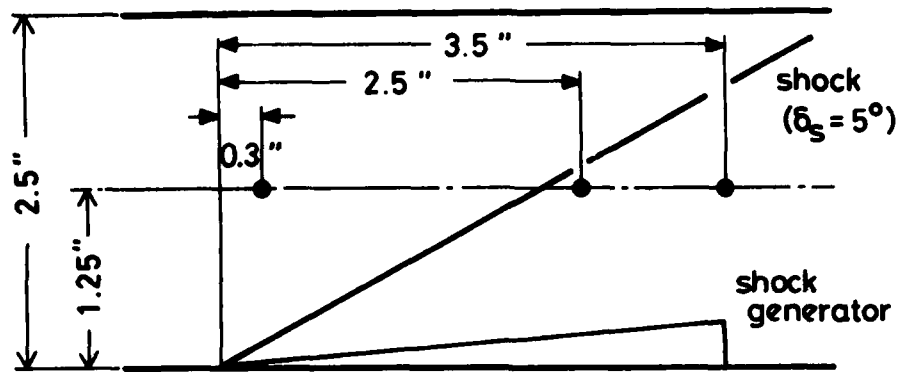


(a) Encapsulated Liquid  
Crystal Picture

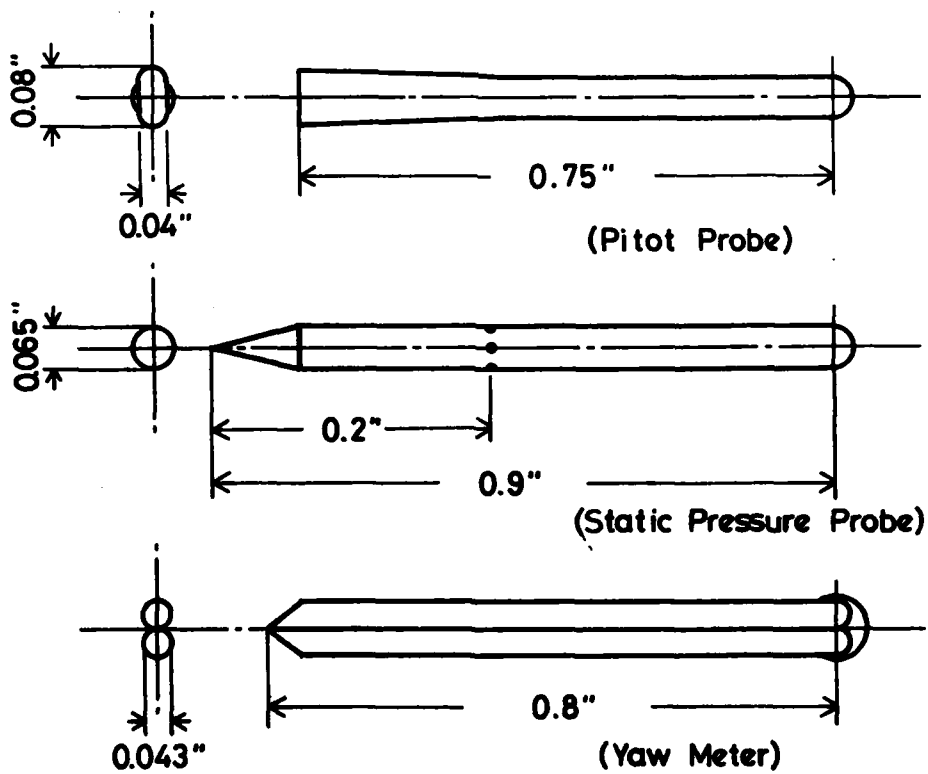


(b) Sectional View of Test Board

Figure 33. Encapsulated liquid crystal technique.



(a) Survey Stations



(b) Probes

Figure 34. Boundary-layer survey stations and probes.

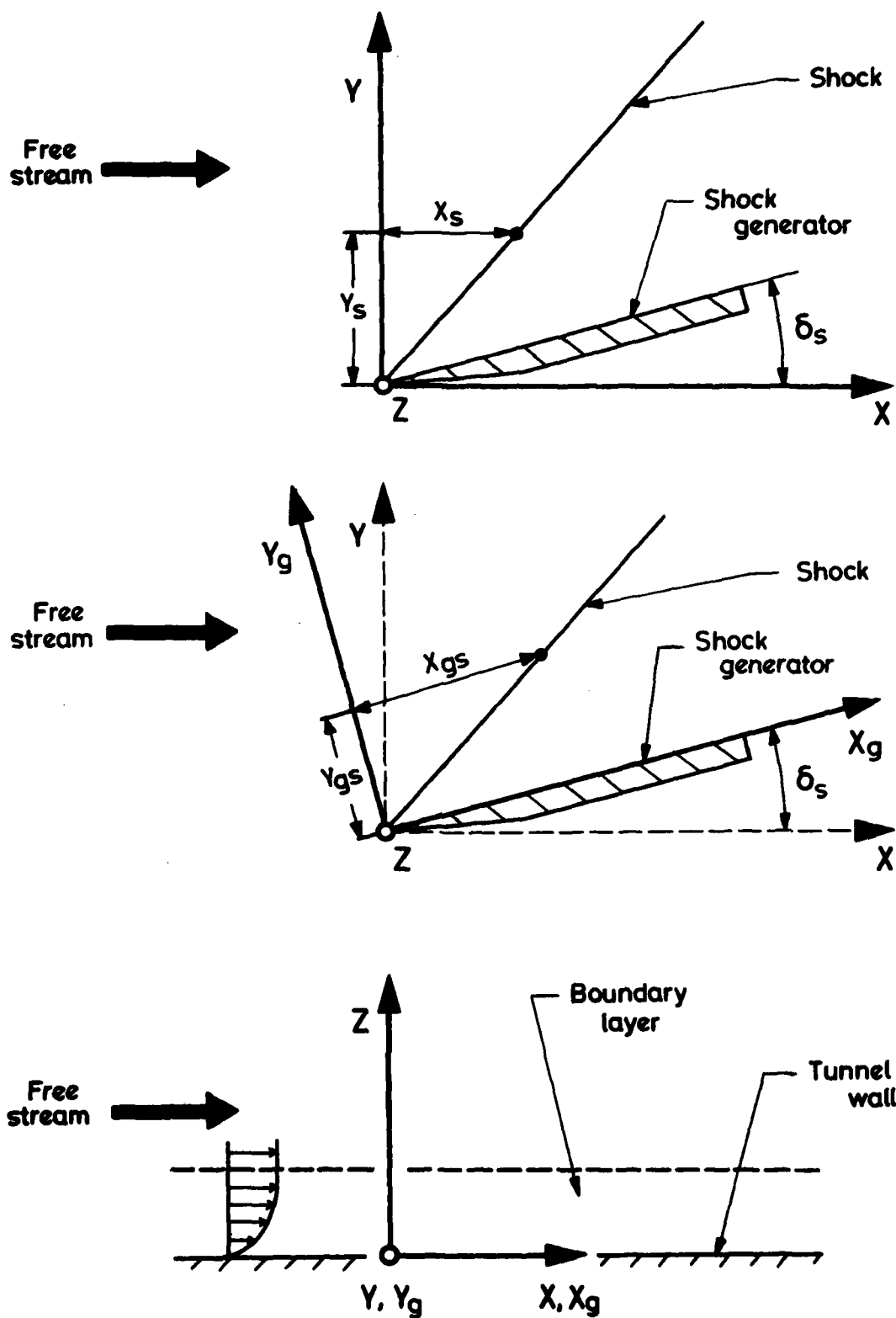


Figure 35. Co-ordinate systems for experimental-data presentation.

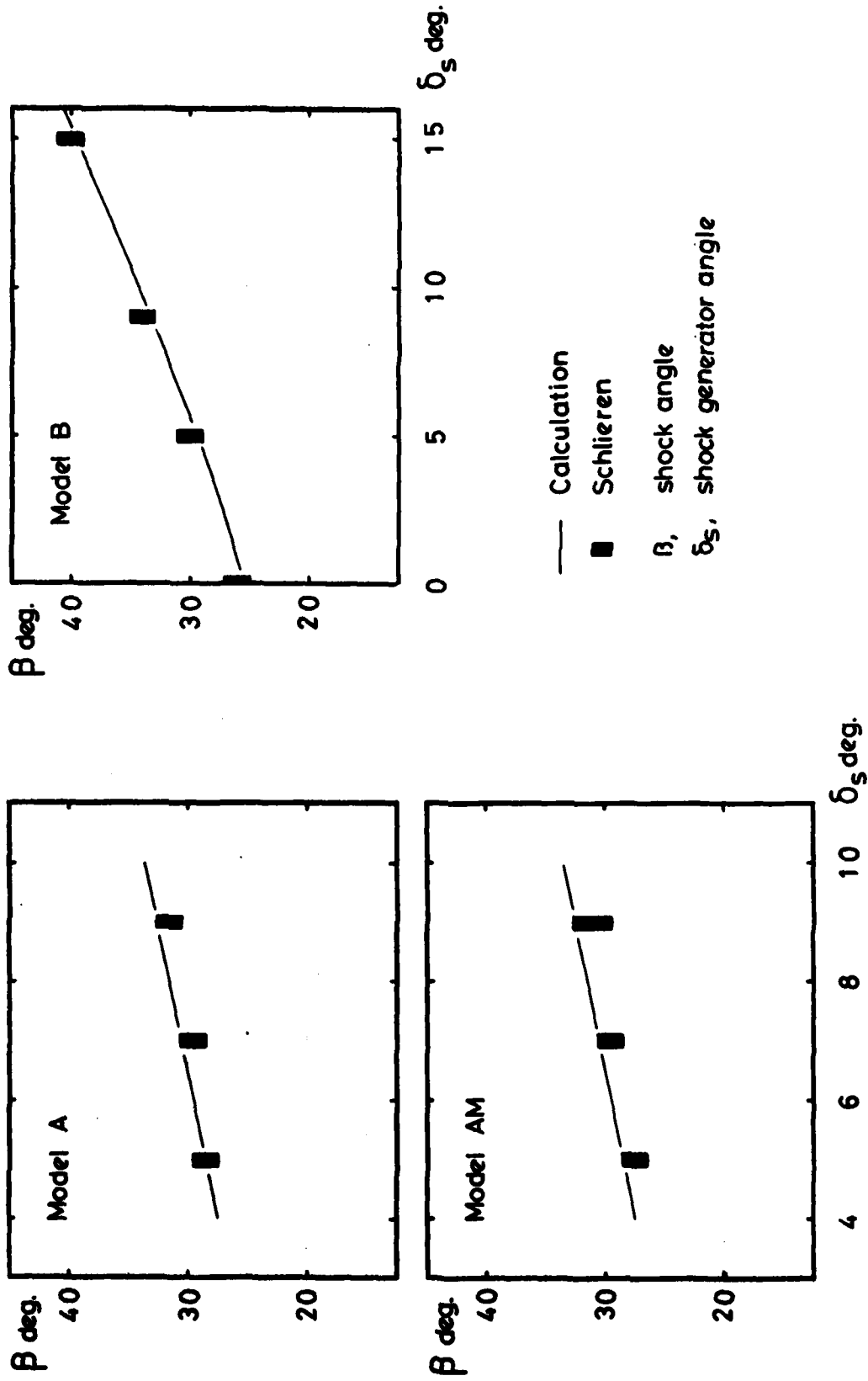
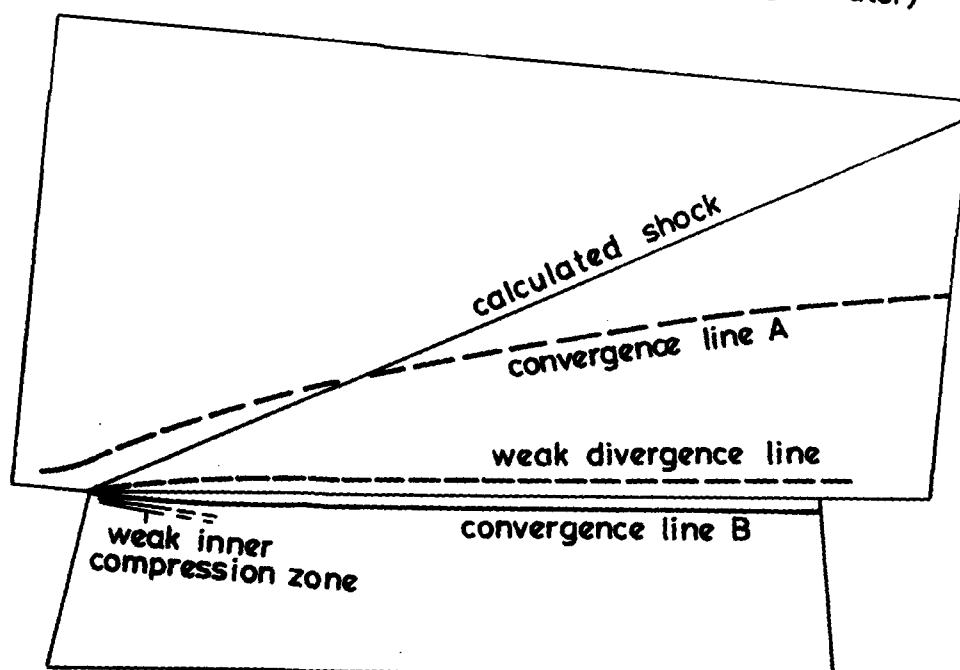
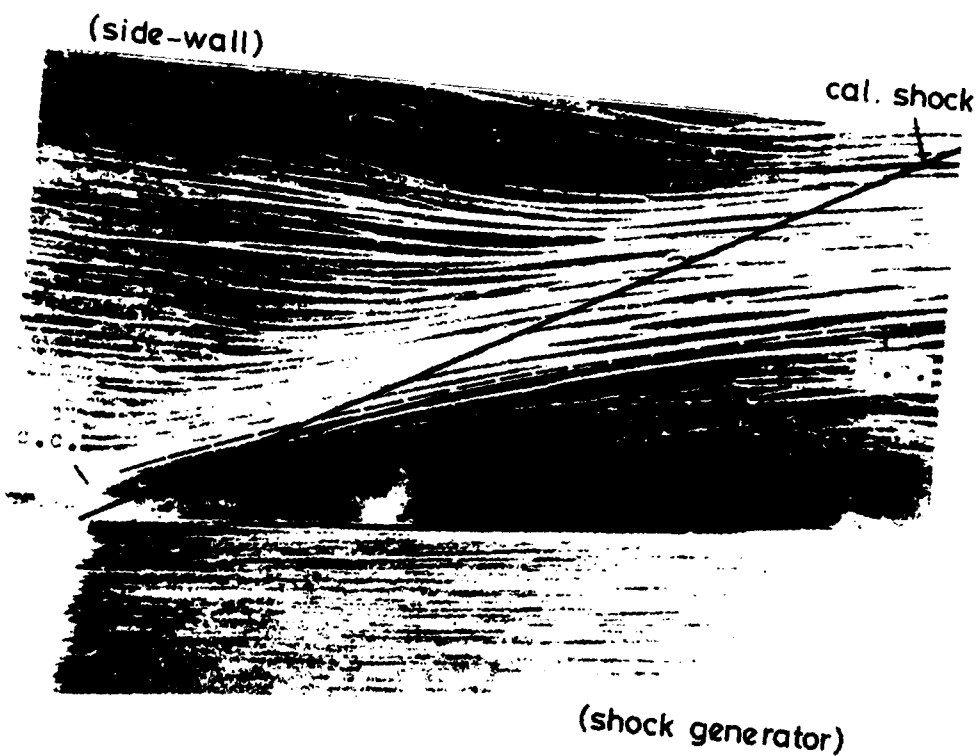
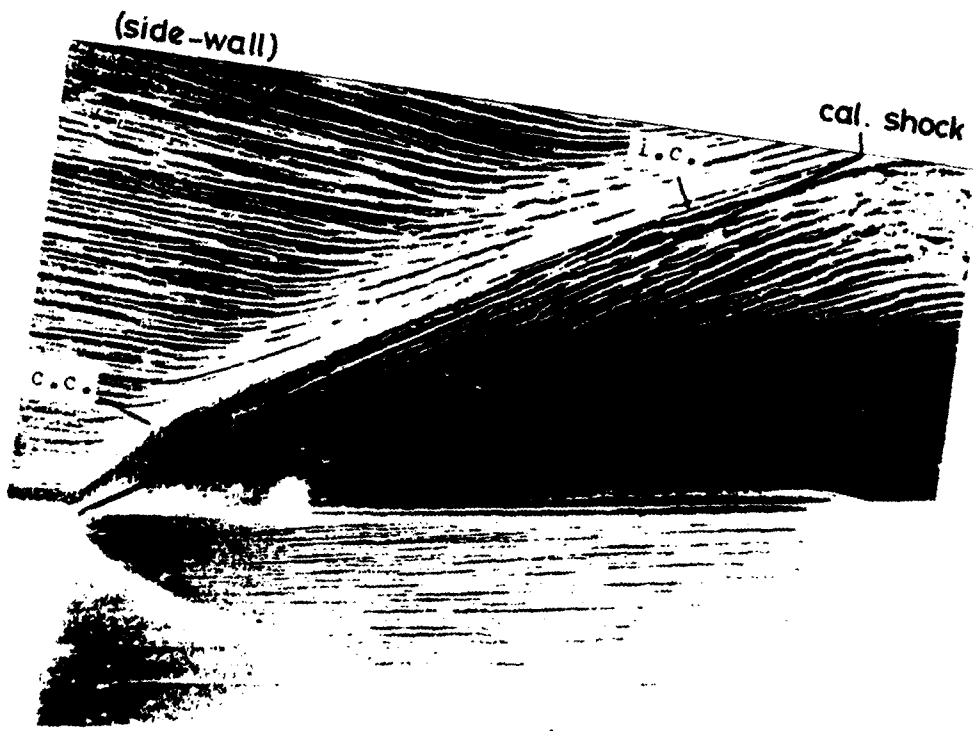


Figure 36. Measured and calculated shock angles.

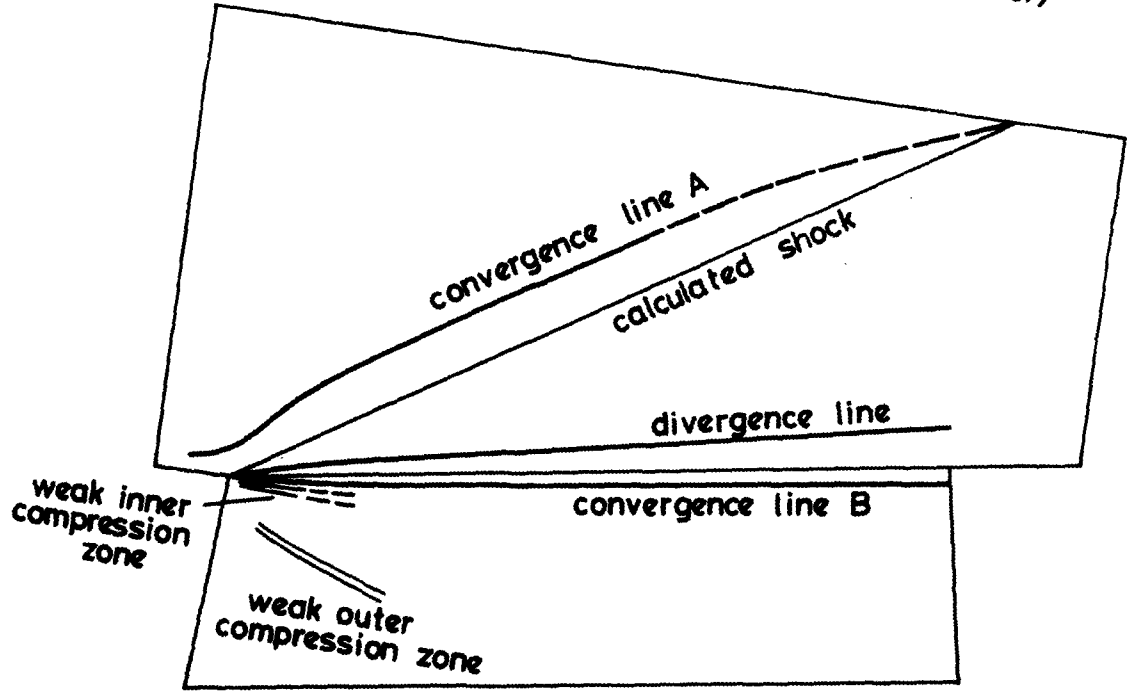


(a) Model A,  $\delta_s = 5^\circ$

Fig. 37 Typical Oil-Flow Patterns

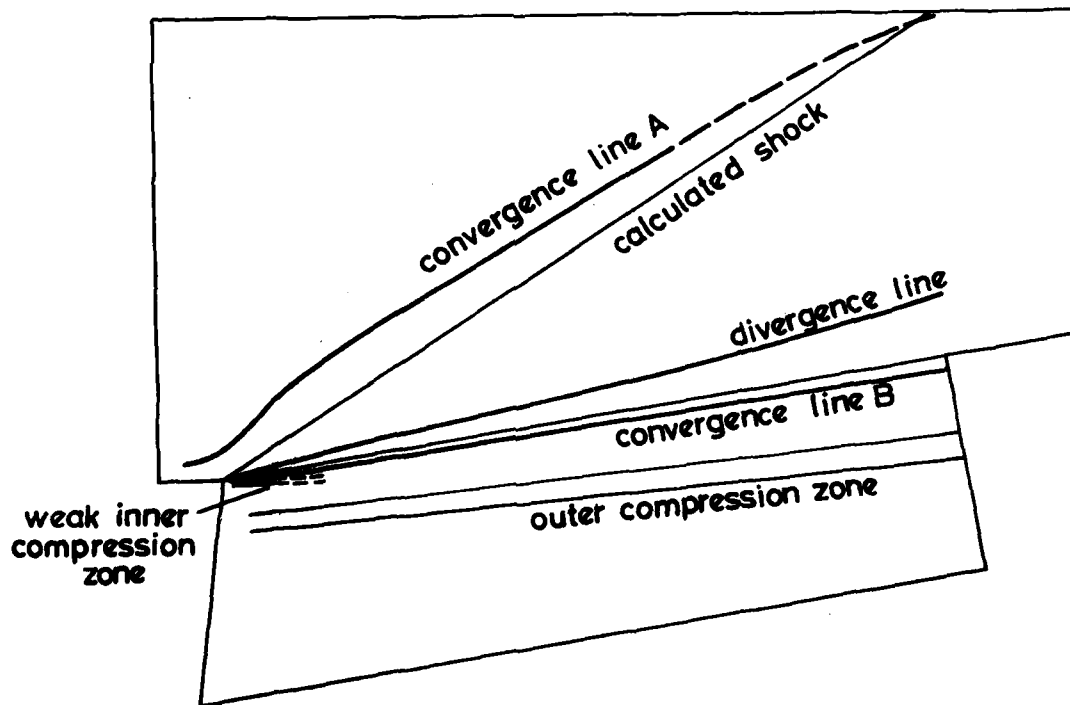
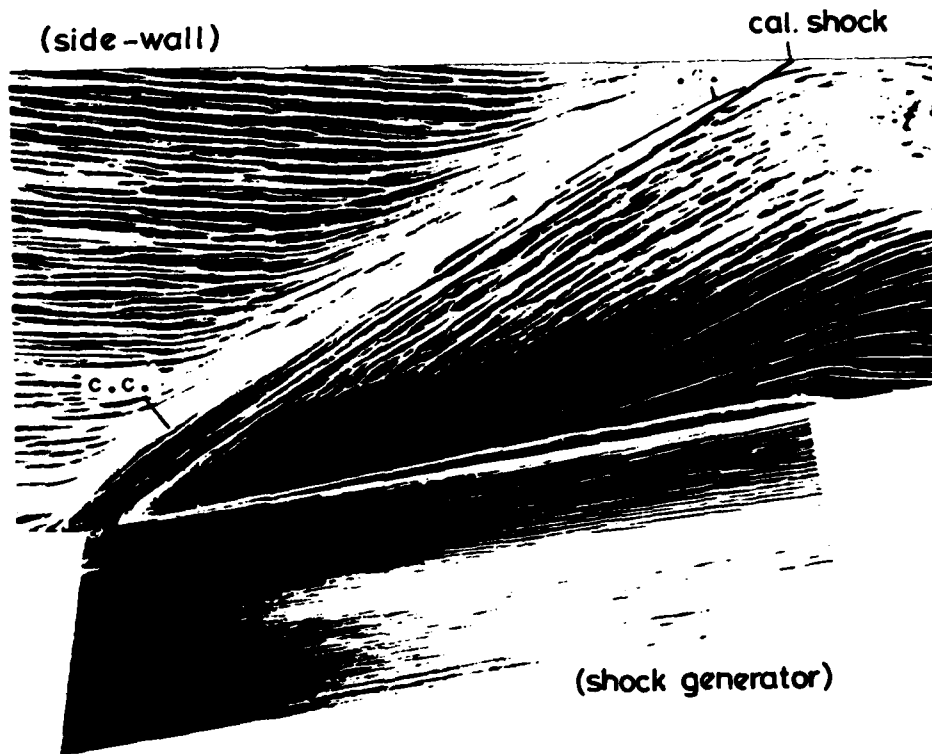


(shock generator)



(b) Model A,  $\delta_s = 9^\circ$

Fig. 37 Contd.



(c) Model AM,  $\delta_s = 9^\circ$

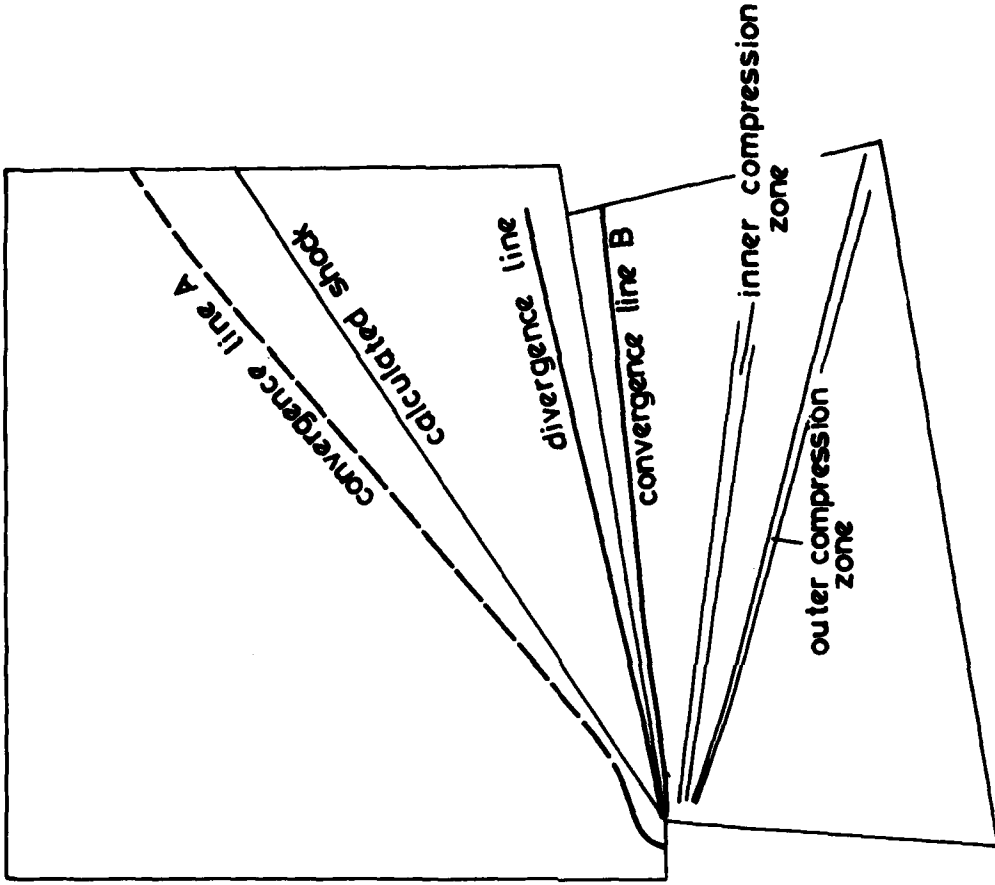
Fig. 37 Contd.

(side-wall)



cal. shock

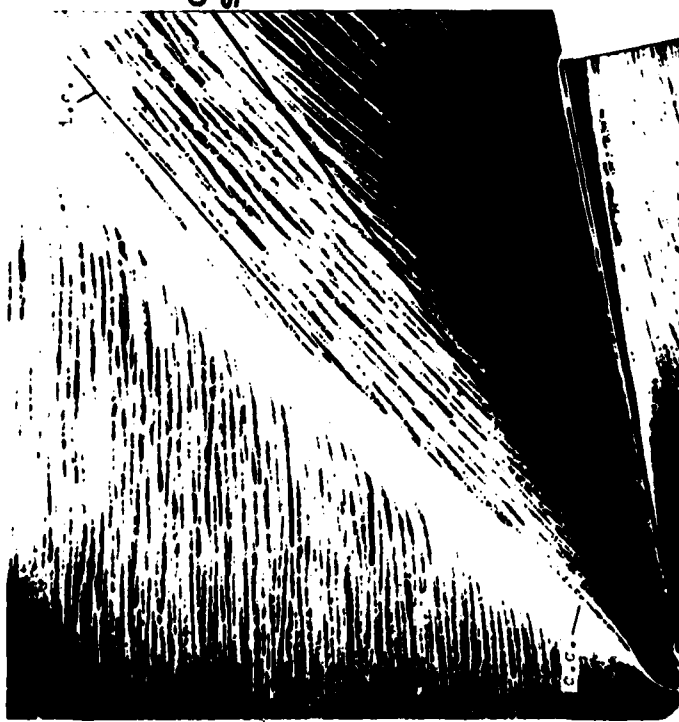
(shock generator)



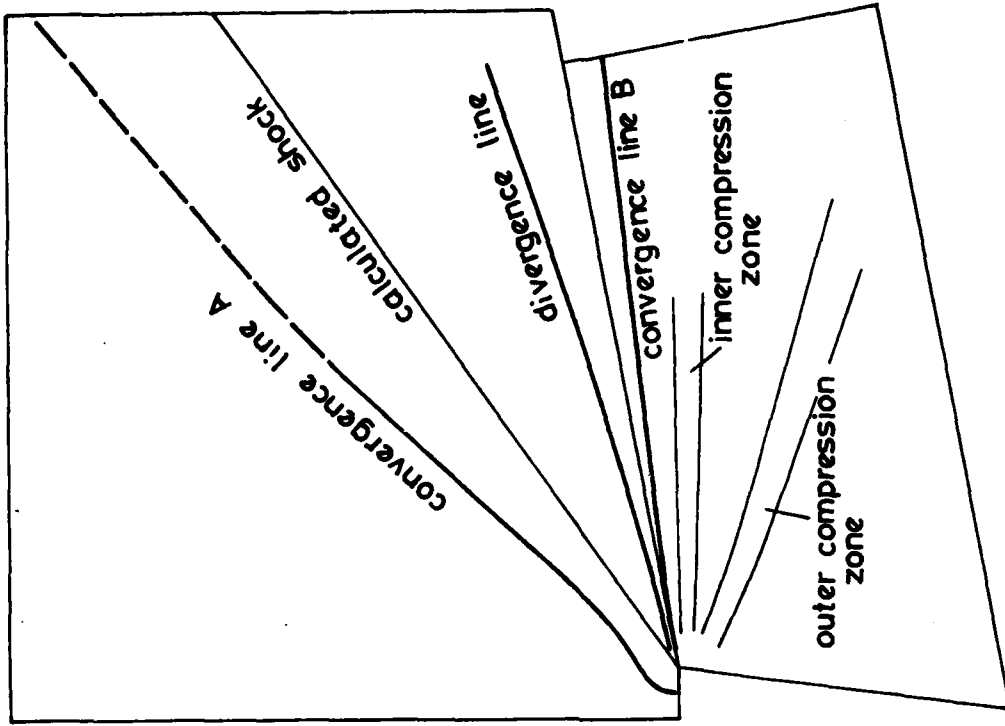
(d) Model B,  $\delta_s = 10^\circ$

Fig. 37 Contd.

(side-wall)



cal.  
shock



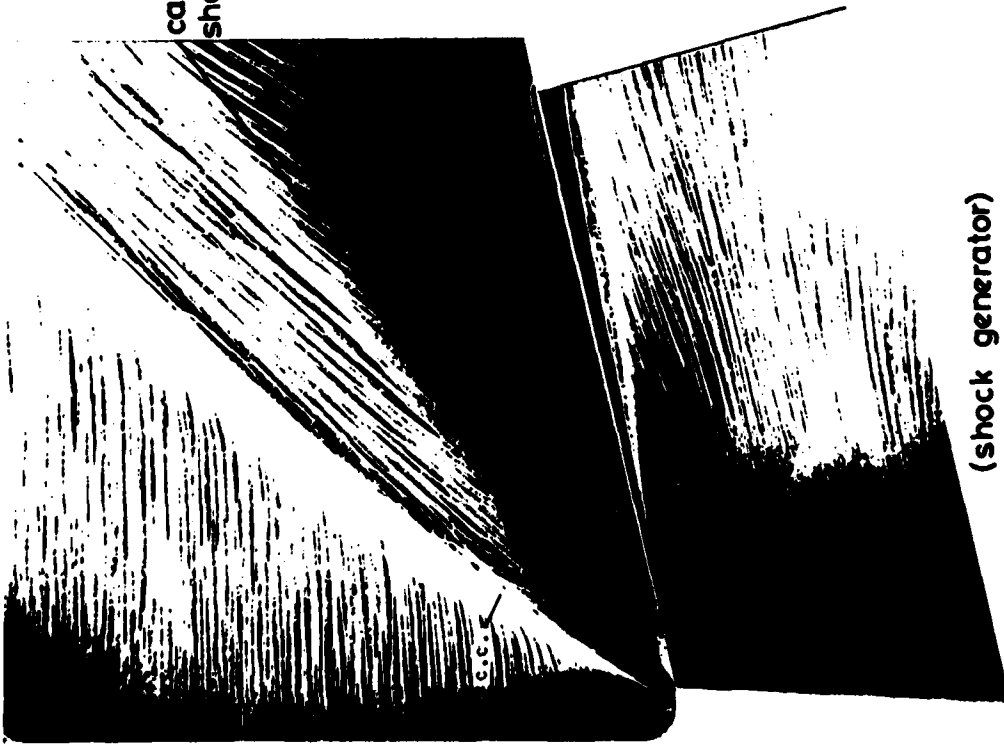
(shock generator)



(e) Model B,  $\delta_s = 11^\circ$

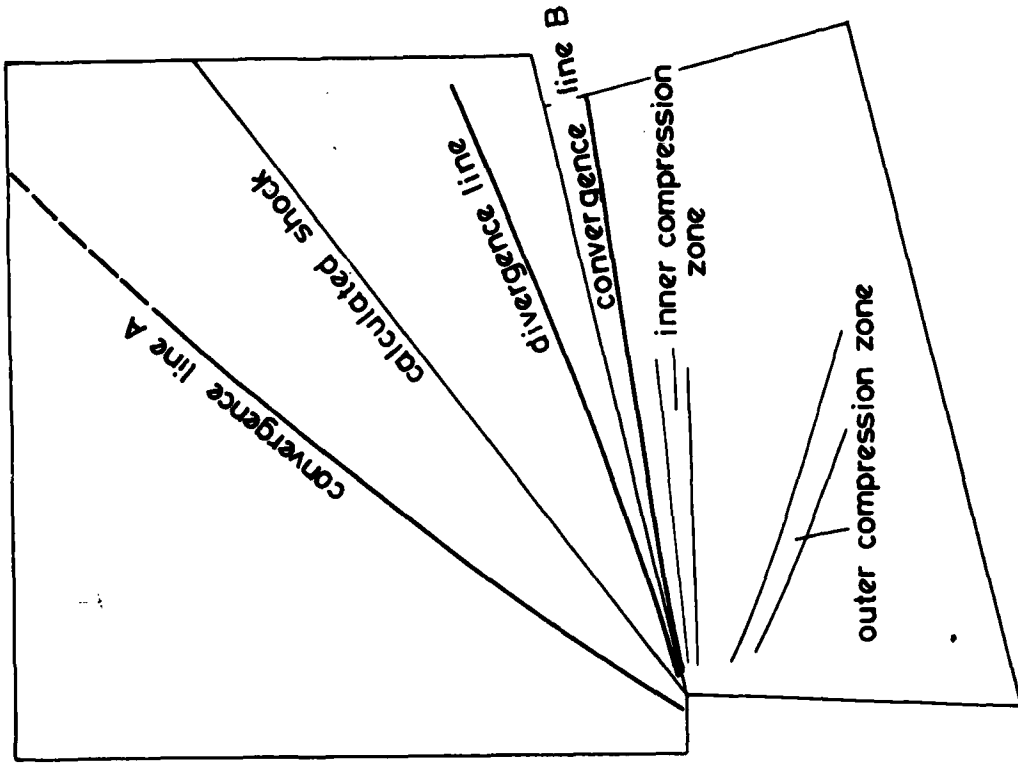
Fig. 37 Contd.

(side-wall)



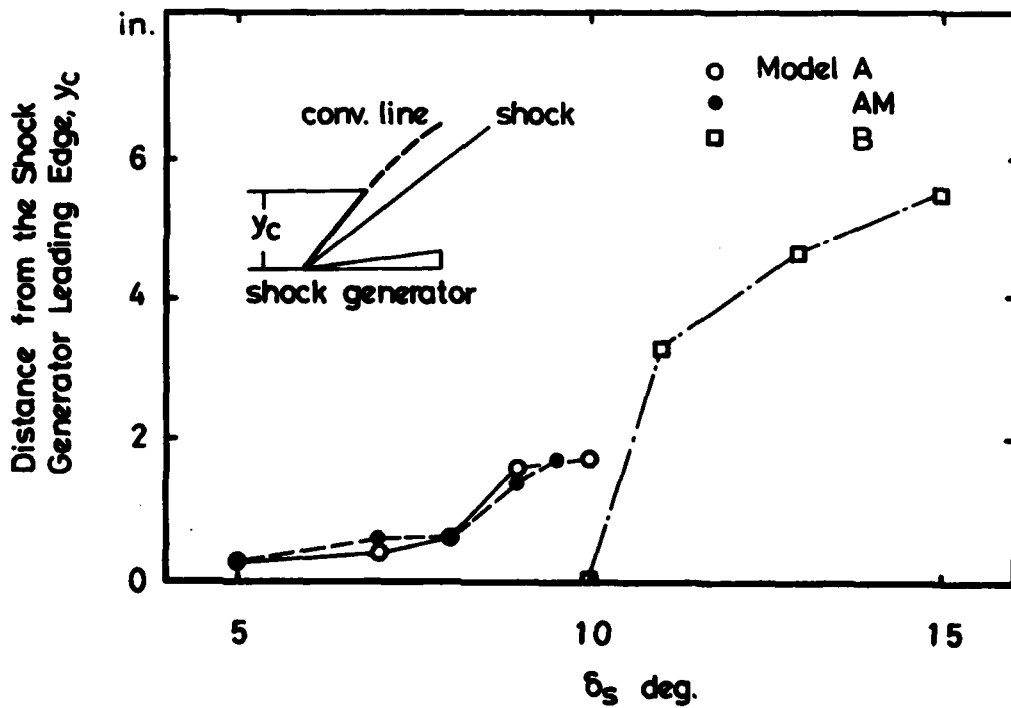
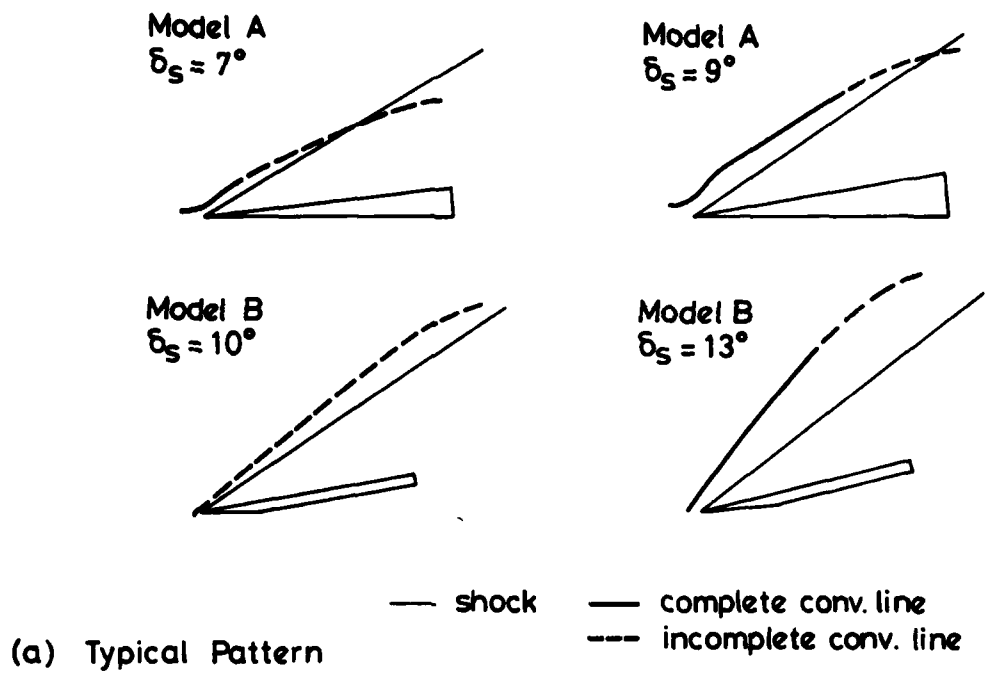
(shock generator)

cal.  
shock



(f) Model B,  $\delta_s = 13^\circ$

Fig. 37 Contd.



(b) Growth of Convergence Line

Figure 38. Convergence lines of side-wall surface flow.

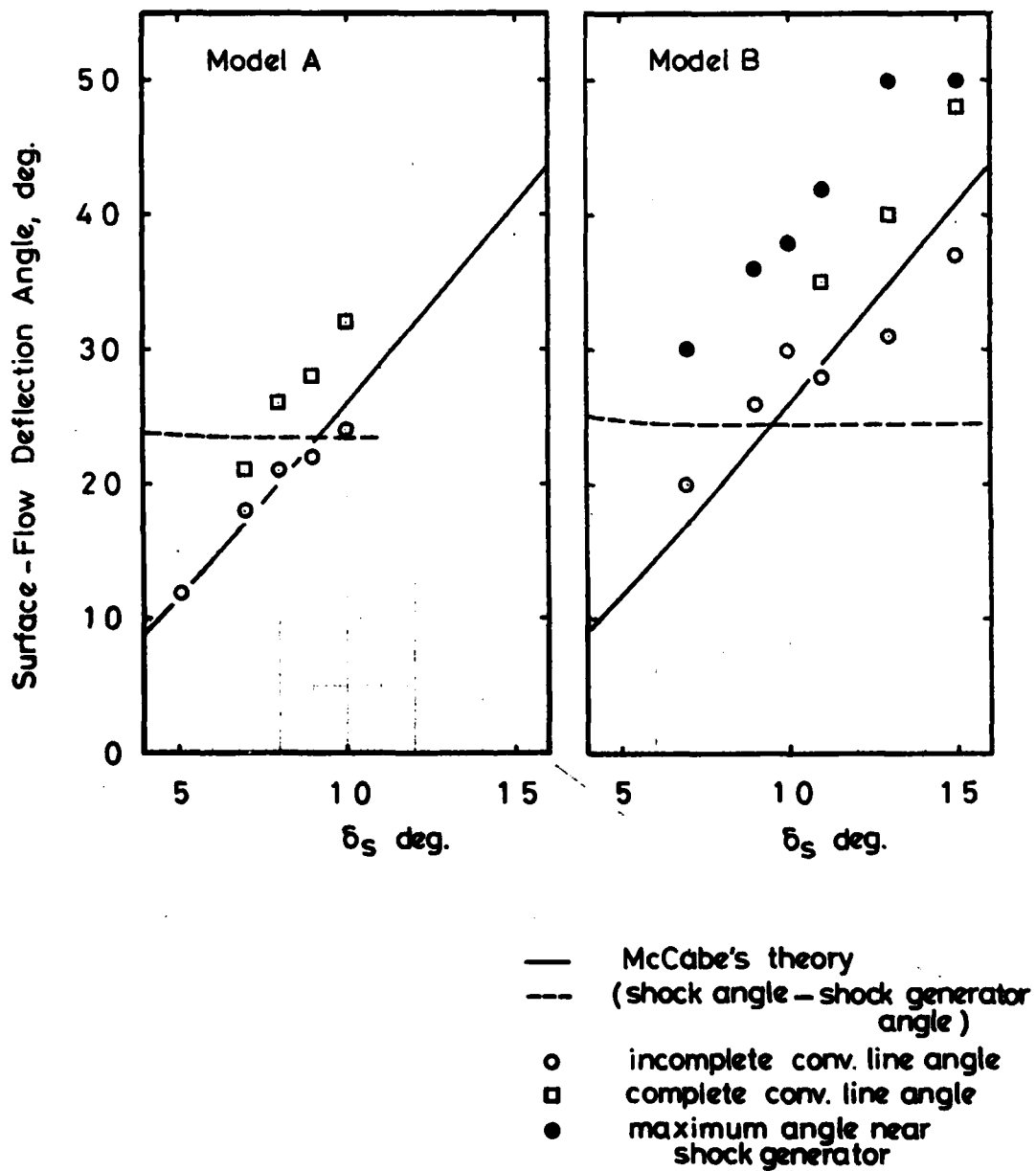
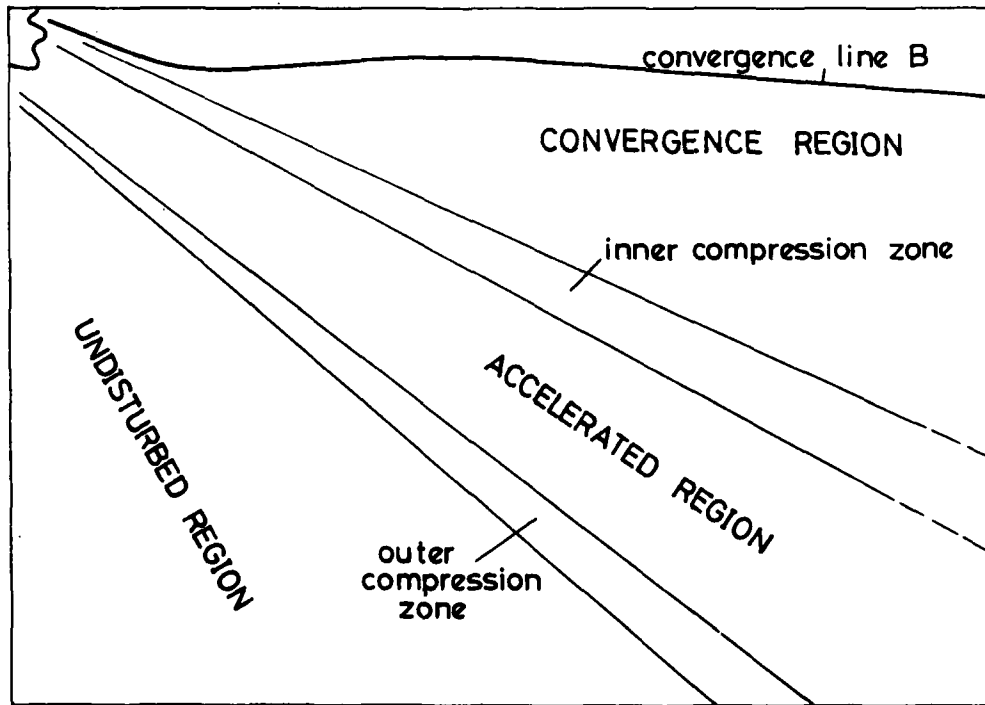
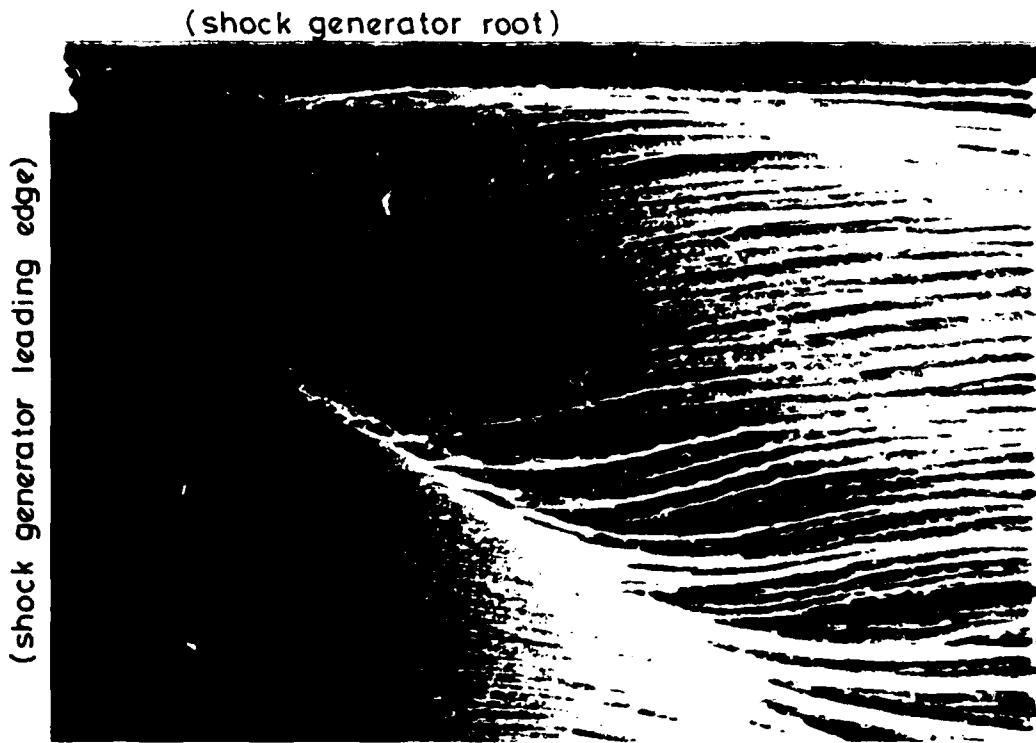


Figure 39. Deflection angles of side-wall surface flow.

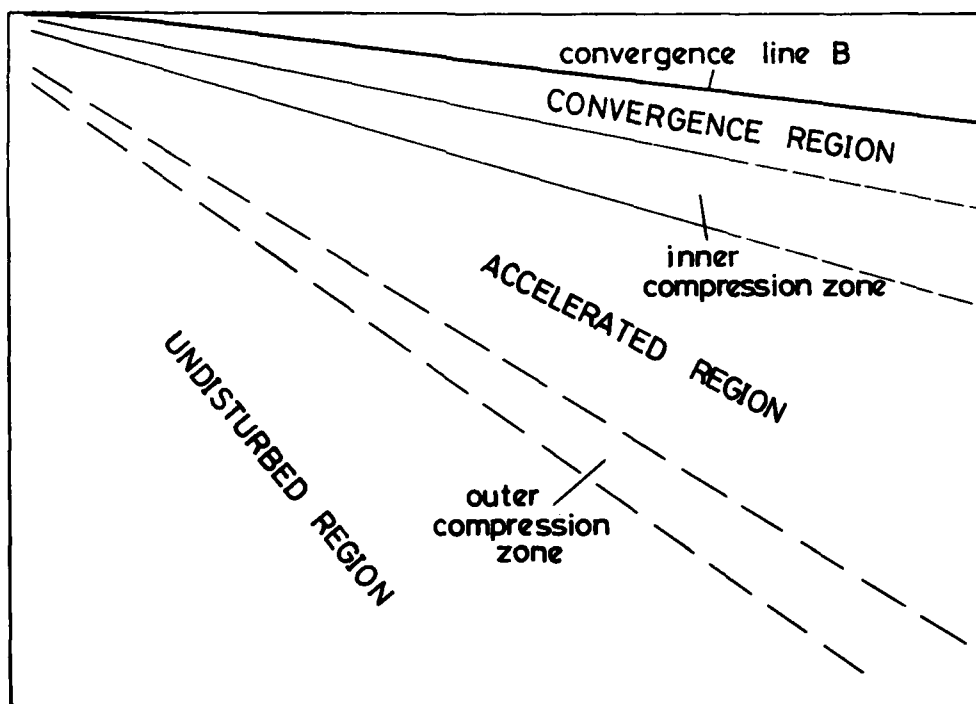
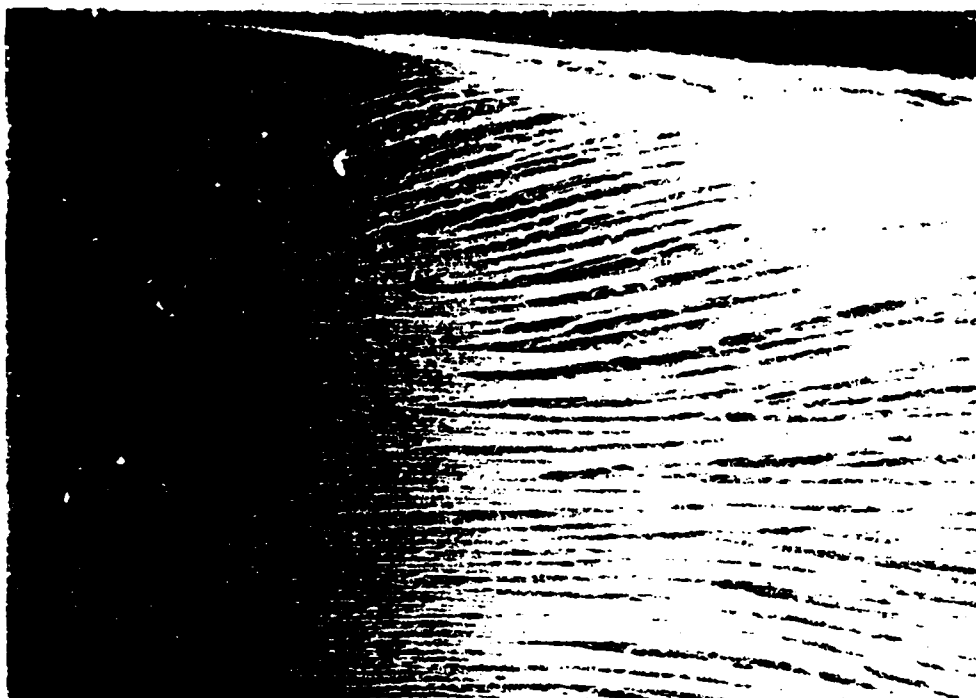


(a) Model B,  $\delta_s = 10^\circ$

Fig.40 Detailed Oil-Flow Patterns on the Shock Generator Surface

(shock generator root)

(shock generator leading edge)



(b) Model B,  $\delta_s = 13^\circ$

Fig. 40 Contd.

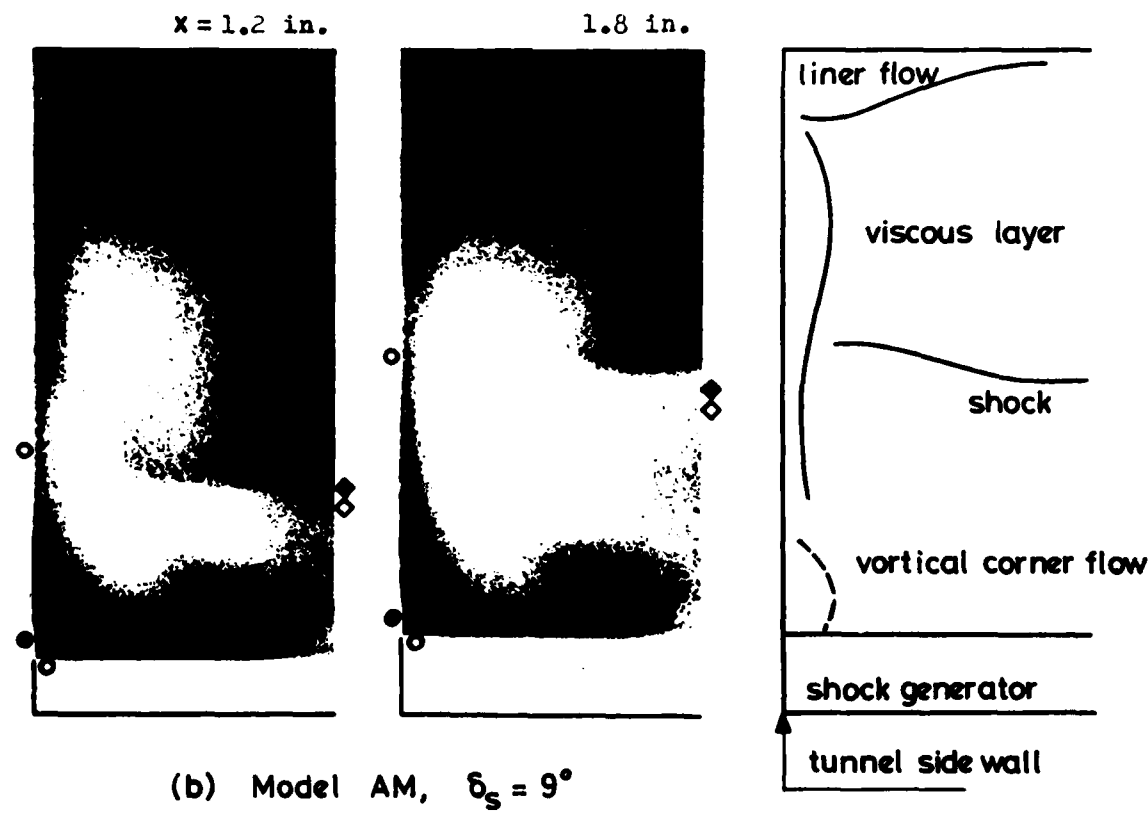
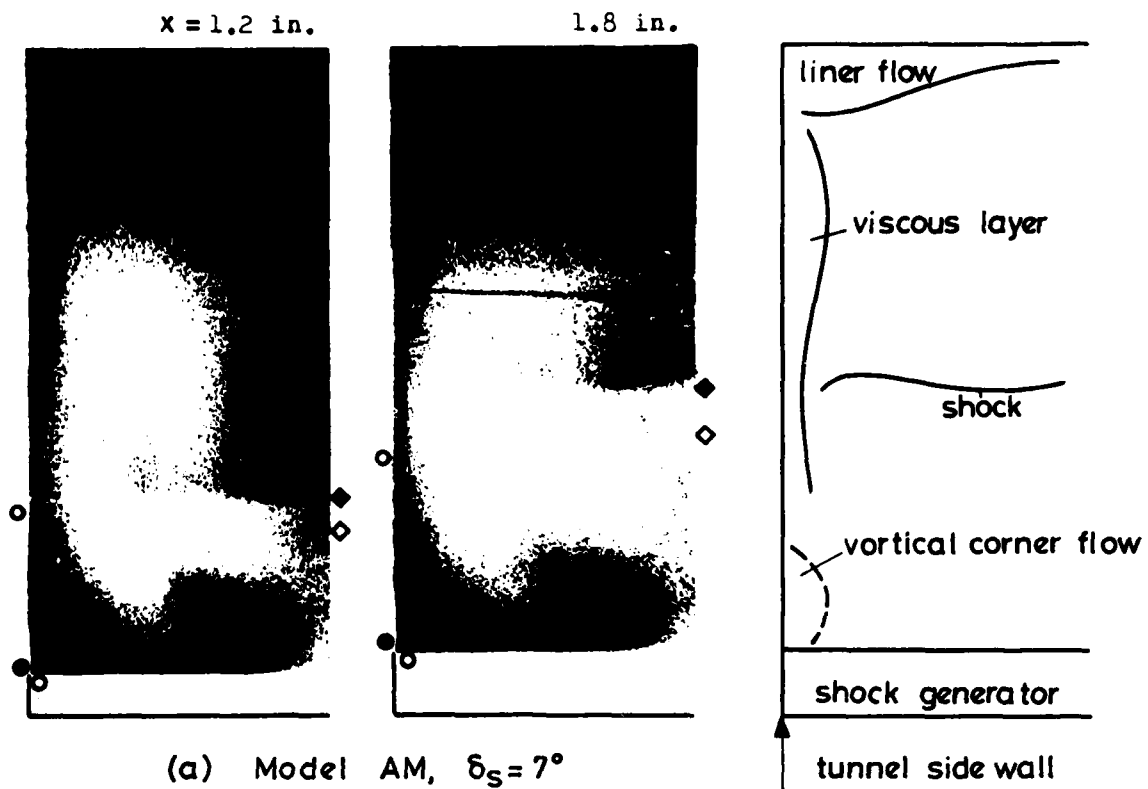


Fig. 41 Typical Vapour-Screen Pictures

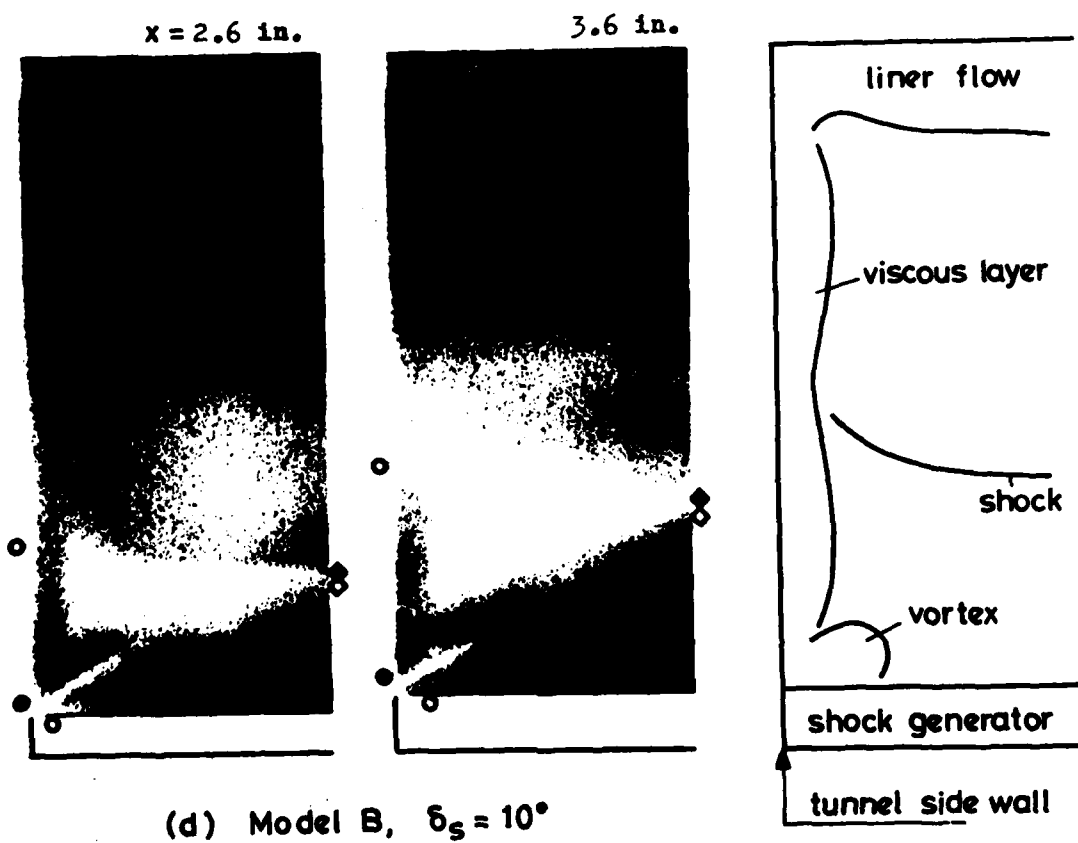
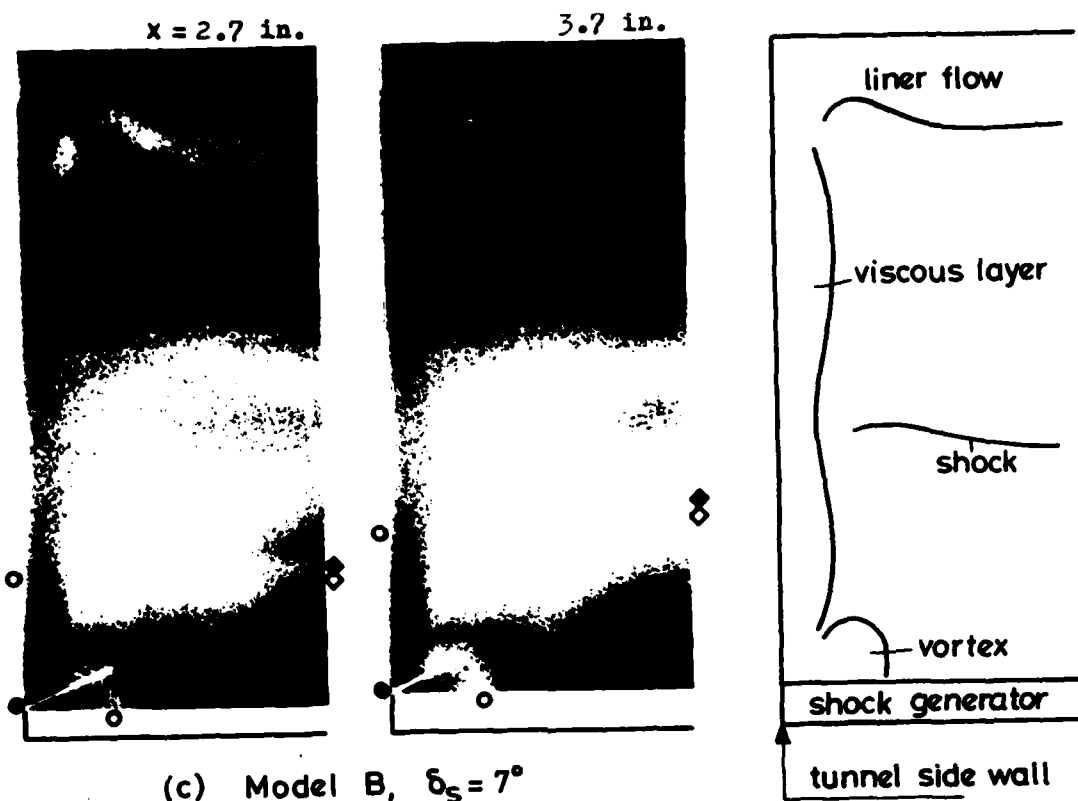
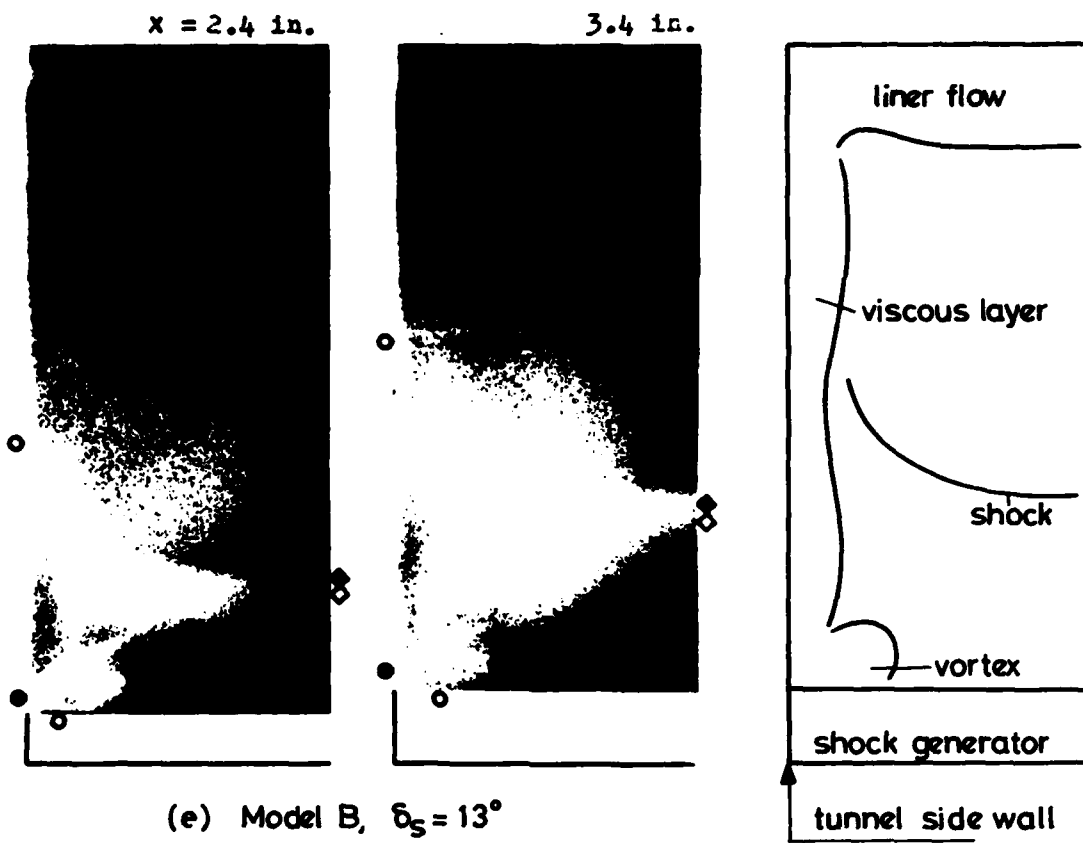


Fig. 41 Contd.



(e) Model B,  $\delta_s = 13^\circ$

Fig.41 Contd.

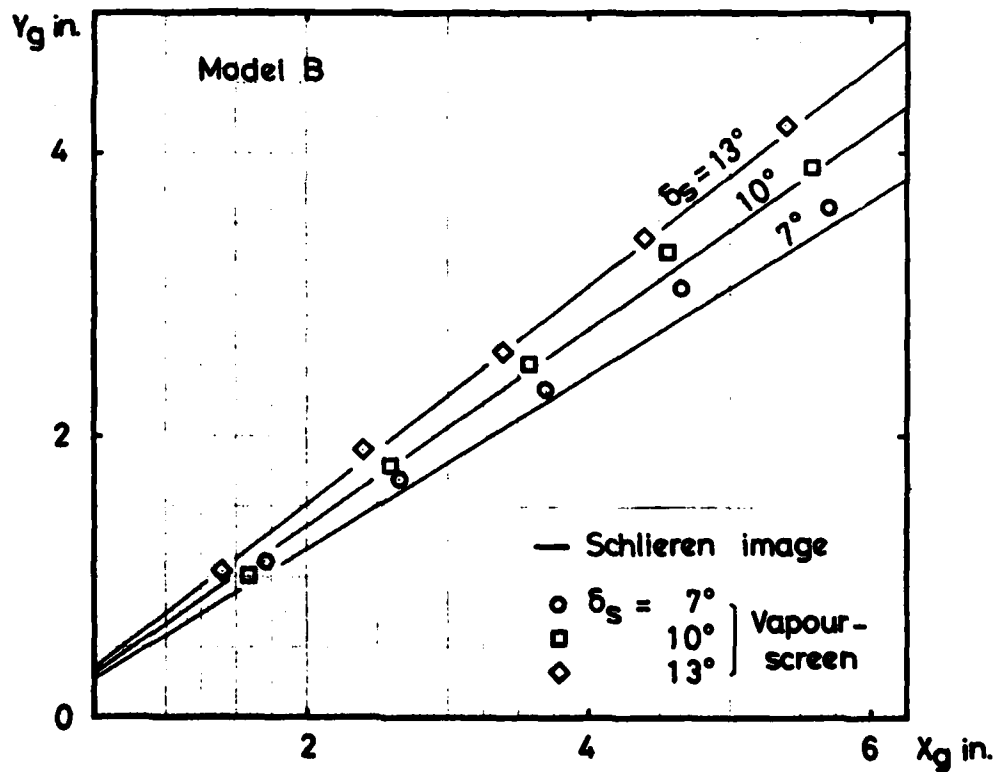
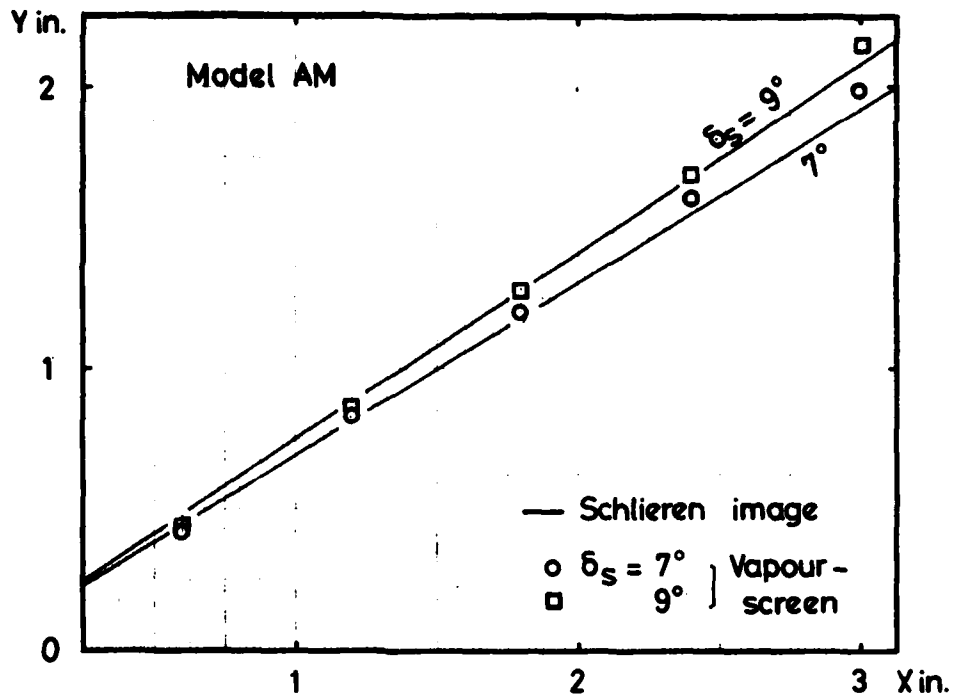


Figure 42. Shock locations as measured from the schlieren and vapour-screen pictures.

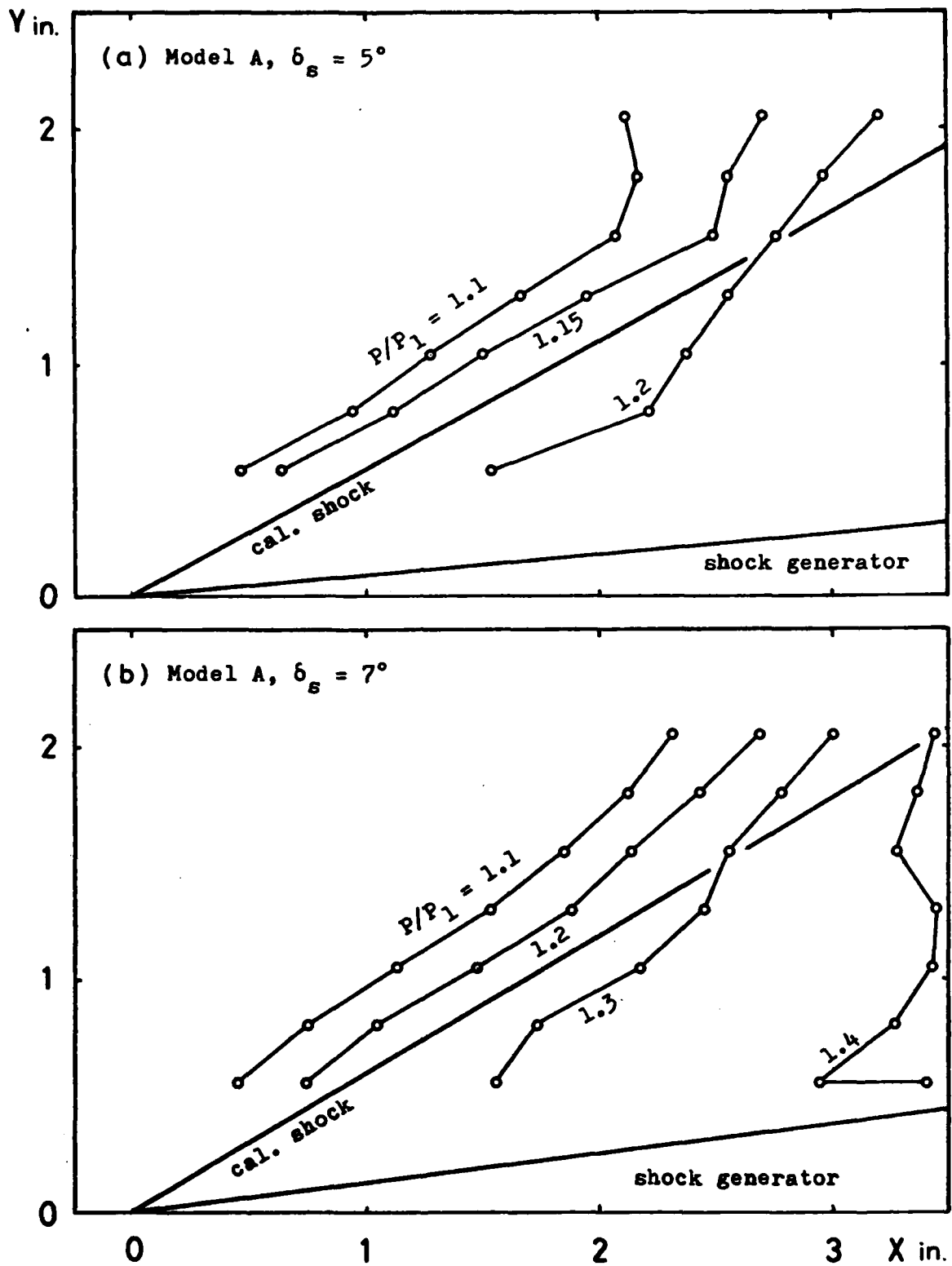


Figure 43. Isobars on the side-wall surface.

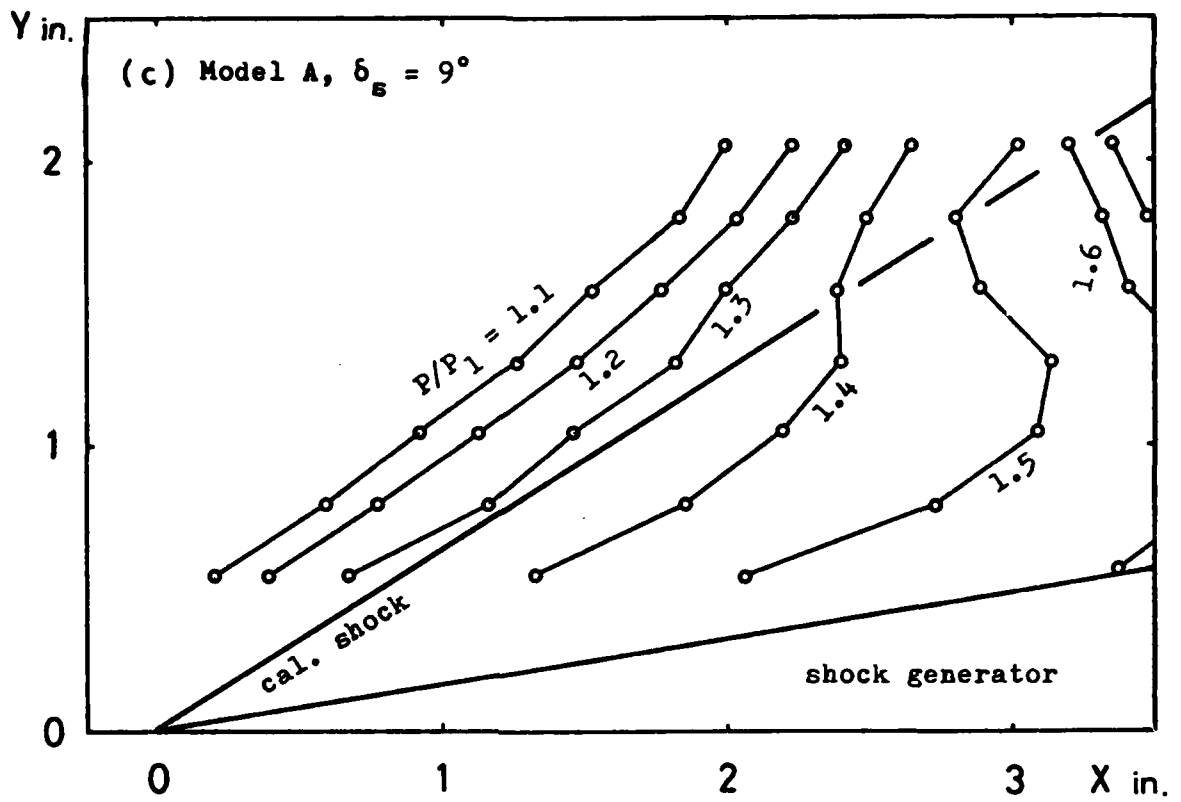


Figure 43. Isobars on the side-wall surface

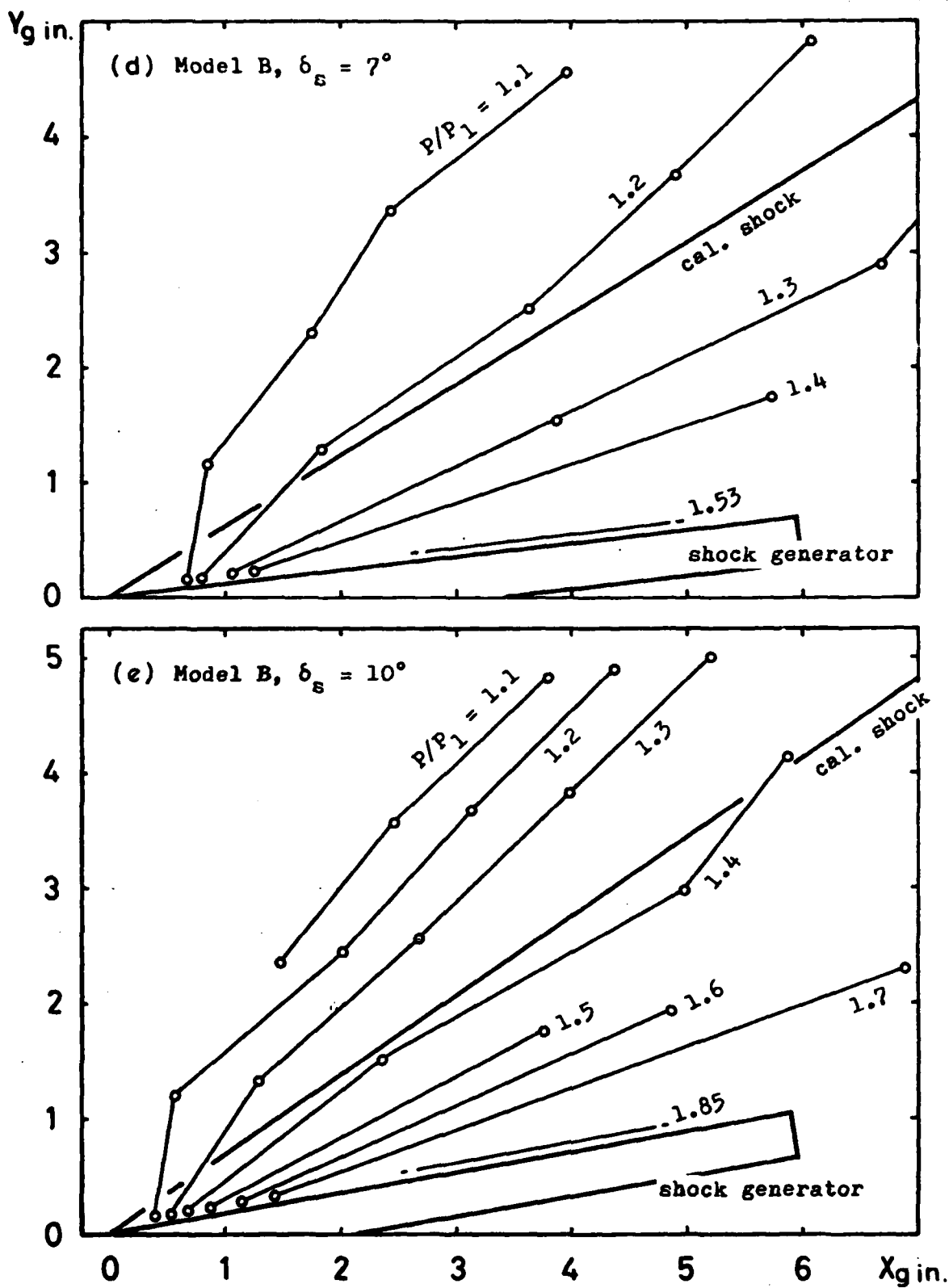


Figure 43. Isobars on the side-wall surface.

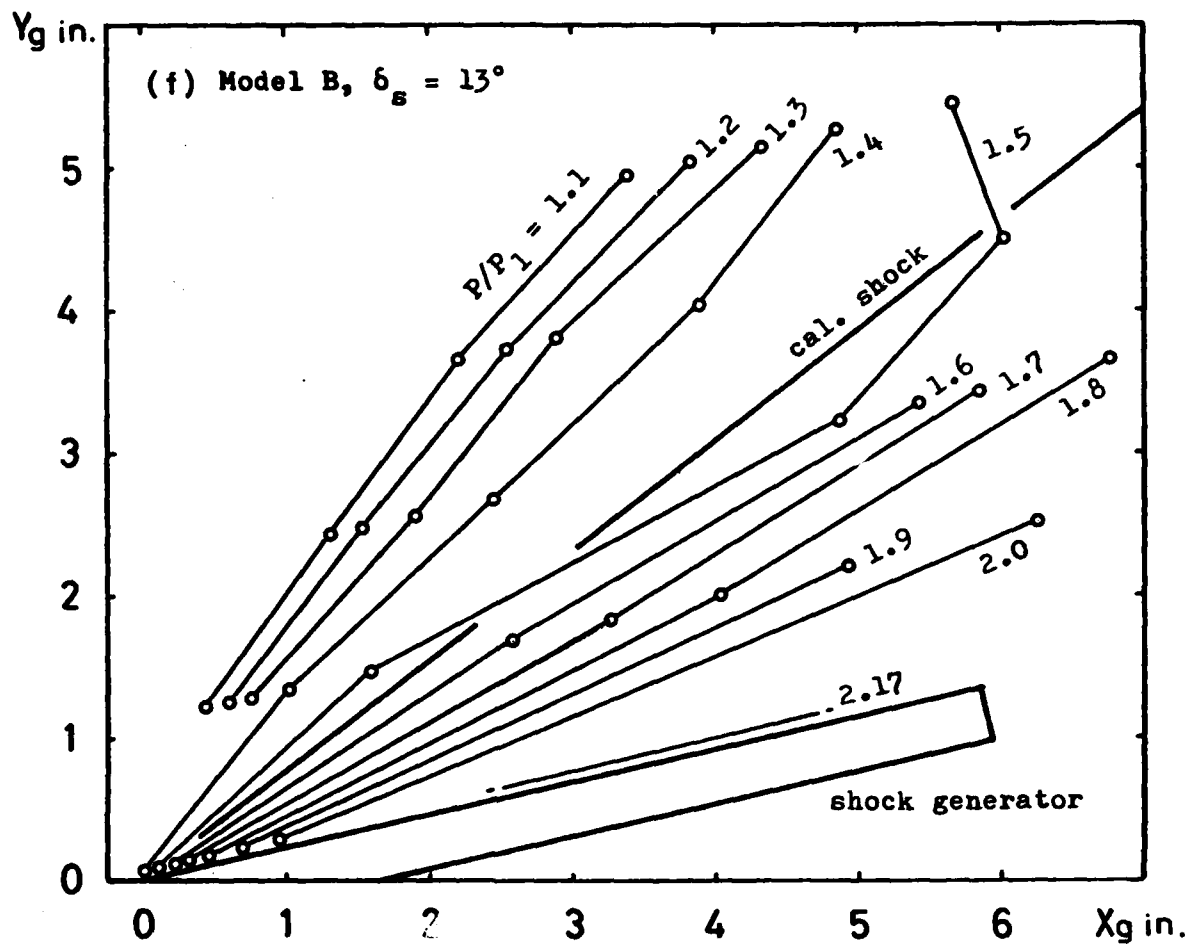
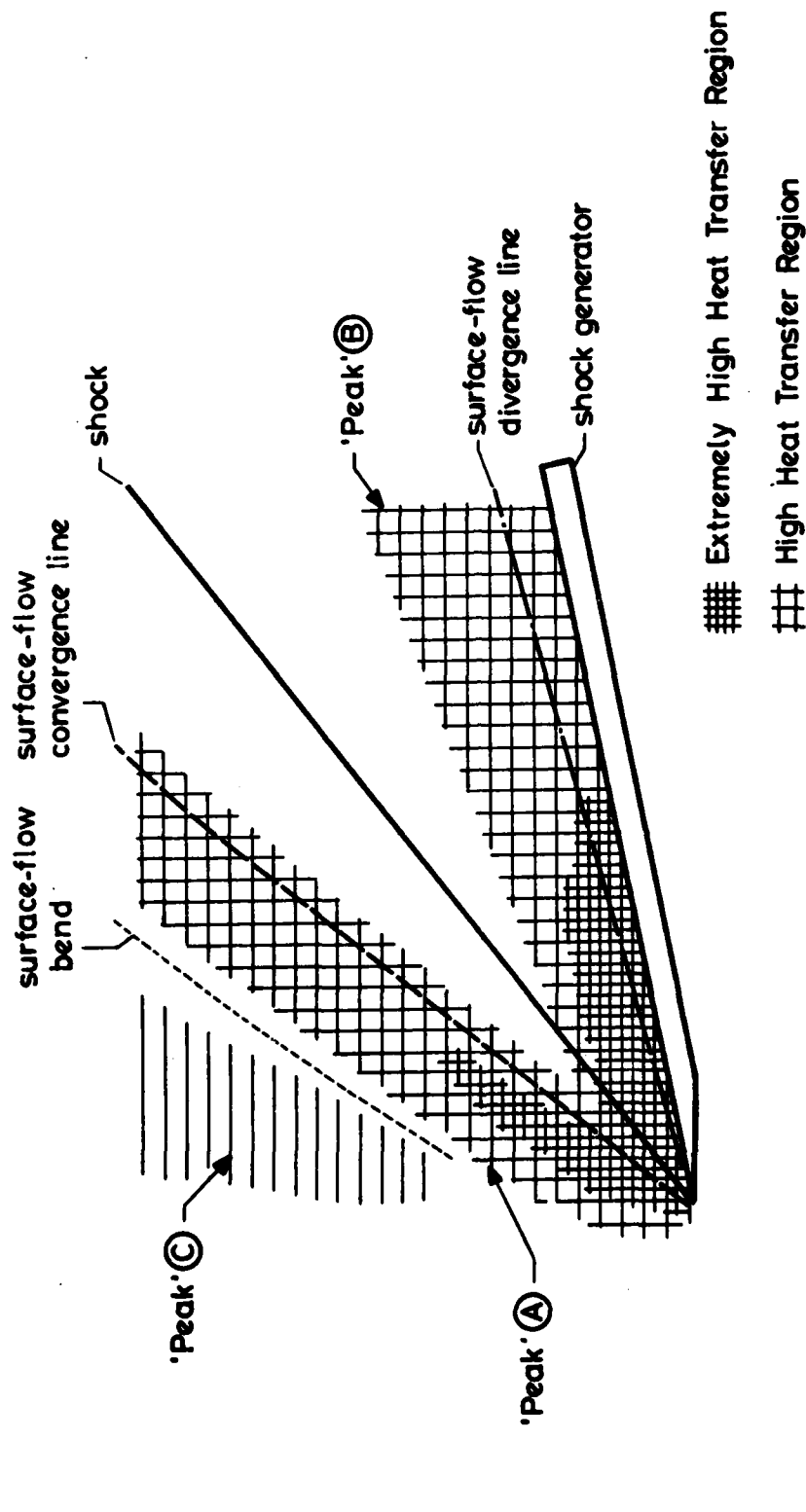


Figure 43. Isobars on the side-wall surface.



(a) Typical Heat Transfer Pattern

Figure 44. Heat transfer on the side-wall surface.

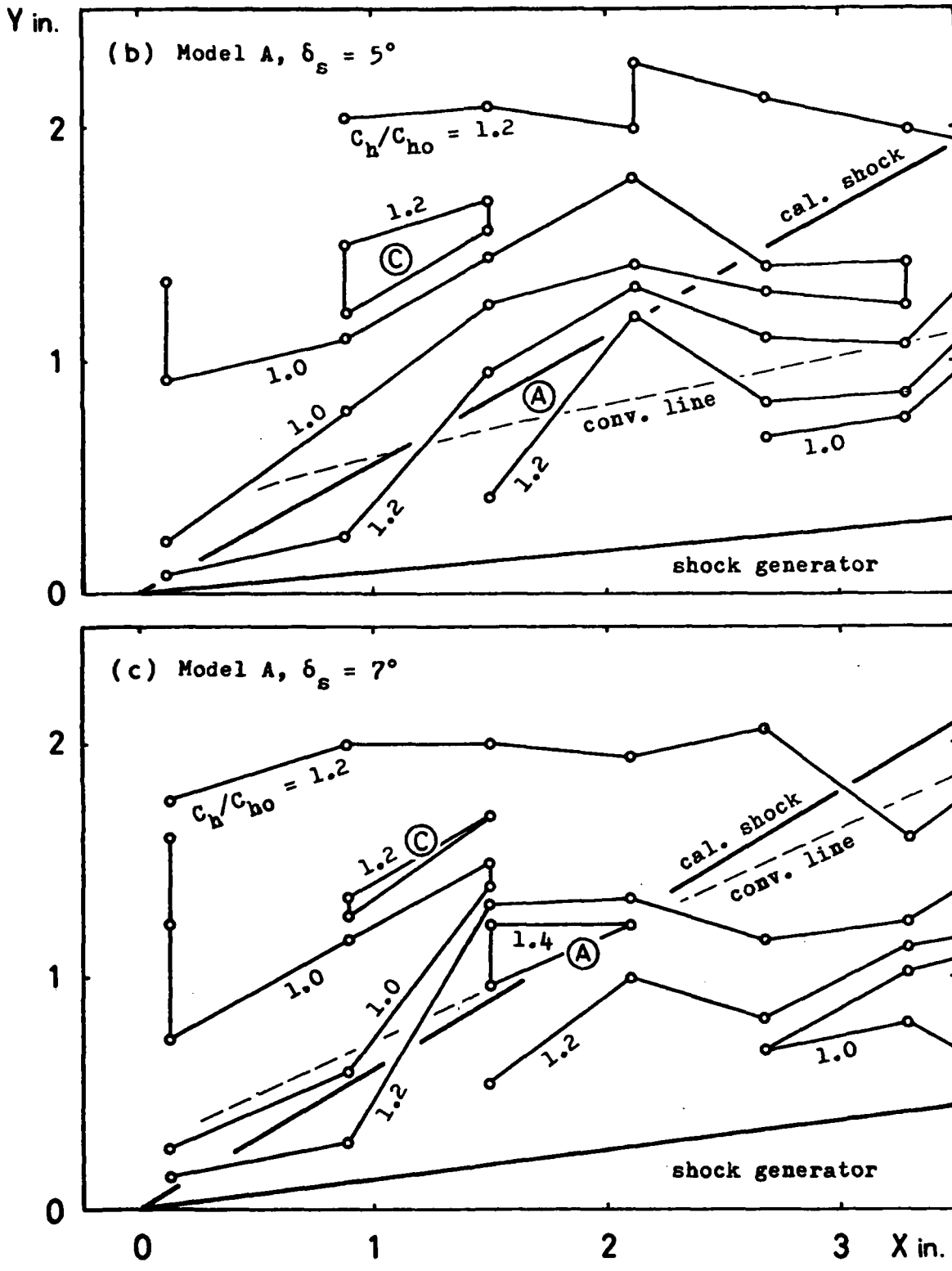


Figure 44. Heat transfer on the side-wall surface.

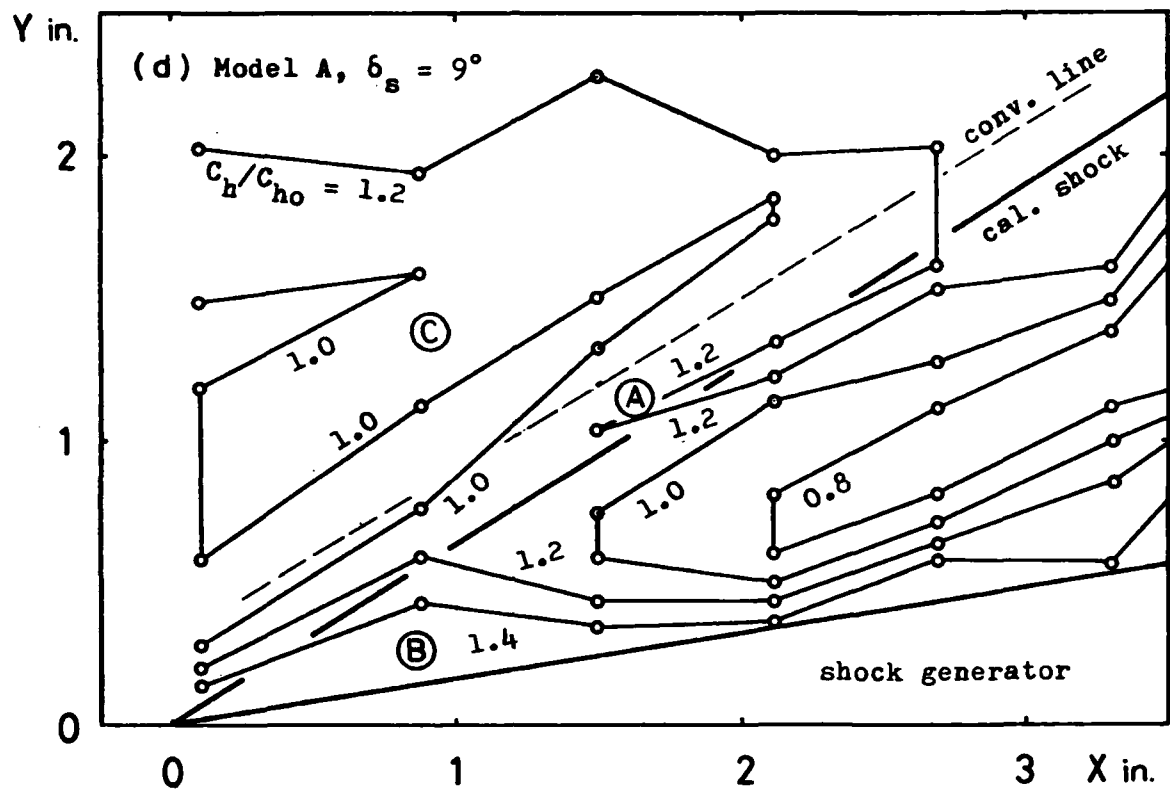


Figure 44. Heat transfer on the side-wall surface.

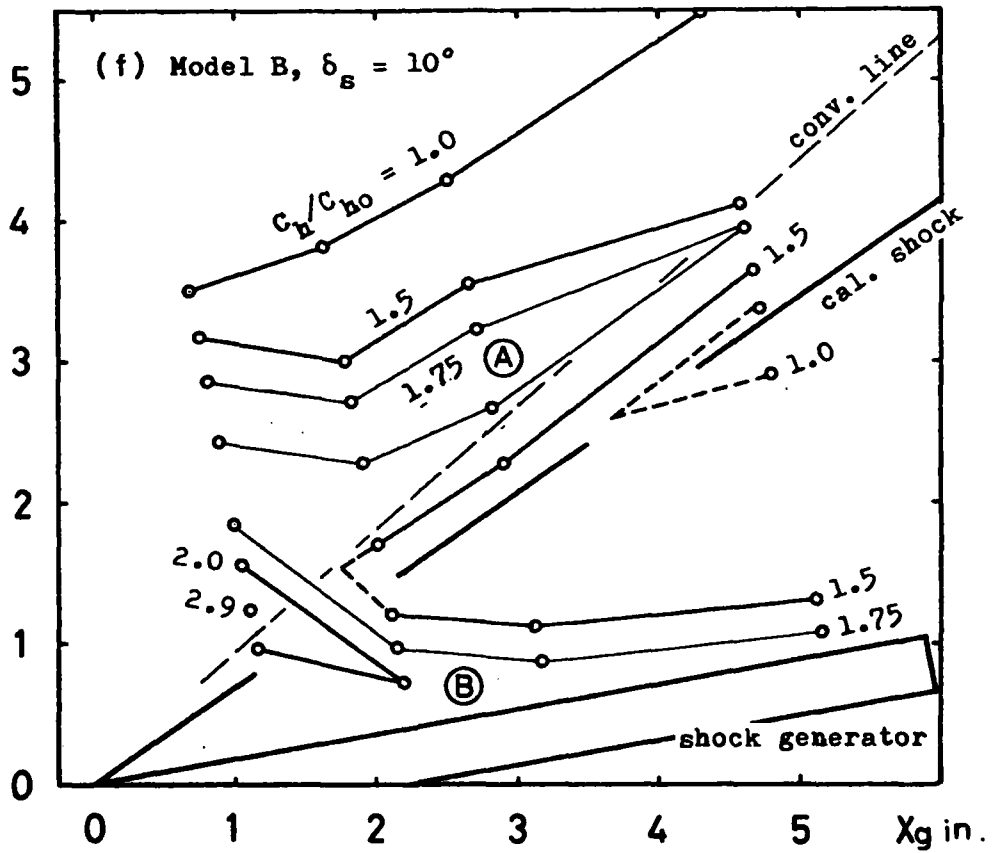
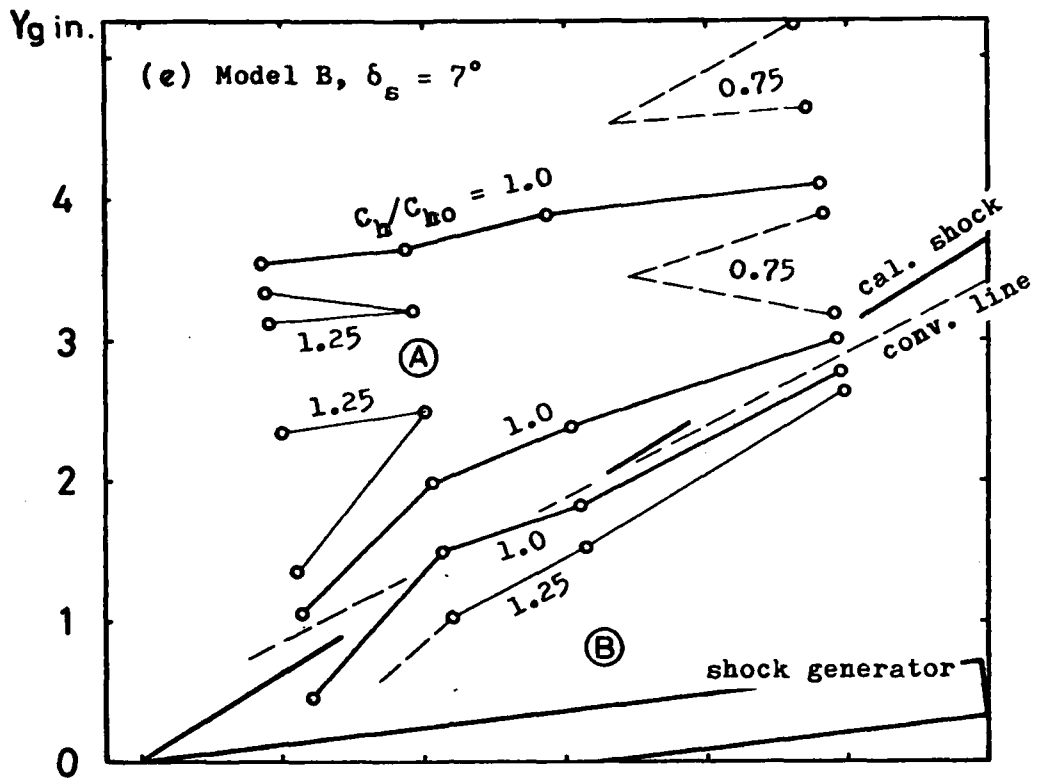


Figure 44. Heat transfer on the side-wall surface.

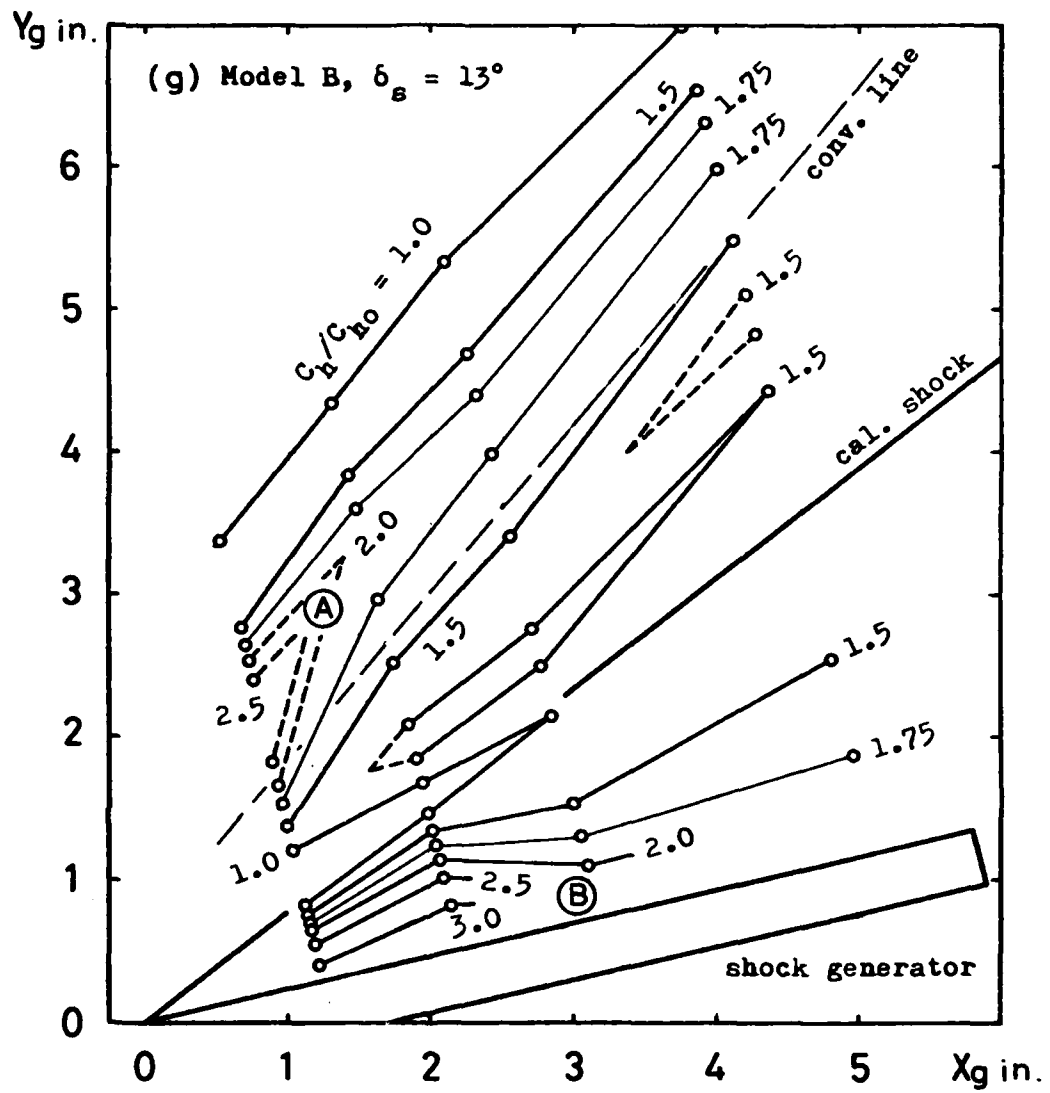
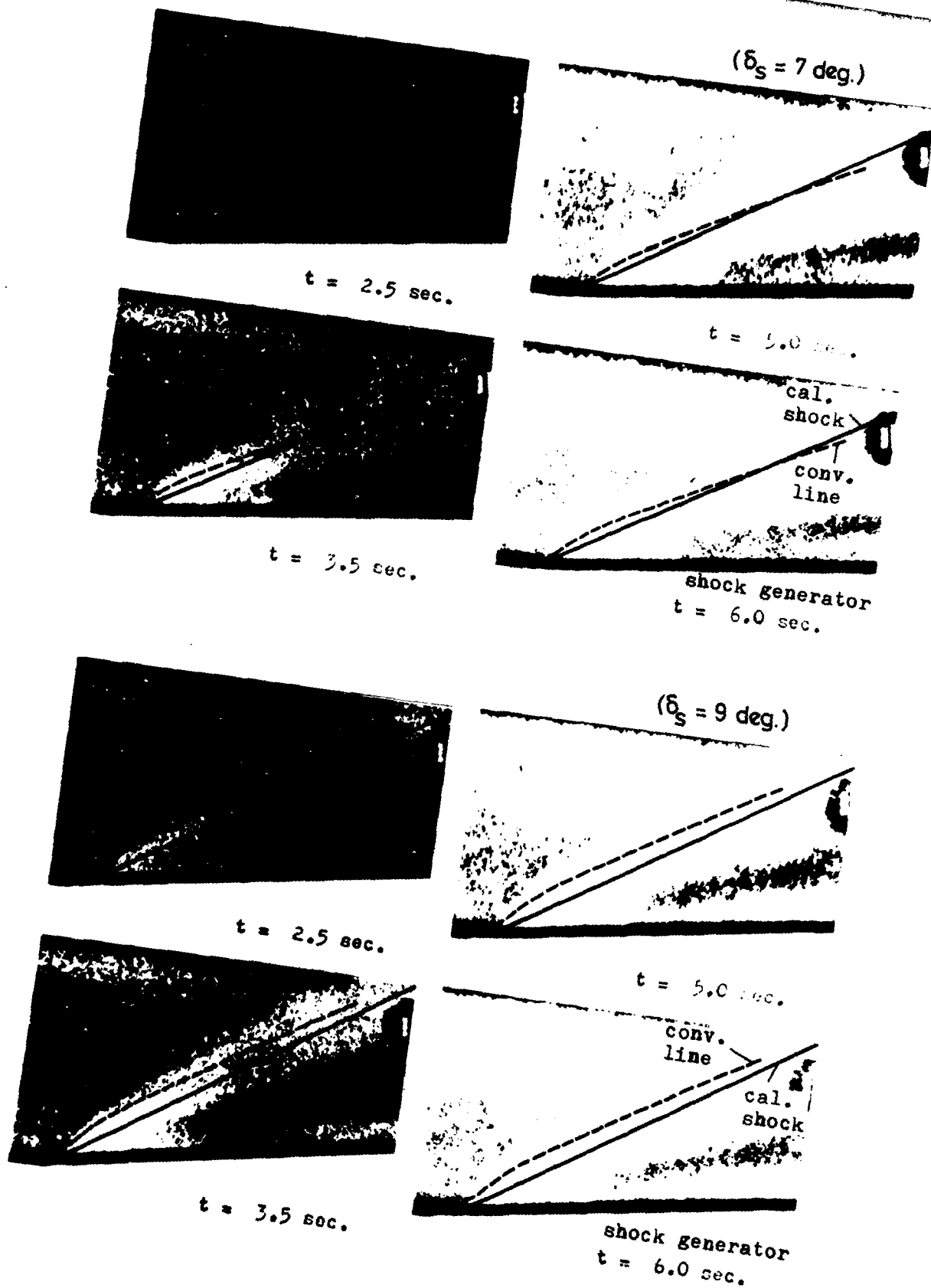


Figure 44. Heat transfer on the side-wall surface.



Blue (dark region) :  $T_w > 20^\circ\text{C}$   
 Yellow (light region):  $T_w < 20^\circ\text{C}$

Figure 45. Typical encapsulated liquid crystal pictures (2.5x2.5 inch tunnel).

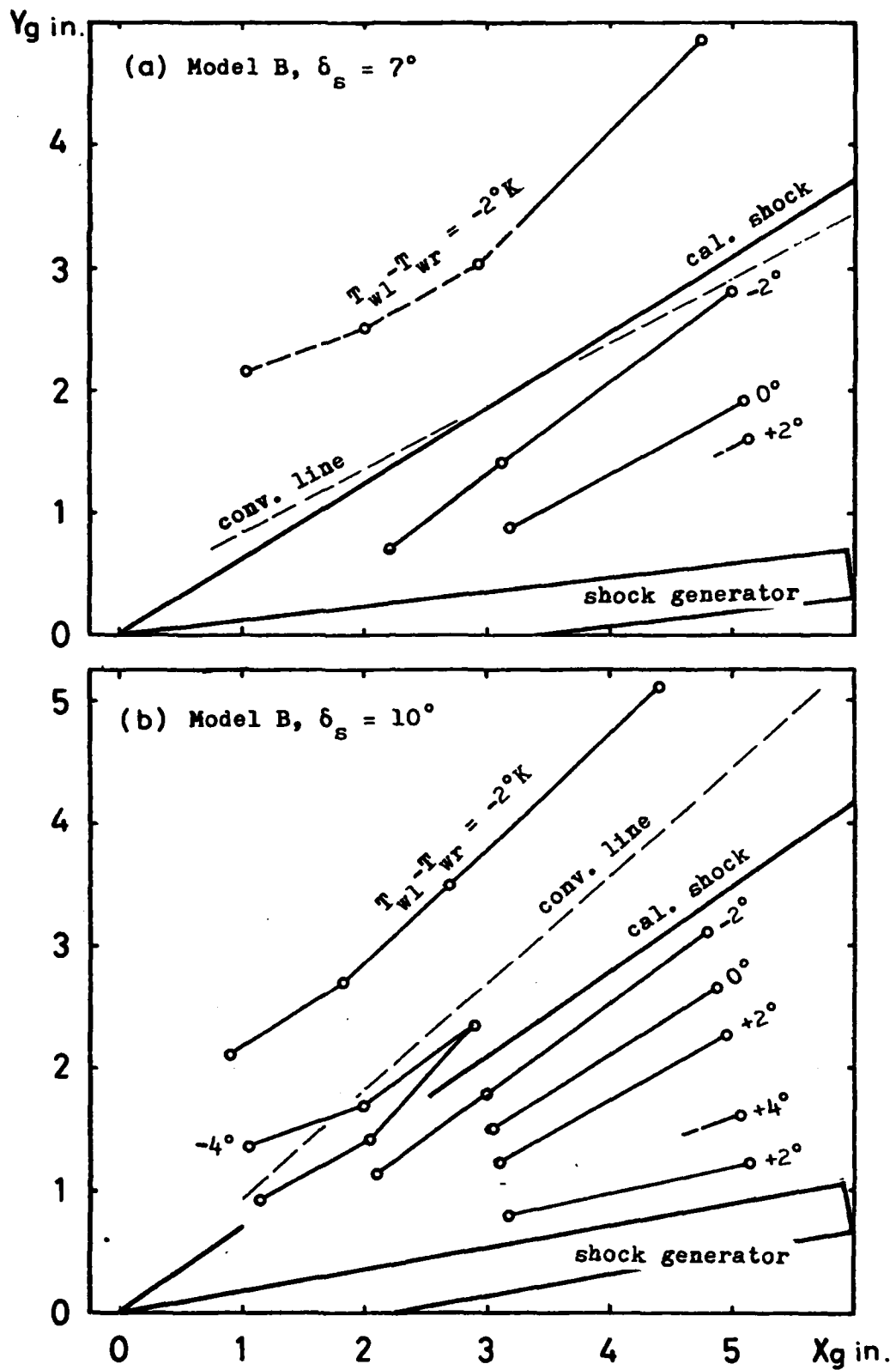


Figure 46. Isothermals on the side-wall surface  
(9 x 9 inch tunnel).

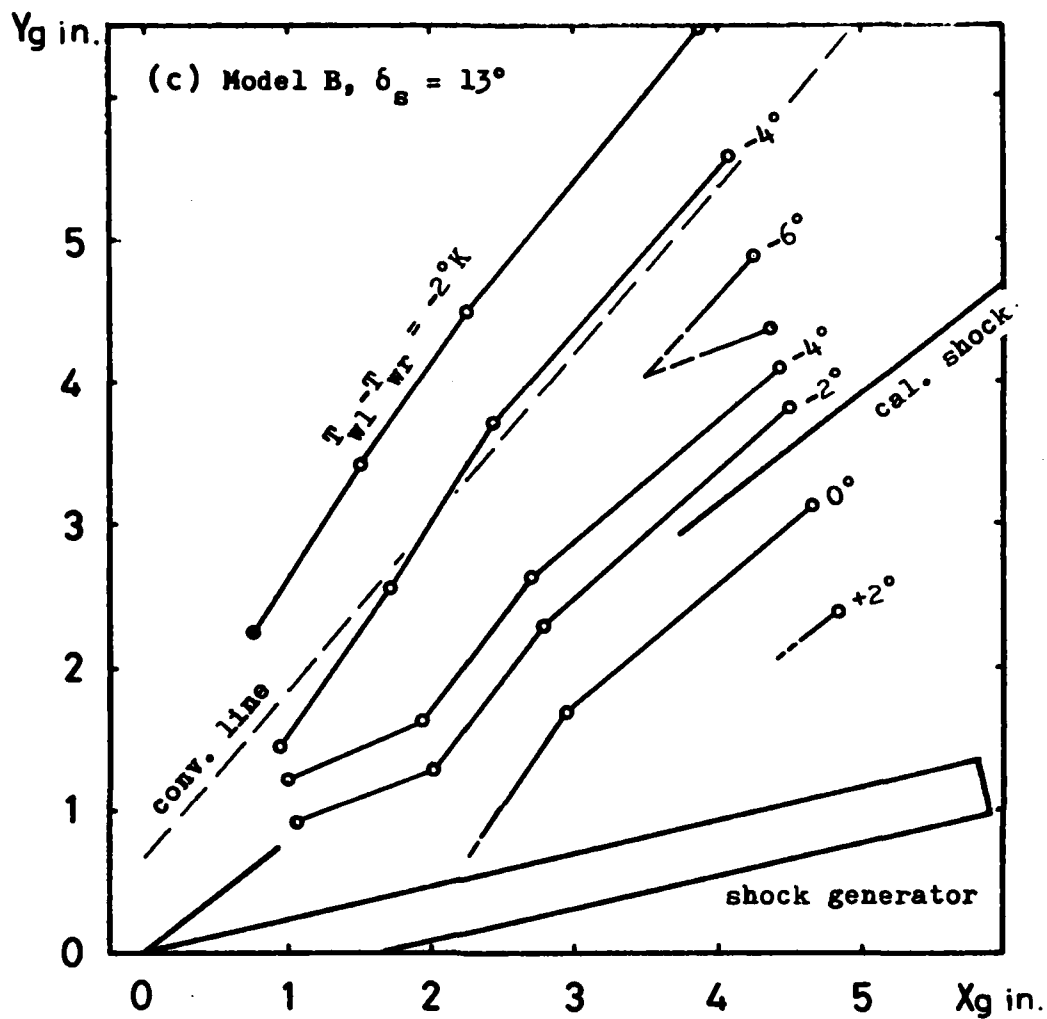


Figure 46. Isothermals on the side-wall surface.  
( 9 x 9 inch tunnel ).

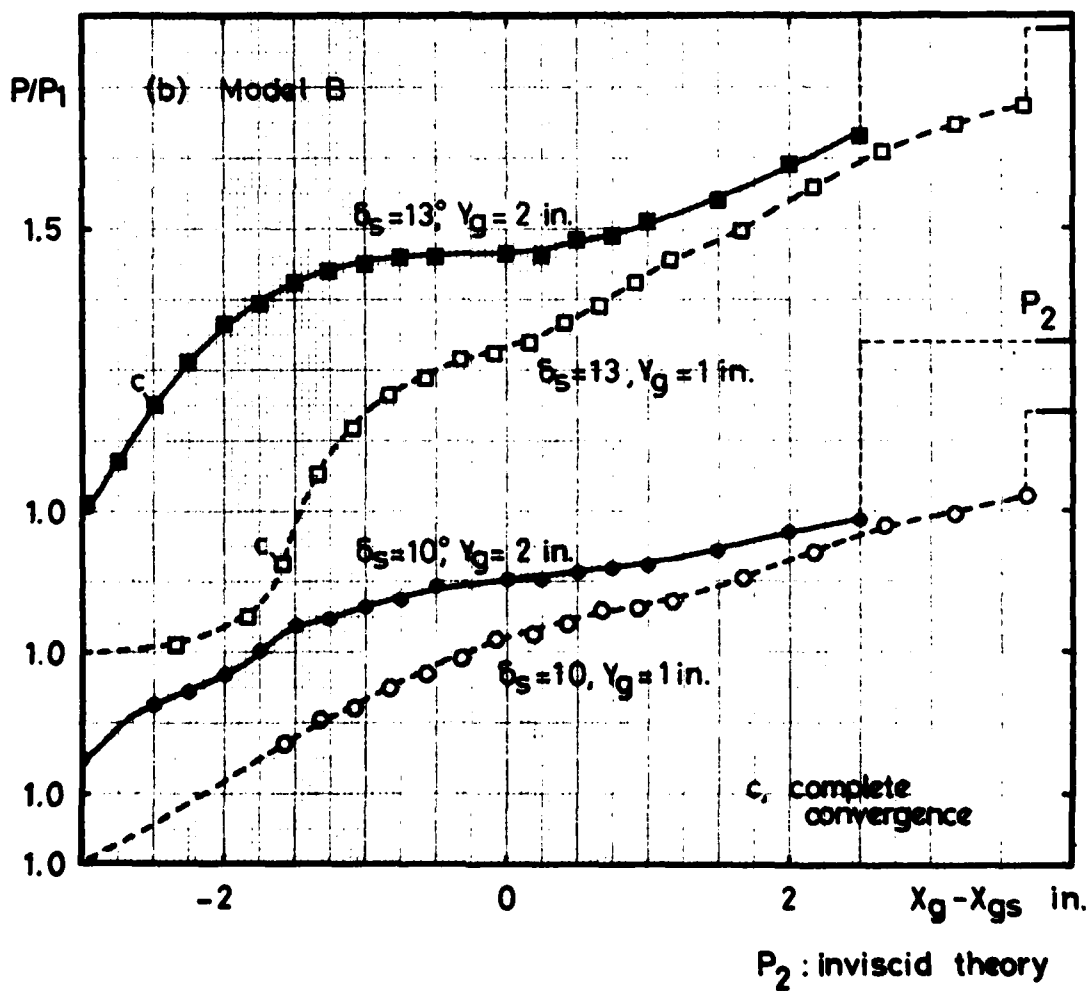
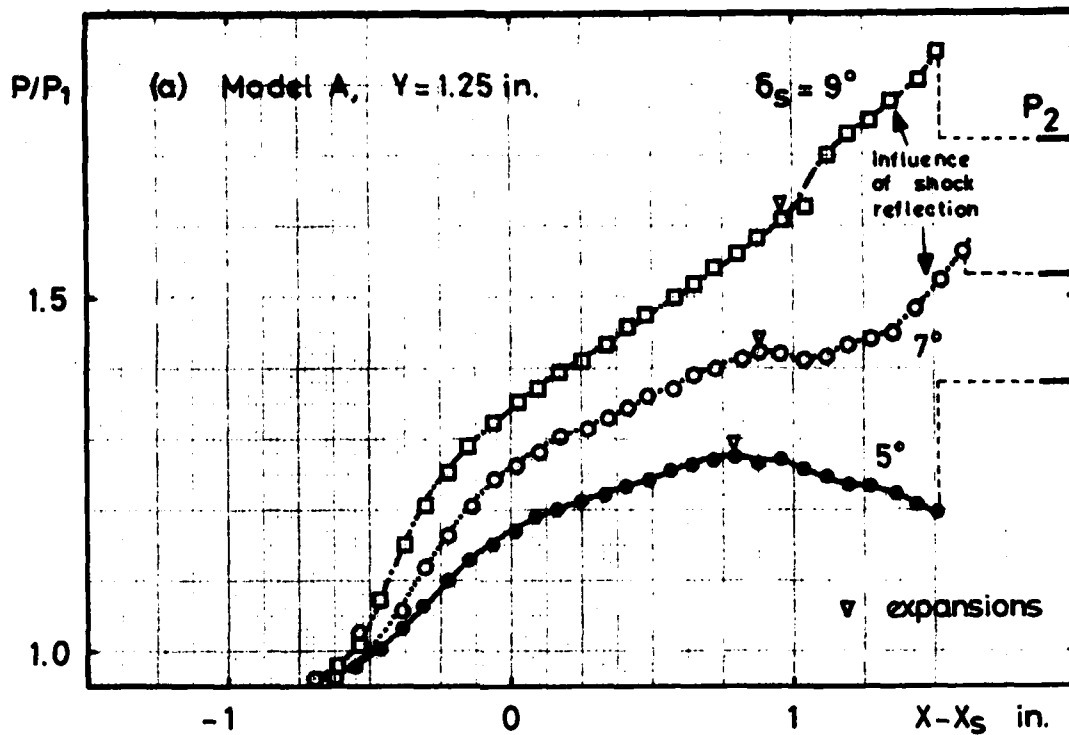
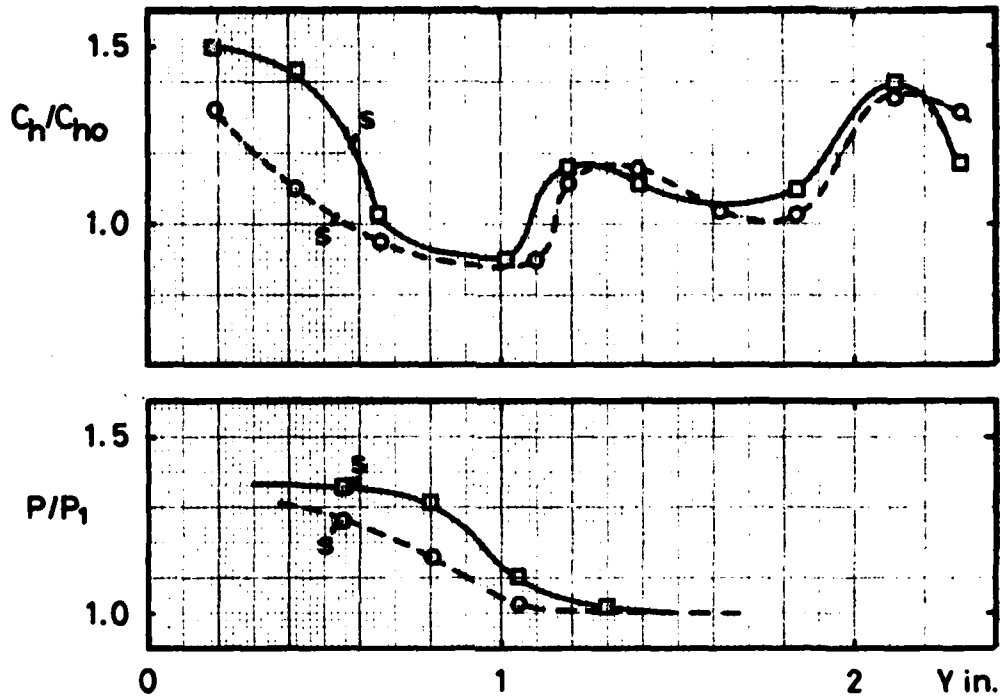
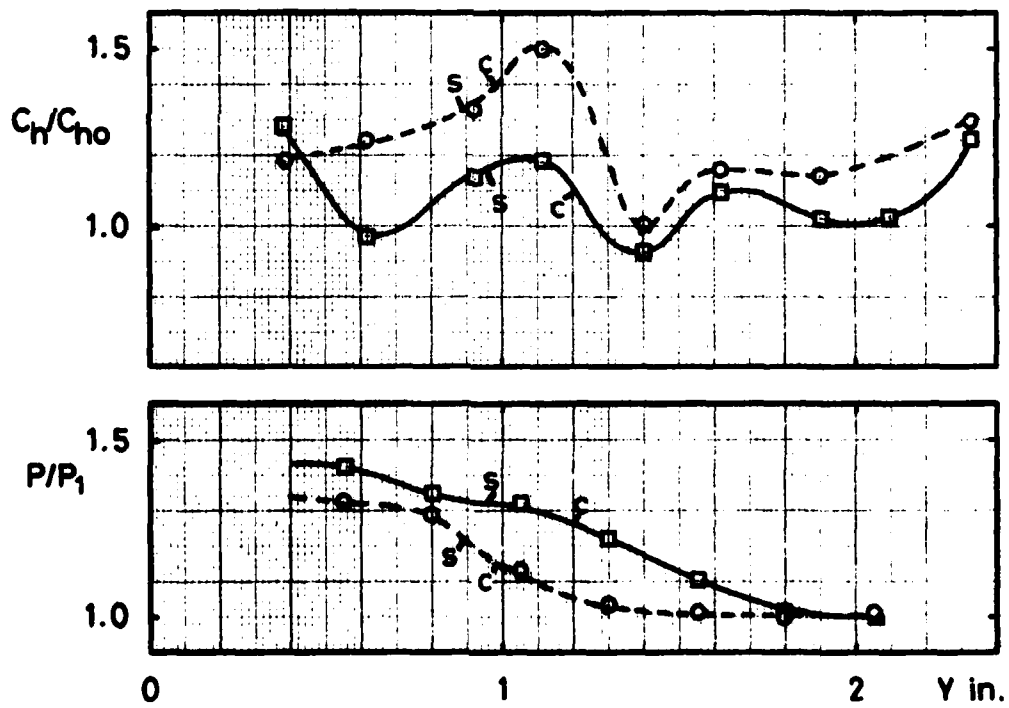


Figure 47. Typical streamwise static pressure distributions.

(a) Model A,  $x = 0.9$  in.



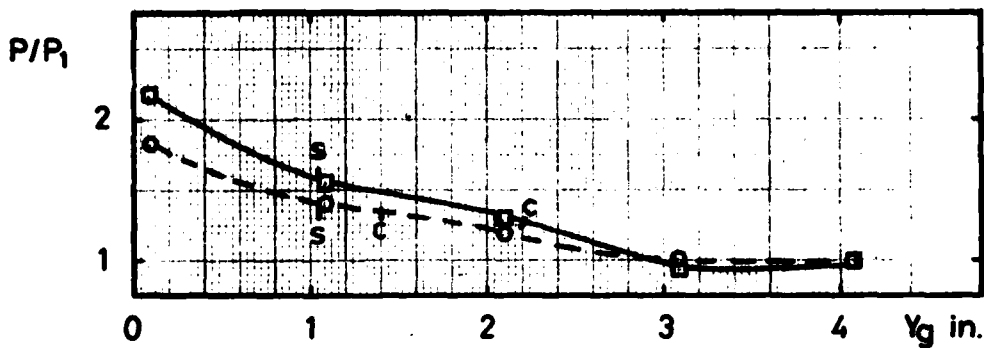
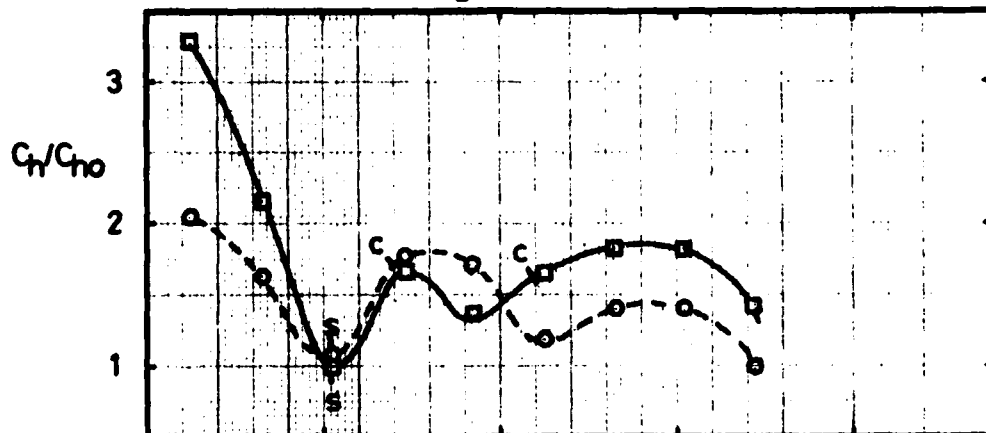
(b) Model A,  $x = 1.5$  in.



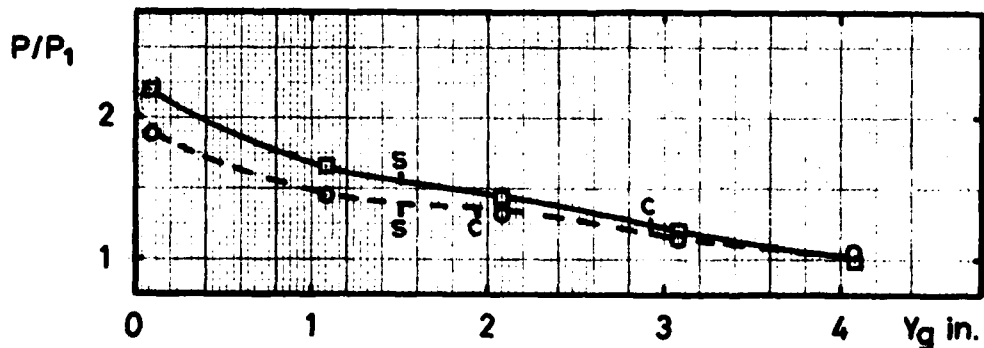
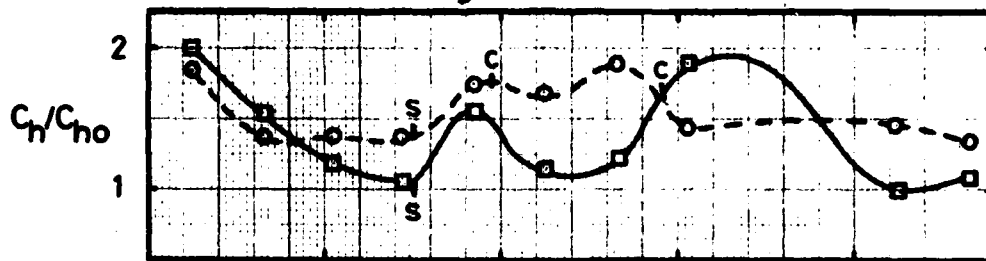
□  $\delta_s = 9$  deg.  
○ " 7 "  
s, shock  
c, conv. line

Figure 48. Static-pressure and heat-transfer distribution.

(c) Model B,  $x_g = 2.25$  in.

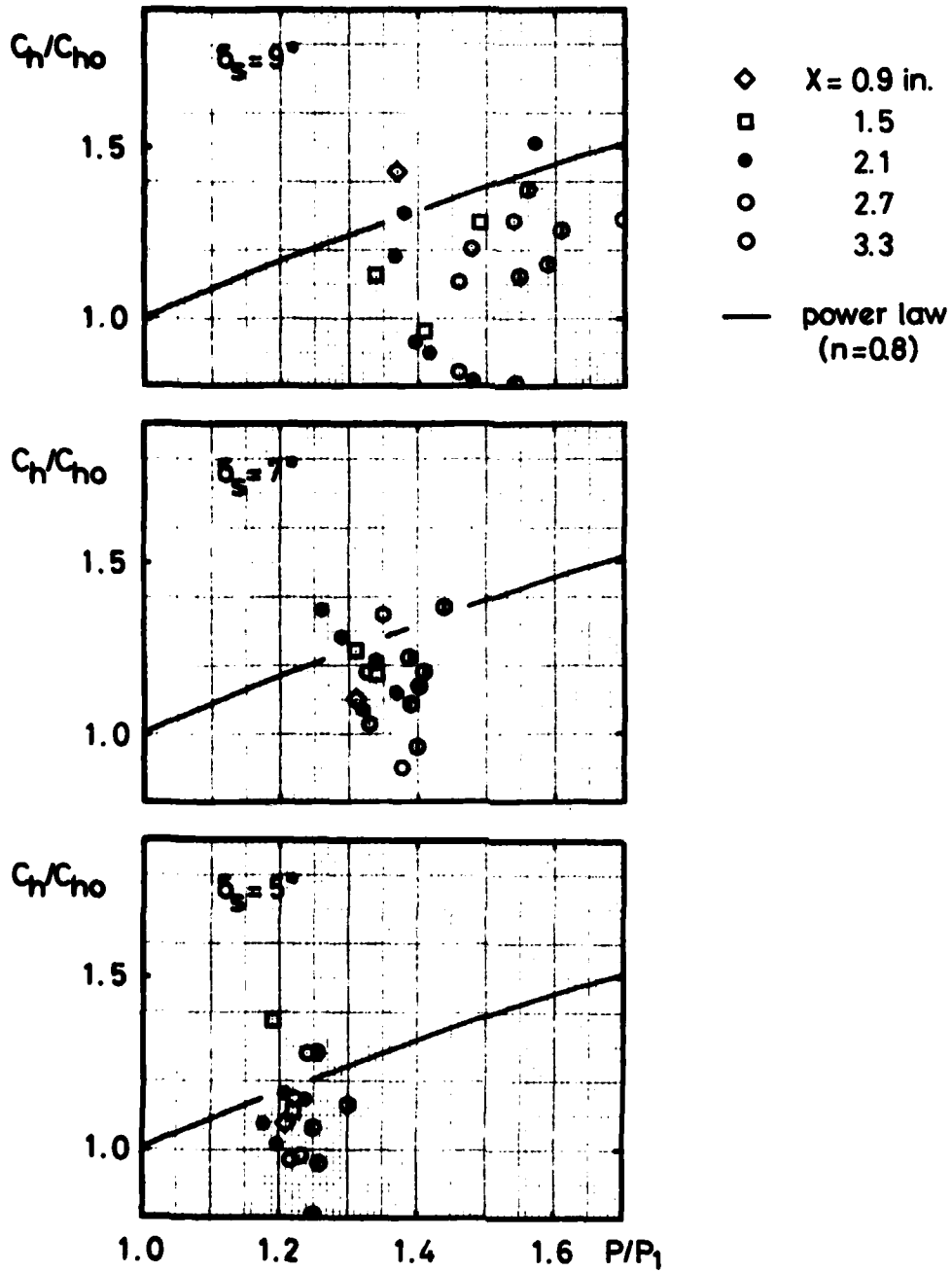


(d) Model B,  $x_g = 3.25$  in.



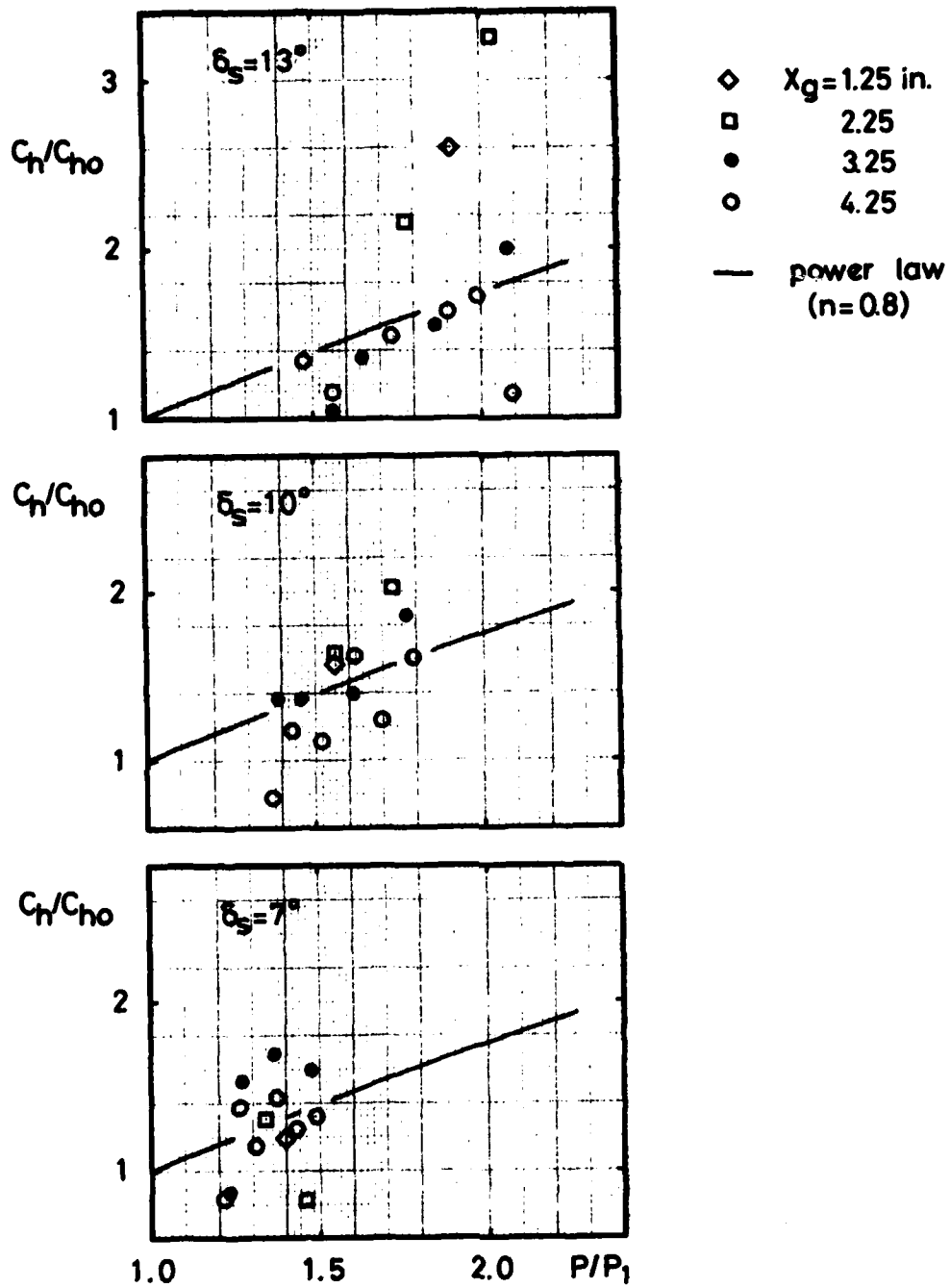
□  $\delta_s = 13$  deg.  
○ " 10 "  
s, shock  
c, conv. line

Figure 48. Static-pressure and heat-transfer distribution.



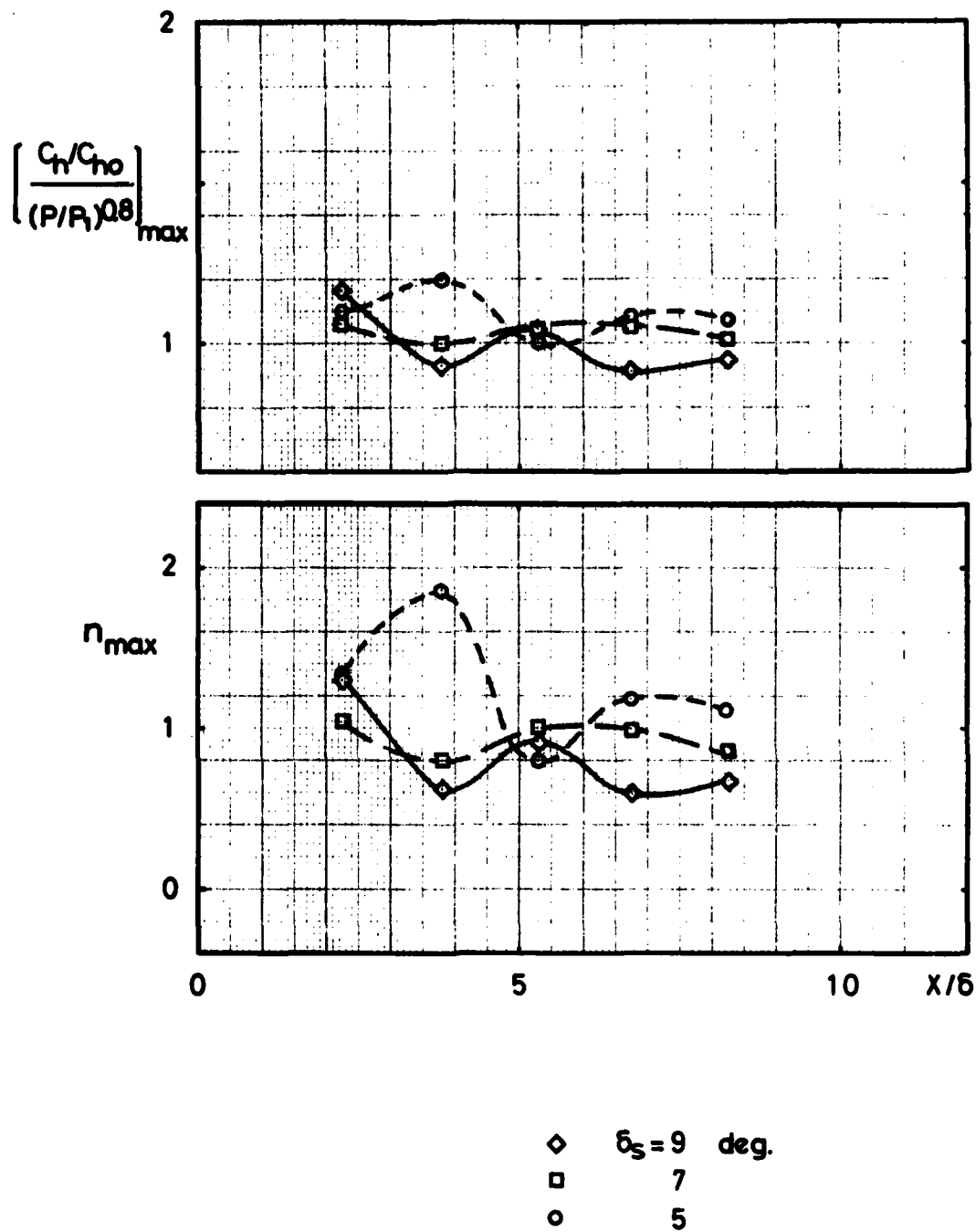
(a)  $C_n/C_{n0}$  vs.  $P/P_1$ , Model A

Figure 49. Correlation between static pressure and heat transfer.



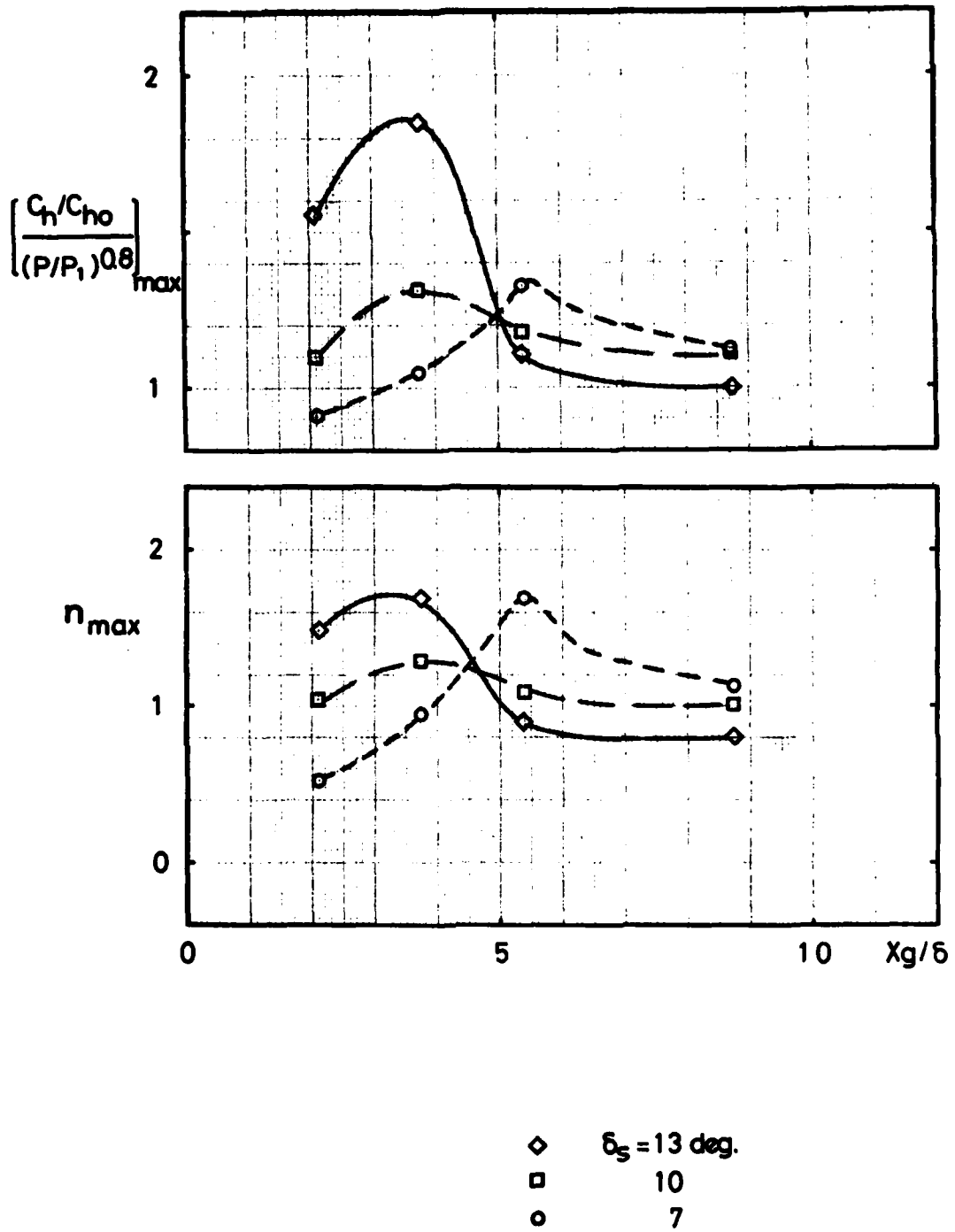
(a) Continued, Model B

Figure 49. Correlation between static pressure and heat transfer.



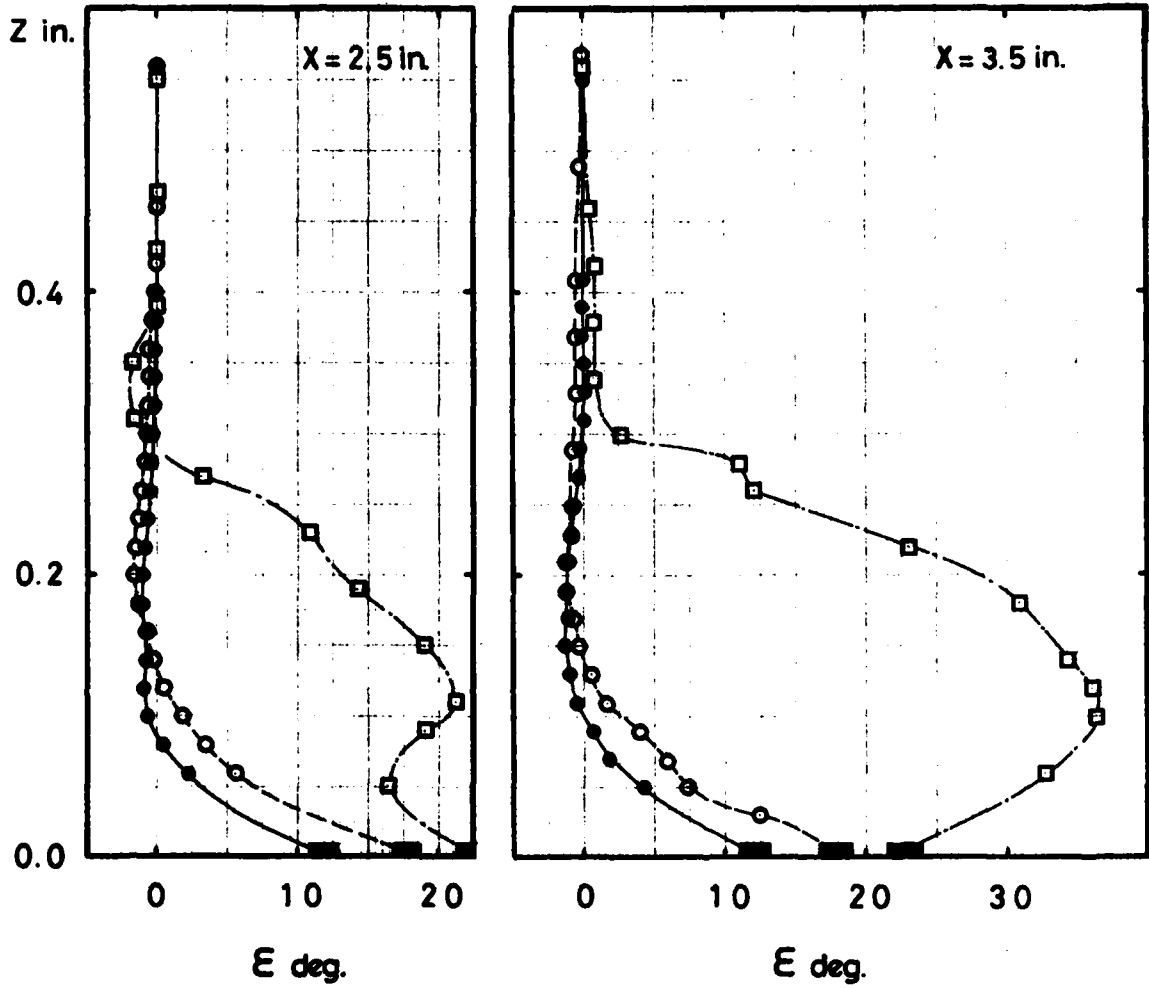
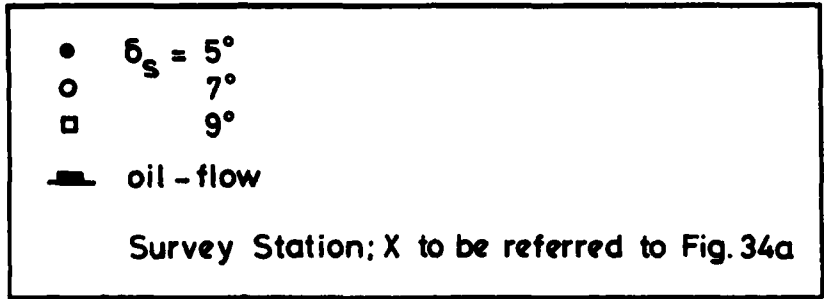
(b) Power Law, Model A

Figure 49. Correlation between static pressure and heat transfer.



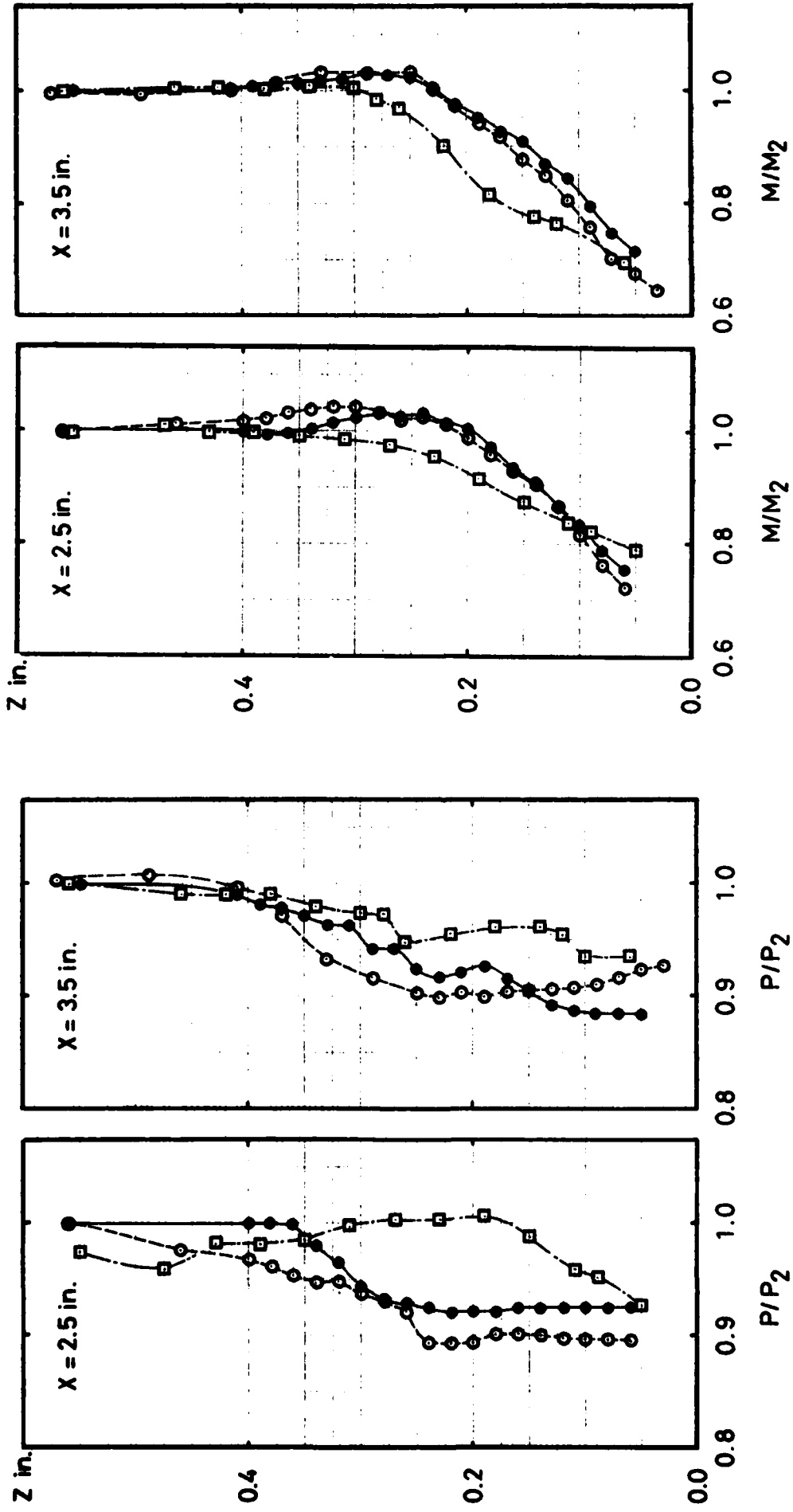
(b) Continued, Model B

Figure 49. Correlation between static pressure and heat transfer.



(a) Flow Deflection Angle

Figure 50. Viscous-layer survey results.



(b) Static Pressure

(c) Local Mach Number

Figure 50. Viscous-layer survey results.

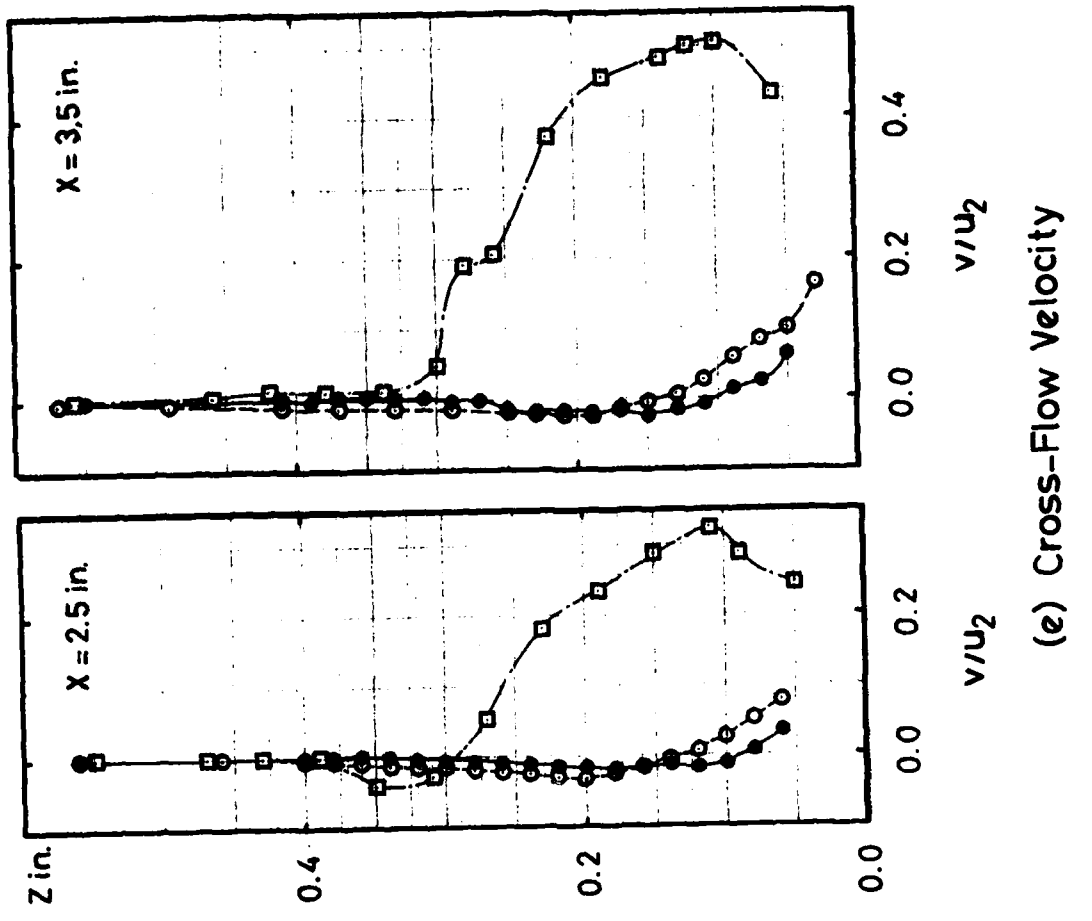
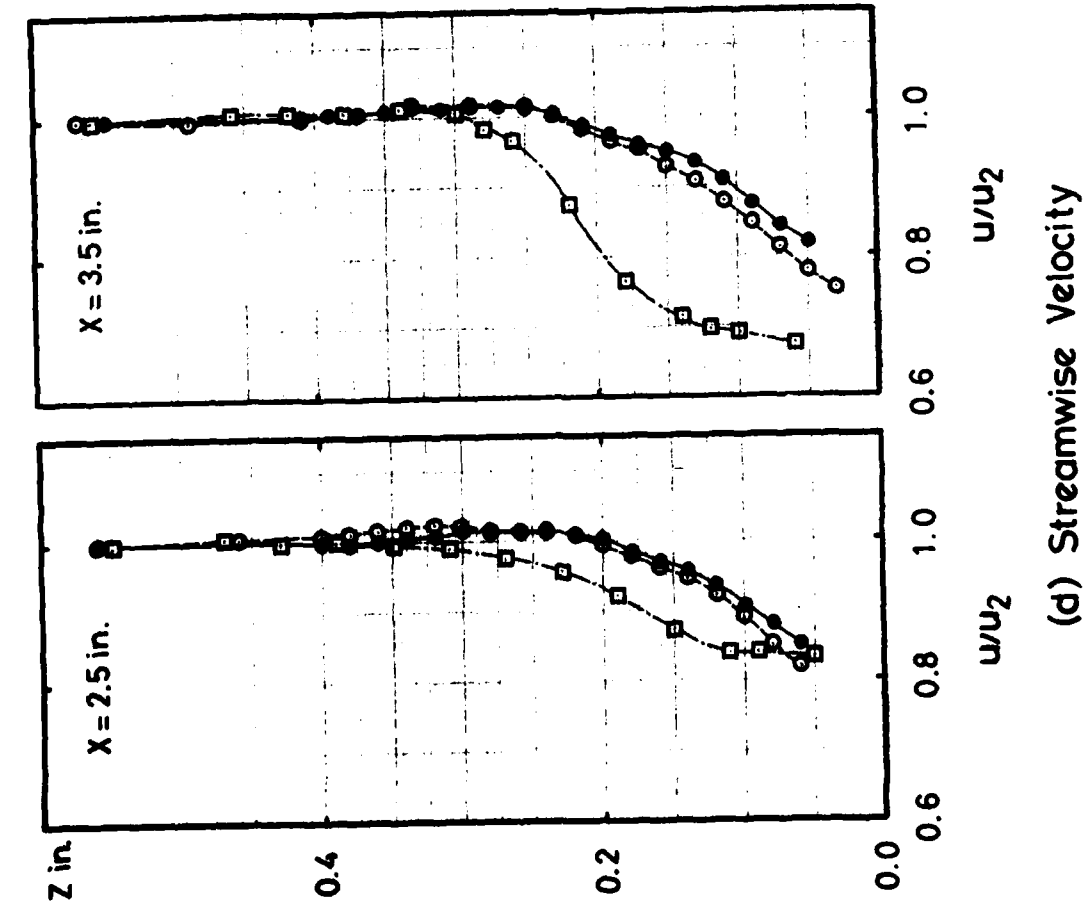


Figure 50. Viscous-layer survey results.

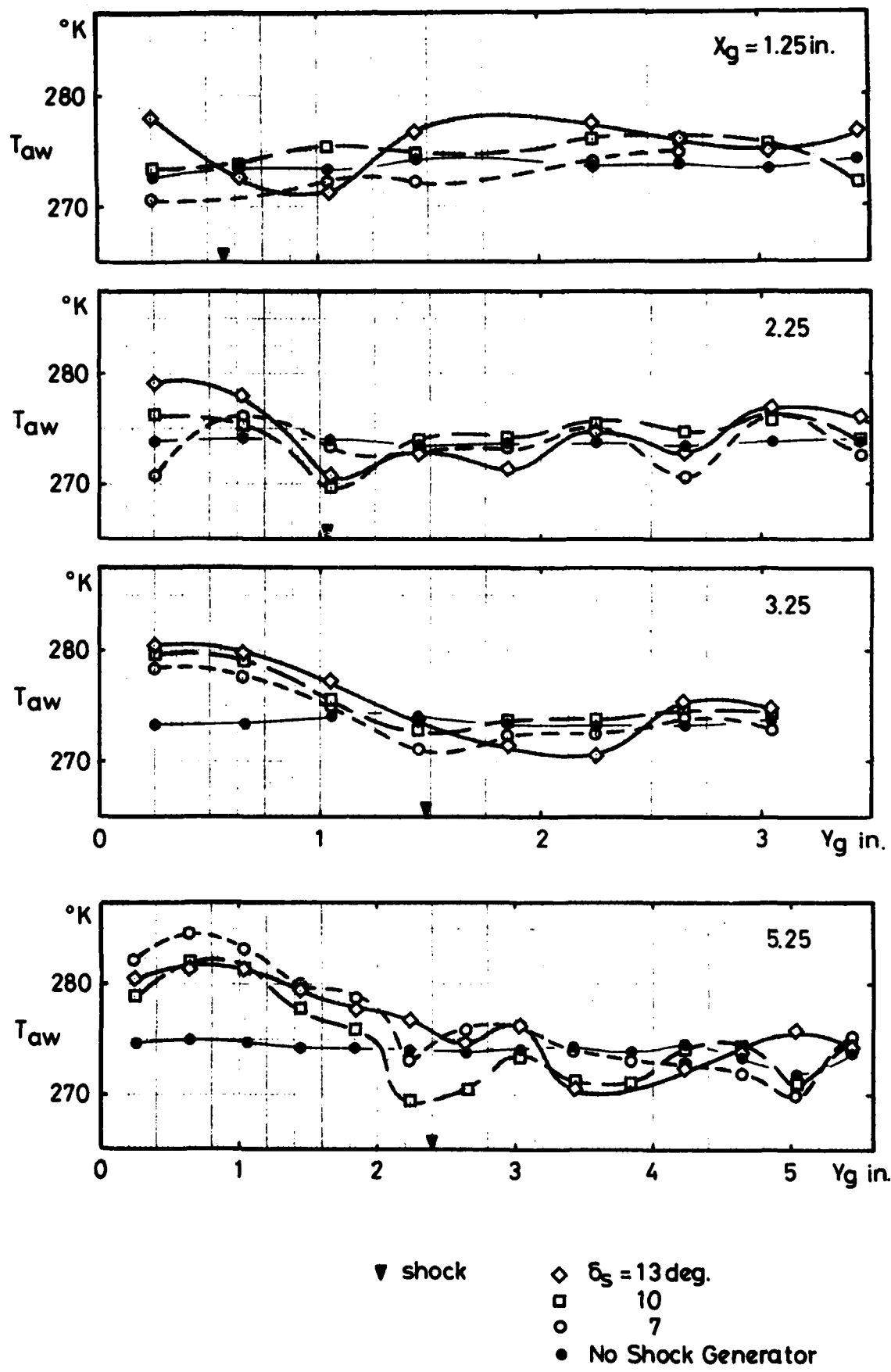


Figure 51. Adiabatic wall temperature distributions.

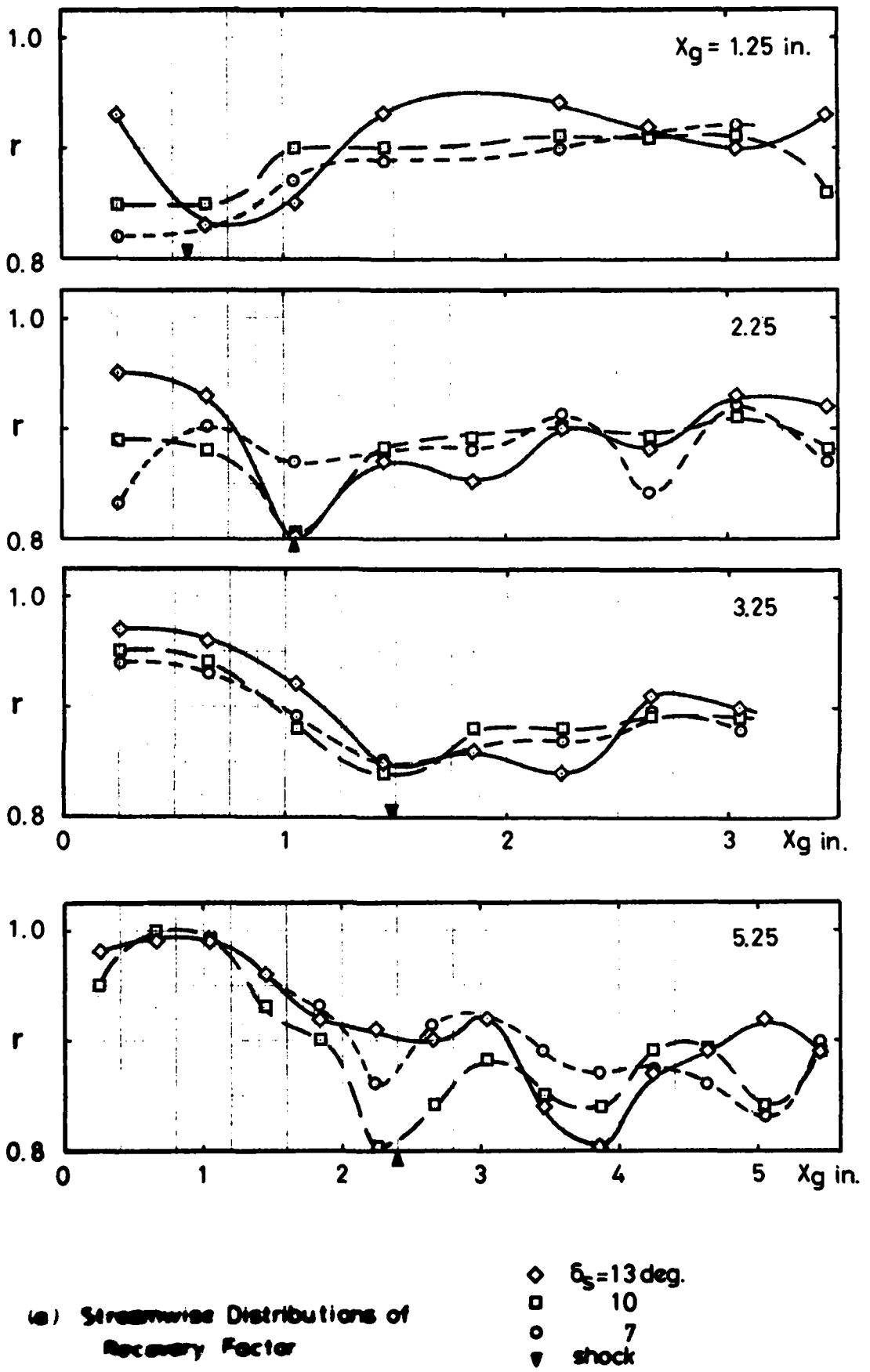


Figure 52 Recovery factor patterns.

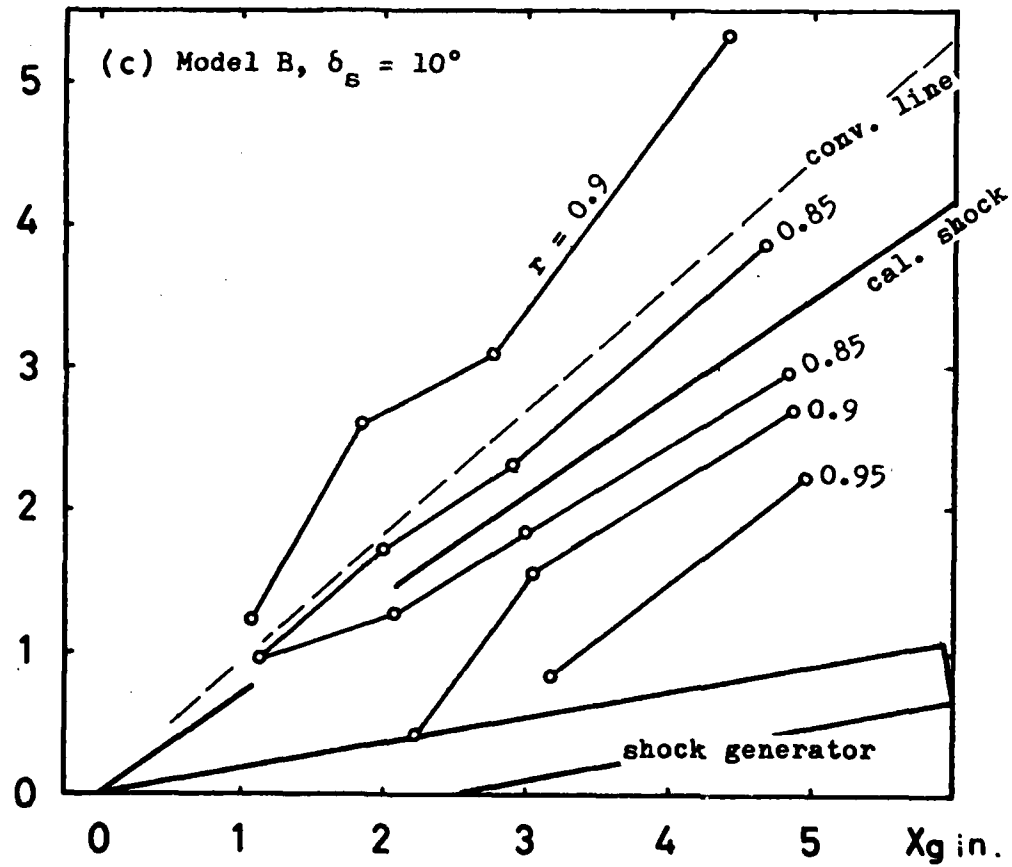
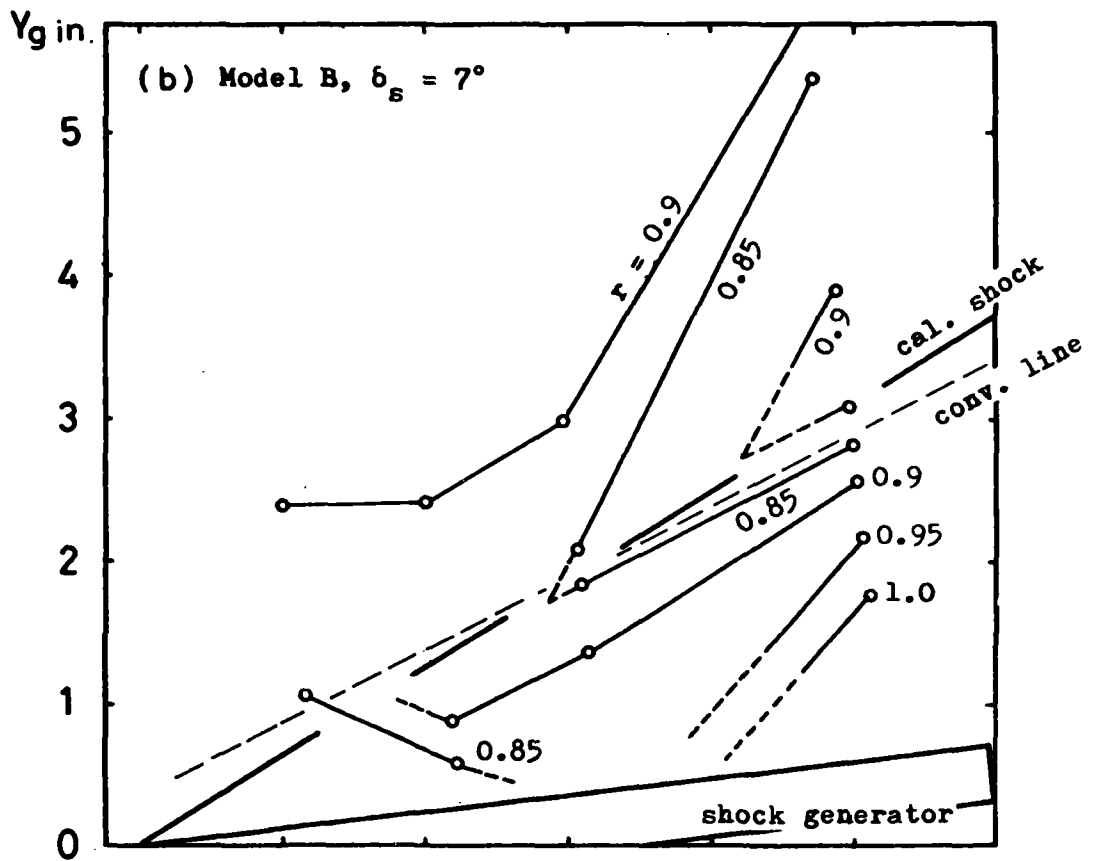


Figure 52. Recovery factor patterns.

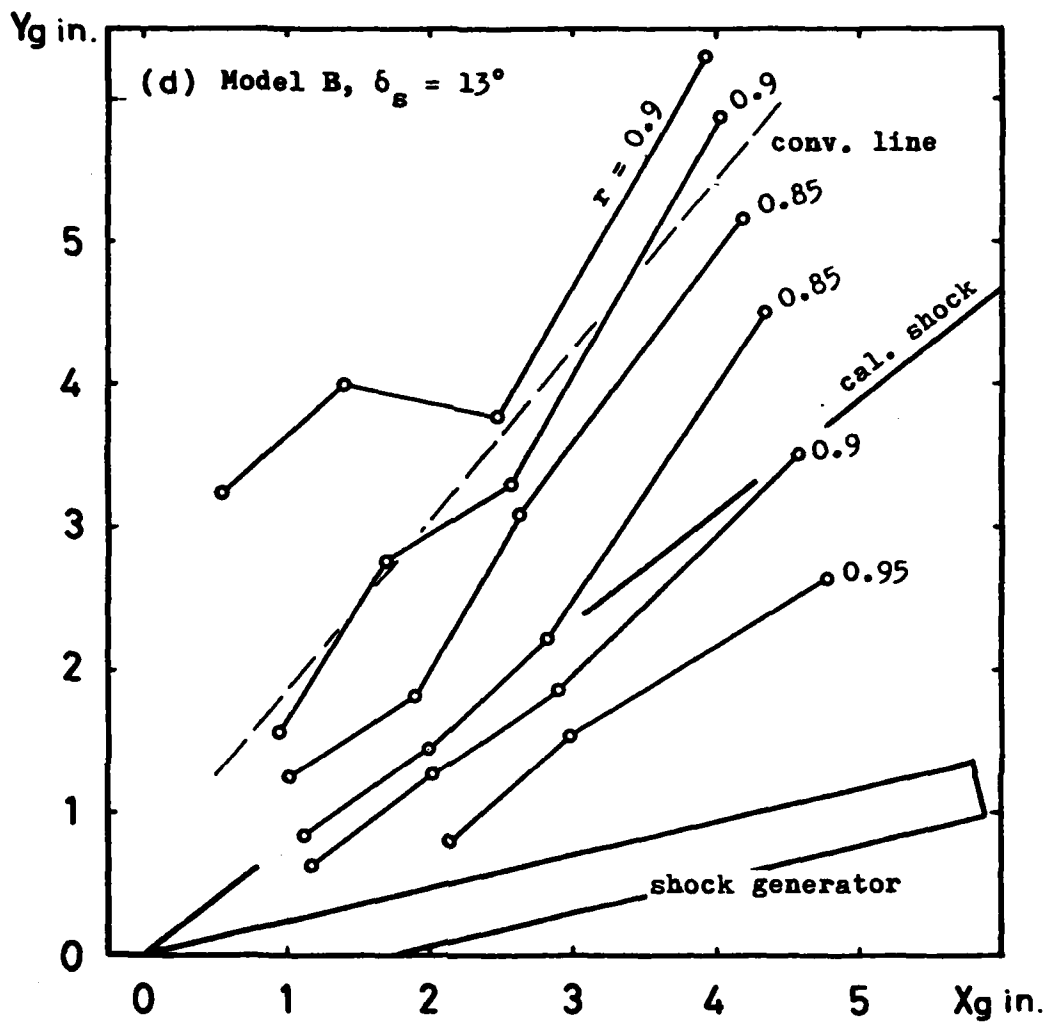
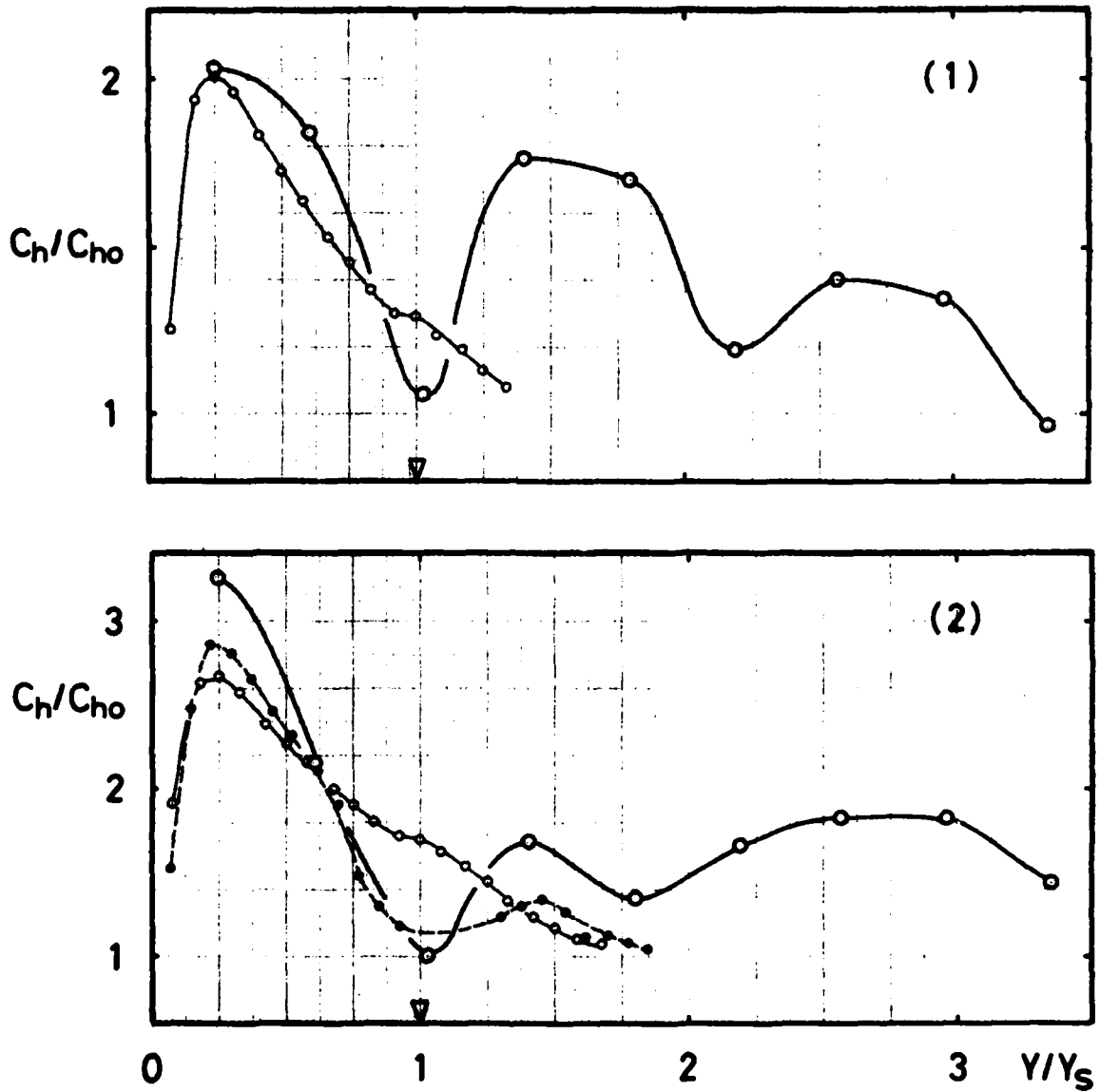
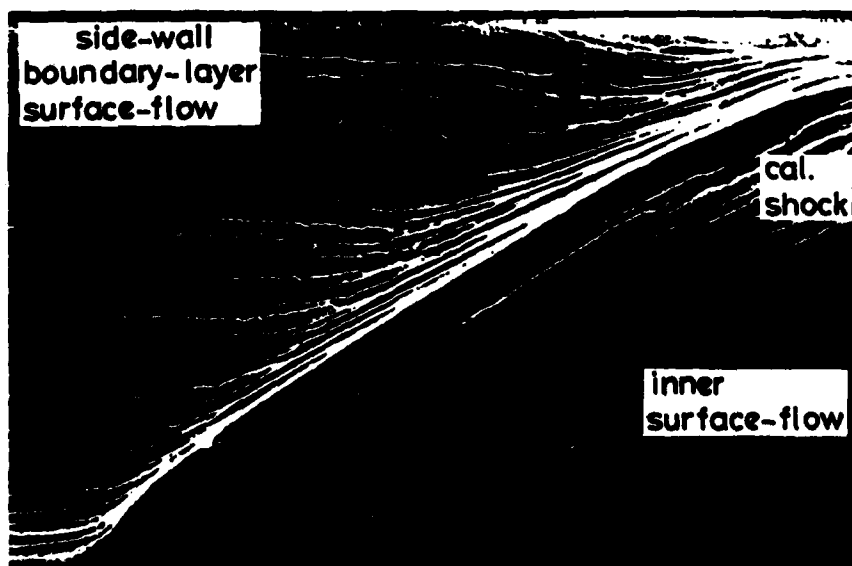
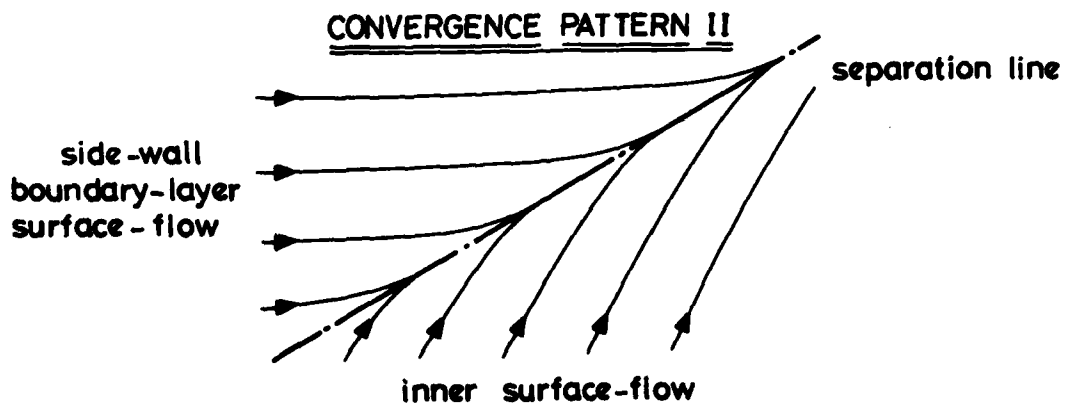
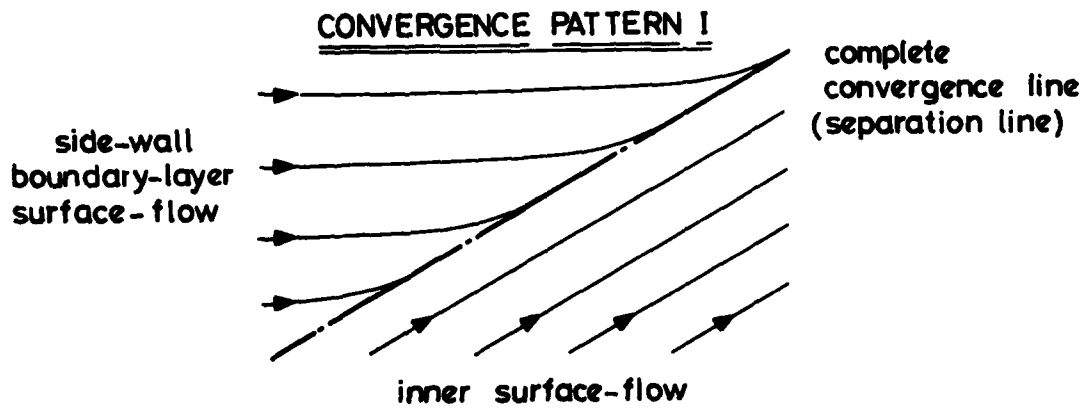


Figure 52. Recovery factor patterns.



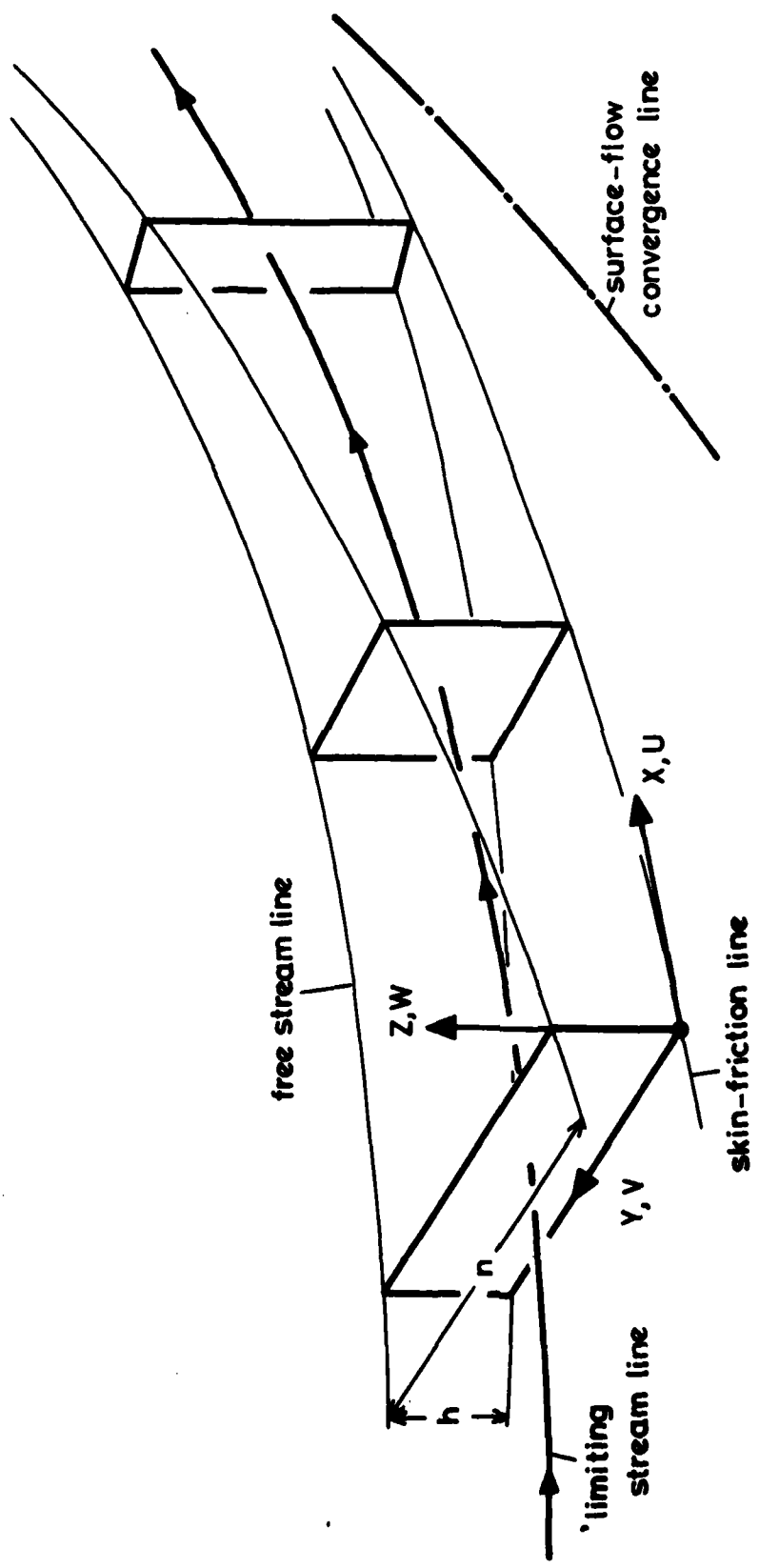
Model B	$X/\delta = 4$	(1) $P/P_1 = 1.8$	(2) $P/P_1 = 2.2$
NEUMANN	$X/\delta = 4$	(1) $P/P_1 = 1.6$	(2) $P/P_1 = 2.4$
(Ref. 17)	$X/\delta = 40$		(2) $P/P_1 = 2.0$

Figure 53. Typical heat transfer distributions.



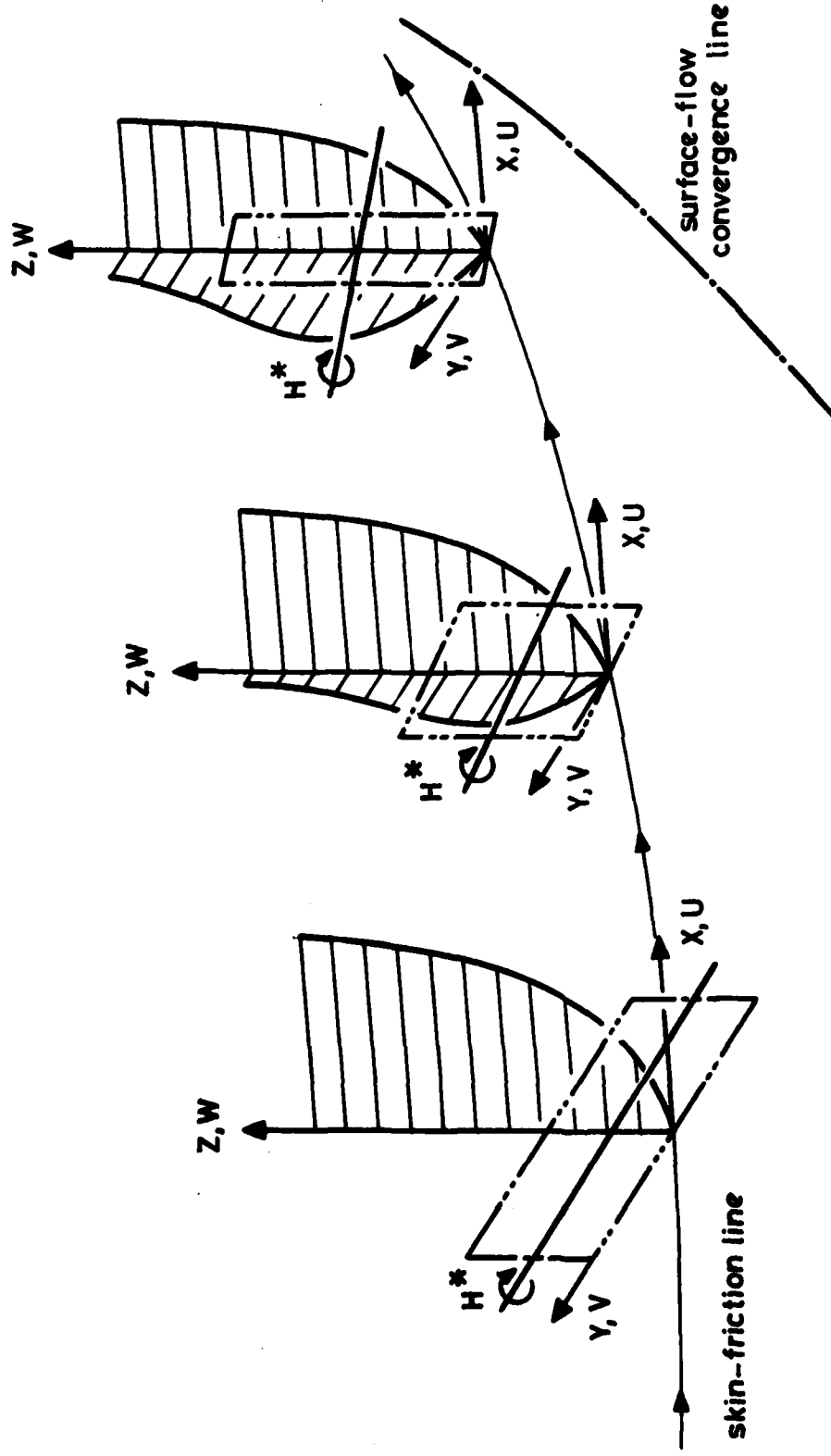
(Oil-Flow Pattern, Model A,  $\delta_s = 9^\circ$ )

Figure 54. Surface-flow convergence patterns.



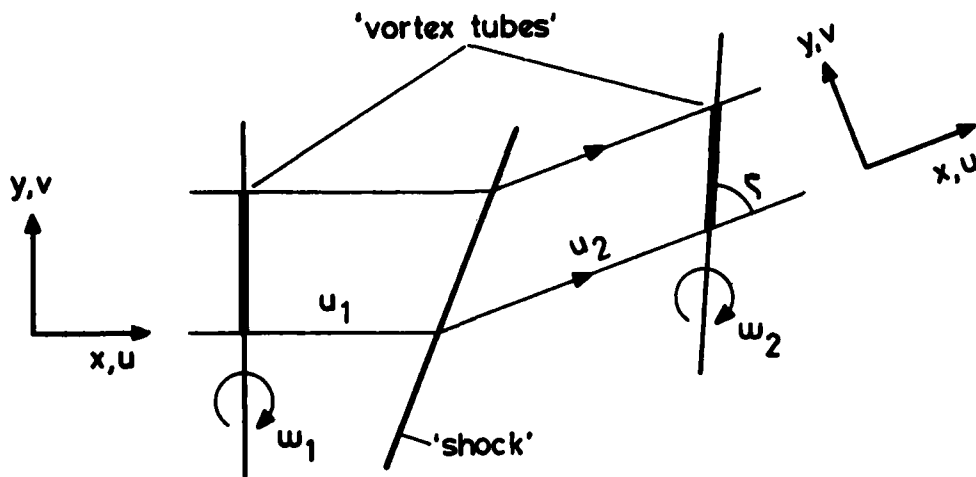
(a) Stream Tube near Convergence Line

Figure 55. Boundary-layer stream tube near the surface-flow convergence line.

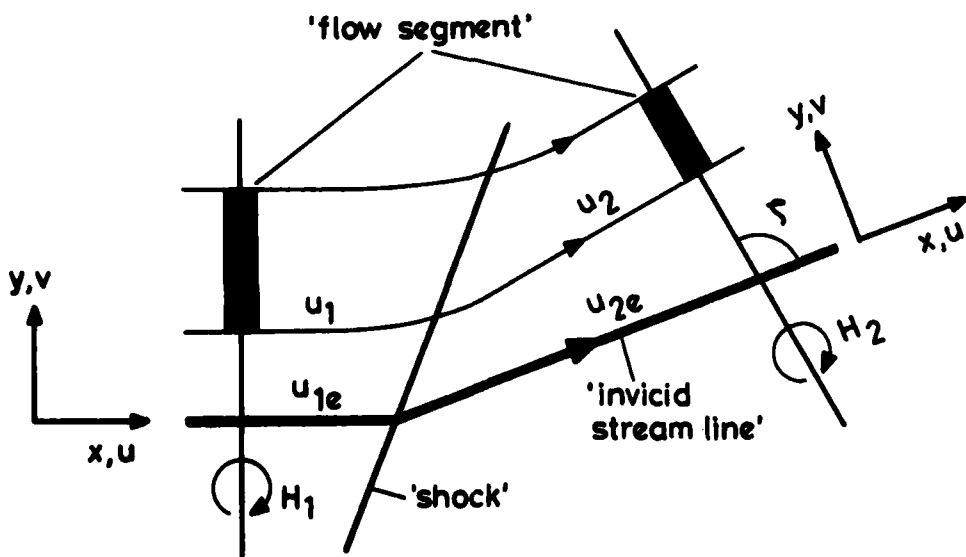


(b) Velocity Profiles and Angular Momentum near Convergence Line

Figure 55. Boundary-layer stream tube near the surface-flow convergence line.



(a) McCabe's Theory



(b) The Present Theory

Figure 56. Co-ordinate systems for surface-flow deflection analyses.

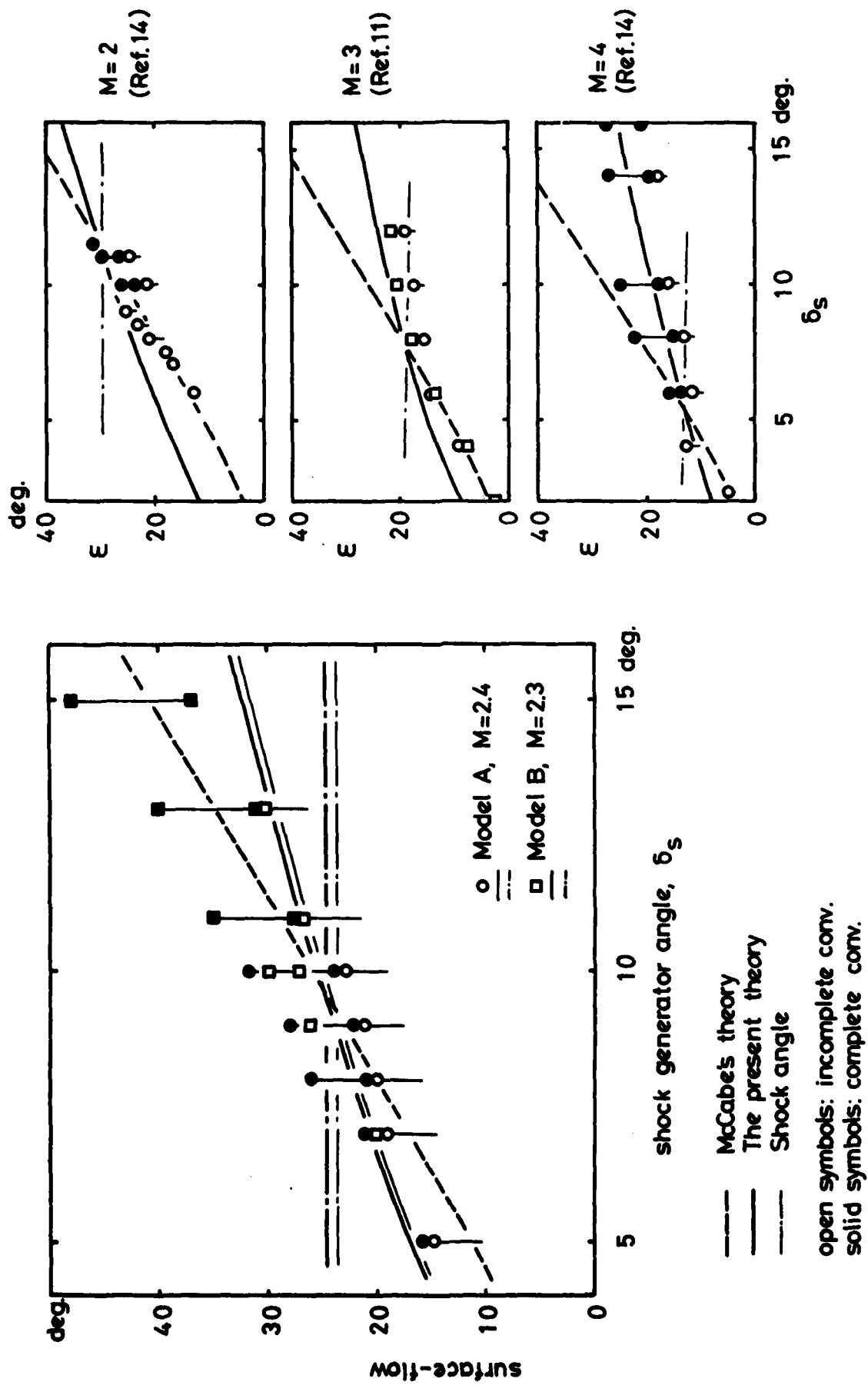
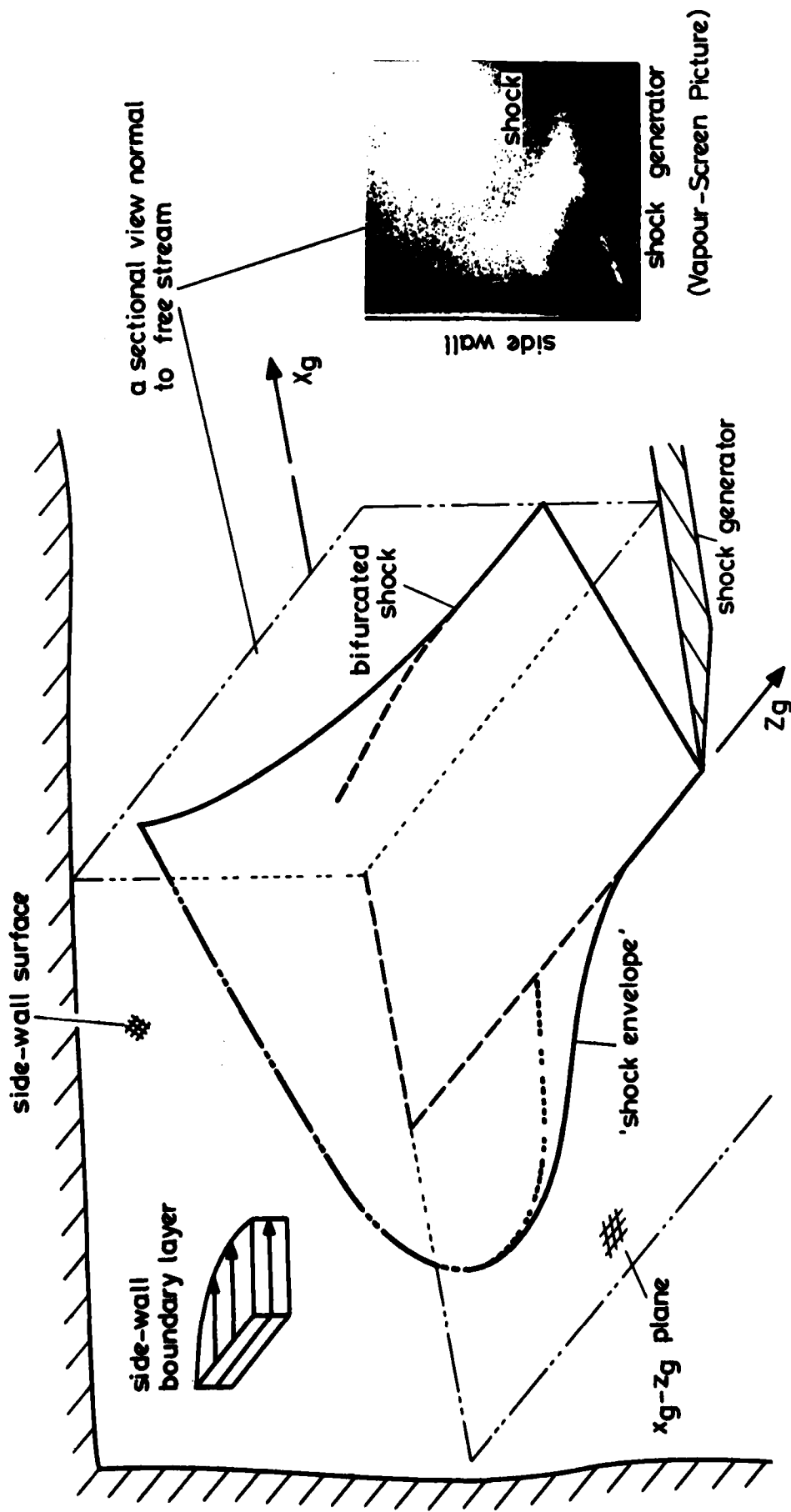
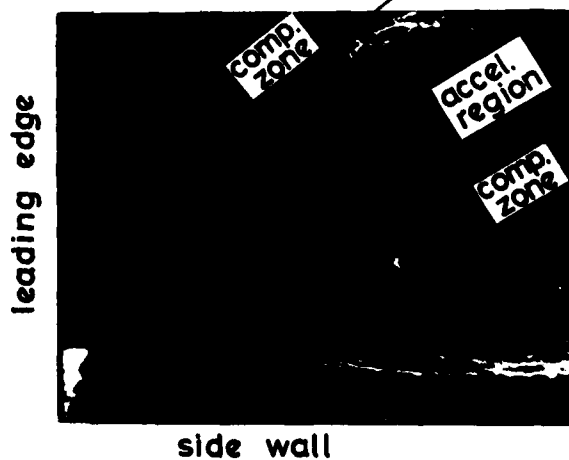
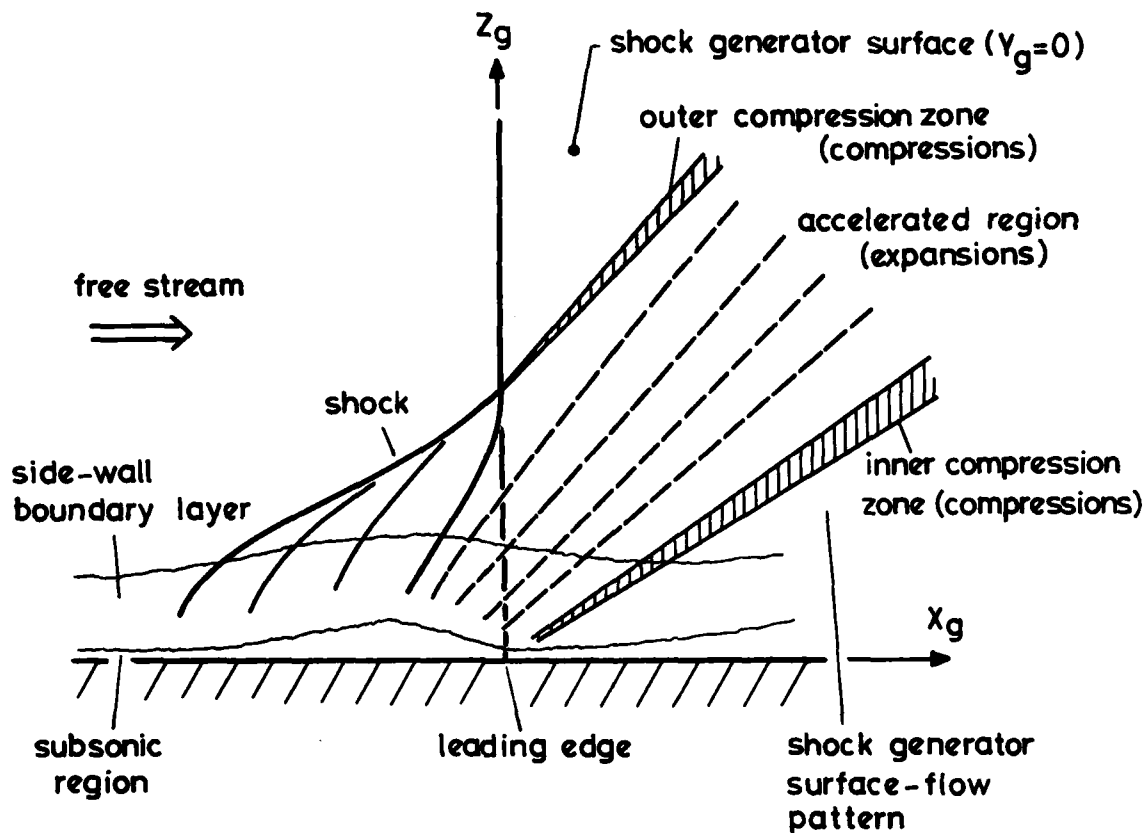


Fig. 57 Surface-Flow Convergence Angle vs. Shock Generator Angle



(a) Shock Envelope near Shock Generator Leading Edge

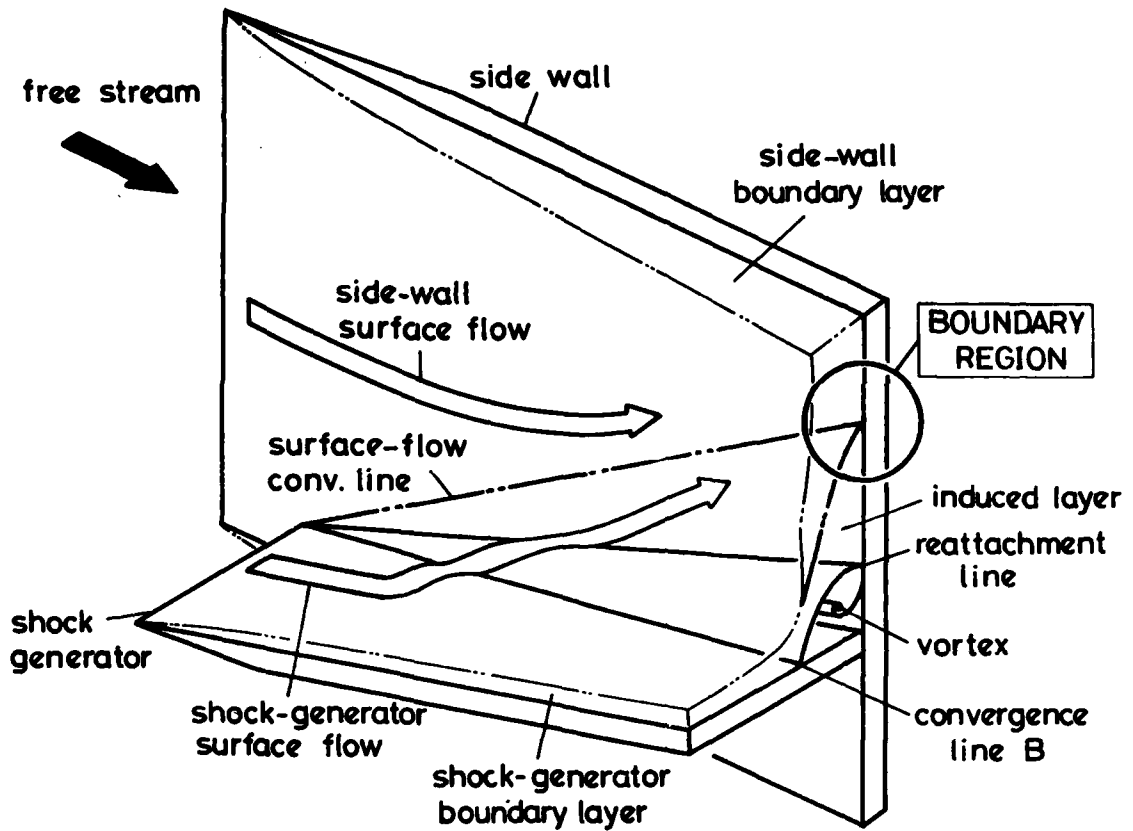
Figure 58. Flow structure near the shock generator root.



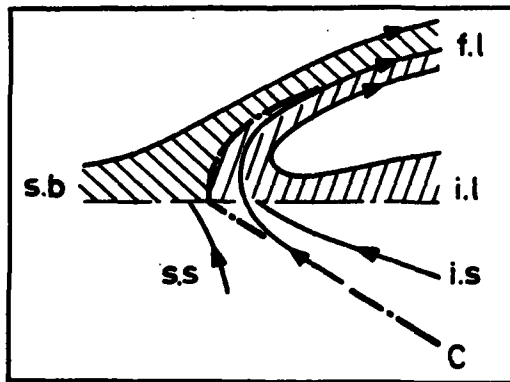
(Oil-Flow Picture)

(b) Flow Structure on  $X_g$ - $Z_g$  Plane ( $Y_g=0$ )

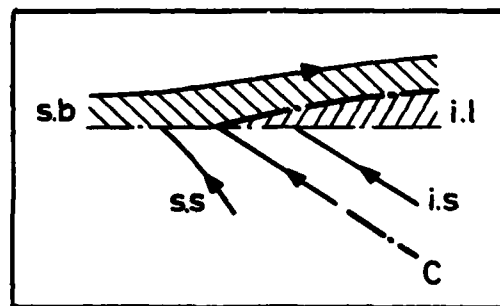
Figure 58. Flow structure near the shock generator root.



(Separated Boundary)



(Attached Boundary)



C conv. line  
 i.l, induced layer  
 i.s, induced-layer surface-flow

f.l, free vortical layer  
 s.s, side-wall boundary layer  
 s.s, side-wall boundary-layer surface-flow

Figure 59. 'Double viscous layer' model.

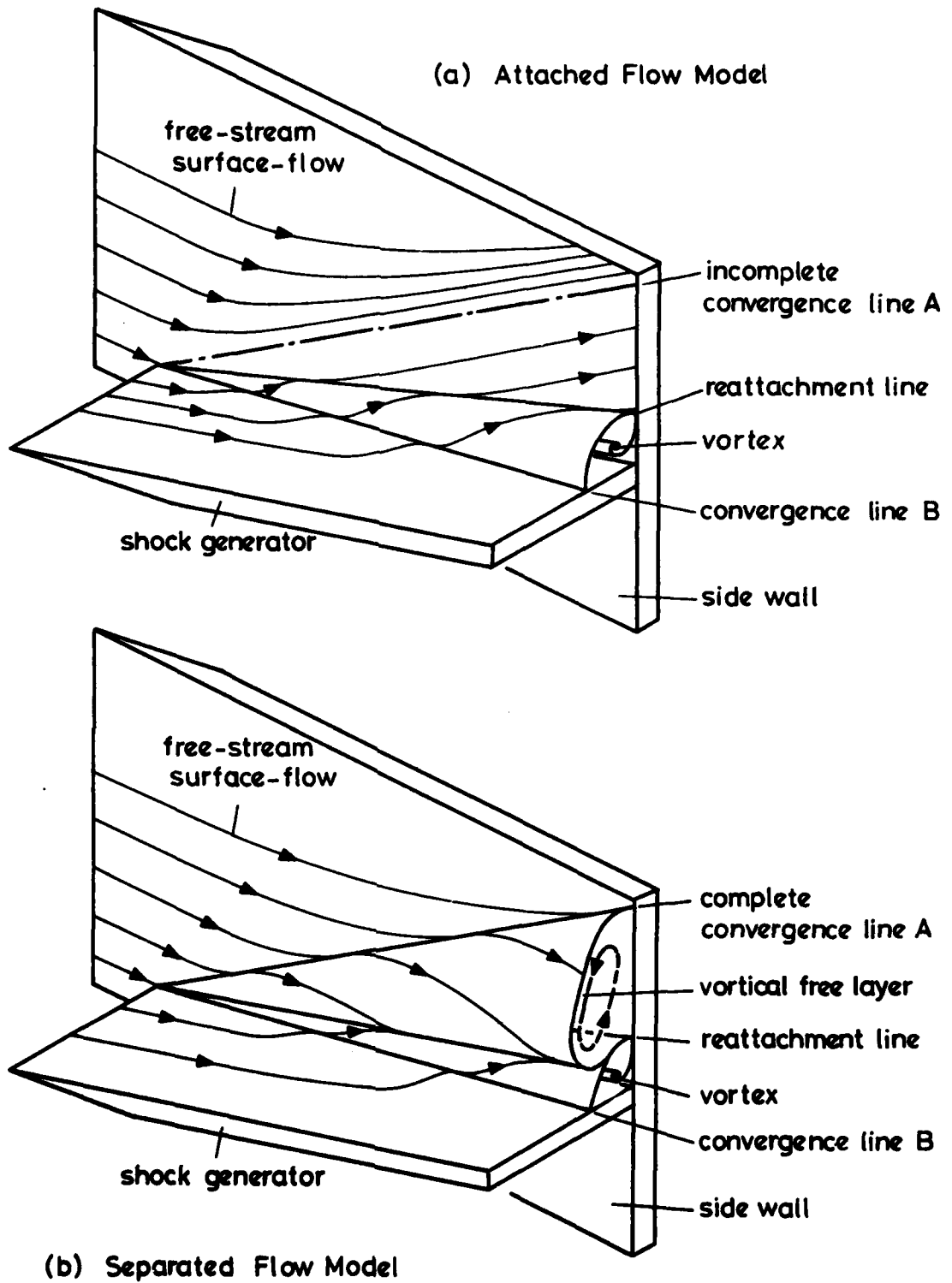
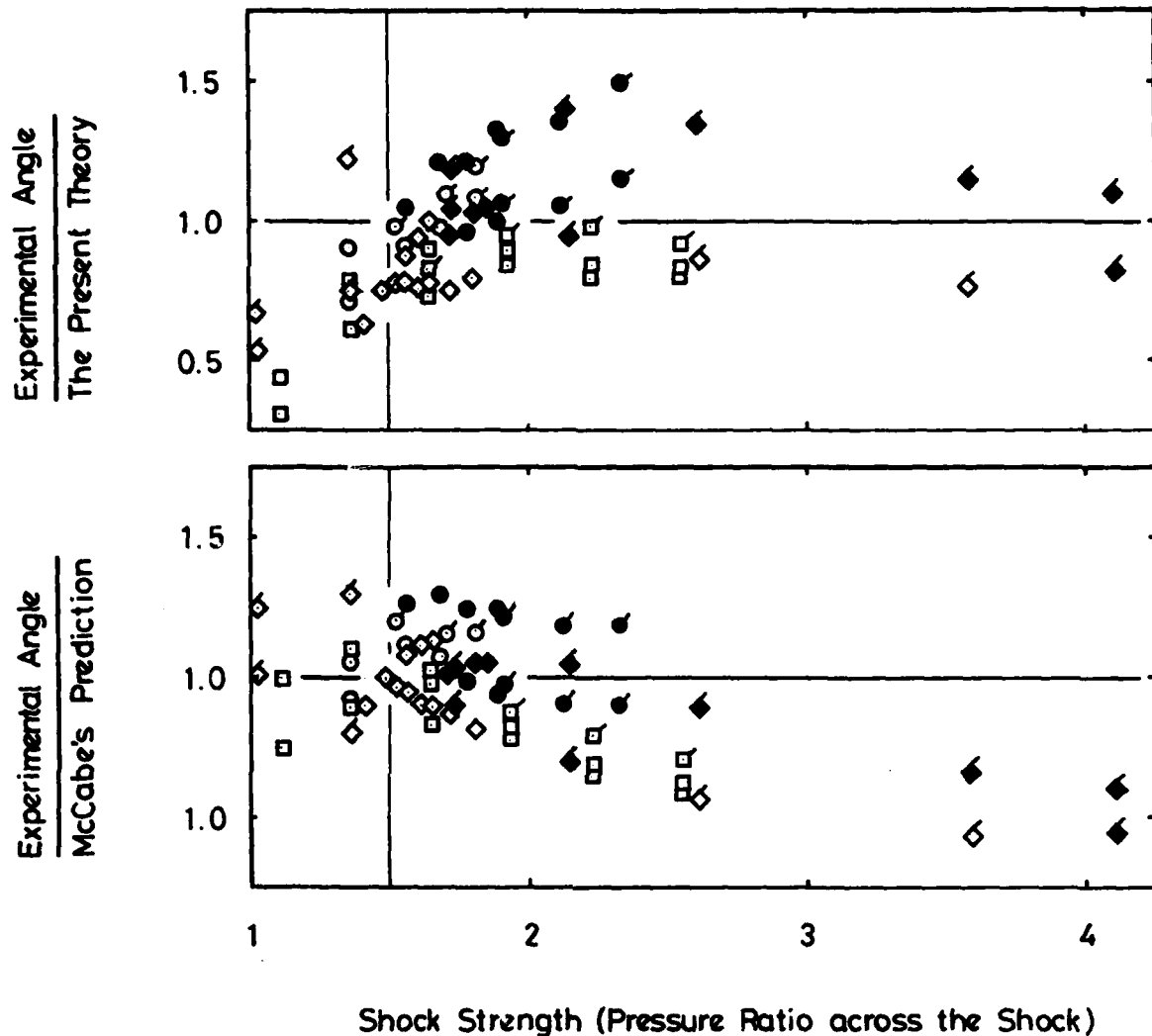


Figure 60. Attached and separated boundaries.



- $\sigma$  Model A and B
- $\sigma$  Ref. 11 (Model 1 and 2)
- ◇  $\sigma$  Ref. 14 (M = 2 and 4)

open symbol: incomplete conv.  
 solid symbol: complete conv.

Figure 61. Correlation of convergence line angle with the appearance of flow separation

AD-A083 703

COLLEGE OF AERONAUTICS CRANFIELD (ENGLAND)

F/G 20/4

INVESTIGATION OF THREE-DIMENSIONAL SHOCK WAVE BOUNDARY LAYER IN--ETC(U)

JAN 80 H KUBOTA

AFOSR-76-3006

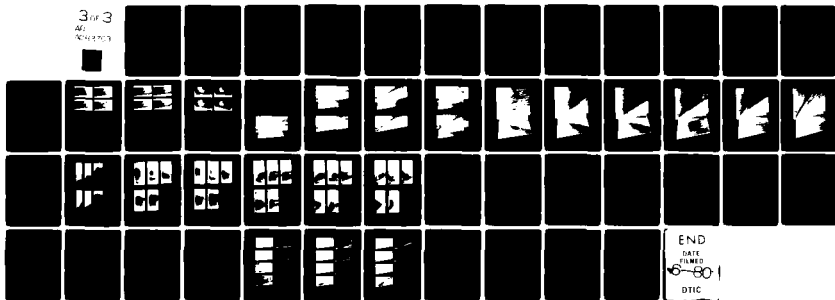
COA-8001

NL

UNCLASSIFIED

3 of 3

44-288623



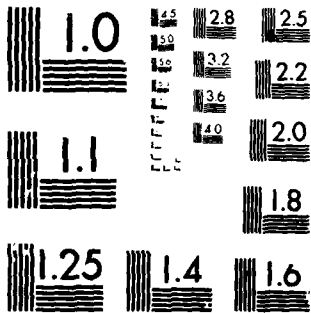
END

DATE

FILMED

6-80

DTIC



MICROCOPY RESOLUTION TEST CHART  
NATIONAL BUREAU OF STANDARDS-1963-A

APPENDIX A THE DERIVATION OF THE BOUNDARY LAYER PROFILES

The boundary layer was surveyed using Pitot and static-pressure probes. These two pressures (and the measured stagnation temperature,  $T_0$ ) gave local Mach number, density and velocity profiles in the boundary layer using the relations outlined below.

The supersonic boundary-layer flow cannot be regarded as isentropic and the measured local Pitot pressure,  $p_p$ , is the stagnation pressure downstream of a normal shock induced by the probe head. Hence the local Mach number,  $M$ , must be derived from Rayleigh's supersonic Pitot formula, i.e.

$$\frac{p}{p_p} = \frac{\left( \frac{2\gamma}{\gamma+1} M^2 - \frac{\gamma-1}{\gamma+1} \right)^{1/(\gamma-1)}}{\left( \frac{\gamma+1}{2} M^2 \right)^{\gamma/(\gamma-1)}} \quad (\text{A} - 1)$$

where  $p$  is the measured local static pressure and  $\gamma$  is the ratio of specific heats assumed to be 1.4 for air.

The calculated Mach number profile can then be used to derive the density profile  $\rho(y)$  from the equation of state,

$$\rho = p/RT, \quad (\text{A} - 2)$$

where  $R$  is the gas constant (287 J/kg. $^{\circ}$ K) and  $T$  is the local temperature calculated from

$$T/T_0 = 1/(1 + \frac{\gamma-1}{2} M^2) \quad (\text{A} - 3)$$

Finally, the resultant velocity profile,  $U^*$ , is derived from

$$\frac{1}{2}\rho U^{*2} = \frac{\gamma p}{2} M^2 \quad (\text{A} - 4)$$

which is the definition of dynamic pressure.

## APPENDIX B HEAT TRANSFER MEASUREMENTS

### B.1. Quasi-Transient Calorimeter Techniques

There are many different techniques for measuring the heat transfer between a solid wall and a moving airstream. They fall roughly into three different categories, according to the temporal behaviour of the measured temperatures (e.g. wall, adiabatic-wall, etc.) which are to be reduced to the heat transfer. The techniques are

- (1) the transient technique in which all the temperatures are variables of time,
- (2) the quasi-transient technique in which only the local wall temperature is regarded as variable with time, and
- (3) the steady-state technique in which the temperatures have no change in time but in space.

Most of these techniques are further divided into

- (1) surface-thermometer techniques, and
- (2) calorimeter techniques.

The difference between the surface-thermometer and calorimeter techniques is small. However, for the calorimeter technique, a small 'calorimeter area' must be locally and separately situated on the wall surface.

To measure the heat transfer distributions in the present shock boundary-layer interaction region, the quasi-transient calorimeter technique was used for both test programmes. However, the details of the technique used were different between the test programmes. This was because of basic differences in the test conditions between them, i.e. intermittent and continuous test conditions. In the 2.5 x 2.5 inch tunnel test programme, a modified 'Princeton University calorimeter technique' (Appendix B.2) was employed.

But for the 9 x 9 inch tunnel programme a 'thin-film-gauge calorimeter technique' (Appendix B.3) was devised and developed. The general principle of these calorimeter techniques is as follows.

The thermal field where the heat transfers between the solid wall and the air occurs is three-dimensional. However, this thermal field may be regarded as one-dimensional, if the component of the heat flux parallel to the wall is negligible in comparison with the normal component (Fig.B1).

The thermal balance at the wall surface may be written using the heat-transfer rate (q) or the heat-transfer coefficient ( $h_a$ ), as follows:

$$q = -k_w \frac{\partial T_w}{\partial z} \quad (B - 1)$$

in the 'wall domain', and

$$q = -k_a \frac{\partial T_a}{\partial z} \quad (B - 2)$$

or

$$q = h_a \{ (T_w)_{z=0} - T_{aw} \} \quad (B - 3)$$

in the 'air domain', where T, k and z are temperature, thermal conductivity and distance from the wall surface respectively, while suffices w, aw and a denote conditions of the wall, the adiabatic wall and the air. In the wall domain, the one-dimensional heat equation may be written as

$$\frac{\partial^2 T_w}{\partial z^2} = \frac{1}{\alpha_w} \frac{\partial T_w}{\partial t} \quad (B - 4)$$

where t is time and  $\alpha_w$  is thermal diffusivity of the wall material defined by in terms of thermal conductivity,  $k_w$ , density,  $\rho_w$  and specific heat,  $c_w$ , ( $\alpha_w = k_w / \rho_w c_w$ .)

Equation (B - 4) can be integrated with respect to  $y$  as

$$\frac{\partial T_w}{\partial z} = \frac{L}{\alpha_w} \frac{dT_m}{dt} \quad (\text{B} - 5)$$

where  $T_m$  is a mean temperature in a small domain,  $Z$ , and  $L$  is defined by

$$L = \int_Z dz \quad (\text{B} - 6)$$

Substituting (B - 5) into (B - 1) gives

$$q = -\rho_w c_w L \frac{dT_m}{dt}, \quad (\text{B} - 7)$$

It must be noted that  $\rho_w c_w L$  is an equivalent thermal-capacity of the wall surface.

## B.2. Slug Calorimeter Technique

It is assumed that a small 'slug' is situated on the wall surface but thermally insulated from it (Fig.B2). When this slug is used as a calorimeter with known thermal capacity,  $C_s$ , and surface area,  $A_s$ , equation (B - 7) may be rewritten as

$$q_s = -\frac{C_s}{A_s} \frac{dT_{ms}}{dt} \quad (\text{B} - 8)$$

where the suffix  $s$  denotes conditions of the slug. Thus, the heat transfer rate from the slug to the air is directly obtained by measuring the time history of  $T_{ms}$ .

From (B - 3) it follows that

$$\frac{q_s}{q} = 1 - \frac{(T_w)_{z=0} - T_{ms}}{(T_w)_{z=0} - T_{aw}} \quad (\text{B} - 9)$$

when  $h_a$  is assumed independent of temperature and the thermal resistance in the slug is small enough for  $T_{ms}$  to represent the surface temperature of the slug. Hence, it is clear from (B - 9) that the heat-transfer rate from the wall to the air (q) can be determined by measuring another heat-transfer rate from the slug ( $q_s$ ), when  $T_{ms} = (T_w)_{y=0}$ , because under these conditions  $q_s/q = 1$ .

### B.3. Thin-Film-Gauge Calorimeter Technique

Let us consider a thin-film-gauge installation (Fig.B3), made up from a thin Pyrex glass plate (the outer wall layer), and a thick aluminium slab (the inner-wall material). The thin-film gauges are sputtered on the glass-plate surface. This configuration can provide a calorimeter for each thin-film gauge, if use is made of the differences in thermal capacity and conductivity between the inner and outer-wall materials. The thermal-conductivities of Pyrex-glass and aluminium are 0.014 and 2.4 J/cm.sec.<sup>o</sup>K respectively. The much larger thermal-conductivity and capacity of the aluminium wall ensures that the temperature of the inner wall is approximately uniform and constant. If the glass-plate surface is heated locally by the thin-film gauge, a temperature distribution is formed in the glass-plate layer, as shown in Fig.B4. This small heated part of the glass-plate is the calorimeter. The advantages and disadvantages of such a calorimeter, as used in the quasi-transient technique, were described in Section 3.5.2.

The thermal field for this calorimeter has two different heat-transfer systems (Fig.B3b), i.e. heat transfer from the calorimeter region of the wall surface

to the air ( $q_a$ ) and heat transfer from the inner wall to the calorimeter ( $q_w$ ). Therefore equation (B - 7) may be written as

$$q_a - q_w = - C^* \frac{dT_g}{dt} \quad (B - 10)$$

where  $T_g$  is the gauge temperature and  $C^*$  is an equivalent thermal-capacity per unit area of the calorimeter (which is discussed in Appendix B4). Equation (B - 3) applied locally gives

$$q_a = h_a (T_g - T_{aw}) \quad (B - 11)$$

$$q_w = h_w (T_{wr} - T_g) \quad (B - 12)$$

where  $h_a$  and  $h_w$  are heat-transfer coefficients corresponding to  $q_a$  and  $q_w$  respectively and  $T_{wr}$  is the inner-wall temperature which is used as a reference value.

From the thermal balance at the wall surface, it is clear that, only when  $dT_g/dt = 0$ , does

$$q = q_a = q_w \quad (B - 13)$$

where

$$T_g = (T_w)_{z=0} \quad (B - 14)$$

Hence this type of calorimeter cannot directly measure the heat-transfer-rate from the calorimeter to the air, but it can be used to measure the heat-transfer-coefficient in the following manner.

Substituting (B - 11) and (B - 12) into equation (B - 10) gives

$$C^* \frac{dT_g}{dt} + (h_a + h_w)(T_g - T_{aw}) = h_w(T_{wr} - T_{aw}) \quad (B - 15)$$

If  $h_a$  and  $h_w$  are assumed independent of temperature, then this equation has only one solution which satisfies the initial condition that

$T_g = T_{gi}$  when  $t = 0$ , i.e.

$$\frac{T_g - (T_w)_{z=0}}{T_{gi} - (T_w)_{z=0}} = \exp\left(-\frac{h_a + h_w}{C^*} t\right) \quad (B - 16)$$

where (B -14) is used to determine the final value of  $T_g$ , i.e.  $(T_w)_{z=0}$  which is a function of  $T_{aw}$ .

It must be noted that the heat-transfer-coefficient appears as a term in the time constant of equation (B -15) and the adiabatic wall temperature affects only amplitude of its solution (B -16). This point can be an advantage when the heat transfer has to be measured under experimental conditions in which there are large local-variations of the temperature difference  $(T_w - T_{aw})$ , as described in Sections 4.4.2. and 5.1.

#### B.4. Equivalent Thermal-Capacity of the Thin-Film-Gauge Calorimeter

The gauge temperature (temperature indicated by the thin-film gauge),  $T_g$ , and the equivalent thermal-capacity per unit area of the calorimeter,  $C^*$ , are related to the temperature distribution in the glass-plate by

$$T_g = \int_s (T_w)_{z=0} ds / \int_s ds \quad (B - 17)$$

and

$$C^* = \int_s \int_z \rho_w C_w T_w dz ds / T_g \quad (B - 18)$$

where  $s$  and  $Z$  are the integration domains defined by the surface area of the calorimeter, and its depth, respectively.

Strictly, discussion of the transient temperature-distribution involves taking account of the thermal penetration depth,  $2\sqrt{\alpha t}$  where  $\alpha$  is the thermal diffusivity. In the present case, the penetration depth for Pyrex-glass is 0.07 inches for a heat pulse of 1 second duration, the glass-plate thickness is 0.058 inches and the time constant of equation (B -16) is of the order of 1 - 10 seconds. Hence it is considered that ignoring the penetration depth does not produce noticeable errors in estimating  $C^*$ .

It can be assumed that the temperature in the inner wall is uniform and constant ( $T_{WT}$ ). Then, under nearly steady conditions ( $dT_w/dt = 0$ ), the one-dimensional heat equation (B - 4) gives a linear solution for the temperature distribution through the glass plate, i.e.

$$T_w = (T_w)_{z=0} - [T_{WT} - (T_w)_{z=0}] z/d \quad (B -19)$$

where  $d$  is the thickness of the glass plate. This temperature distribution suggests some types of thermal models to determine the equivalent thermal capacity.

The simplest model is that the thin-film gauge provides constant temperature over its surface and (B -19) is applied throughout the whole region, (Fig.B4a). In this case, the equivalent thermal capacity is given by

$$C^* = \frac{1}{2} \rho_w C_w d \quad (B -20)$$

However, this value of the thermal capacity gives poor agreement with the experimental results for bare-plate heat-transfer measurements. Moreover, it is physically unrealistic to have discontinuities in the temperature distribution. The best agreement with the experimental results

for a bare flat plate is obtained using the 'parabolic thermal-model', as described in Section 3.5.2. This model has a parabolic surface-temperature distribution across the width of the gauge, as proposed by Busing (Ref.28), and a parabolic region of thermal influence of maximum depth  $d$ , (Fig.B4b). The equivalent thermal capacity of this model is

$$C^* = \frac{1}{3} \rho_w C_w d \quad (B - 21)$$

When the glass-plate surface is heated by the thin-film gauge and the temperature distribution in the calorimeter reaches a steady state, the maximum temperature in the glass-plate layer is at the surface. The temperature distribution through the layer is given by (B -19). When the 'heating process' is changed to the 'cooling process' to indicate the gauge-temperature time-history corresponding to (B -16), the temperature distribution through the layer changes and the maximum temperature will occur at some point within the layer. The thin-film gauge on the wall surface operates with this 'locally' transitional surface-temperature variation and indicates a 'transitional period' in its temperature time history, see Fig.29a. After this temperature re-distribution in the calorimeter, it is difficult to estimate the equivalent thermal capacity. However, if the heated region of the glass plate is so thin (compared with the thermal penetration depth) that the calorimeter region can be treated as a lump, then it can be assumed that the equivalent thermal capacity estimated initially by (B -18) is still valid even after the re-distribution.

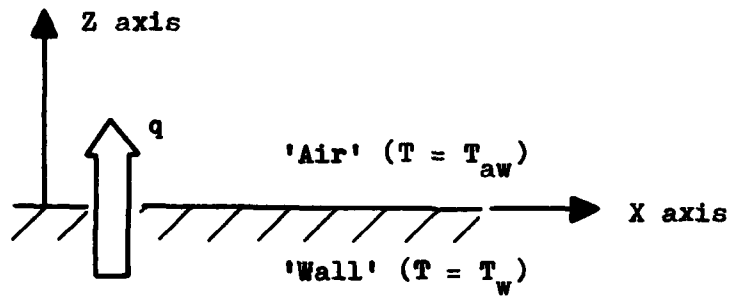


Fig. B1 One-Dimensional Thermal Field

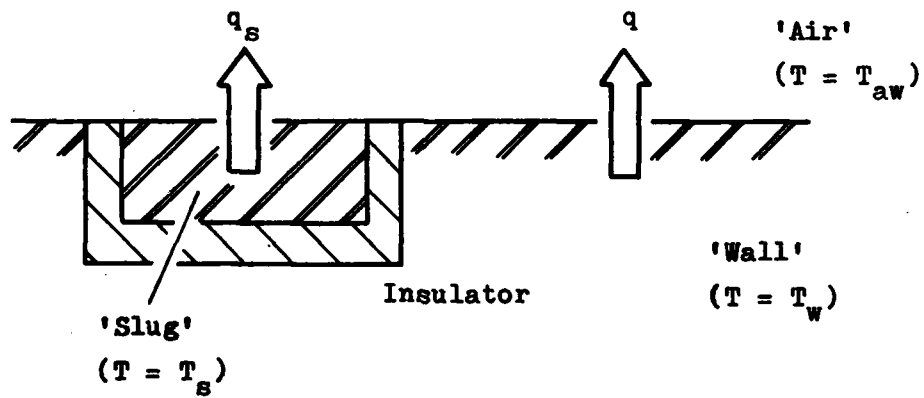


Fig. B2 Slug Calorimeter

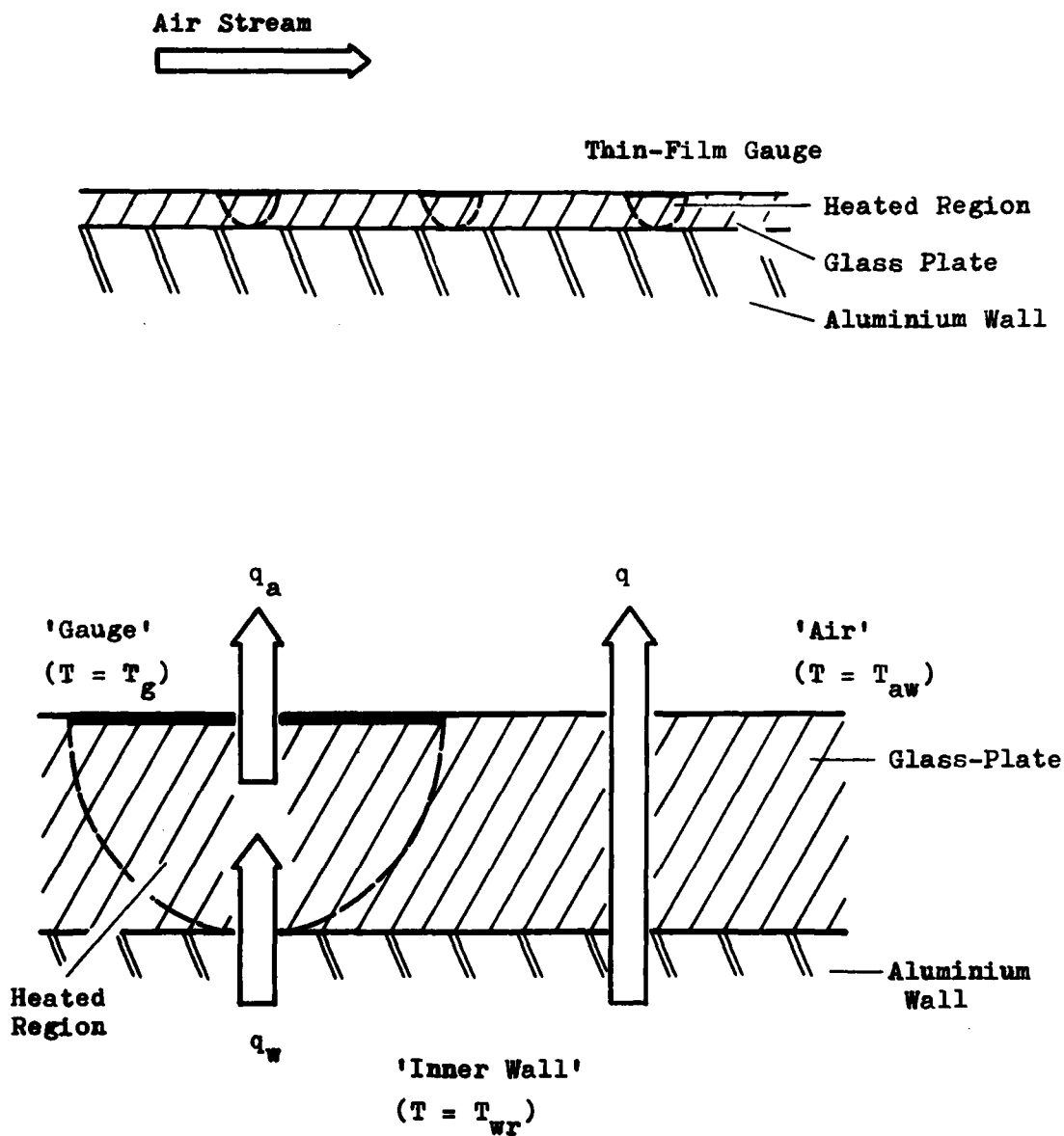
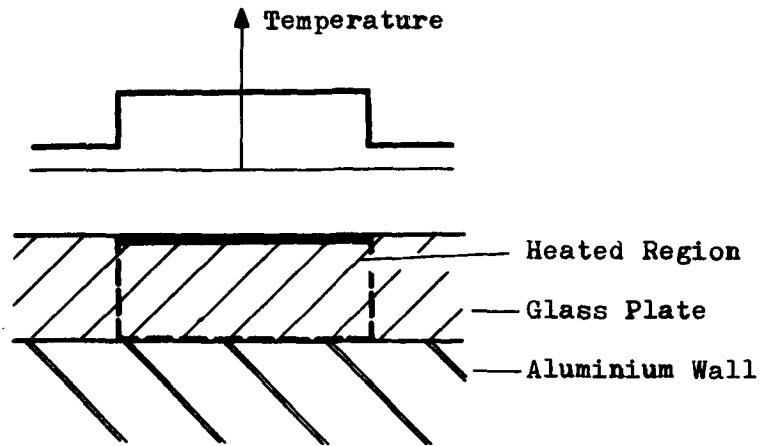
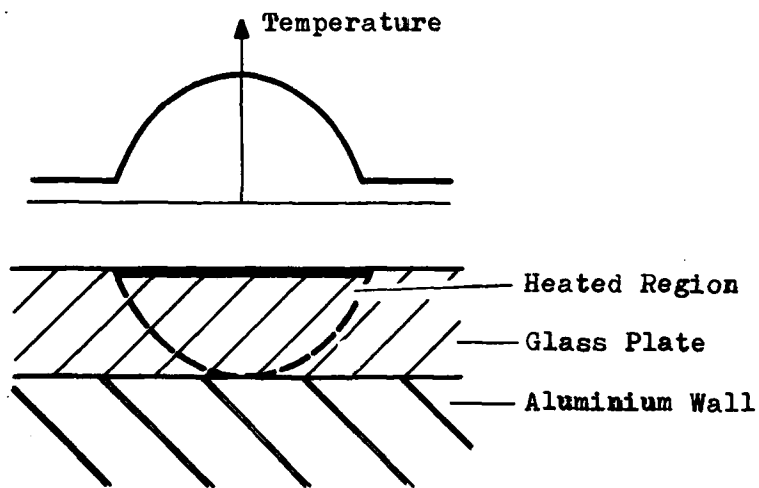


Fig. B3 Thin-Film Gauge Calorimeter

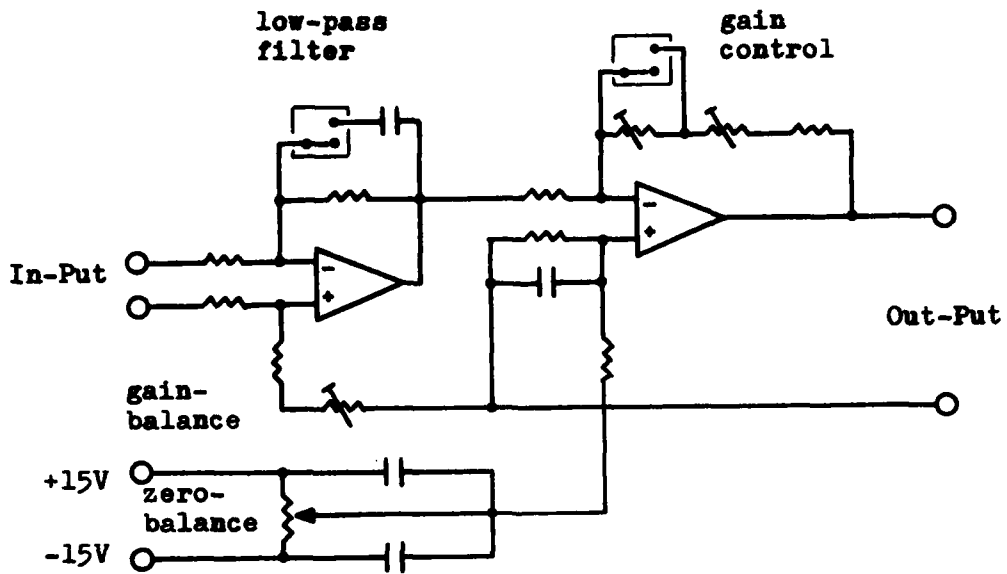


(a) Rectangular Model

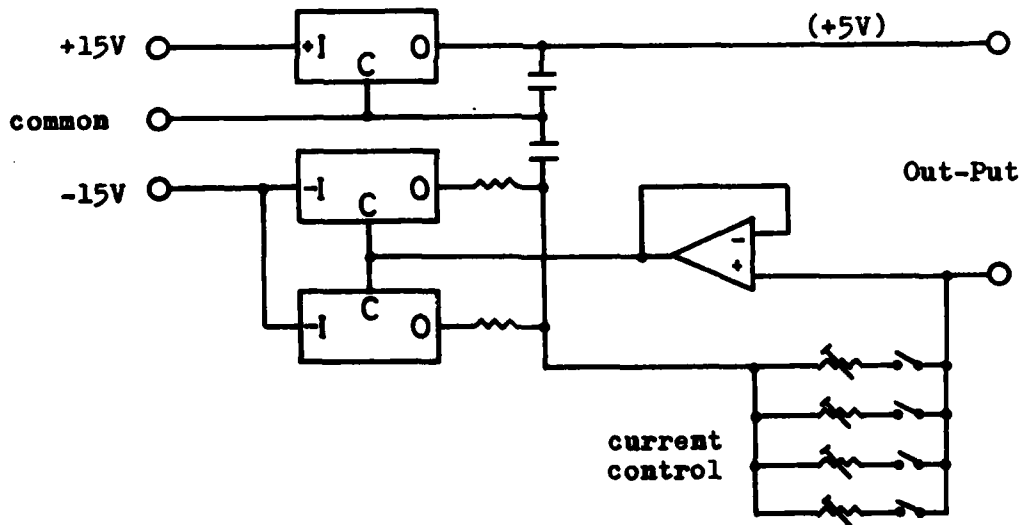


(b) Parabolic Model

Fig. B4 Equivalent Thermal-Capacity Models



(a) Differential Amplifier



(b) Current Regulator

Fig. B5 Electronic Circuit for the Thin-Film Gauge Calorimeter Technique

APPENDIX C

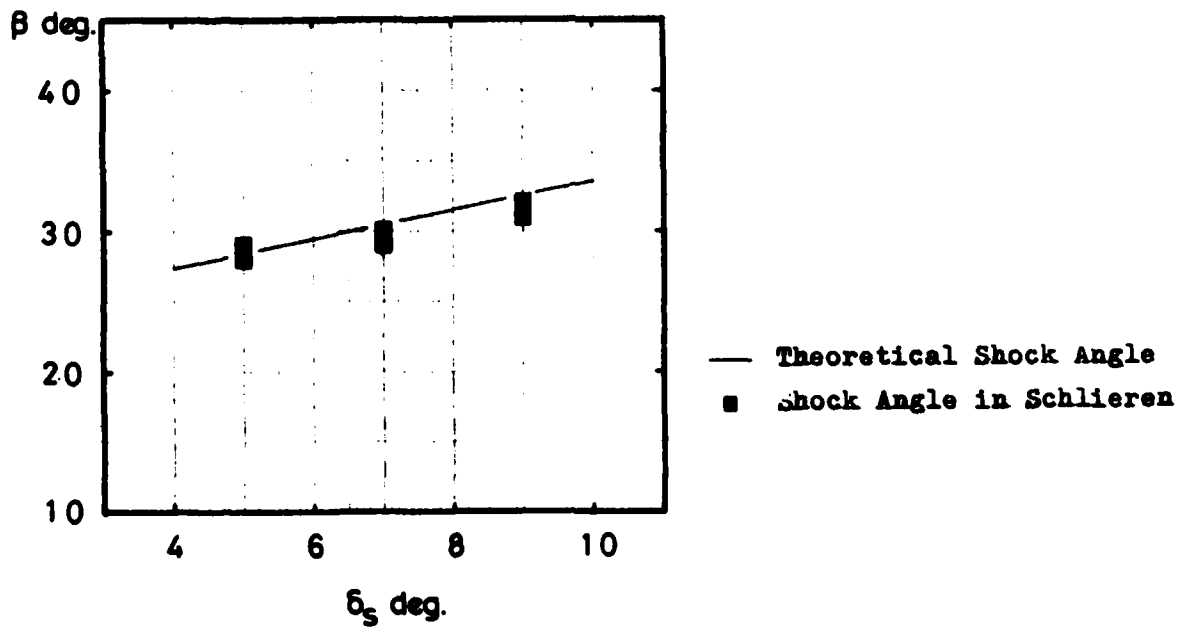
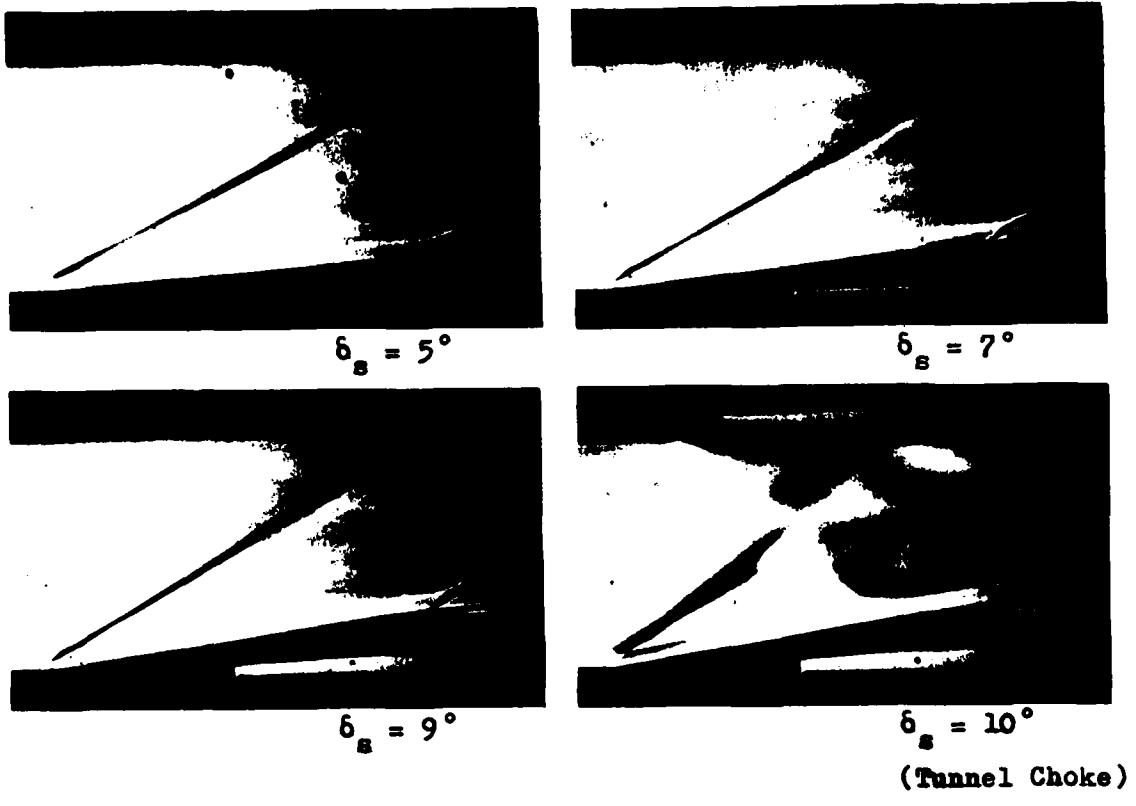


Fig. C1 Schlieren Pictures (Model A),  $M = 2.4$

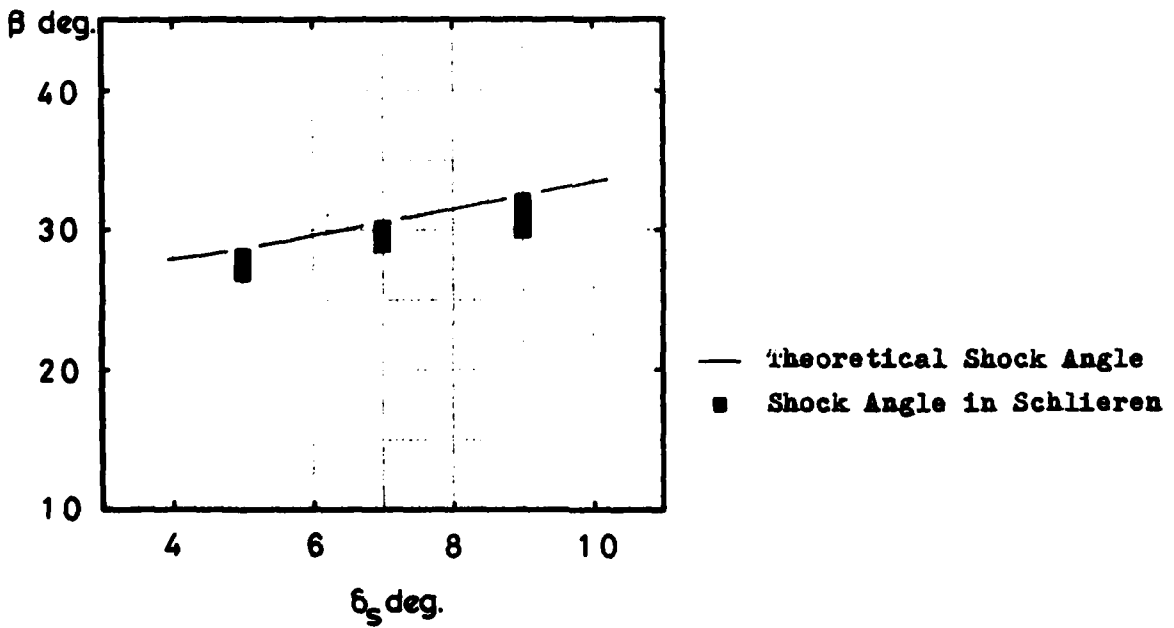
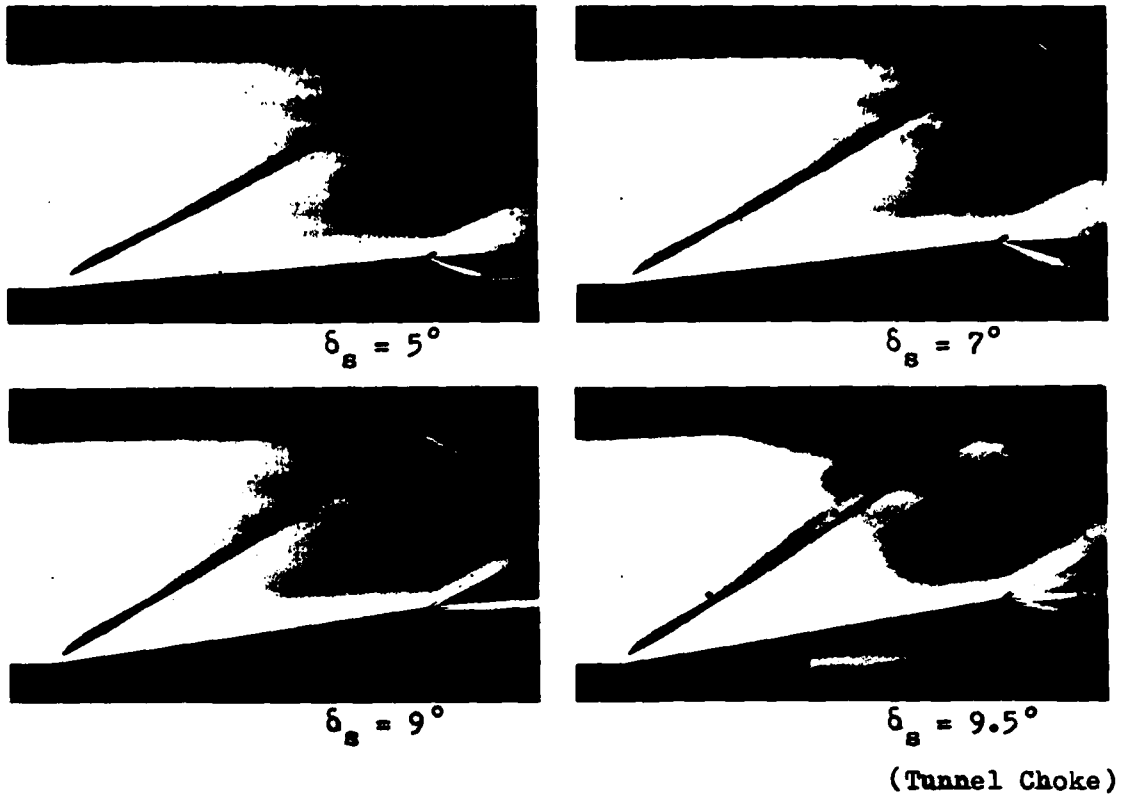


Fig. C2 Schlieren Pictures (Model AM),  $M = 2.4$

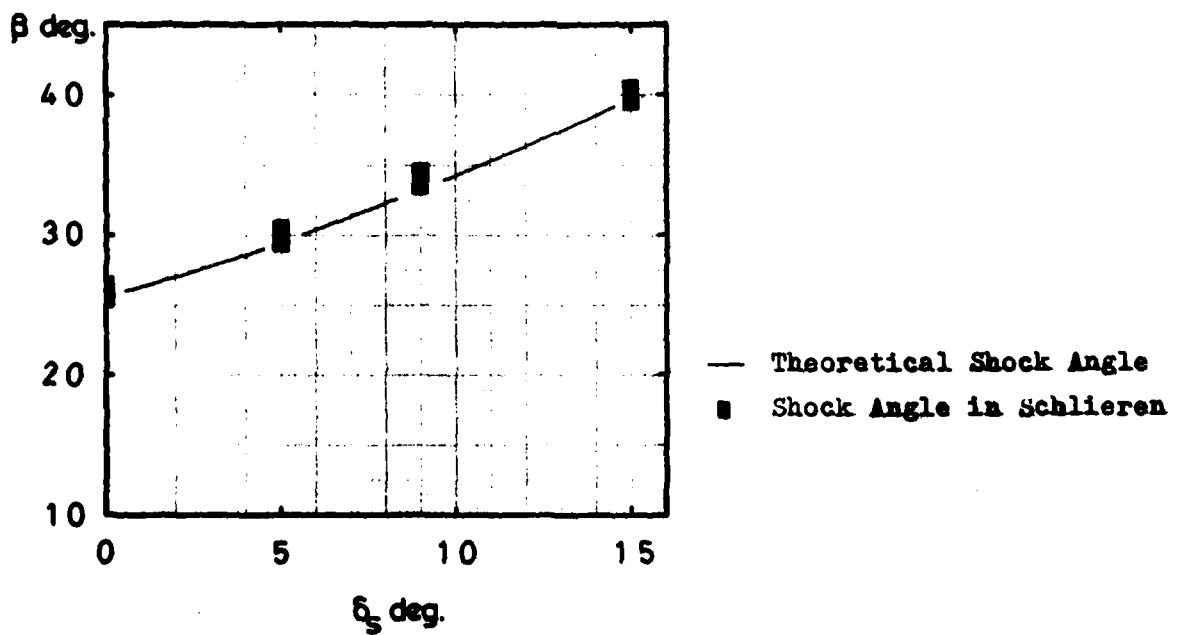
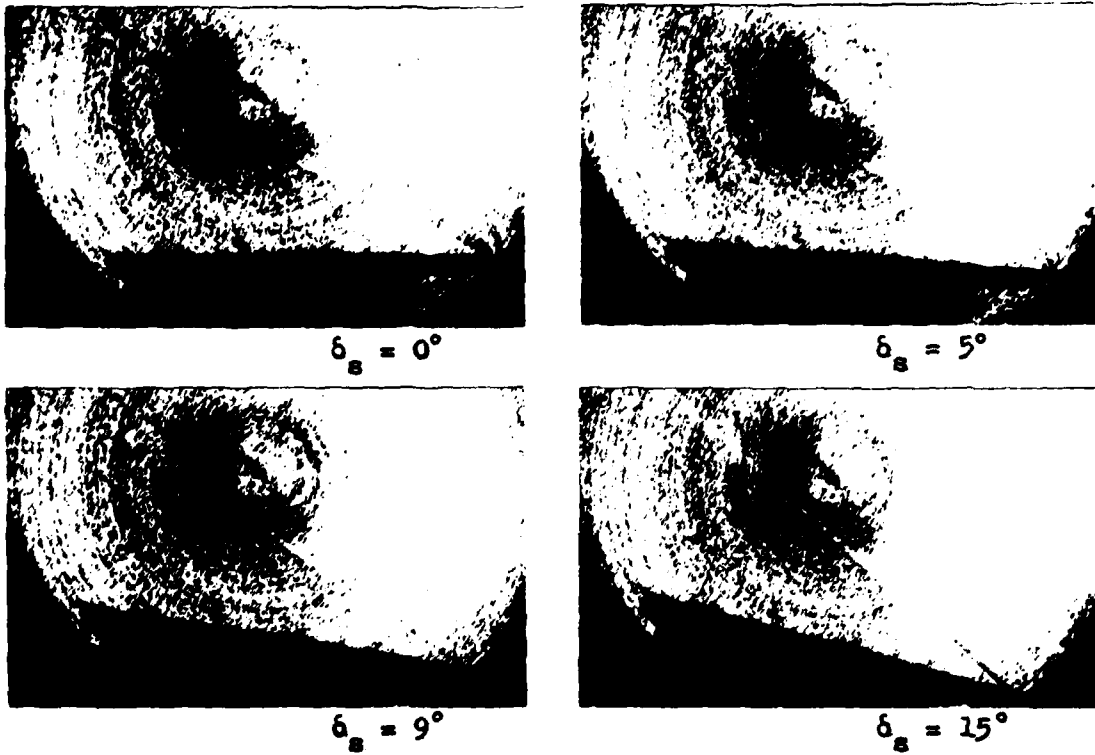
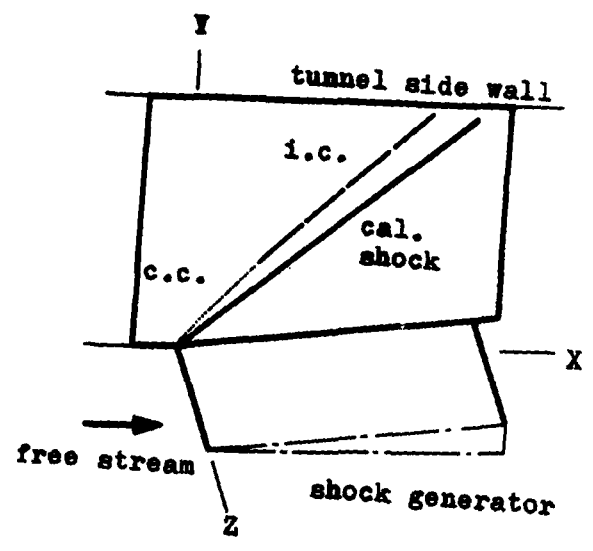


Fig. C3 Schlieren Pictures (Model B),  $M = 2.3$

APPENDIX D



c.c., complete convergence  
 i.c., incomplete convergence  
 cal. shock, calculated shock location

Fig. D1 Schematics of Oil-Flow Patterns

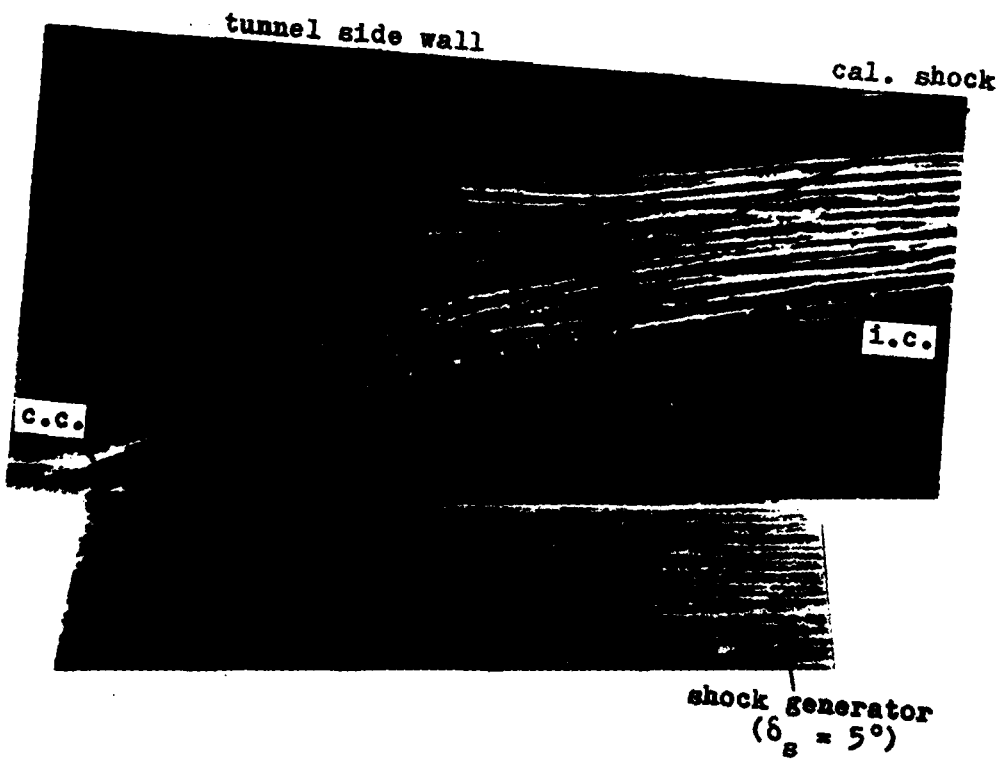


Fig. D2 Oil-Flow Patterns (Model A),  $M = 2.4$

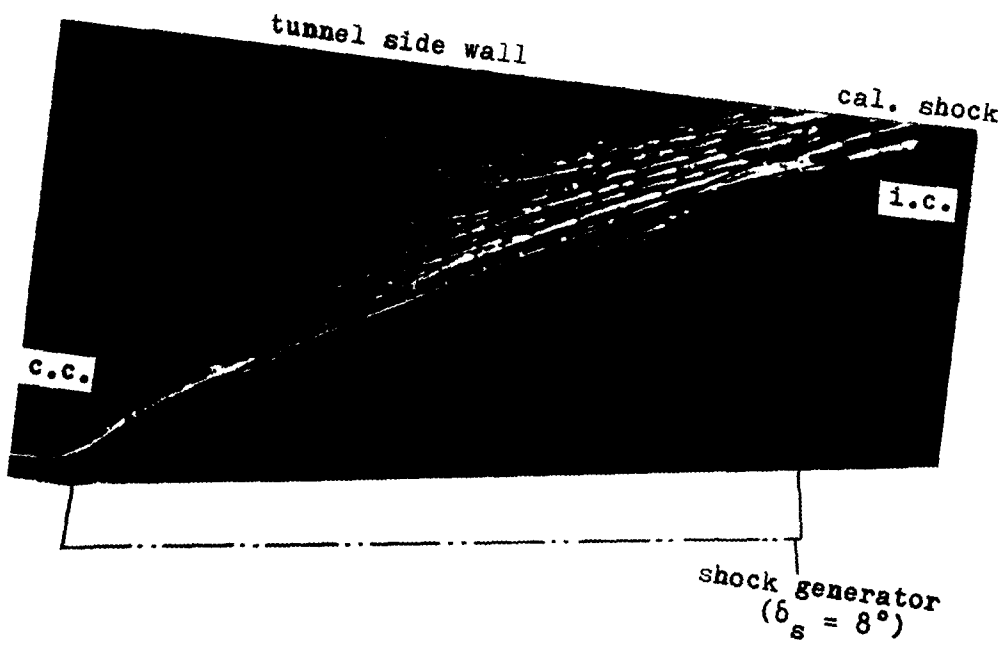
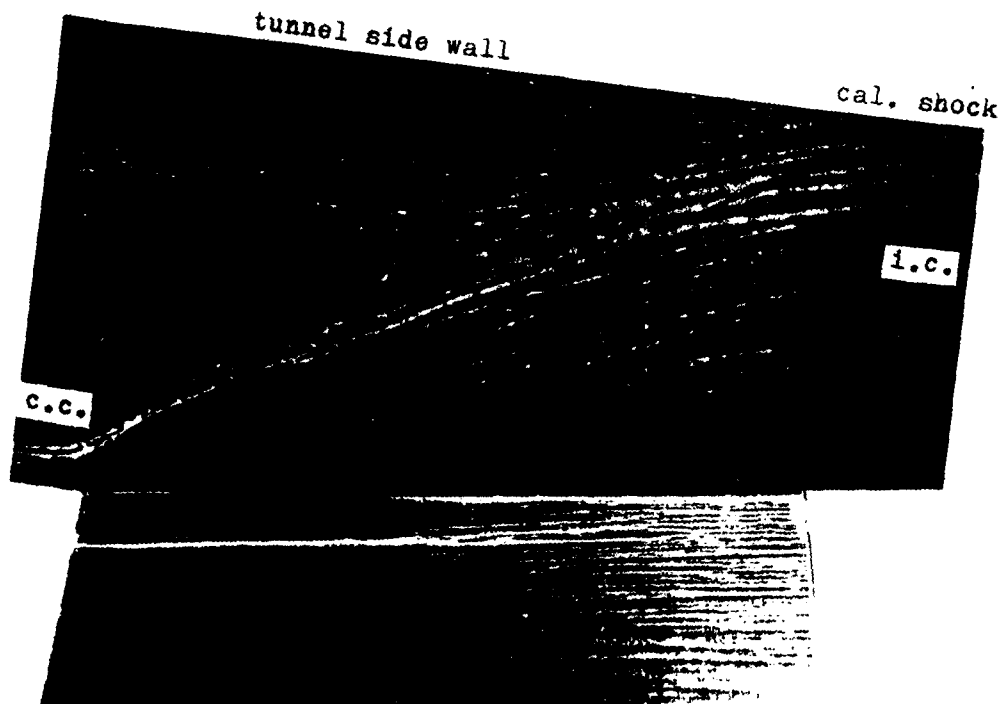
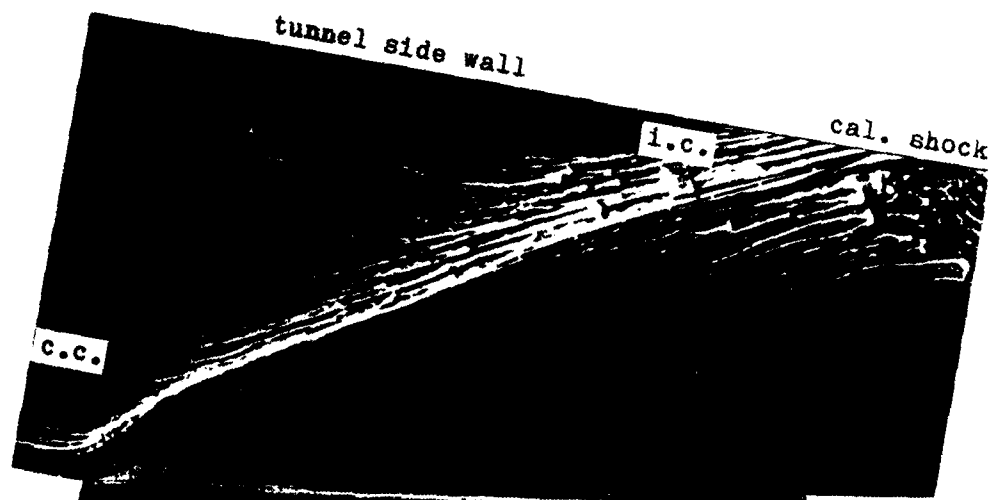
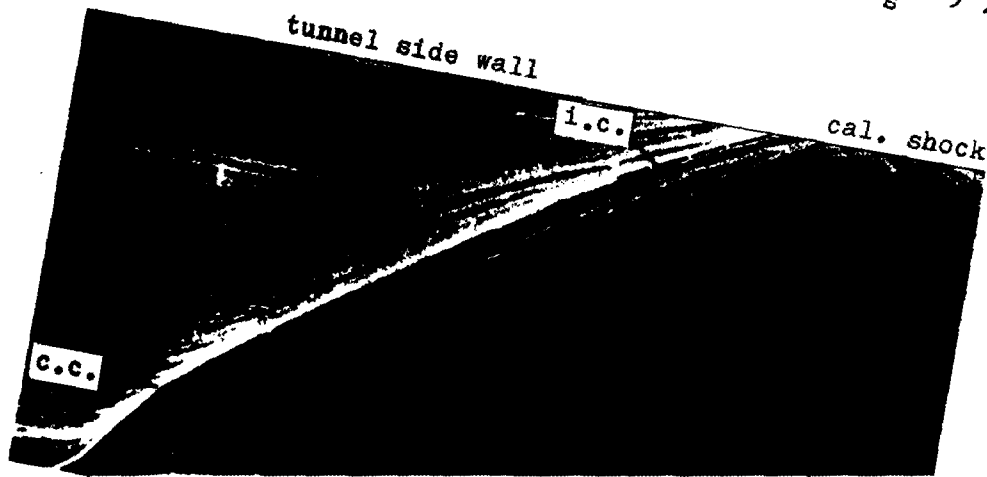


Fig. D2 Continued. (b)  $M = 2.4$



shock generator  
( $\delta_s = 9^\circ$ )



shock generator  
( $\delta_s = 10^\circ$ )

Fig. D2 Continued. (c)  $M = 2.4$

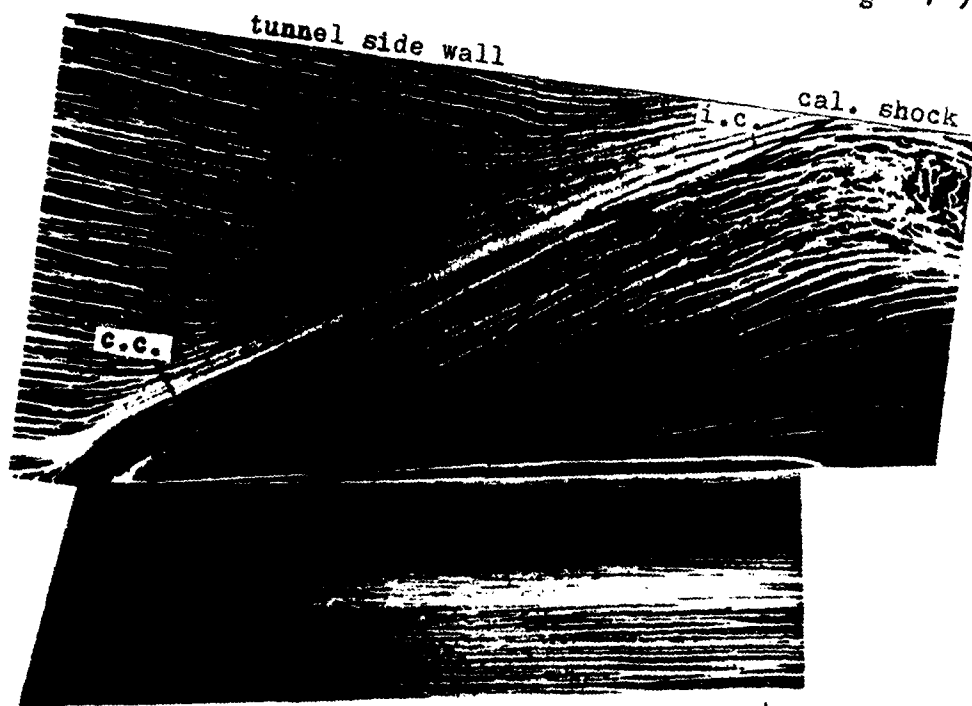
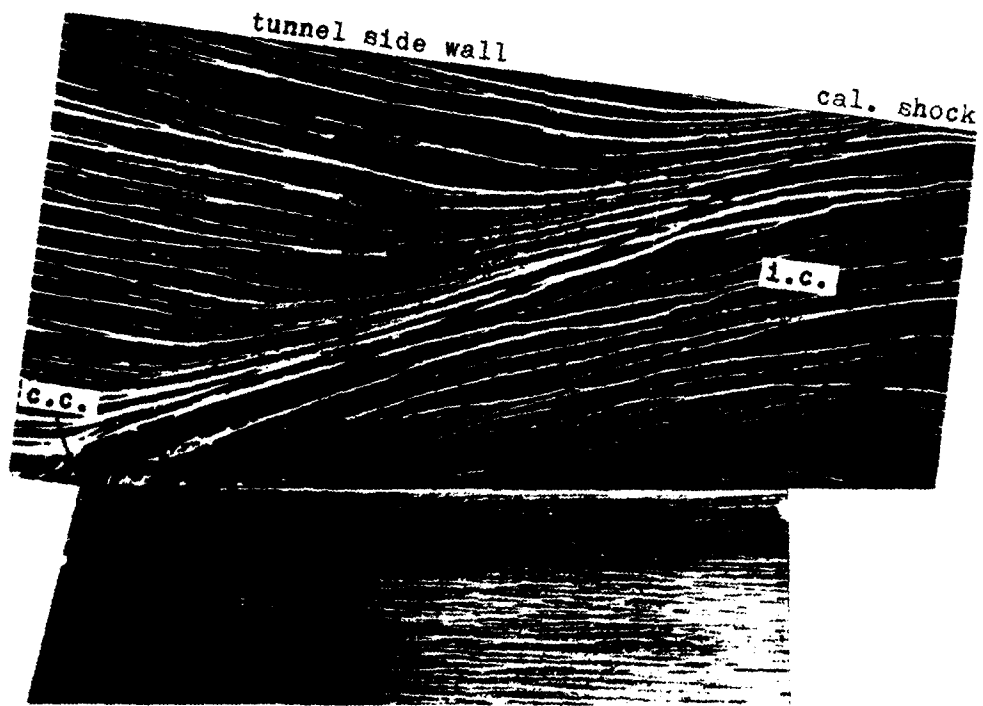


Fig. D3 Oil-Flow Patterns (Model AM),  $M = 2.4$

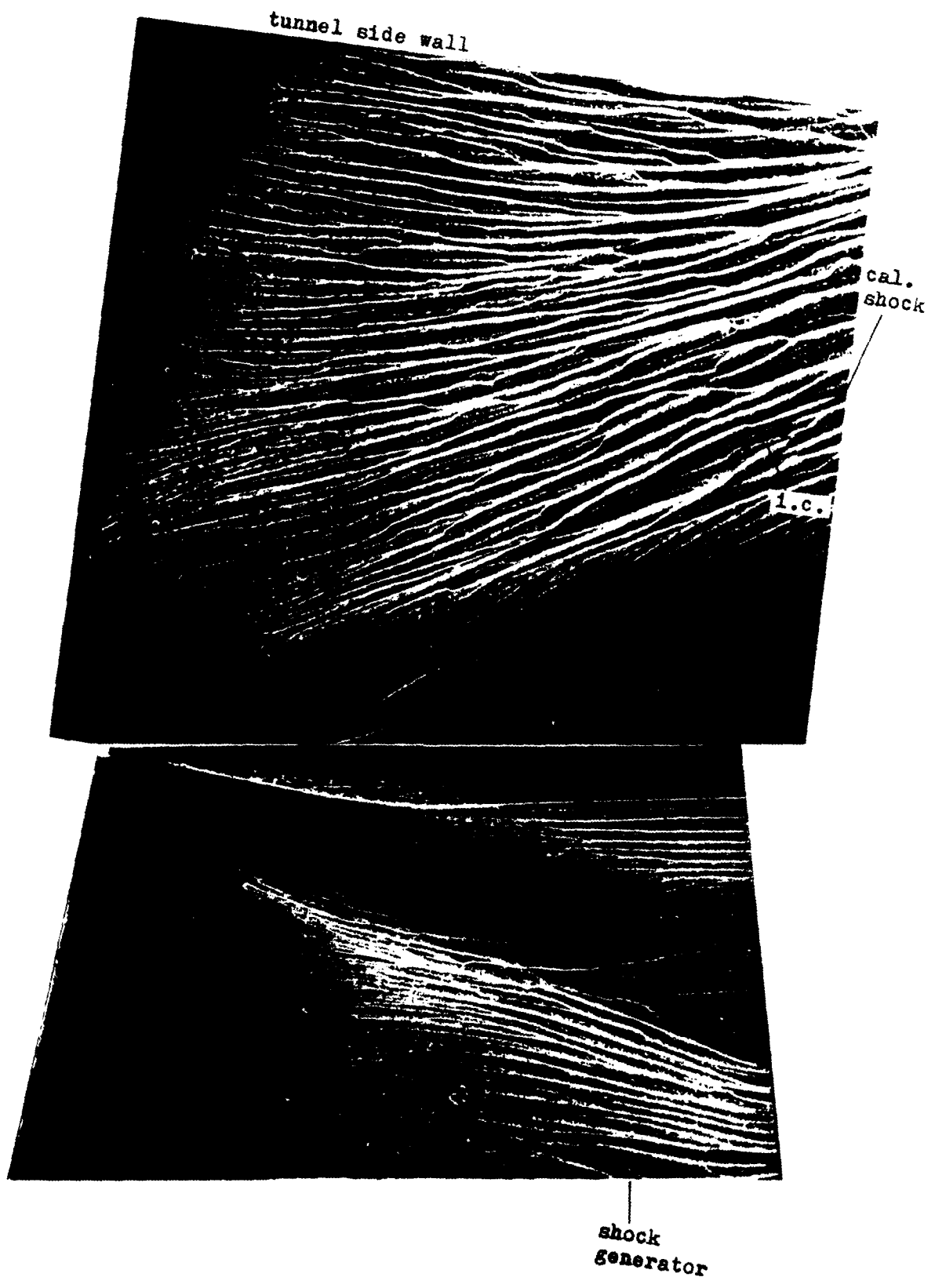


FIG. D4 Oil-Flow Patterns (Model B) (a)  $M = 2.3$ ,  $\delta_s = 7^\circ$

tunnel side wall

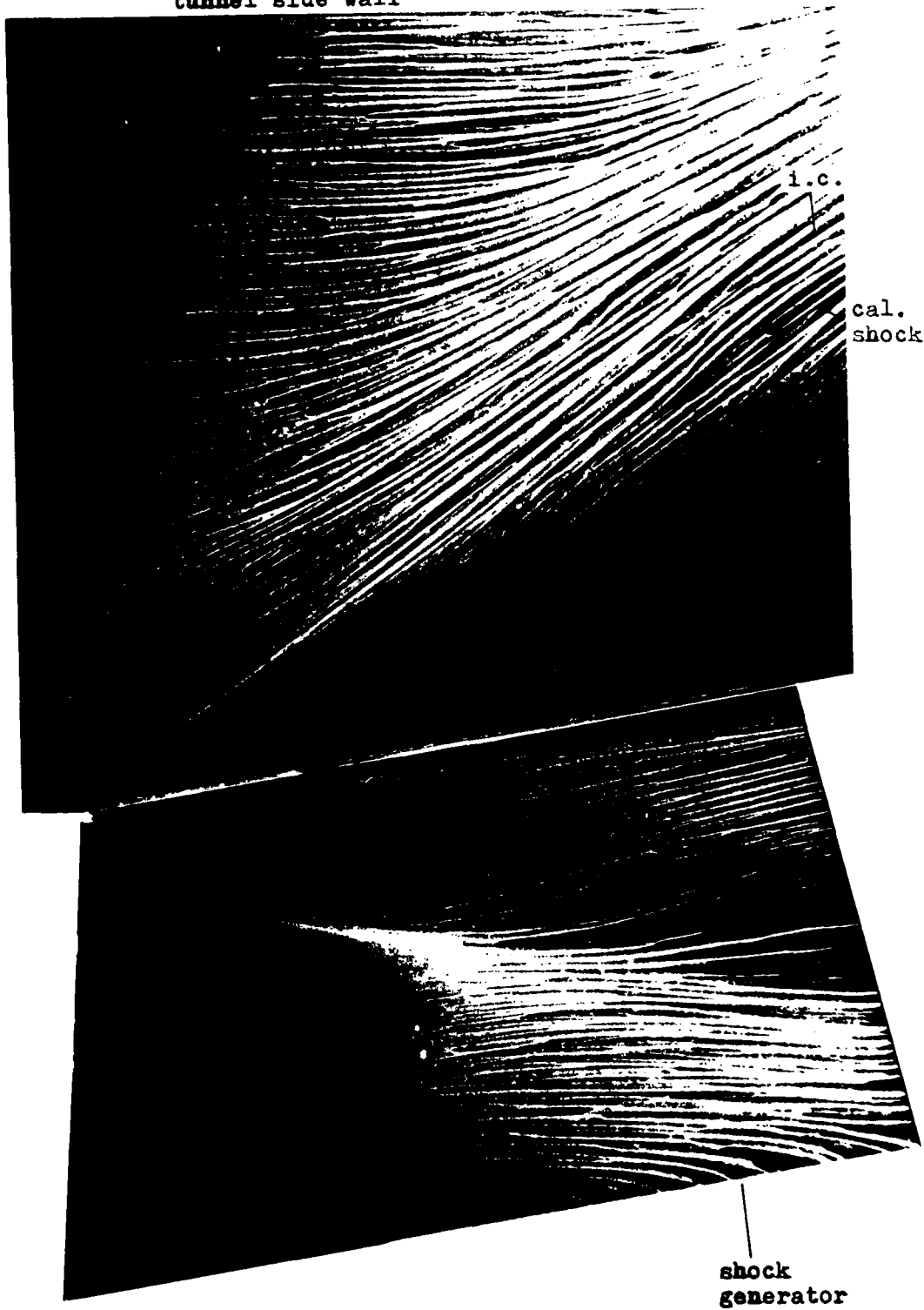


Fig. D4 Continued. (b)  $M = 2.3$ ,  $\delta_s = 9^\circ$

tunnel side wall

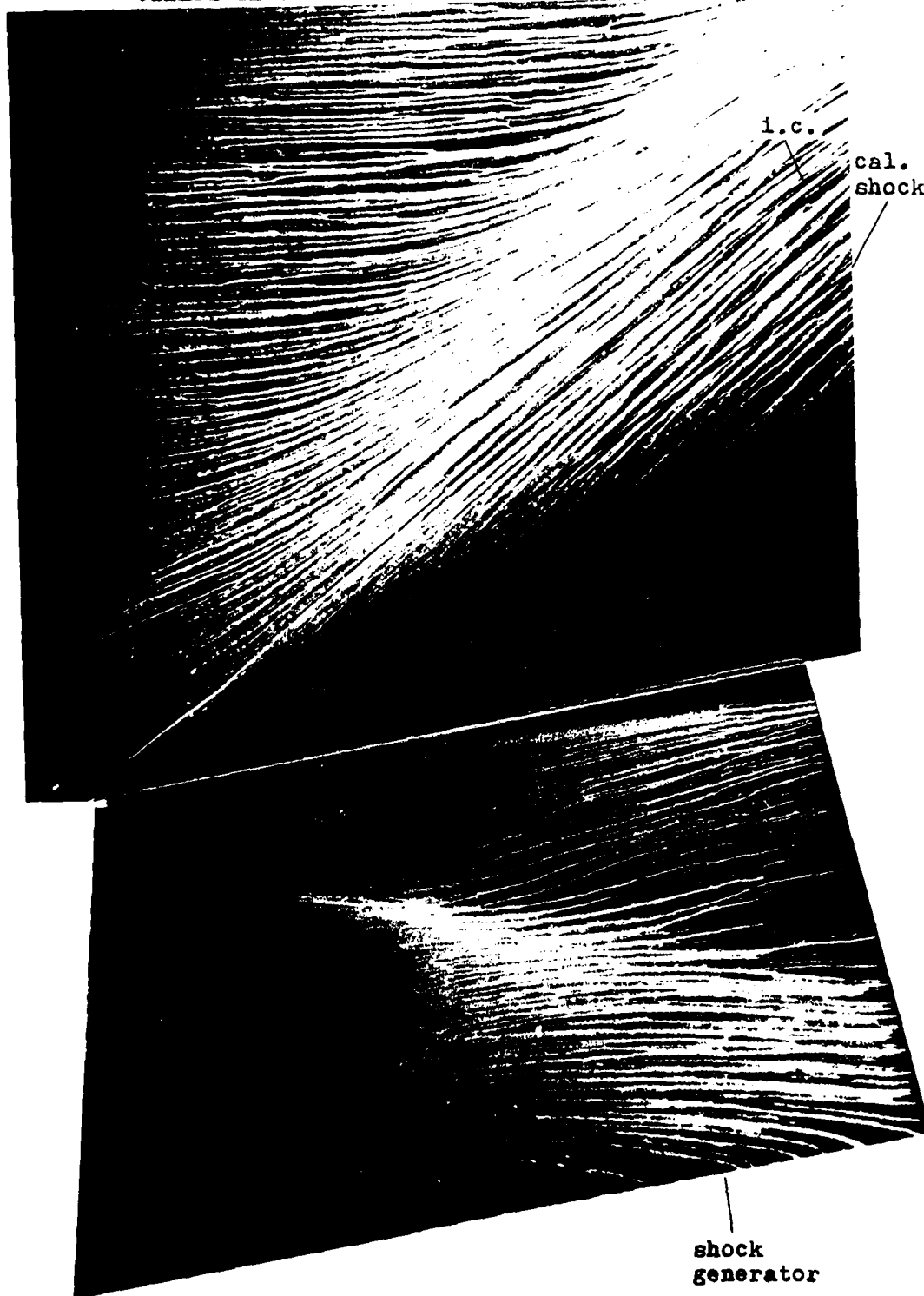


Fig. D4 Continued. (c)  $M = 2.3$ ,  $\delta_g = 10^\circ$

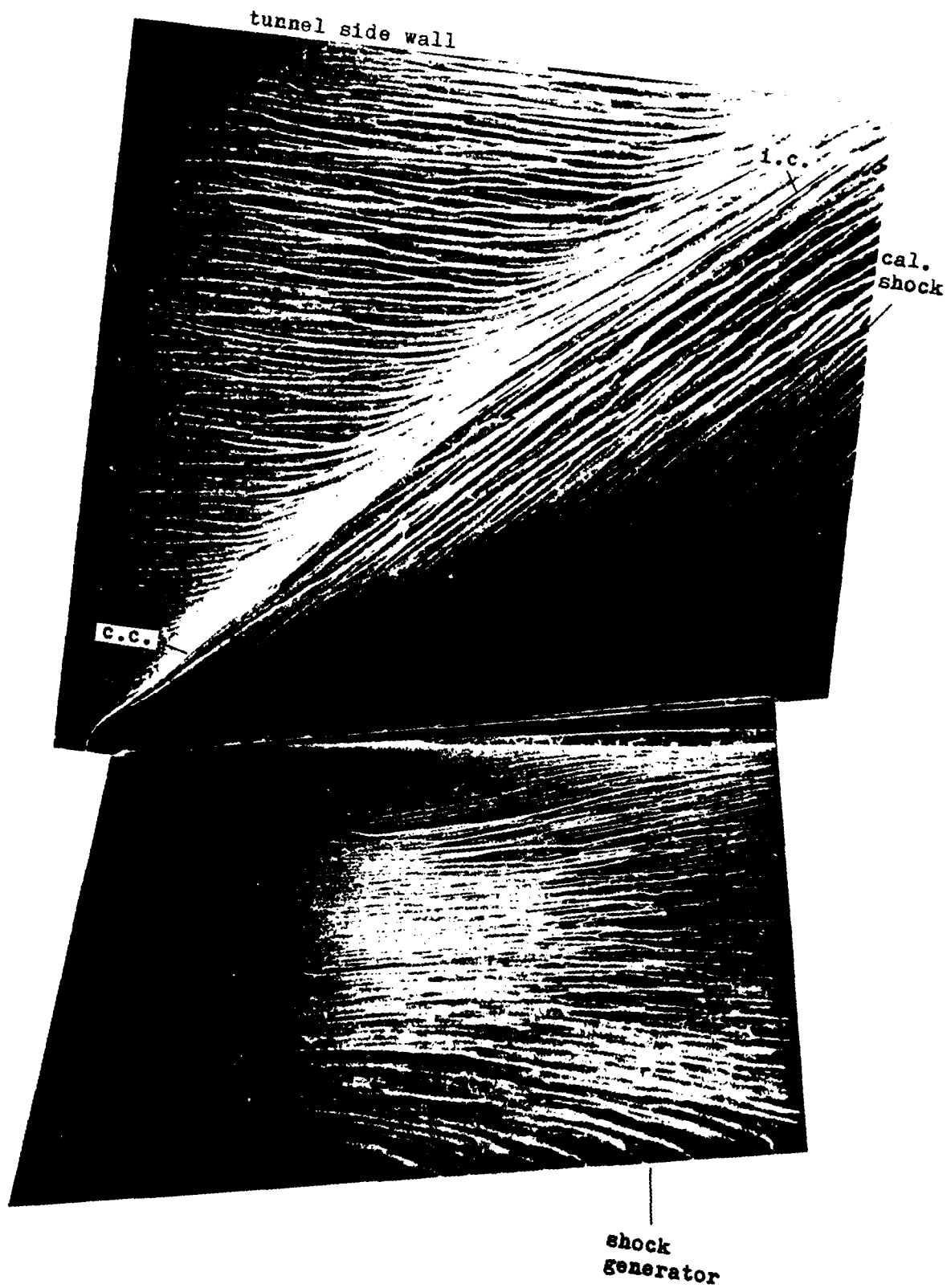


Fig. D4 Continued. (d)  $M = 2.3$ ,  $\delta_s = 11^\circ$

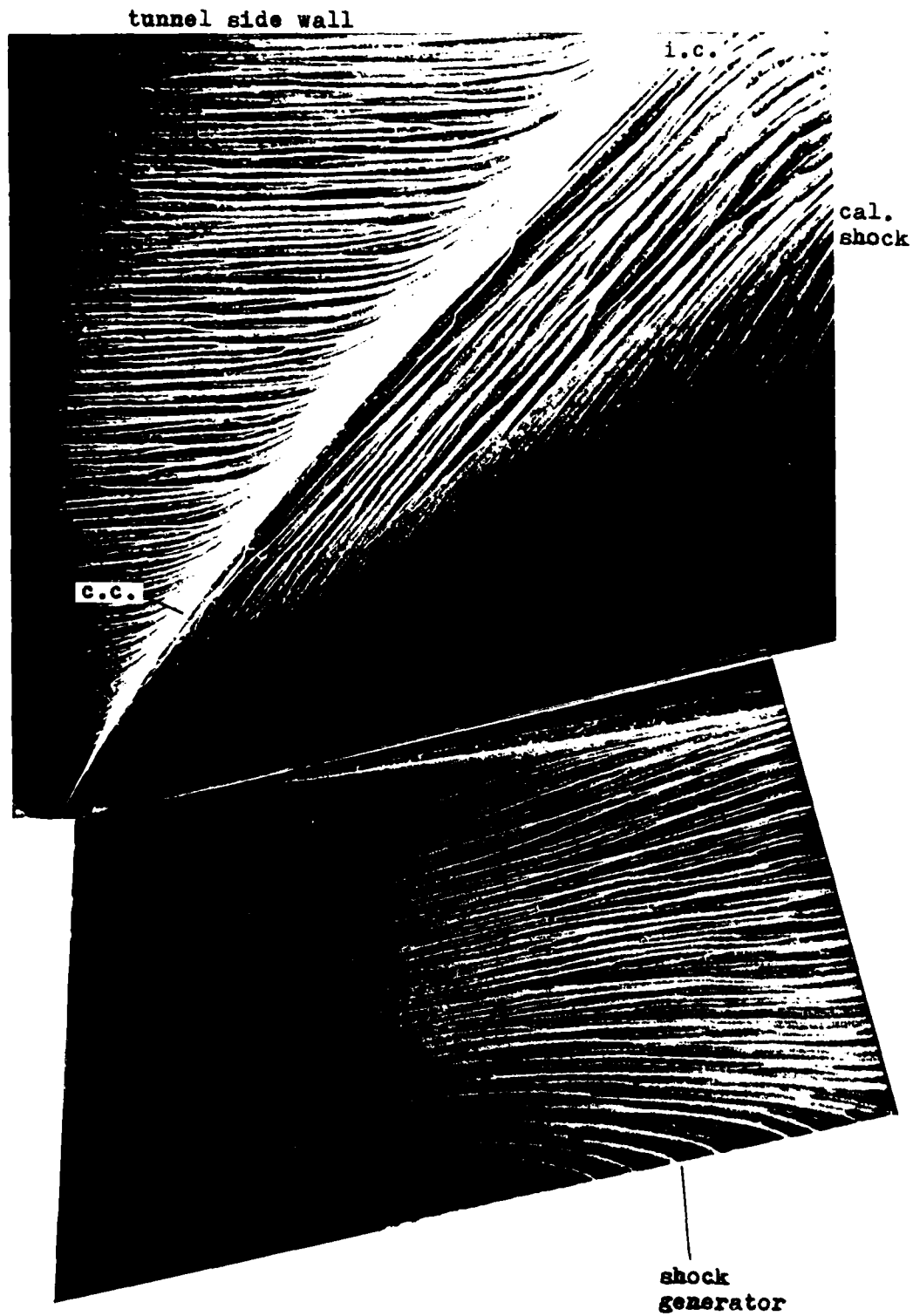


Fig. D4 Continued. (e)  $M = 2.3$ ,  $\delta_g = 13^\circ$

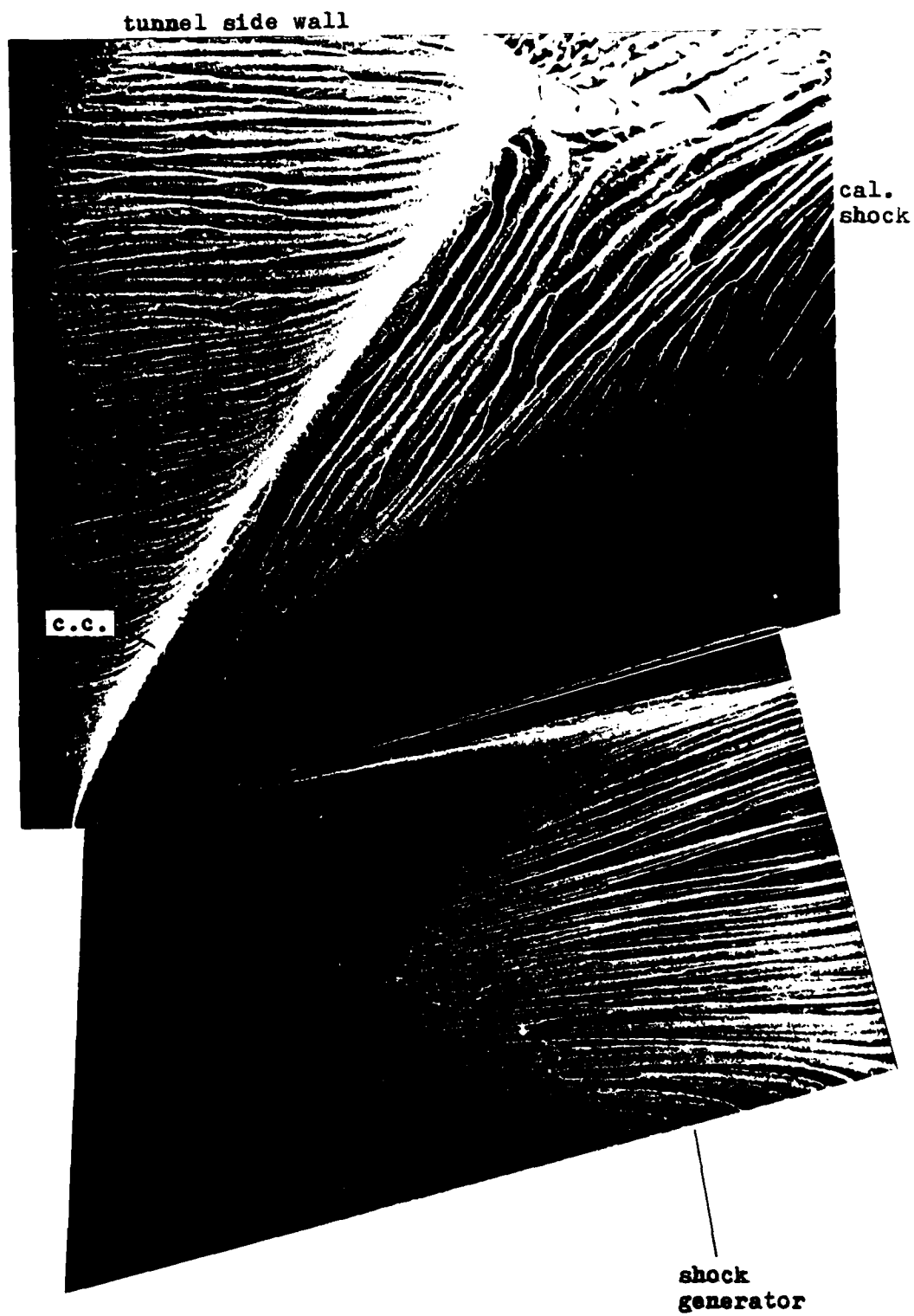


Fig. D4 Continued. (f)  $M = 2.3$ ,  $\delta_g = 15^\circ$

APPENDIX E

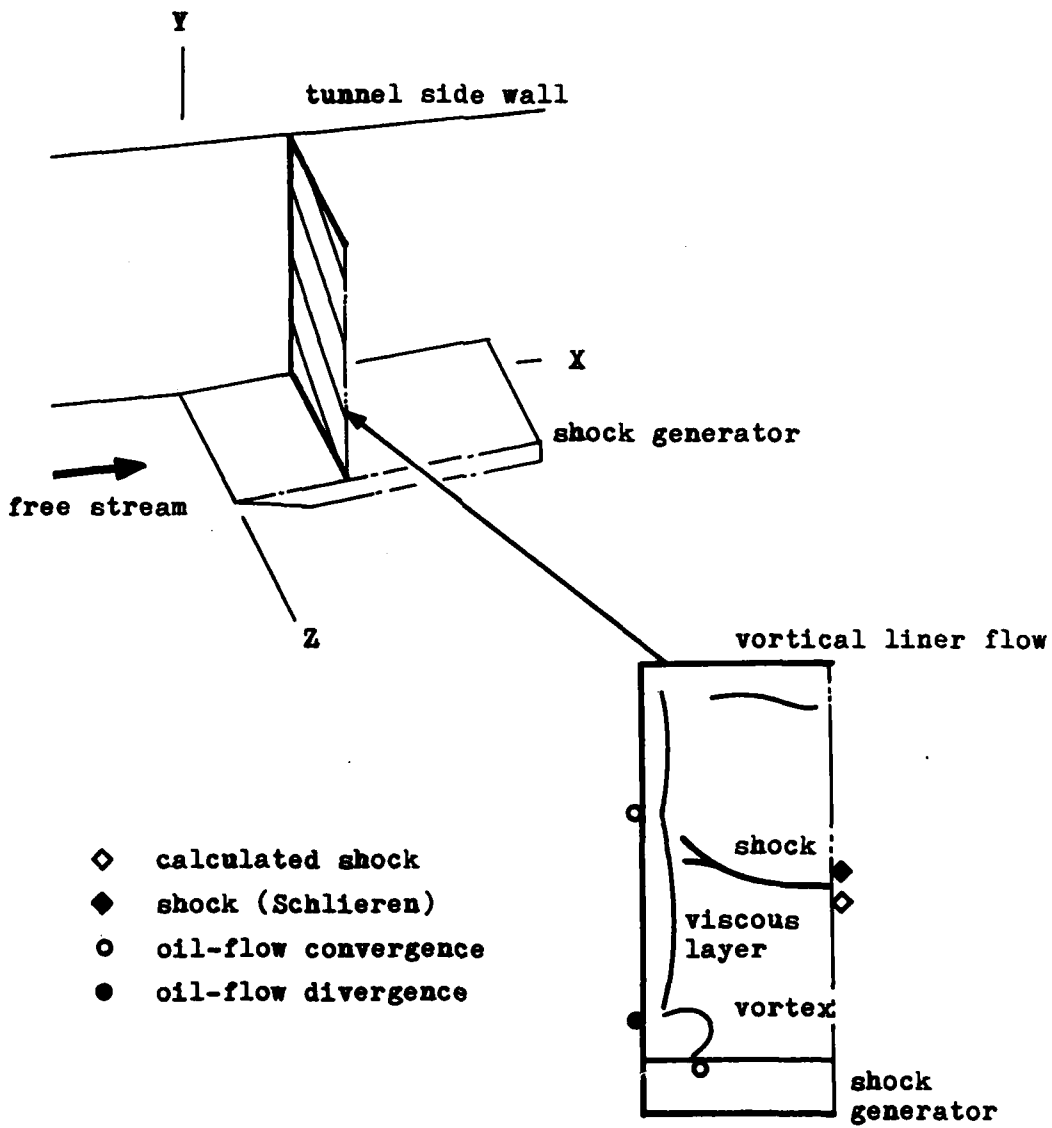


Fig. E1 Schematic of Vapour-Screen Pictures

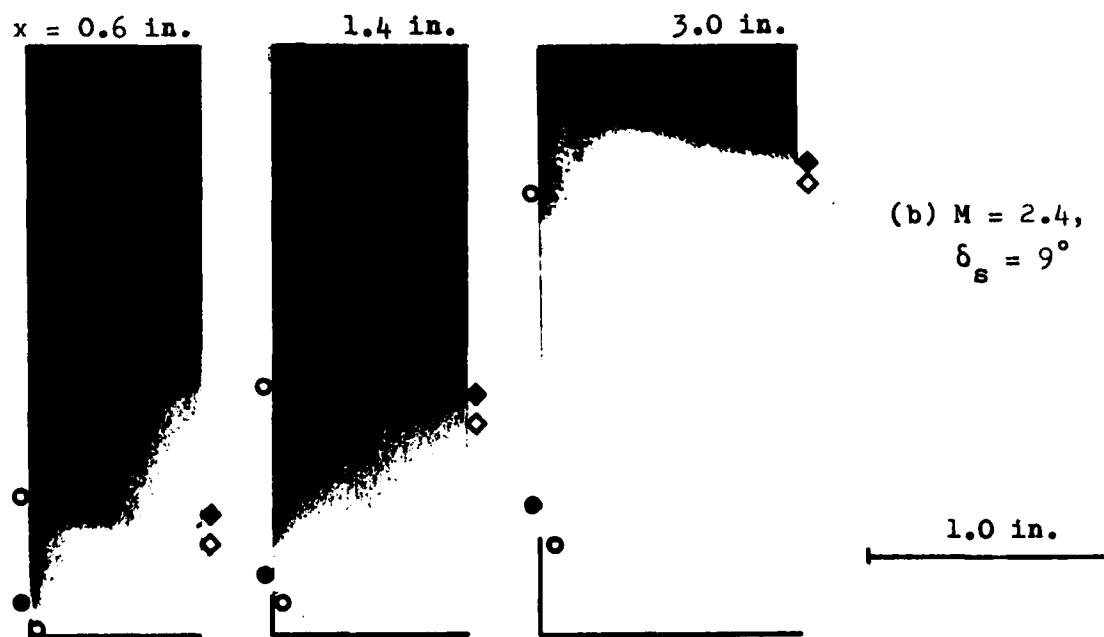
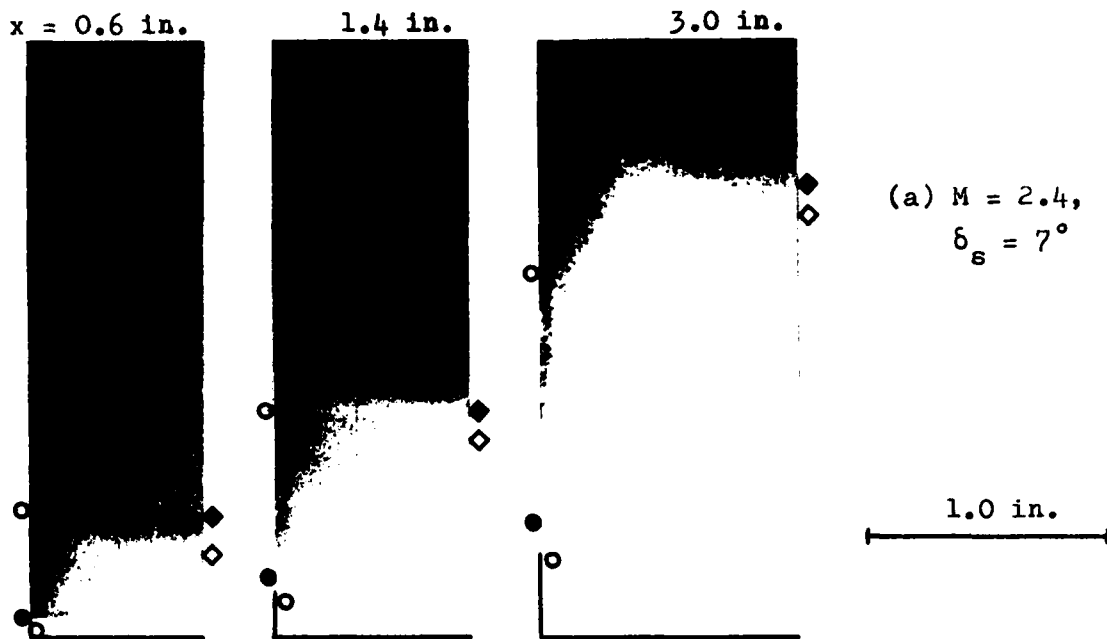


Fig. E2 Vapour-Screen Pictures (Model A)

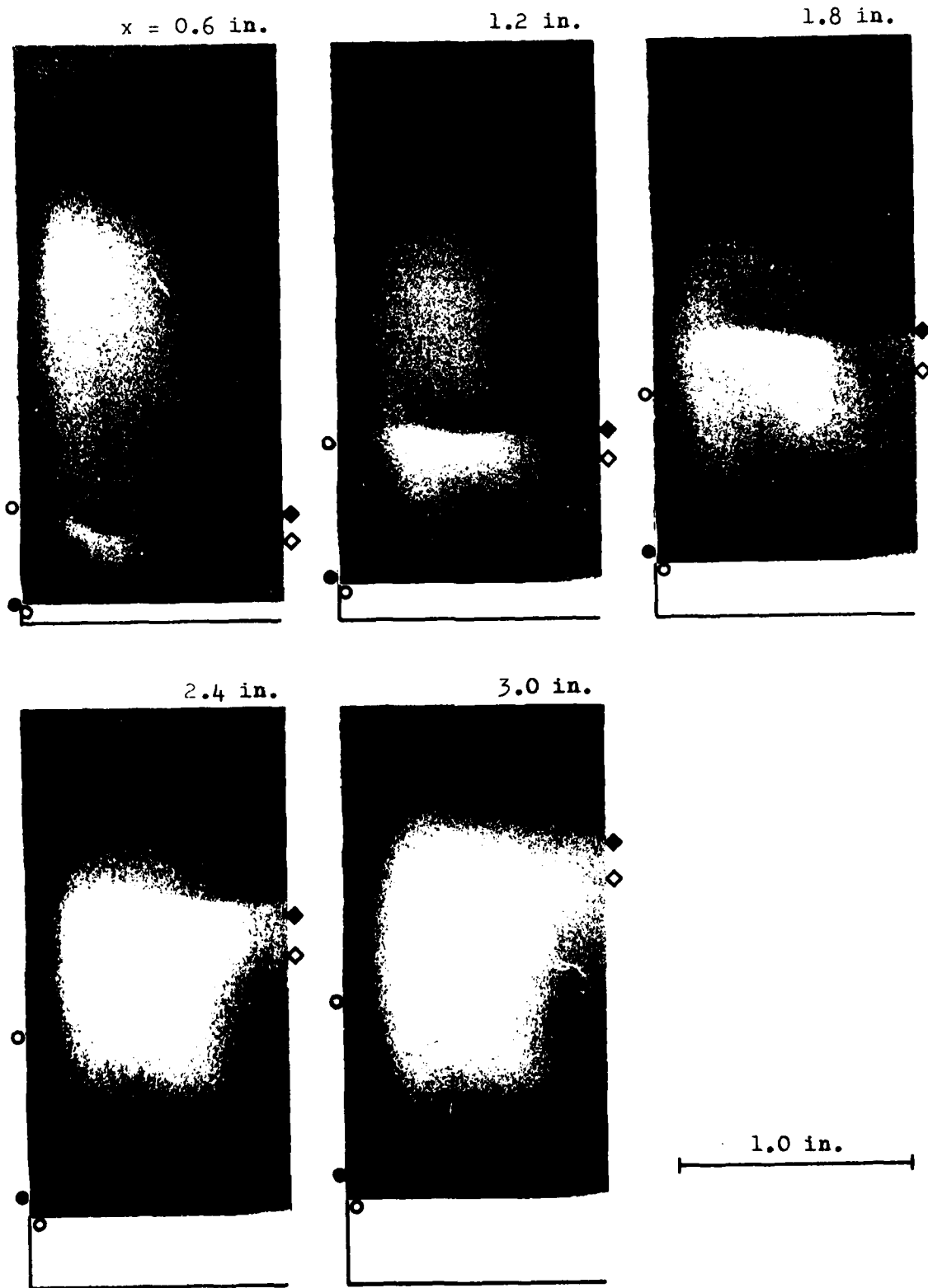


Fig. E3 Vapour-Screen Pictures (Model AM) (a)  $M = 2.4$ ,  $\delta_s = 7^\circ$

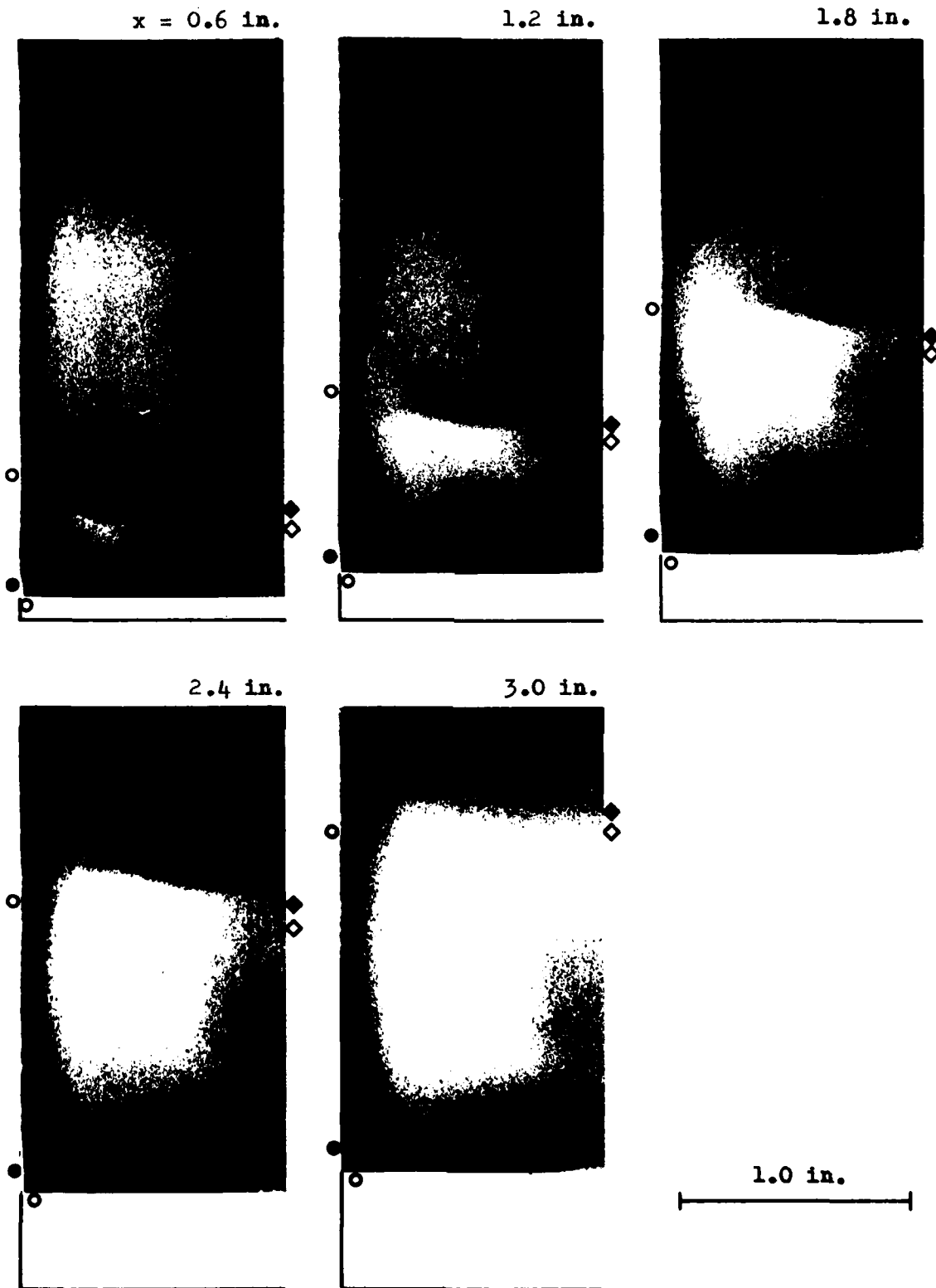


Fig. E3 Continued. (b)  $M = 2.4$ ,  $\delta_s = 9^\circ$

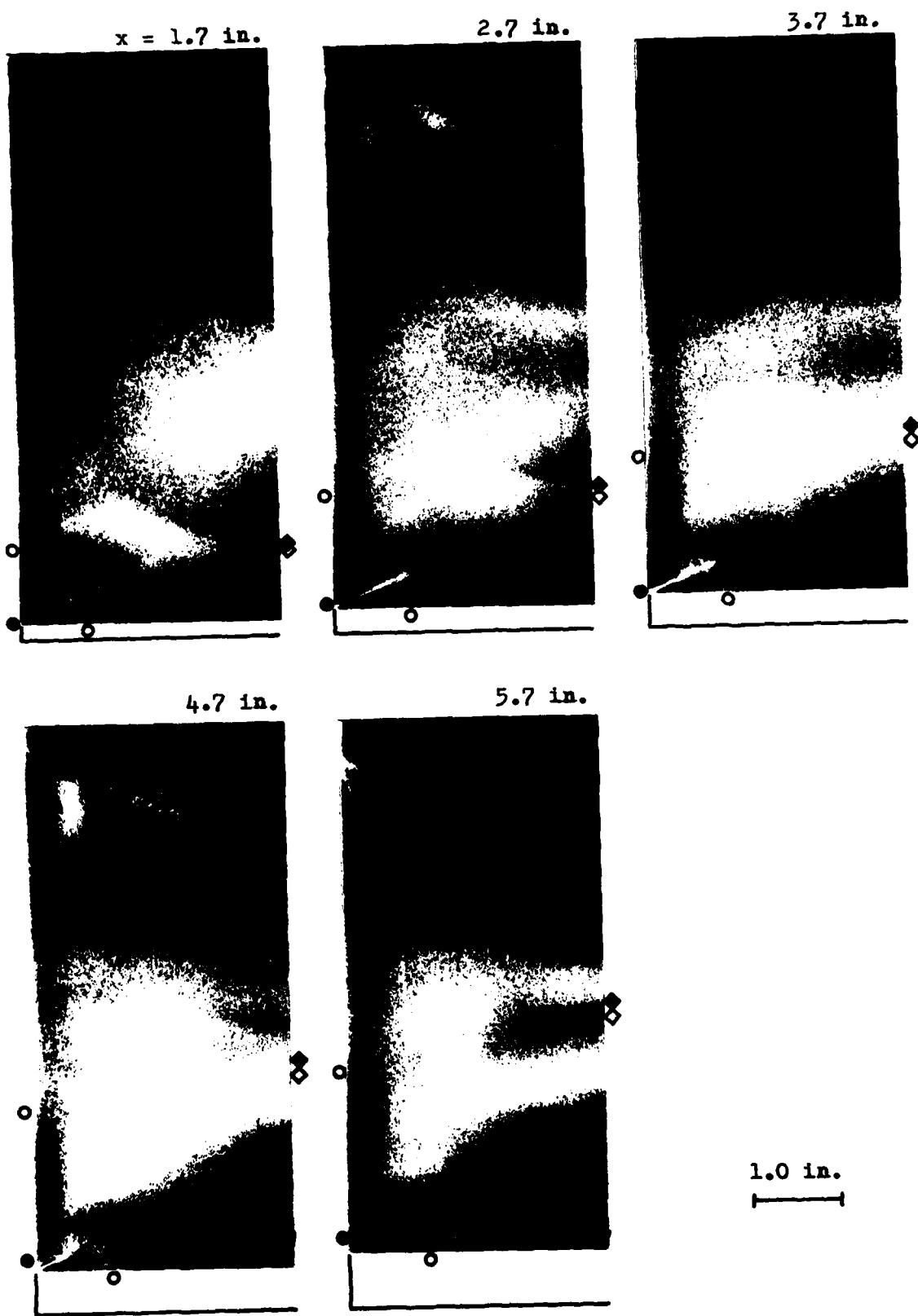


Fig. E4 Vapour-Screen Pictures (Model B) (a)  $M = 2.3$ ,  $\delta_s = 7^\circ$

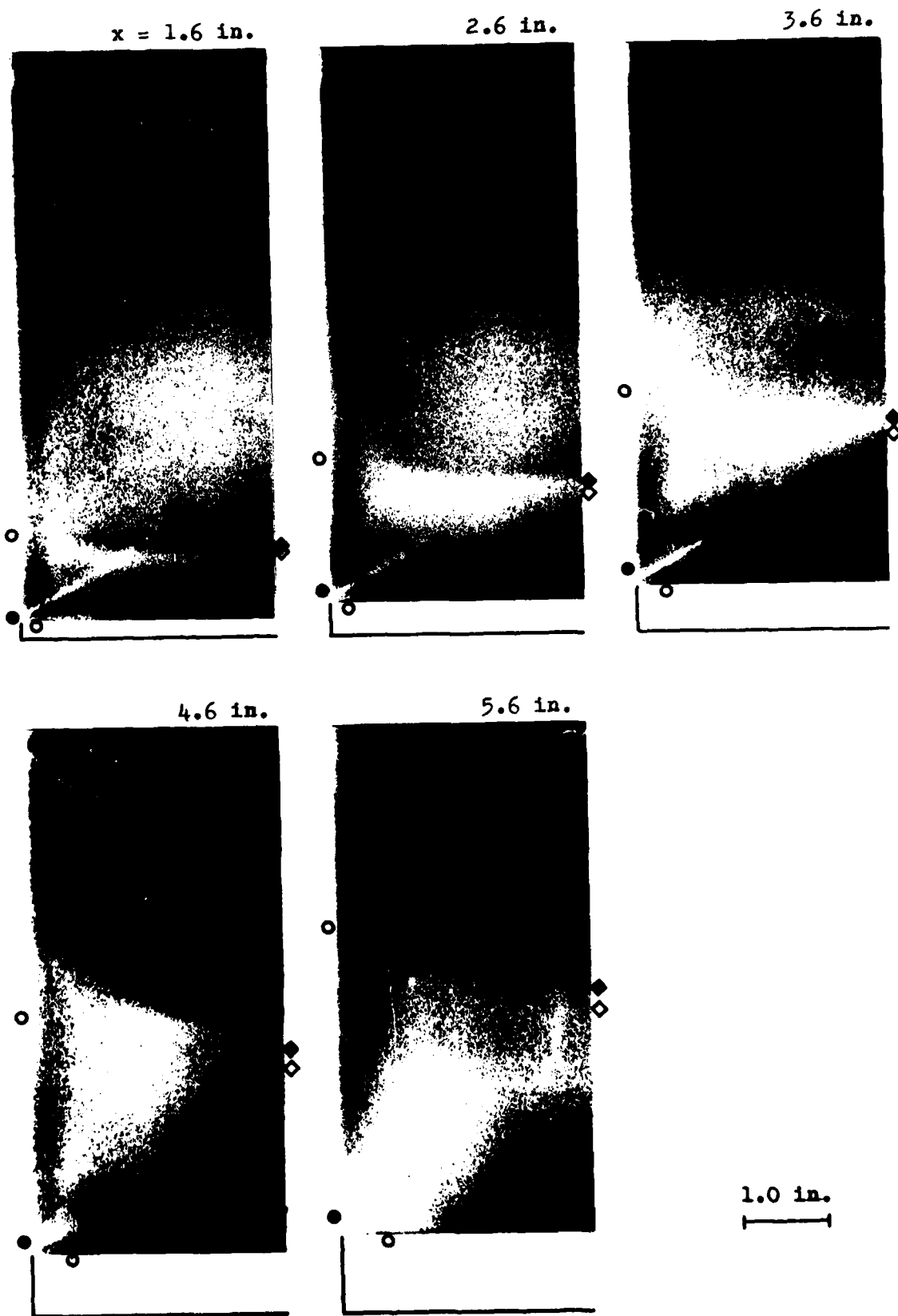


Fig. E4 Continued. (b)  $M = 2.3$ ,  $\delta_s = 10^\circ$

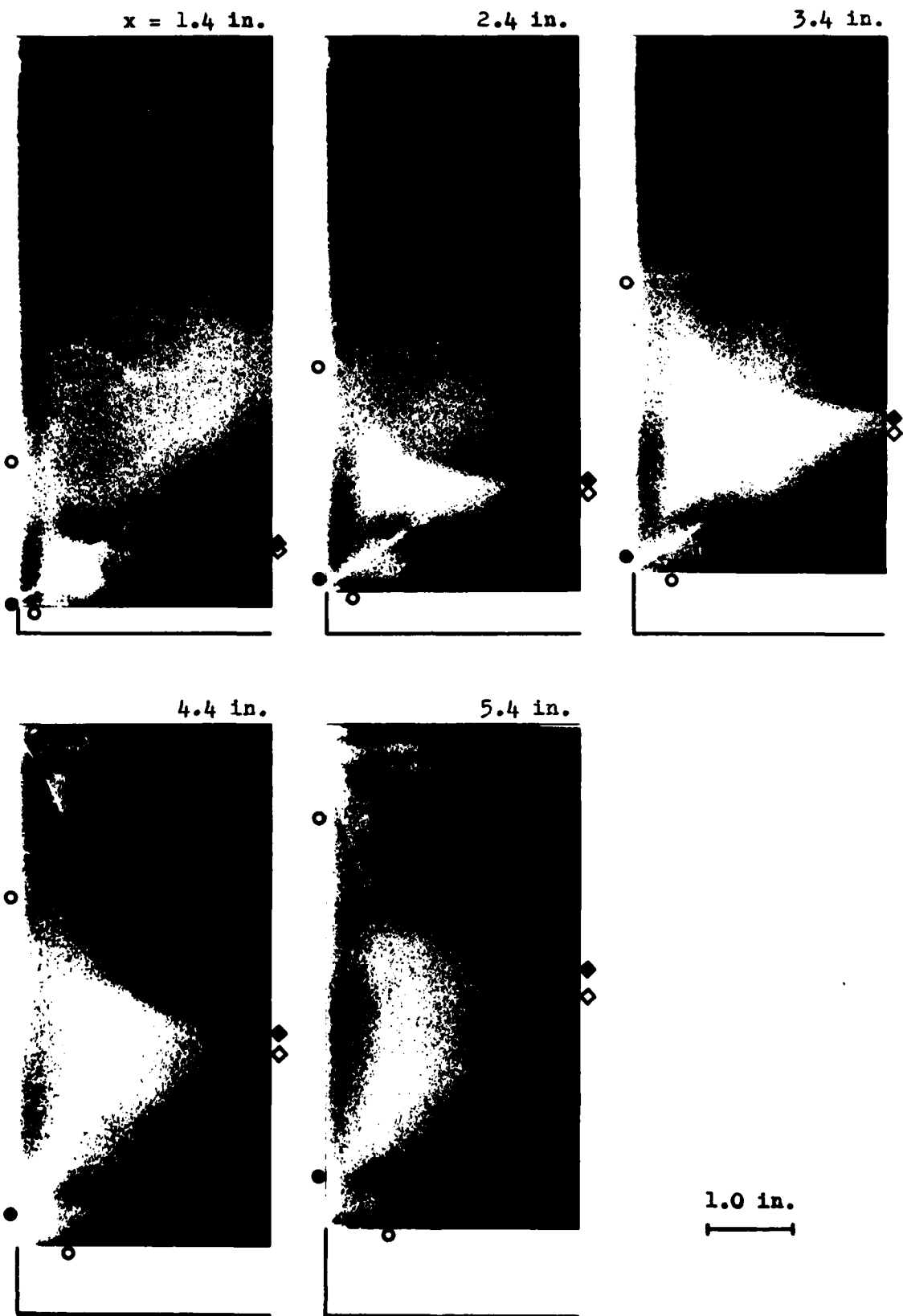


Fig. E4. Continued. (c)  $M = 2.3$ ,  $\theta_g = 13^\circ$

I  
I

APPENDIX F

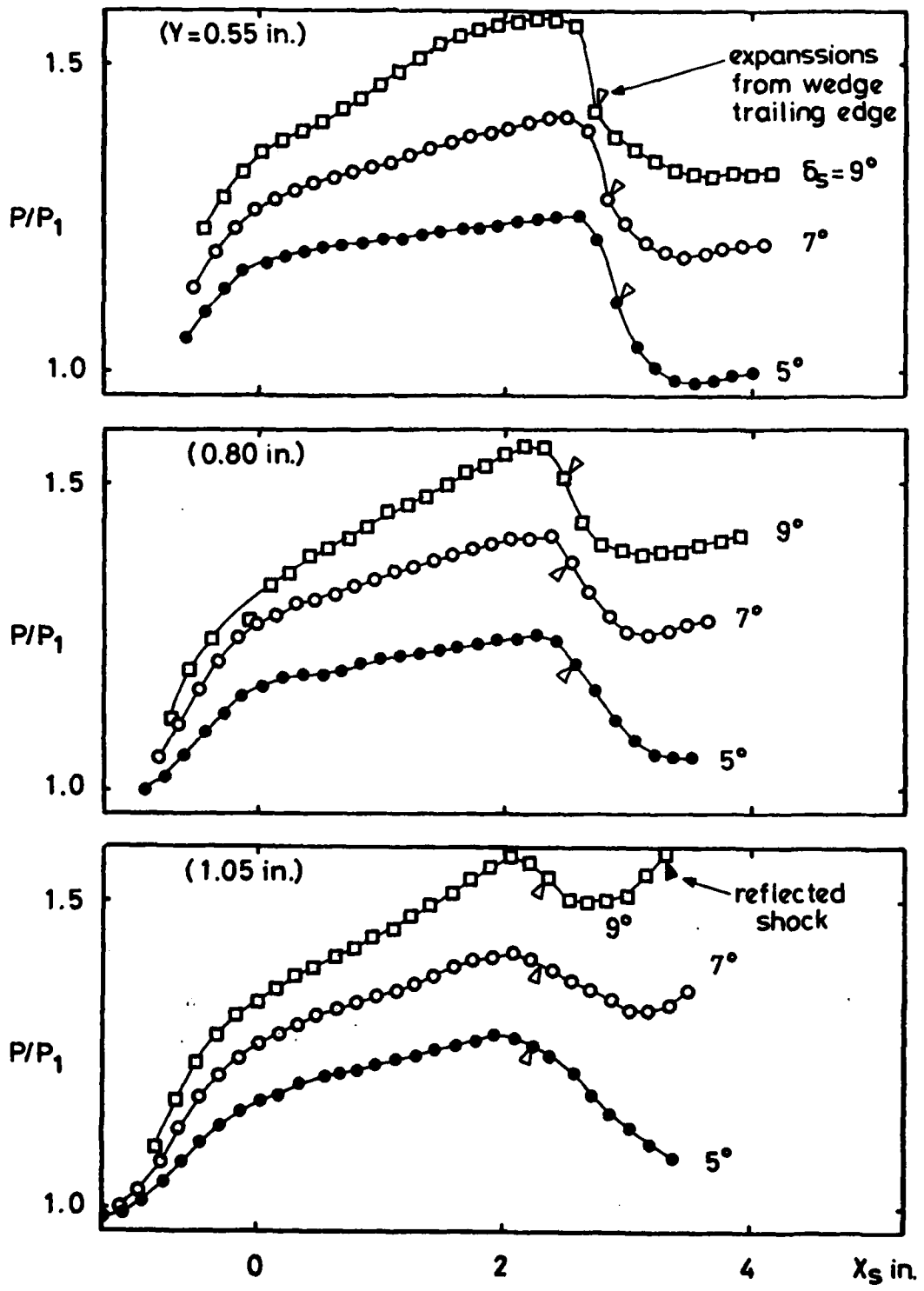


Fig. F1 Static Pressure Distributions (Model A)  
 (a)  $M = 2.4$

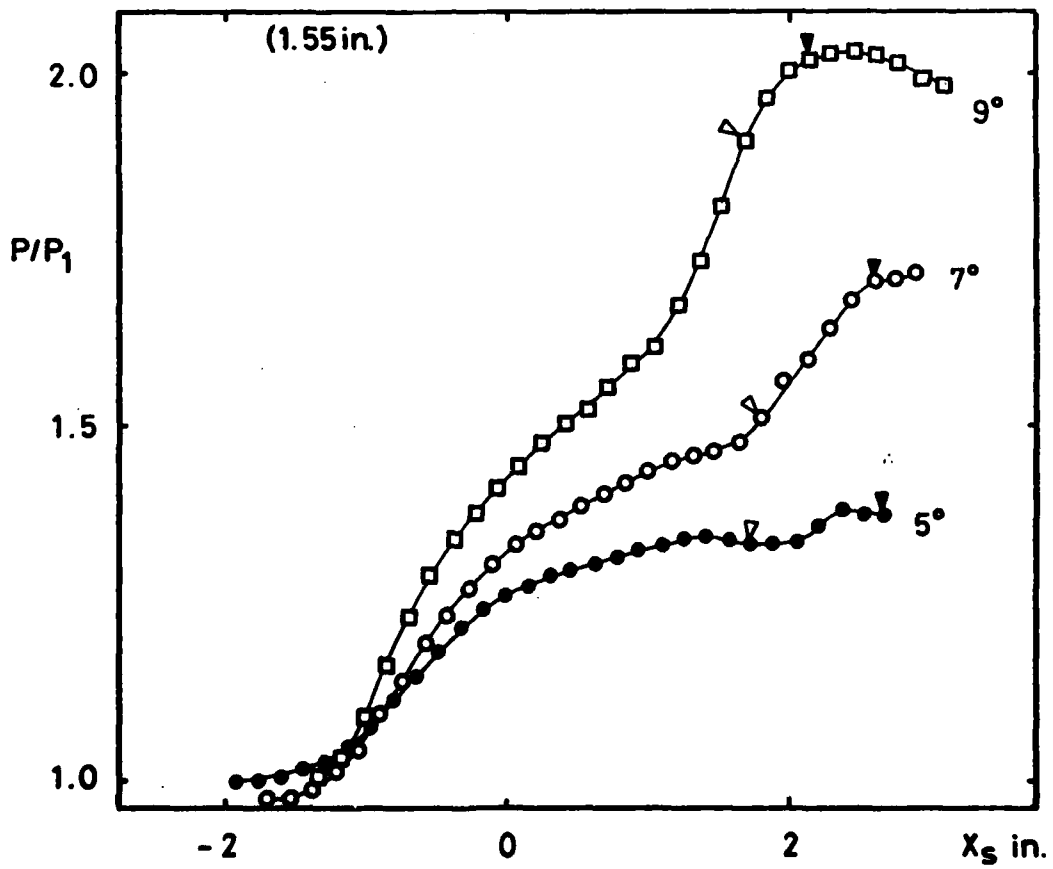
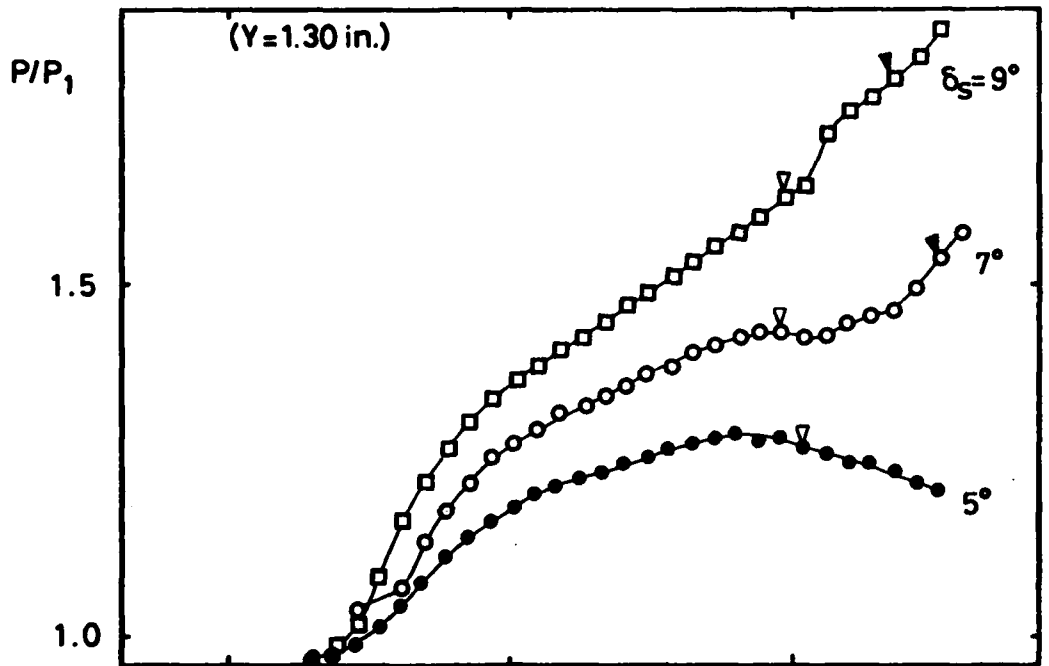


Fig. F1 Continued. (b)  $M = 2.4$

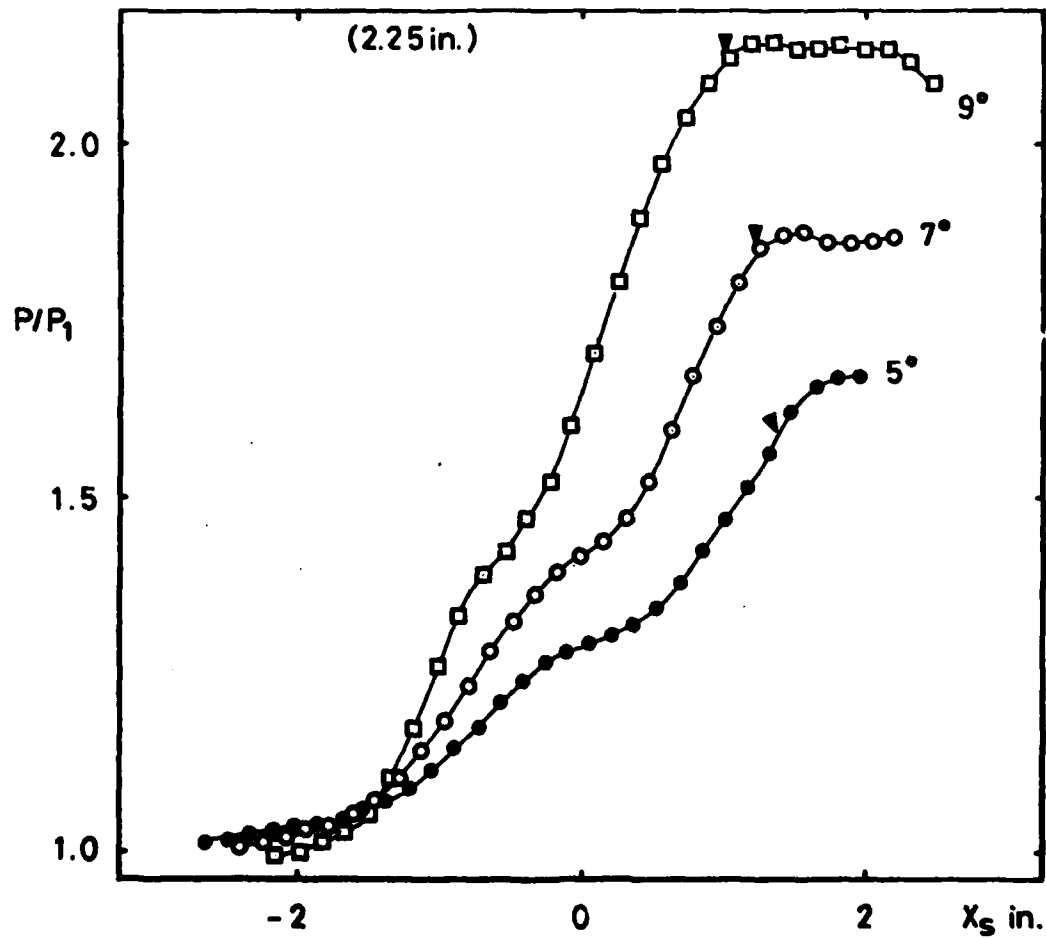
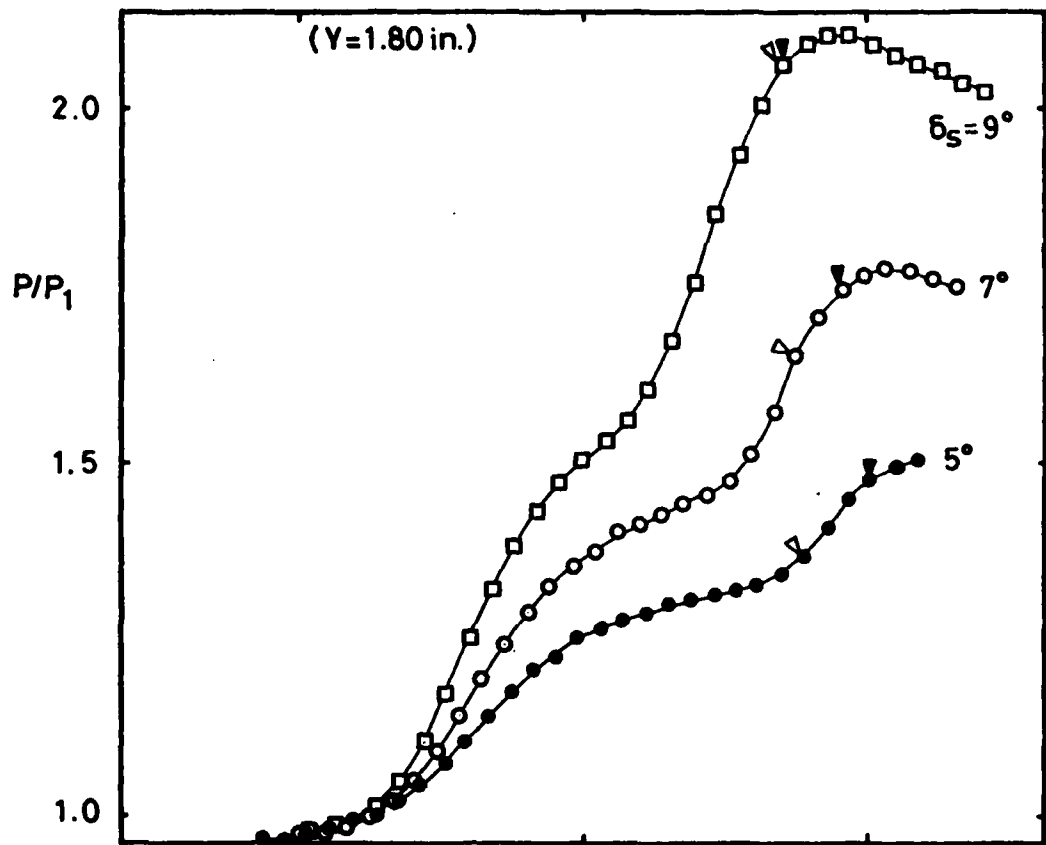


Fig. F1 Continued. (c.)  $M = 2.4$

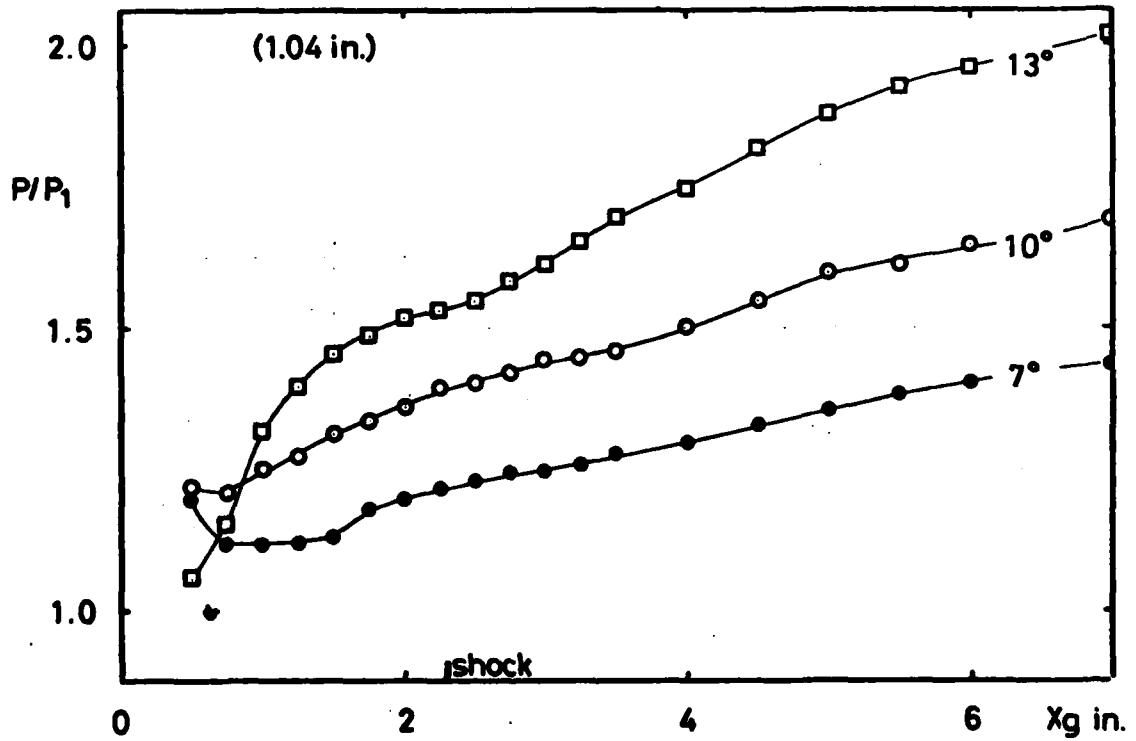
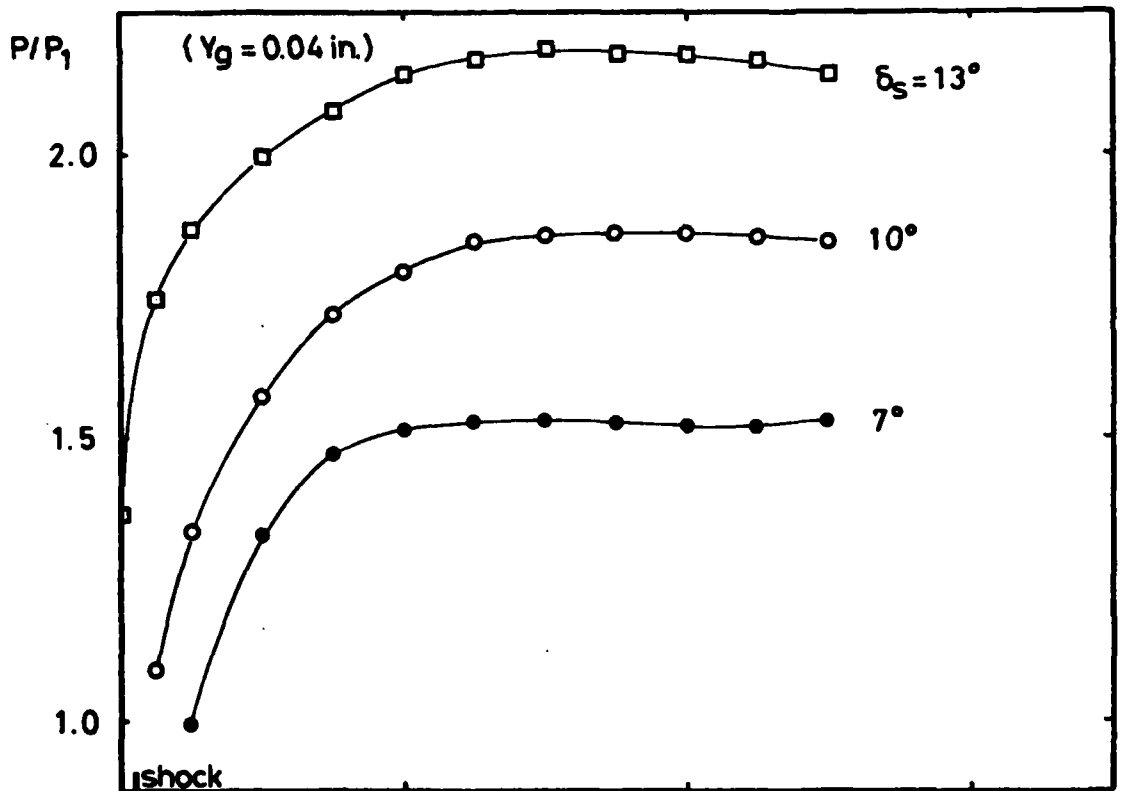


Fig. F2 Static Pressure Distributions (Model B)  
(a)  $M = 2.3$

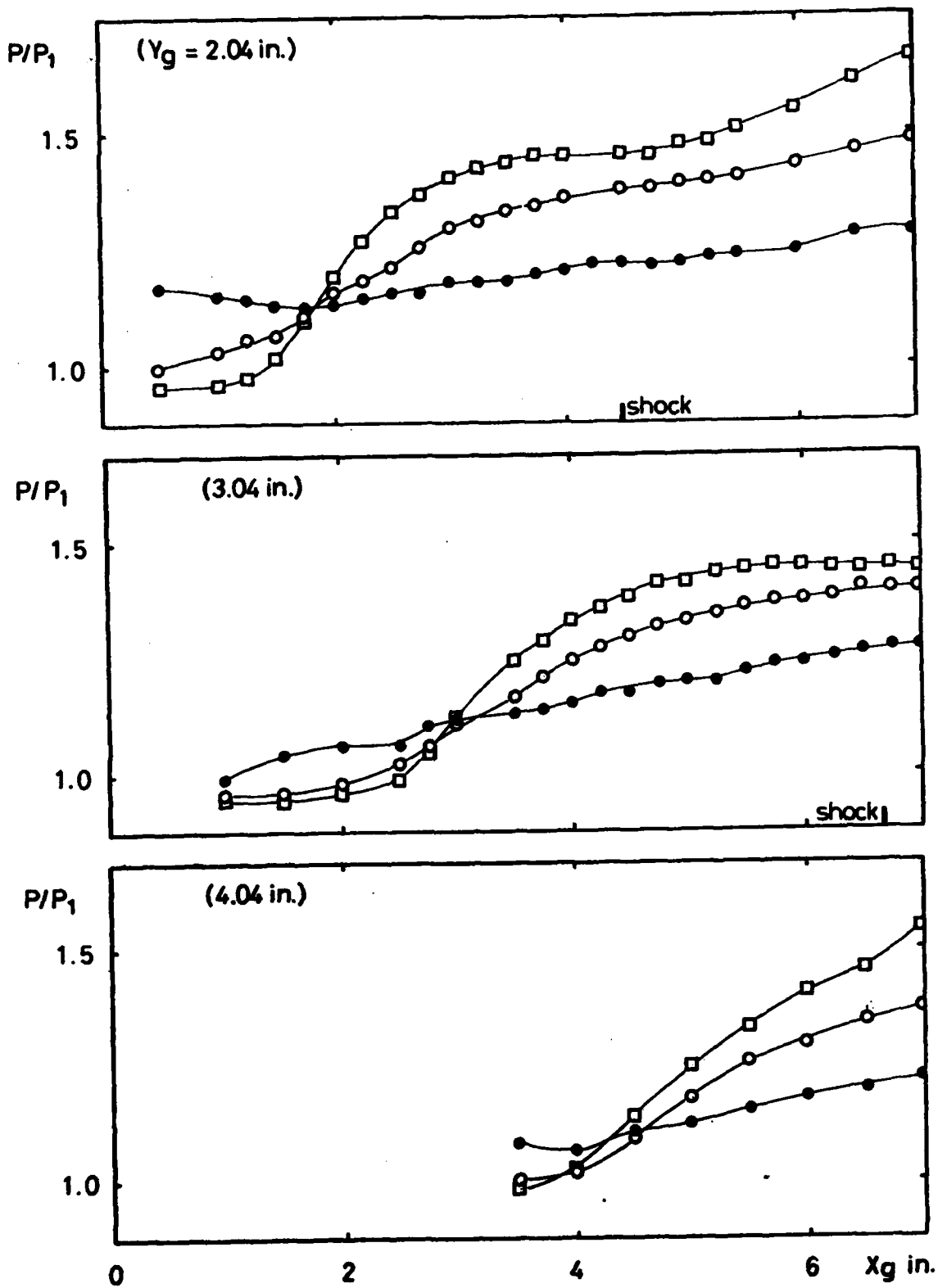


Fig. F2 Continued. (b)  $M = 2.3$

APPENDIX G

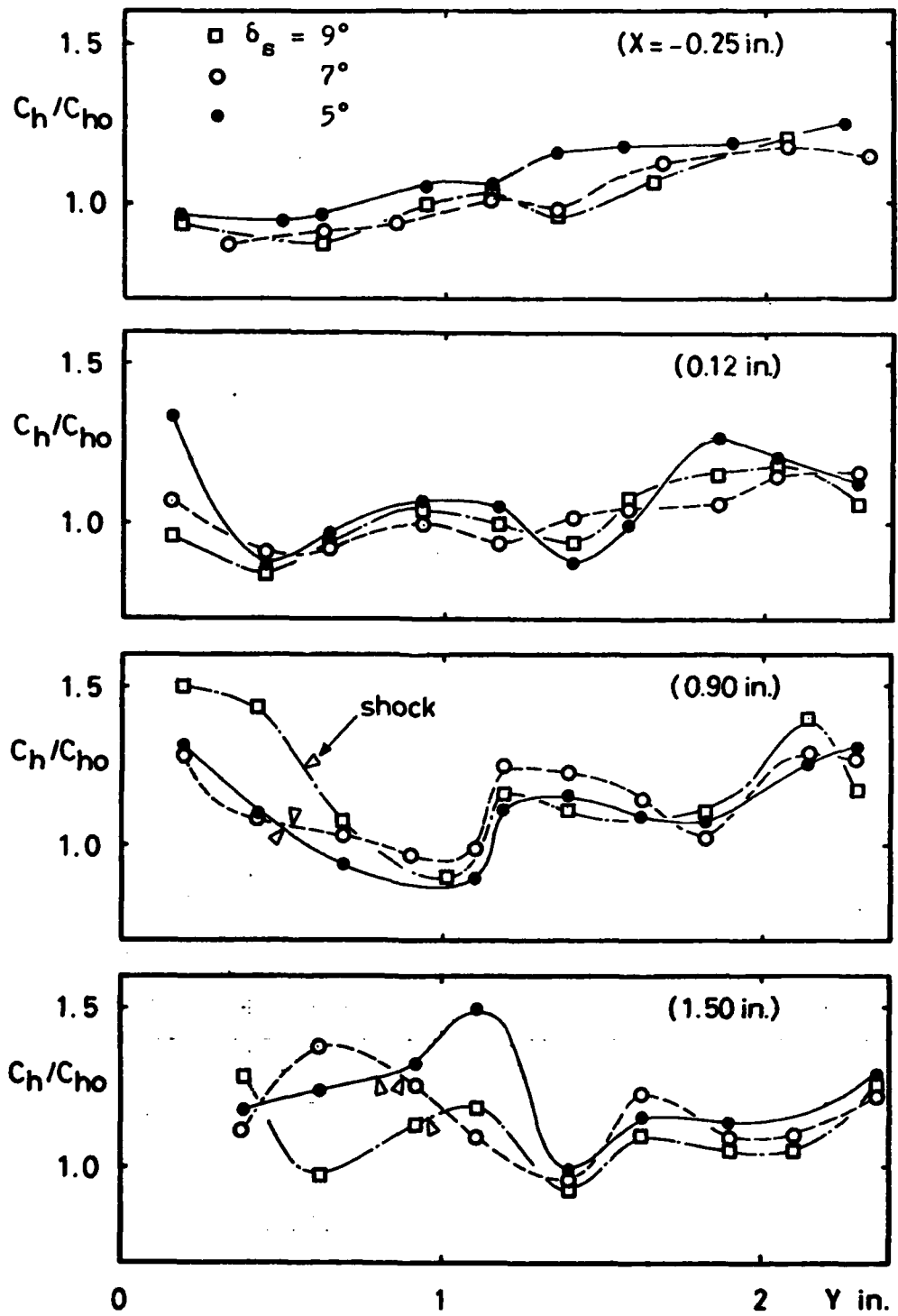


Fig. G1 Heat Transfer Distributions (Model A)  
(a)  $M = 2.4$

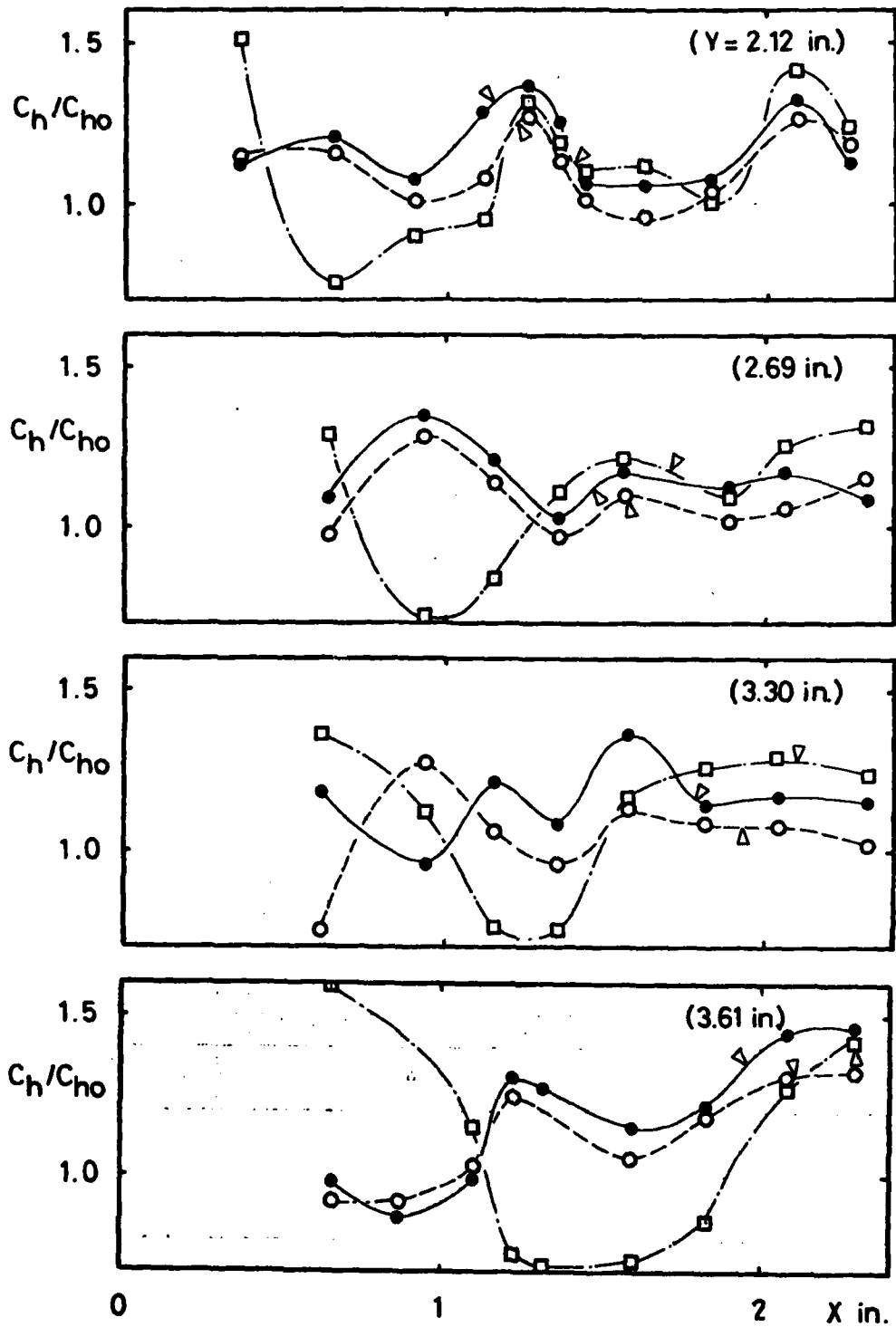


Fig. G1 Continued. (b)  $M = 2.4$

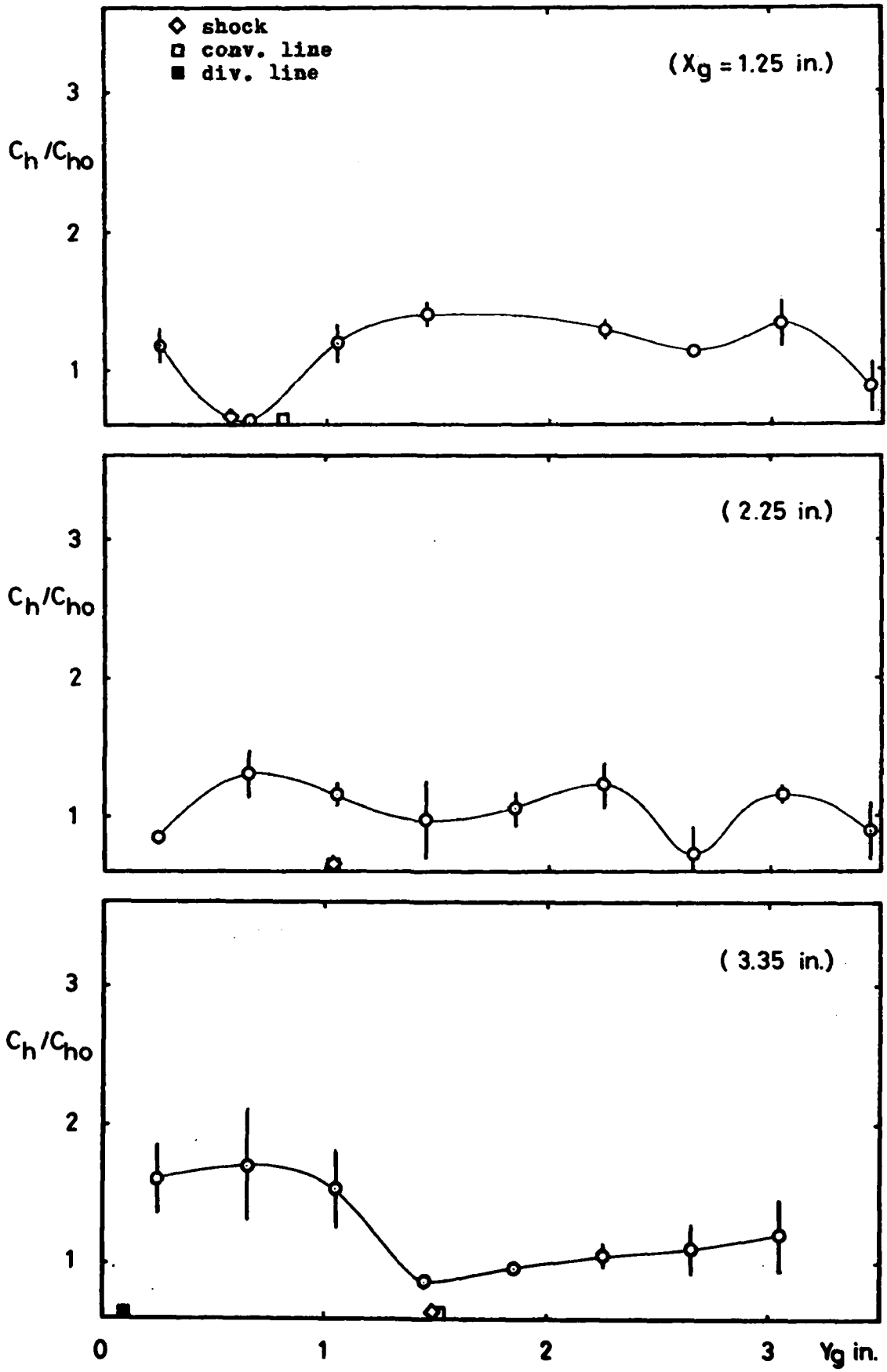


Fig. G2 Heat Transfer Distributions (Model B)  
 (a)  $M = 2.3, \delta_g = 7^\circ$

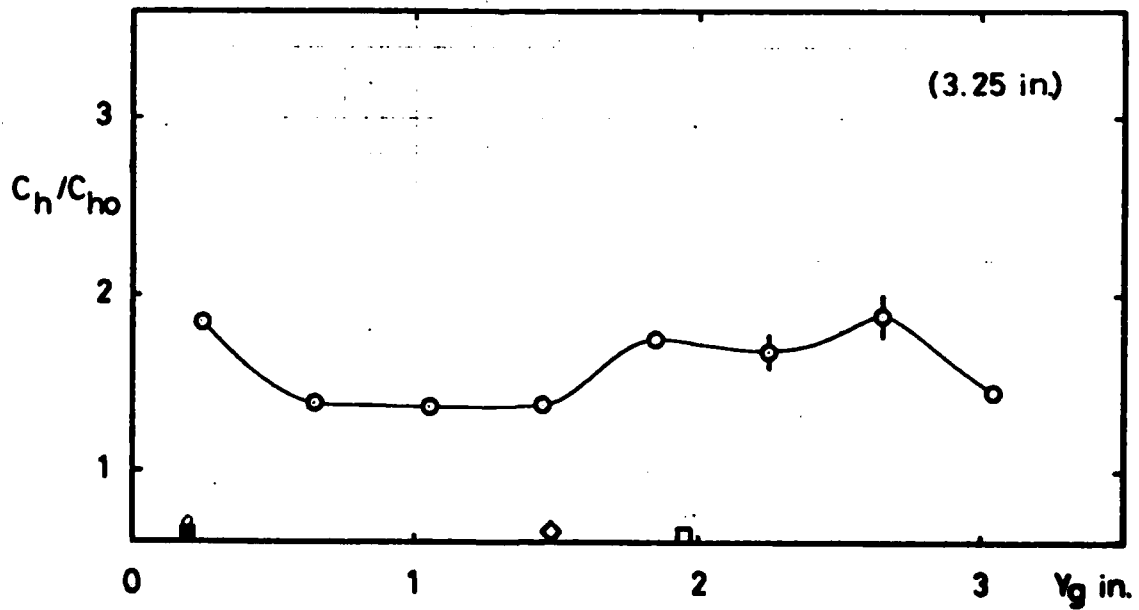
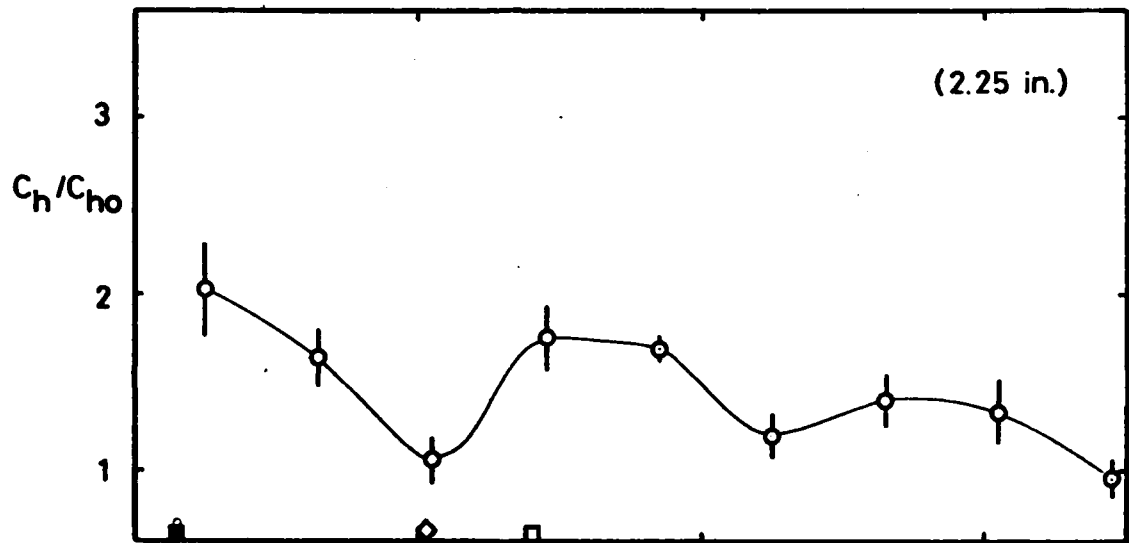
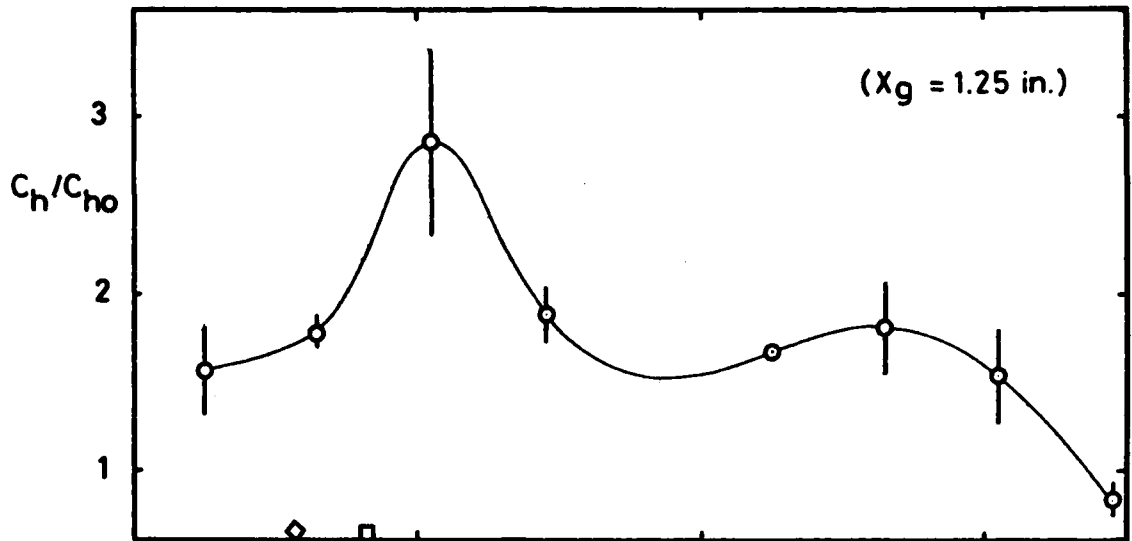


Fig. G2 Continued. (b)  $M = 2.3$ ,  $\theta_g = 10^\circ$

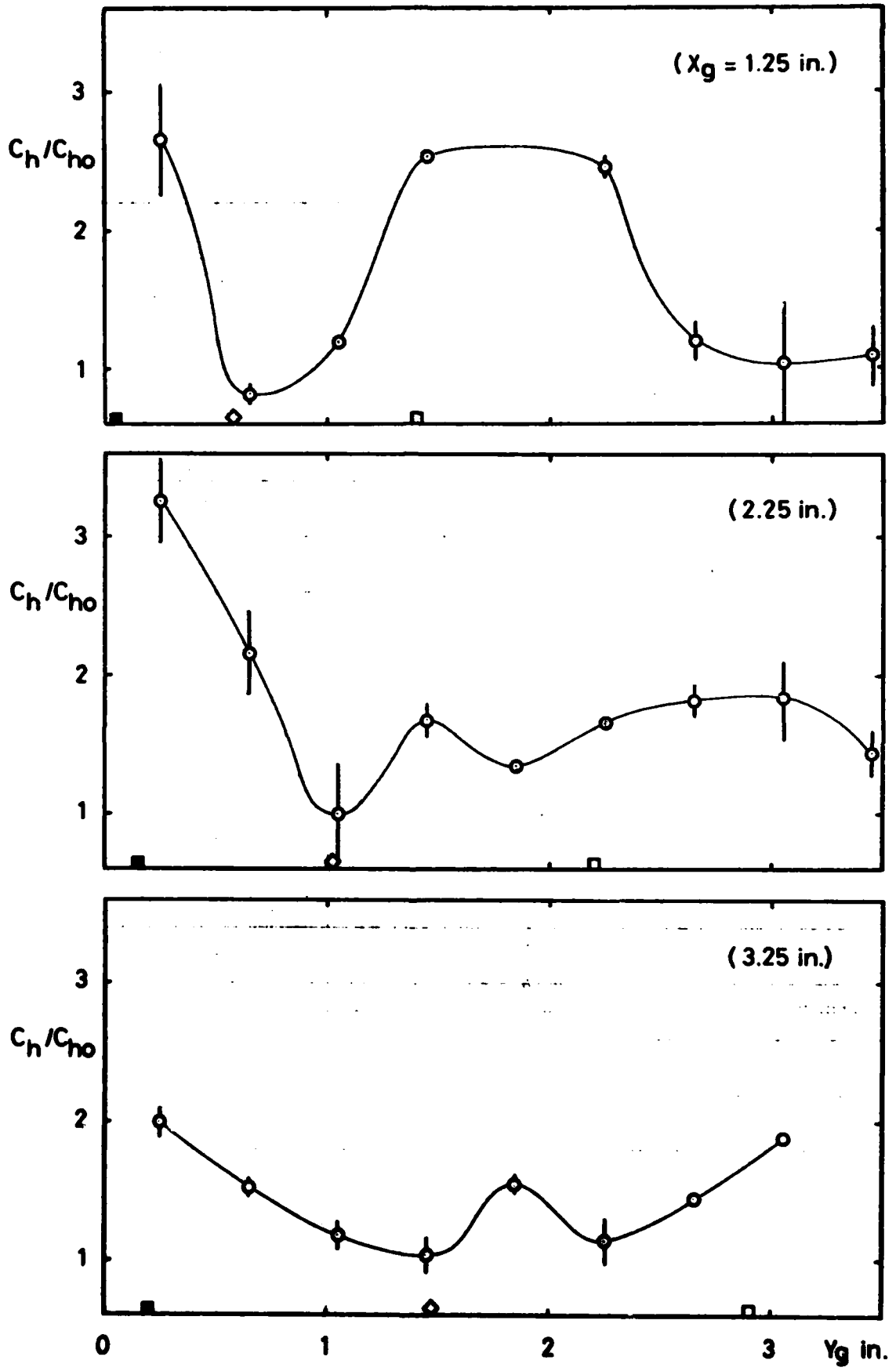


Fig. G2 Continued. (c)  $M = 2.3$ ,  $\theta_g = 13^\circ$

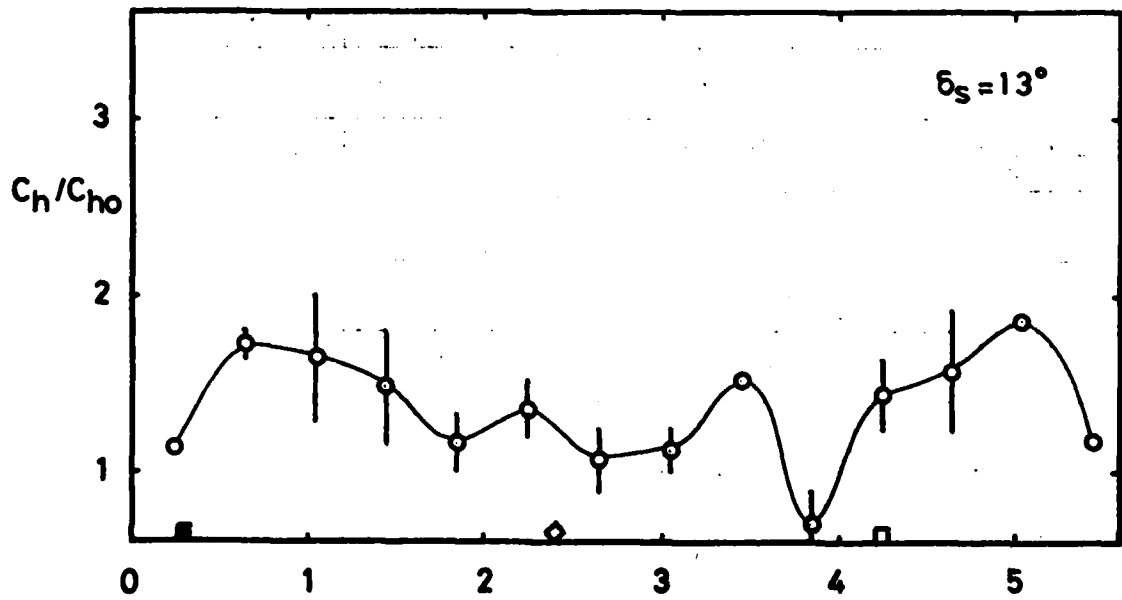
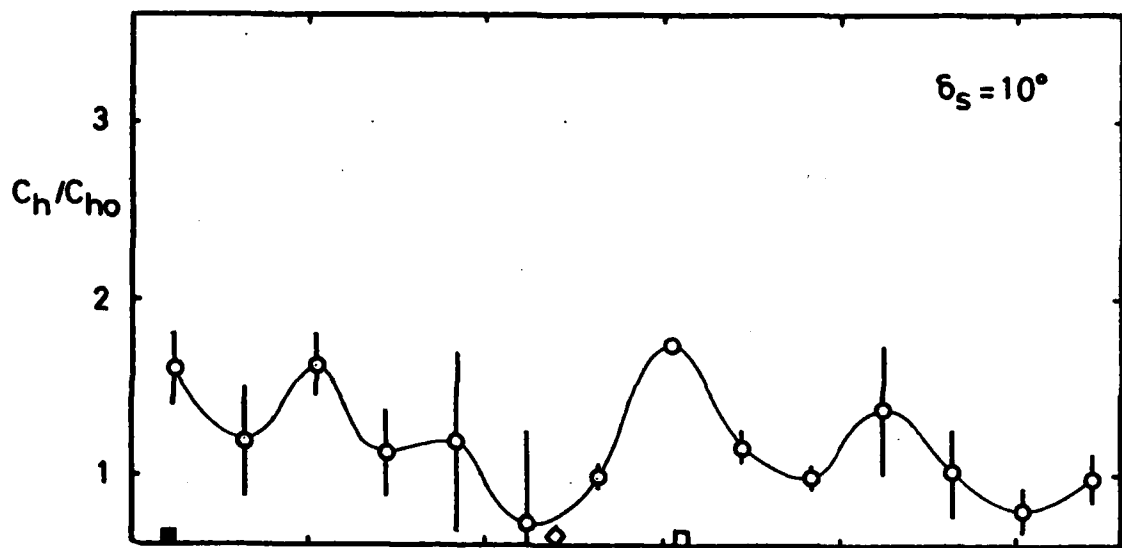
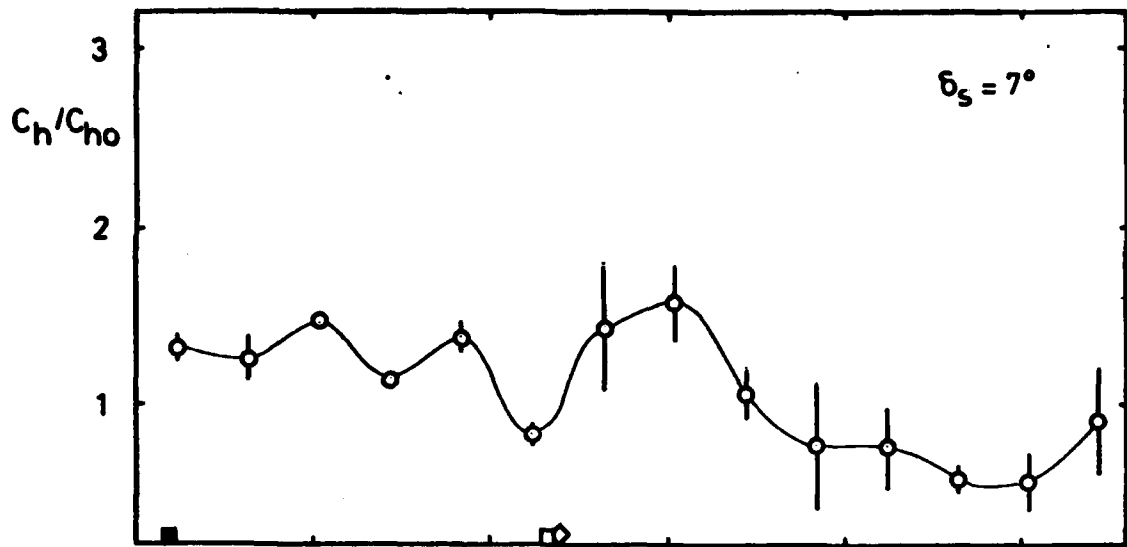


Fig. G2 Continued. (d)  $M = 2.3$ ,  $X_g = 5.25$  in.

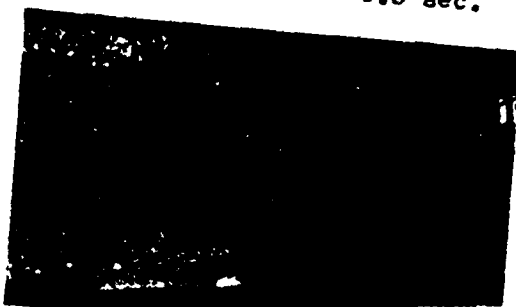
APPENDIX H



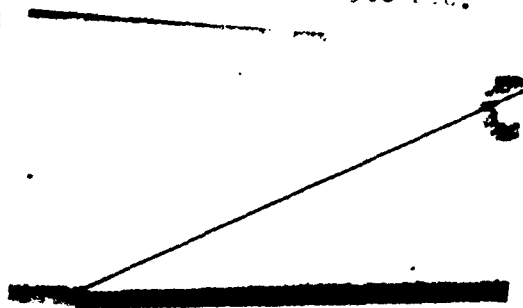
t = 0.0 sec.



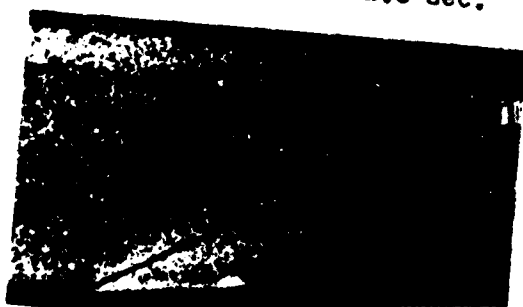
t = 5.0 sec.



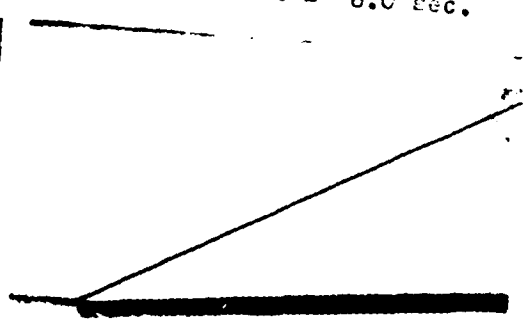
t = 2.0 sec.



t = 6.0 sec.



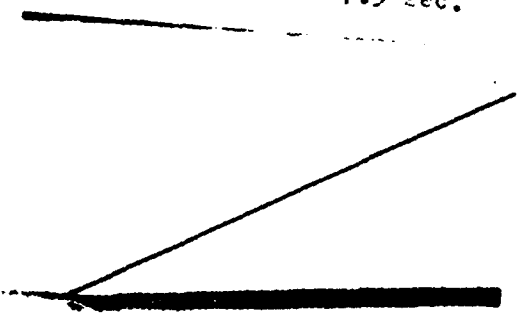
t = 2.5 sec.



t = 7.5 sec.



t = 3.5 sec.



t = 10.0 sec.

Fig. H Encapsulated Liquid Crystal Pictures (Model A)  
(a)  $M = 2.4$ ,  $\delta_s = 5^\circ$

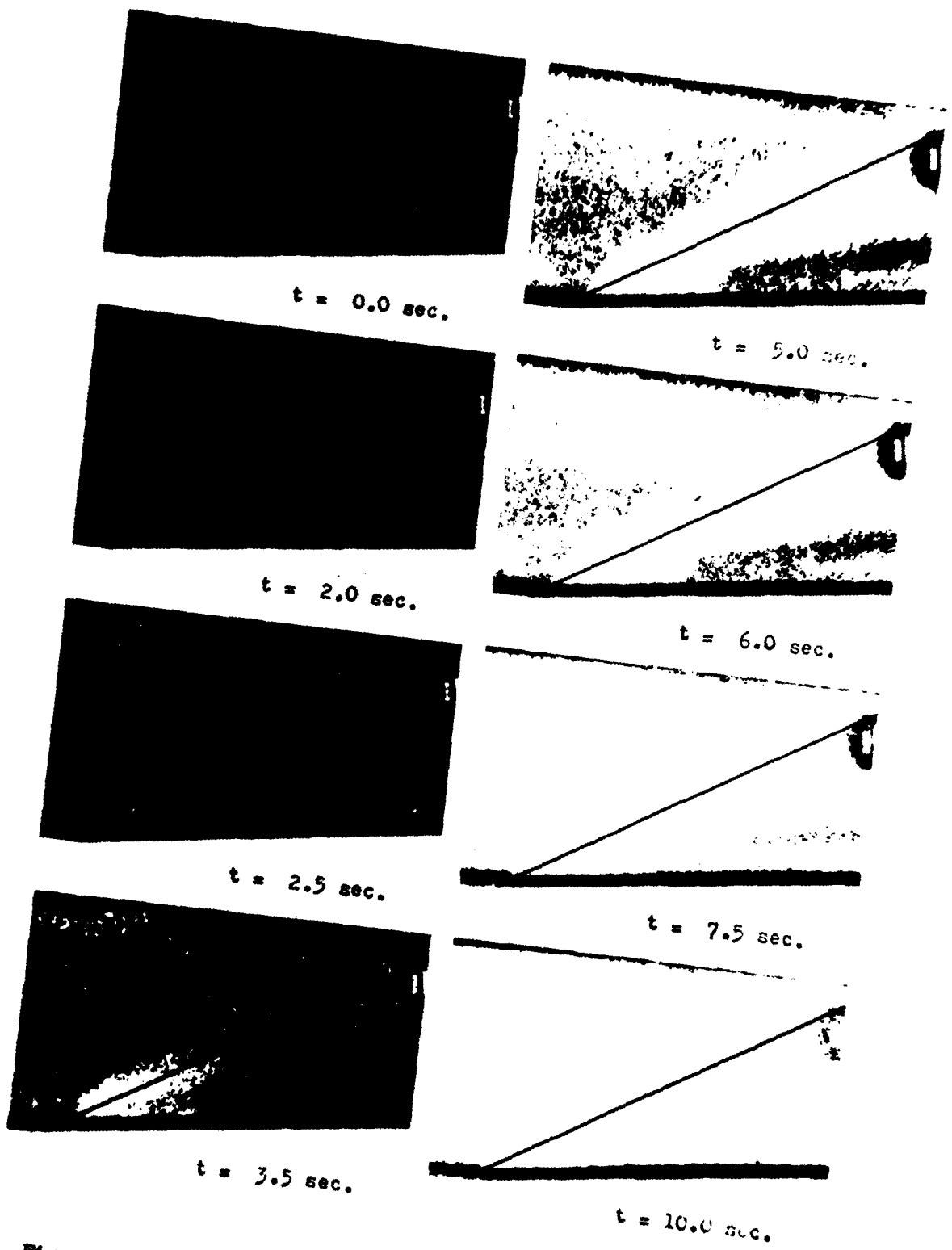
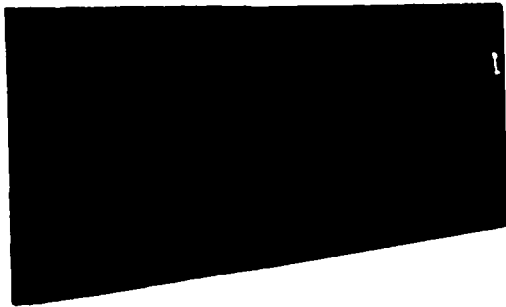


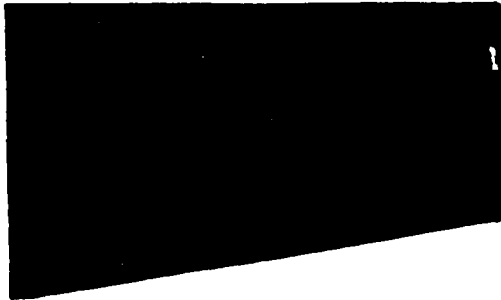
Fig. H Continued. (b)  $M = 2.4$ ,  $\delta_g = 7^\circ$



t = 0.0 sec.



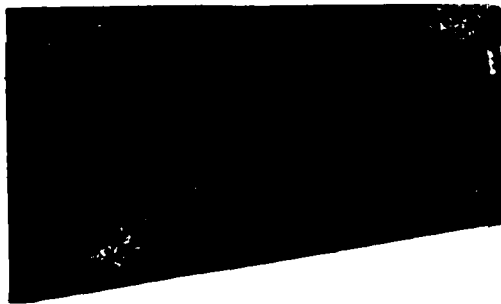
t = 5.0 sec.



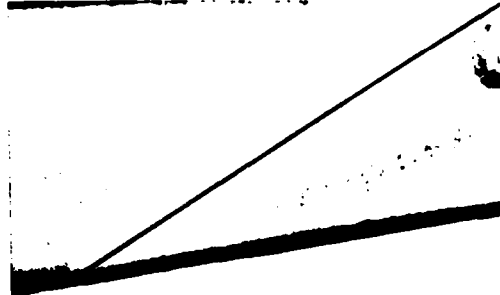
t = 2.0 sec.



t = 6.0 sec.



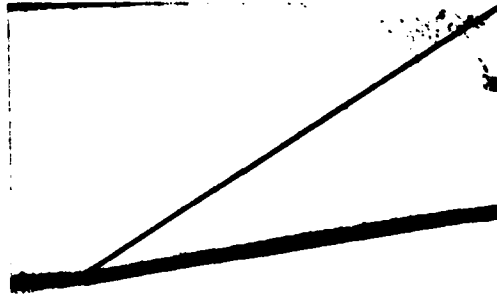
t = 2.5 sec.



t = 7.5 sec.



t = 3.5 sec.



t = 10.0 sec.

Fig. H Continued. (c)  $M = 2.4$ ,  $\delta_g = 9^\circ$

APPENDIX I

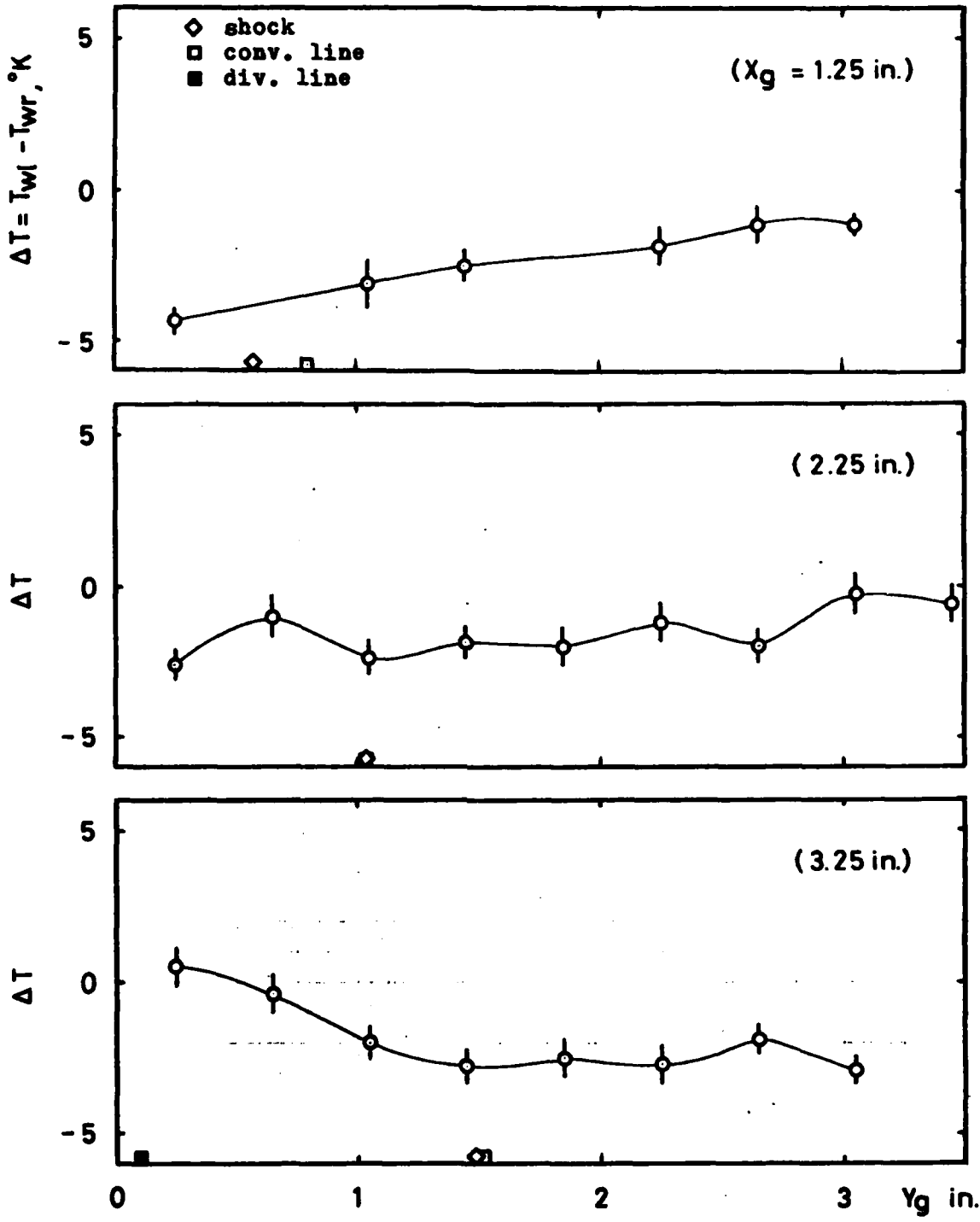


Fig. I Surface Temperature Distributions (Model B)  
 (a)  $M = 2.3$ ,  $\delta_s = 7^\circ$

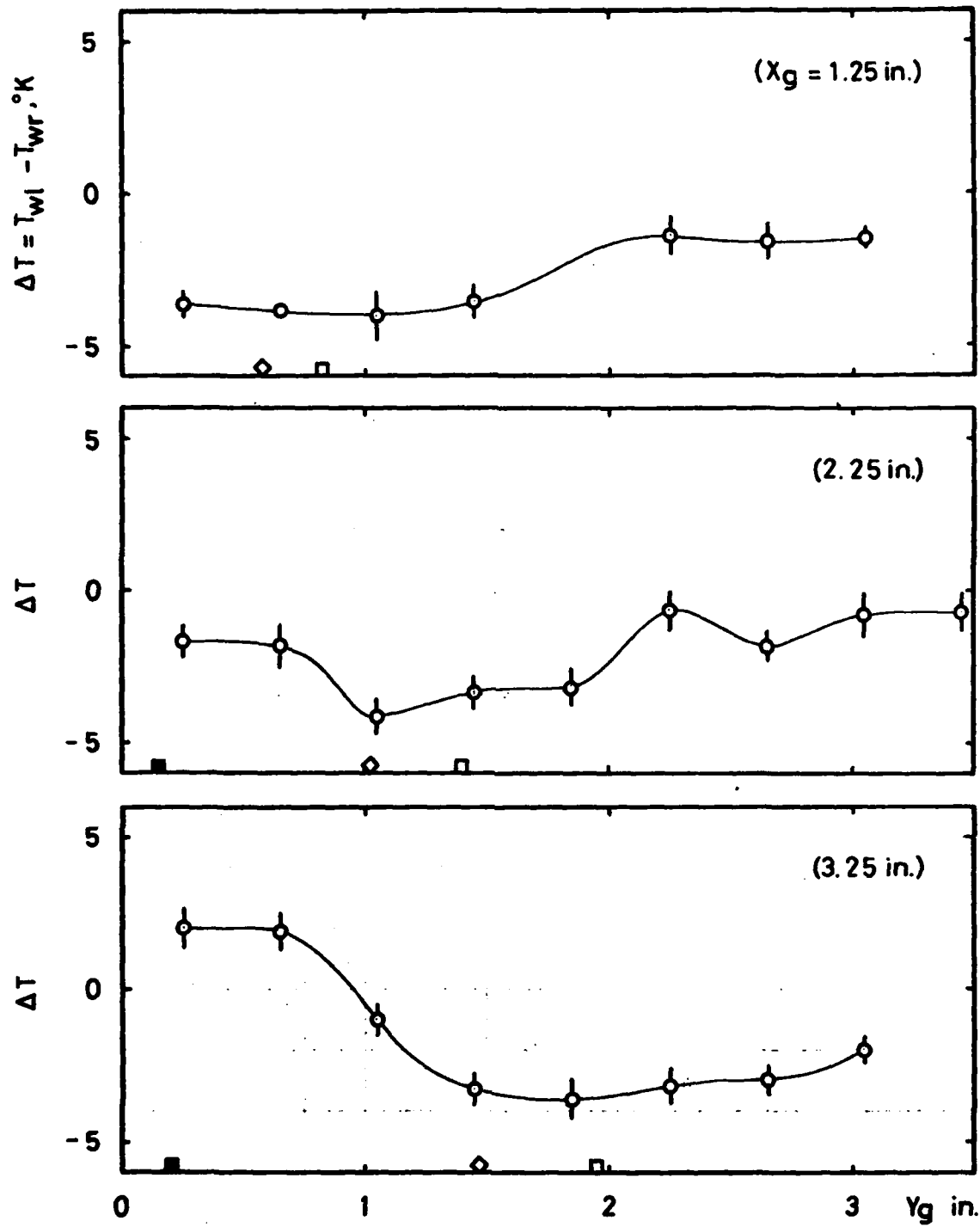


Fig. I Continued. (b)  $M = 2.3$ ,  $\delta_g = 10^{\circ}$

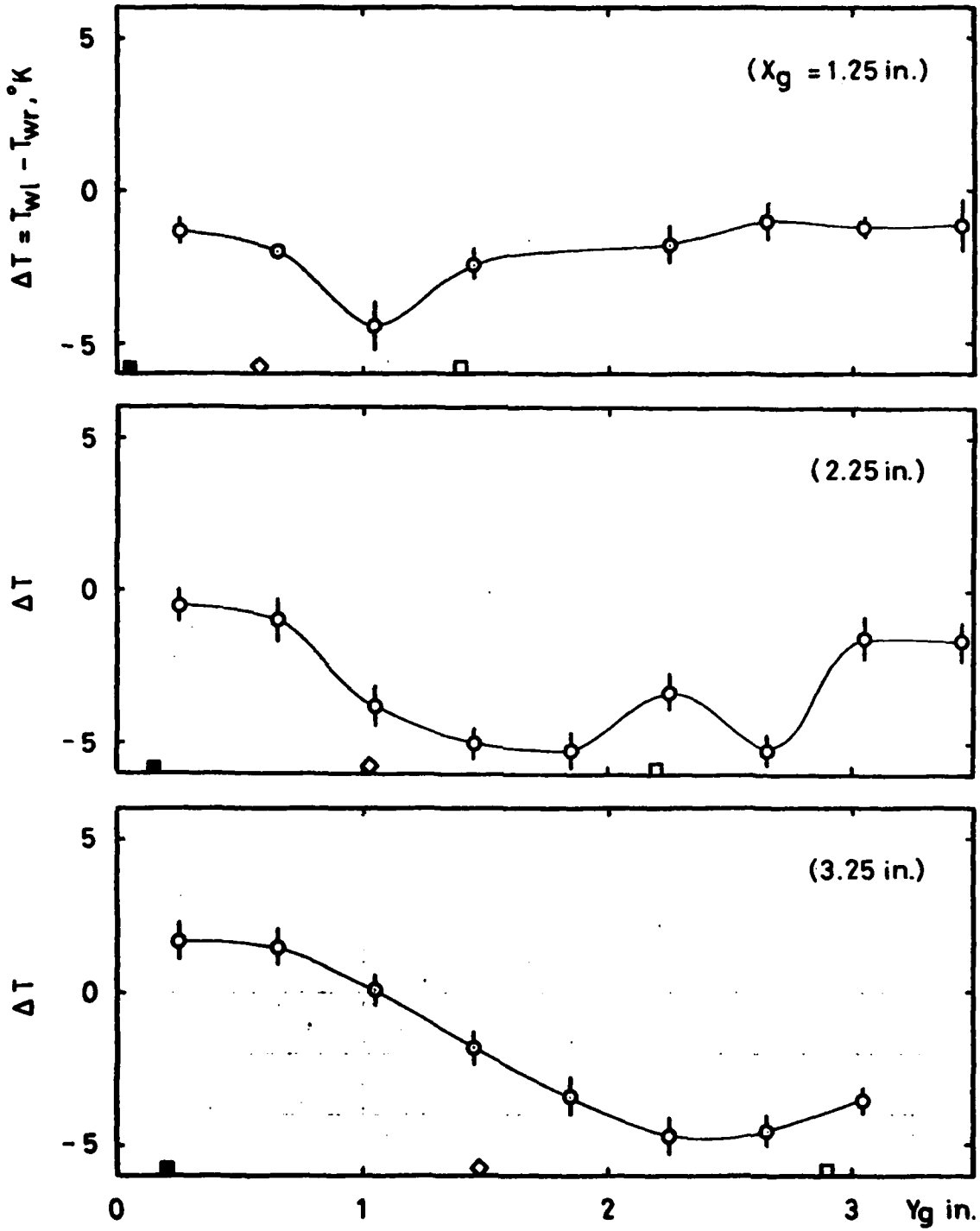


Fig. I Continued. (c)  $M = 2.3$ ,  $\delta_g = 13^\circ$

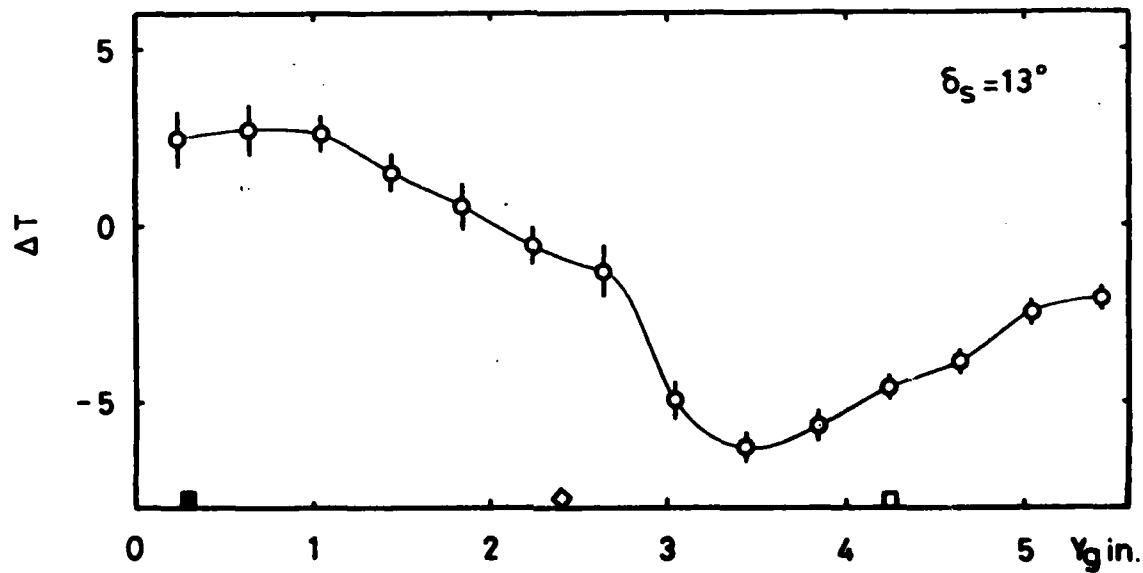
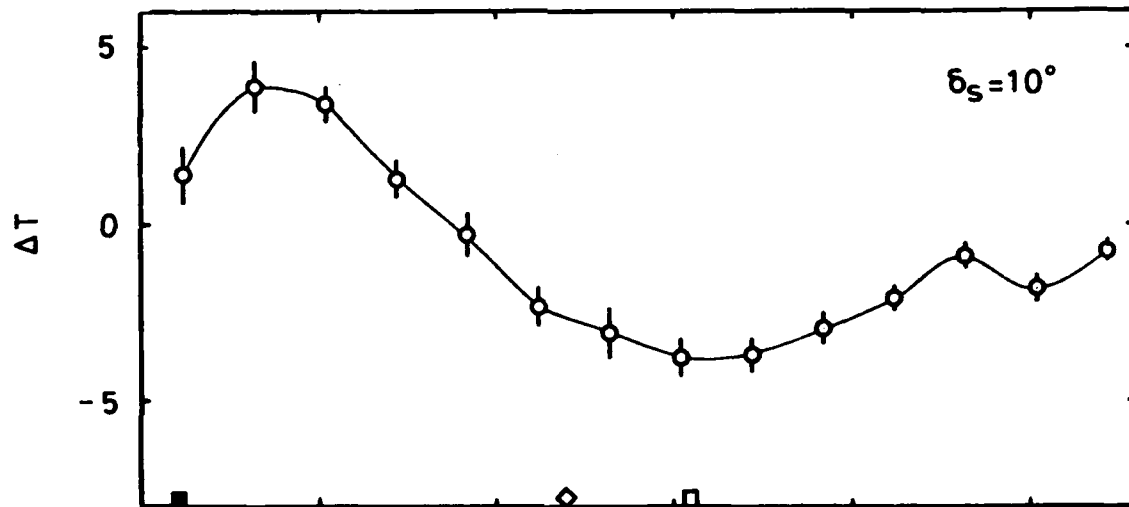
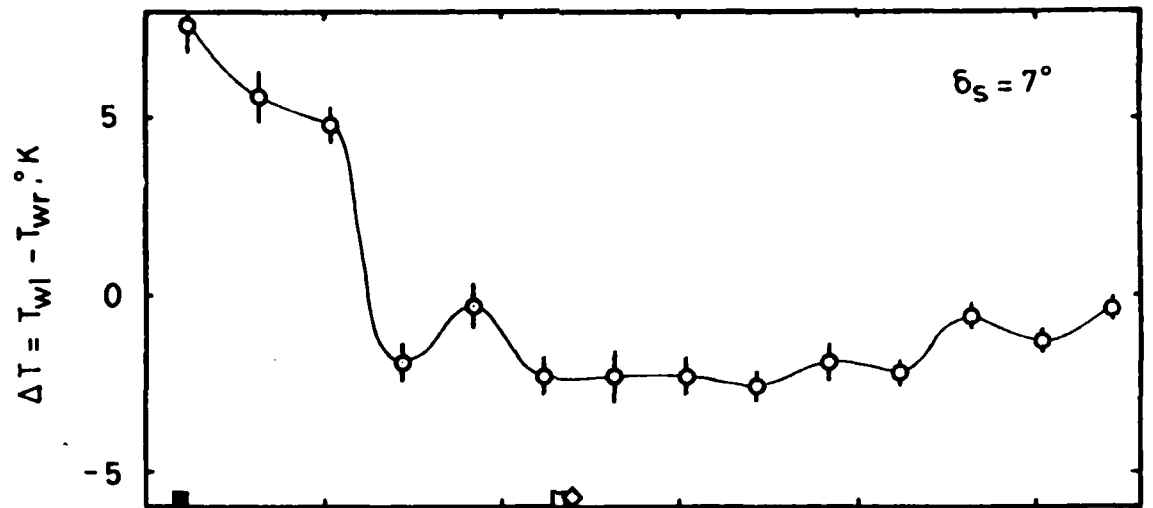


Fig. I Continued. (d)  $M = 2.3$ ,  $X_g = 5.25$  in.

